High Voltage Coefficient Piezoelectric Materials for Underwater Transducer Applications

Thomas Elliot Hooper

Submitted in accordance with the requirements for the degree of
Doctor of Philosophy

The University of Leeds

Functional Materials, Products & Devices

School of Chemical and Process Engineering

Primary Supervisor: Professor Andrew J Bell
Secondary Supervisor: Professor Steven J Milne

June 2020

The candidate confirms that the work submitted is his own, except where work which has formed part of a jointly authored publication has been included. The contribution of the candidate and the other authors to this work has been explicity indicated below. The candidate confirms that appropriate credit has been given within this thesis where reference has been made to the work of others.

The work in Chapter 4 of the thesis has appeared in publication as follows:
T. E. Hooper & A. J. Bell, Landau-Devonshire derived phase diagram of the $BiFeO_3$-$PbTiO_3$ solid solution, Journal of Applied Physics **127**, 104102 (2020)
I was responsible for generating data and figures, and writing of manuscript.
The contribution of other authors was supervision and advice, and providing feedback and edits of manuscript.

Acknowledgements

I would first and foremost like to thank my supervisor Professor Andrew Bell for his guidance, inspiration and encouragement through the years. His drive for more data, higher quality data and more thorough analysis and interpretation has made me a better scientist than I thought I could ever be.

I would also like to thank my industrial supervisor Dr. Laura Stoica from Thales UK Ltd for her continuous assistance, constructive feedback and stimulating conversations of all things from single crystals to manganese; the vastness of space to the perfect coffee.

I am truly indebted to the efforts of Rob Simpson throughout the years for his technical support and teaching of practical skills that have not only helped me during my time as a PhD student but will continue to help me throughout my career.

I gratefully acknowledge the help of Dr. Stephen Collins for proof-reading and insightful feedback, Mr. Stuart Micklethwaite with scanning electron microscopy, Dr. Andrew Britton for his help with X-ray photoelectron spectroscopy, Dr. Richard Foster for his assistance with MatLab and Dr. Philippa Shepley for her help with impedance spectroscopy data processing.

A big thank you to the Electroceramics group at the University of Leeds both past and present, particularly Dr. Sam Parry and Dr. Anton Goetzee-Barral. It has been a pleasure to work alongside you.

Thank you to everyone in the Acoustics team at Thales UK Ltd who made my placement informative and comfortable. Particular thanks go to Dr. Andrew Mathieson for sharing his vast knowledge of piezoelectric devices and industry standard testing of piezoelectric materials. Thank you also to Mr. Alan Elliott formerly of Thales UK Ltd for his interest and enthusiasm in this project.

Greatly appreciated is the help from Dr. Tim Comyn of Ionix Advanced Technologies for his advice on material processing and characterisation. Furthermore, I acknowledge the help of Dr. Tim Stevenson also of Ionix Advanced Technologies and Mr. Graham Brown of the University of Leeds for their assistance in crucible welding.

Thank you to the external examiner, Professor Tim Button, and internal examiner, Professor Rik Drummond-Brydson, for taking the time to assess this work and for the stimulating conversation and feedback.

Finally, an enormous thank you to my Mum, Dad, Joe, Gabbi and Mark for their relentless support, encouragement, positivity and patience through thick and thin. You always believed in me, even at times when I didn't believe in myself - I dedicate this thesis to you.

Abstract

An investigation into the piezoelectric voltage coefficient (g_{ij}) has been carried out from a fundamental materials science perspective. For single crystals, the tetragonality is found to be the structural driving force for high polarisation and g_{ij} coefficients. Textured ceramics also exhibit high g_{ij} values due to the degree of grain and polarisation orientation. For polycrystalline ceramics, the presence of grains and grain boundaries and the associated elastic stresses suppresses g_{ij} at high tetragonalities.

Landau-Devonshire theory has been applied to $BiFeO_3$-$PbTiO_3$ to highlight its potential as a high g_{ij} candidate. Initially the compositional dependence is modelled by applying Vegard's law between the Landau coefficients of each end member. Whilst this manages to replicate the experimentally constructed phase diagram, the spontaneous strain behaviour is incorrectly described. The second method models the compositional dependence as an external tensile stress which acts to elongate the unit cell within the tetragonal phase, and as a shear stress within the rhombohedral region to reduce the angle between the polarisation and [001]. Using this method, the g_{33}, g_{31}, g_{15} and g_h for $0.70BiFeO_3$-$0.30PbTiO_3$ are calculated to be 0.208, -0.061, 0.078 and 0.087 Vm/N, respectively; significantly larger than current military grade devices and previously reported materials.

Nb-doping of $0.65BiFeO_3$-$0.35PbTiO_3$ has been carried out to reduce conductivity. For all doping regimes, the low-signal AC and DC conductivity decreases by up to an order of magnitude. Initially Nb-doping hinders the piezoelectric activity however once annealed, g_{33} values improve by up to 10 times for some compositions. Impedance spectroscopy, P/x-E loops and X-ray photoelectron spectroscopy show that the piezoelectric behaviour is dictated by the degree of defect distribution, with annealed samples possessing a more distributed defect network and an increase in domain wall mobility. A cooling rate study showed that whilst a more randomly distributed defect structure is achieved compared to unannealed samples, quenching decreases the piezoelectric activity due to the larger intergranular stress when transitioning through T_C.

Contents

List of Figures

List of Tables

List of Abbreviations

ABO_3	General formula for a perovskite
AC	Alternating Current
BF	Bismuth Ferrite
BFPT	Bismuth Ferrite Lead Titanate
CPE	Constant Phase Element
DC	Direct Current
DIS	Dielectric Impedance Spectroscopy
EDX	Energy Dispersive X-ray
FE	Ferroelectric
ICDD	International Centre for Diffraction Data
IPA	Iso-2-propanol
MPB	Morphotropic Phase Boundary
P-E	Polarisation - Electric Field
PMN-PT	Lead Magnesium Niobate - Lead Titanate
PT	Lead Titanate
PZT	Lead Zirconate Titanate
RVS	Receiving Voltage Sensitivity
SEM	Scanning Electron Microscopy
SONAR	SOund Navigation And Ranging
XRD	X-Ray Diffraction
XPS	X-ray Photoelectric Spectroscopy

List of Symbols

a_C	Cubic lattice parameters
a_R	Rhombohedral lattice parameters
a_T	Tetragonal short-axis lattice parameters
A	Area
Å	Angstrom (10^{-10}m)
B	Constant phase element pre-exponential factor
c_T	Tetragonal long-axis lattice parameters
C	Capacitance
C'	Real capacitance
C''	Imaginary capacitance
C_{CW}	Curie-Weiss Constant
d	Distance
d_{ij}	Piezoelectric charge coefficient
D	Electric displacement
e'	Electron
E	Electric field
E_A	Activation energy
E_b	Breakdown field
E_C	Coercive field
f	Frequency
F	Force

F_t	Tolerance factor-electronegativity function
g_{ij}	Piezoelectric voltage coefficient
ΔG	Gibbs free energy
G_L	Landau free energy
G_{EL}	Elastic free energy
G_{COUP}	Electrostrictive free energy
G_{ES}	Electrostatic free energy
$\mathrm{h}^{\cdot}$	Hole
I	Current
j	$\sqrt{-1}$
k	Electromechanical coupling factor
k_b	Boltzmann constant
M*	Complex modulus
M'	Real modulus
M''	Imaginary modulus
M_{ij}	Hydrophone sensitivity
m	Dielectric relaxation distribution parameter
p_i	Incident pressure of an acoustic wave
P	Polarisation
P_i	Orthogonal polarisation along the [100] (i=1), [010] (i=2) and [001] (i=3)
P_{max}	Maximum polarisation
P_R	Remanent polarisation
P_S	Spontaneous polarisation
q	Charge
Q_{ij}	Electrostriction coefficients
Q_m	Mechanical quality factor

R	Resistance
r_A	Ionic radius of A-site ion
r_B	Ionic radius of B-site ion
r_O	Ionic radius of oxygen ion
R_{wp}	Weighted R-profile
R_{exp}	Expected R-fraction
s_{ij}	Elastic compliance
t	Time
t_G	Goldschmidt tolerance factor
T	Temperature
T_C	Curie temperature
$tan\delta$	Dielectric loss factor or dissipation factor
V	Voltage
x_i	Strain
X_i	Stress
Y*	Complex admittance
Y'	Real admittance
Y''	Imaginary admittance
Z*	Complex impedance
Z'	Real impedance
Z''	Imaginary impedance
α_{ijk}	Landau coefficients or dielectric stiffness coefficients
Λ	Activation energy pre-exponential factor
ϕ	Electrical phase shift
Γ	Power density of an active sonar transducer
$\epsilon*$	Complex permittivity

ϵ_r	Relative permittivity
ϵ'	Real permittivity
ϵ''	Imaginary permittivity
ϵ_0	Permittivity of free space
ζ	Impermittivity
η	Dielectric susceptibility
λ	Wavelength
σ	Conductivity
σ_{AC}	AC conductivity
σ_{DC}	DC conductivity
μ	Electric dipole moment
ω	Angular frequency
ξ	Dielectric stiffness
χ	Electronegativity
Θ	Angle in degrees

Chapter 1

Introduction

The ability of piezoelectric materials to convert mechanical energy into electrical energy and vice versa has resulted in them being exploited in applications such as transducers and actuators for many decades [1]. Often the figure of merit for a piezoelectric material is the piezoelectric charge coefficient (also referred to as the d_{ij} coefficient) which represents the amount of surface charge per pascal. Lead zirconate titanate (Pb(Zr,Ti)O_3 or PZT) has been the cornerstone of piezoelectric devices due to its high performance and versatility through doping and compositional variation with some compositions reaching a d_{33} of ≈750pC/N [2]. However over the past couple of decades the development and commercial availability of high performance piezoelectric single crystals with d_{33} values of ≈2000pC/N have revolutionised military and medical applications [3].

For some applications it is desirable to have a high voltage output achieved through using piezoelectric materials possessing a higher piezoelectric voltage coefficient also known as the g_{ij} coefficient. The relationship between the charge coefficient and the voltage coefficient is analogous to the fundamental circuit equation $q = CV$ where q is charge, C is capacitance and V is voltage, where in the case of piezoelectric materials the capacitive element is represented through the permittivity, ϵ_{33}. Whilst the direct relationship between the piezoelectric charge and voltage coefficient suggest that high performance PZT and piezoelectric single crystals will also result in high g_{ij}, an increased d_{ij} is often coupled with an increased permittivity and therefore the g_{ij} coefficient remains relatively constant in these materials.

Modified lead titanate polycrystalline ceramics have been a favoured choice for hydrophone applications with mentions of its popularity going back to the 1980s [4]. Whilst there has been a significant improvement in active sensors due to the developments mentioned previously, the same cannot be said for passive sensors and therefore the drive for industry improvements is the ultimate motivation of this project. Significantly large g_{ij} coefficients have been achieved through the use of composites in which commercially available PZT is machined into an array of pillars and surrounded by a resin [5]. Whilst this method has been extremely successful in attaining high voltage coefficients, it is a time consuming and costly effort and therefore the need for 'plug-in-and-play' bulk piezoelectric materials that mimic established manufacturing routes are still desirable. Furthermore the more recent increase in demand for applications involving the internet-of-things, energy harvesters and chargers for *in situ* fatigue monitors have also motivated research into high g_{ij} materials [5, 6].

1.1 Aims & Objectives

Within this project there are two main aims:

- To understand the mechanisms from a fundamental materials science perspective that drive a high piezoelectric voltage coefficient and study the scientific and practical limitations
- Use this knowledge to propose other materials that may outperform current military grade devices

1.2 Thesis Structure

This thesis consists of six chapters, the first being this introduction. The second chapter provides definitions and background information to material scientists which do not necessarily have a specialist knowledge of piezoelectric and ferroelectric materials. The definitions and information provided is useful for understanding the remaining chapters in this thesis.

Chapter 3 begins investigating the piezoelectric voltage coefficient from a materials science perspective and aims to understand the mechanisms behind a high g_{ij} coefficient in single crystals and single domains, polycrystalline systems and ultimately explores the scientific and practical limitations. These theories are supported using data from a range of piezoelectric materials from literature. Using the knowledge gained from the first part of this chapter, potential material candidates are suggested and an overview of previous work of high g_{ij} materials is covered with a brief mention of the industrial scalability.

Motivated by the observation in Chapter 3 that tetragonality is a significant structural mechanism for high g_{ij} coefficients, Chapter 4 uses Landau-Devonshire theory to describe the solid solution of bismuth ferrite lead titanate and demonstrates the potential of this material as a high g_{ij} candidate from a theoretical perspective.

Chapter 5 involves the fabrication and electrical, structural and chemical analysis of Nb-doped bismuth ferrite lead titanate polycrystalline ceramics with the aim of combatting the infamous conductivity of this solid solution.

The final chapter concludes the thesis and covers the future work that may further this research topic.

Chapter 2

Background Information

2.1 Structural Properties of Materials

A lattice is formed when atoms arrange themselves in such a way as to form an ordered array of points. To understand the crystallography of a lattice it can be broken up into unit cells. These cells are the smallest repeating division of a material and contain all the structural and symmetry information that allows for the macroscopic structure to be understood [7]. The dimensions (a, b, c) and the angles (α, β, γ) of a unit cell are known as lattice parameters and can be used to describe its physical properties (Figure 2.1).

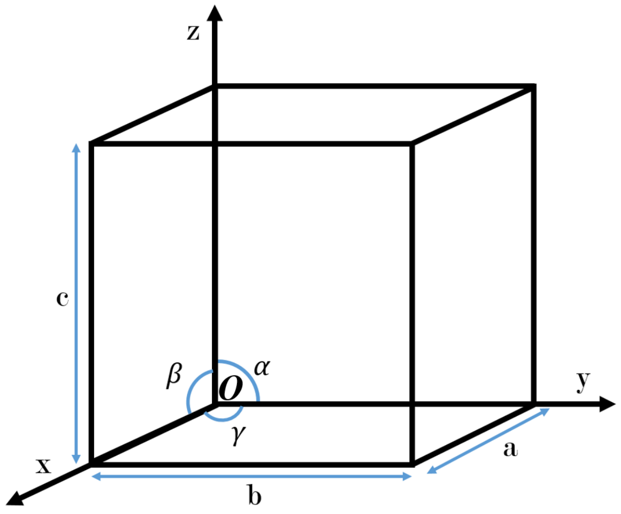

Figure 2.1: Schematic of a unit cell and parameters

2.1.1 Bravais Lattice

Variations in the unit cell parameters give rise to different crystal structures. These are cubic, tetragonal, orthorhombic, rhombohedral, hexagonal, monoclinic and triclinic.

Table 2.1 lists the crystal structures and the corresponding lattice parameters [8].

Table 2.1: The seven crystal systems and their corresponding lattice parameters

System	Lattice Parameters
Triclinic	$a \neq b \neq c$ $\alpha \neq \beta \neq \gamma \neq 90°$
Monoclinic	$a \neq b \neq c$ $\alpha = \gamma = 90°; \beta \neq 90°$
Orthorhombic	$a \neq b \neq c$ $\alpha = \beta = \gamma = 90°$
Tetragonal	$a = b \neq c$ $\alpha = \beta = \gamma = 90°$
Hexagonal	$a = b \neq c$ $\alpha = \beta = 90°; \gamma = 120°$
Rhombohedral	$a = b = c$ $\alpha = \beta = \gamma \neq 90°$
Cubic	$a = b = c$ $\alpha = \beta = \gamma = 90°$

All crystal systems exhibit one of the seven crystal systems listed in Table 2.1. Placing a lattice point at each corner of the unit cell will give rise to seven different lattice structures. However, Auguste Bravais demonstrated that alternative arrangements of atoms can be made within the unit cell such as face-, body-, and base-centering, whilst retaining the requirement that all point lattices possess identical surroundings. Combining the seven crystal structures in Table 2.1 and these alternative atomic arrangements gives rise to the 14 Bravais lattices shown in Figure 2.2 [8, 9].

2.1.2 Symmetry & Space Groups

An important consideration of crystallographic symmetry is the ability to describe the crystal's appearance after point operations or translation. A combination of the symmetry and lattice parameters gives rise to 230 space groups [9]. A commonly used notation of space groups is the Hermann-Mauguin notation. These notations consist of four symbols, the first of which relates to the lattice type:

P	Primitive
I	Body-centered
F	Face-centered
C	Base-centered
R	Rhombohedral

The two space groups that are most applicable to this project are $P4mm$ and $R3c$. $P4mm$ describes a primitive cell exhibiting four-fold symmetry and possesses two mirror

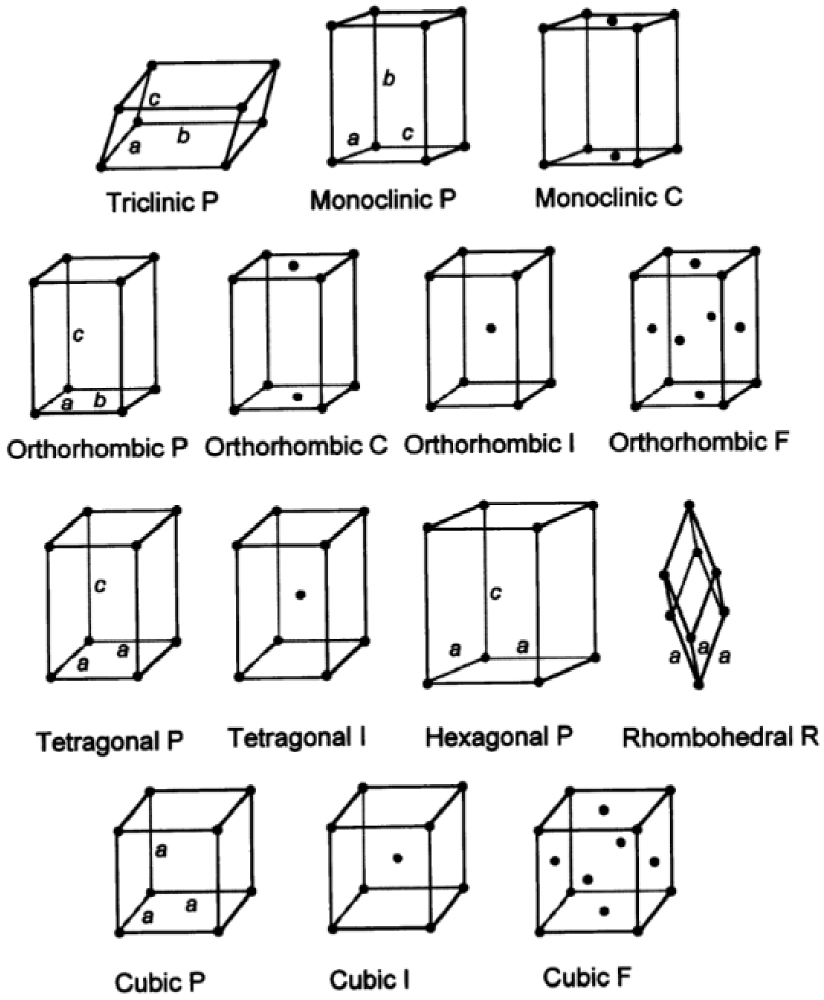

Figure 2.2: The 14 Bravais Lattice [9]

planes, and $R3c$ describes a rhombohedral unit cell with three-fold rotational symmetry and a glide plane in the c-axis.

2.1.3 Lattice points, planes and directions

Atoms or planes of atoms within a unit cell can be located by using Cartesian coordinates relative to the origin. Using Figure 2.3 as an example, the point P relative to the origin O is 011, vector OQ is [111] and plane R is a (001) plane.

Furthermore the appropriate notation is dependent on reference to either a single vector or plane or a family of directions or planes:

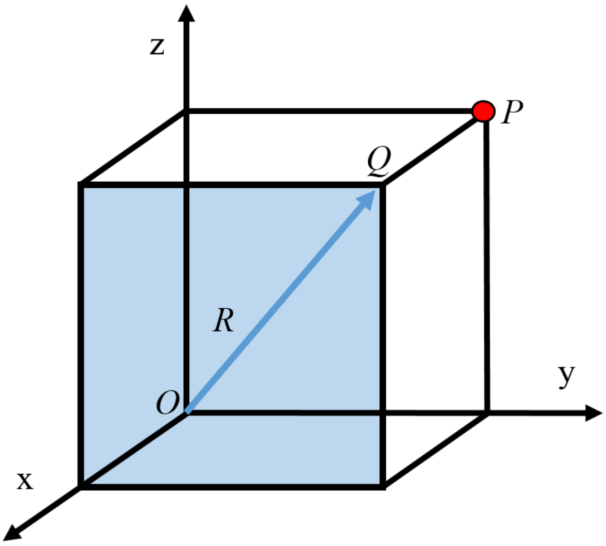

Figure 2.3: Illustration demonstrating points, vectors and planes within a unit cell

$$[001] = \text{single direction vector along z axis}$$

$$\langle 001 \rangle = [001], [010], [100] - \text{family of directions}$$

$$(001) = \text{single plane perpendicular to } [001] \text{ vector}$$

$$\{001\} = (001), (010), (100) - \text{family of planes}$$

2.1.4 Perovskite Structure

The perovskite structure is one of much scientific and technological interest due to its ability to exhibit interesting structural and electrical properties such as pyro- and piezoelectricity. The perovskite structure is one that adopts the formula ABO_3, in which A ions are located at the corners of the unit cell, and the B ion is surrounded by an oxygen octahedral cage [10].

Although an ideal perovskite adopts a cubic structural phase, many oxide perovskites deviate from this and adopt symmetries depending on the relative size of the ions [11]. The stability of a perovskite can be described using the Goldschmidt tolerance factor, t_G, shown in Equation 2.1 [10]:

$$t_G = \frac{r_A + r_O}{\sqrt{2}(r_B + r_O)} \tag{2.1}$$

Where r_A, r_O and r_B are the ionic radii of the A-, O- and B-site ions, respectively. The value for the tolerance factor can give a good indication as to the structural phase

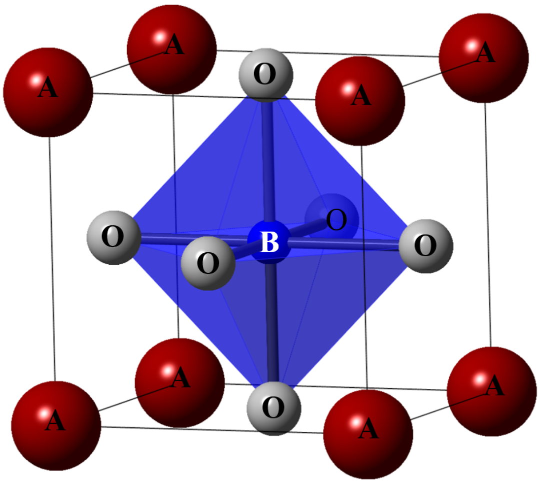

Figure 2.4: Schematic of a perovskite lattice structure

of the material [10]. A tolerance factor >1 indicates a tetragonal phase whereas a tolerance of <1 implies a rhombohedral phase [12].

2.1.5 Defects

Within a crystalline structure there are many categories of defects such as line, planar and point defects. Point defects generalise the description of defects that occur due to missing atoms (vacancy defects), the substitution of atoms with foreign ions (substitutional defects), and the occupation of site within the crystal structure which are usually unoccupied (interstitial defects) [1]. An example of planar defects involves grain and phase boundaries which describe the abrupt difference in crystallographic orientation between two regions. In the case of ceramics, these two regions manifest themselves as separate grains which grow and meet during sintering. Another example of a planar defect are stacking faults which arise due to the local disruption between stacking layers. Atoms that may normally follow an face-centered cubic ABCABC sequence may adopt close-packed ABABAB sequence, resulting in an ABCBCABC stacking sequence [13]. Line defects refer to the misalignment of atomic planes within a lattice and can be subcategorised into edge and screw dislocations. Edge dislocations are visualised as an insertion or removal of a plane of atoms that disrupt the local crystal structure by causing surrounding atoms to expand or collapse in order to accommodate. Screw dislocations are formed when planes of atoms are twisted with respect to each other similar to a twisted piece of flat ribbon, however unlike edge dislocations, screw dislocations do not possess any additional or missing planes [14].

Although all defects have an influence on the mechanical and electrical properties of electroceramics, this thesis will mainly focus on the effects of point defects, more specifically vacancy and substitutional defects on the electrical properties of materials (section 2.2.4). Subsequently, the mechanisms of point defects will be described using Kröger-Vink Notation where possible.

2.1.5.1 Kröger-Vink Notation

Kröger-Vink notation is a useful method in describing chemical reactions whilst removing the ambiguity between vacancies with an associated charge and valence state charge notations on isolated ions. Kröger-Vink notation often takes the form V_B^A where V is the lattice vacancy or ion, B is site location and A is relative charge [1]. For example, O_O^X indicates an oxygen ion located on an oxygen site and shows no relative charge difference, however $Nb_{Ti}^{\bullet}$ describes a niobium ion located on a titanium site with a single positive relative charge, as titanium is often 4+ and niobium 5+. Table 2.2 summarises the different notations and corresponding definitions.

Table 2.2: Kröger-Vink notations and corresponding definitions

Notation	Definition
V	Lattice vacancy
h	Hole
e	Electron
$'$	Relative negative charge
$\bullet$	Relative positive charge
X	Neutral charge

2.2 Electrical Properties of Materials

2.2.1 Dielectrics and Polarisation

When two equal and opposite charges are positioned such that the distance between them is much smaller than the distance from the observer, an electric dipole is formed. An electric dipole moment (μ) is described as the product of the charge (q) and distance (d) between them as shown in Equation 2.2 [15]:

$$\mu = q.d \tag{2.2}$$

A dielectric material is defined as an insulator or non-conductive material which under the application of an electric field can exhibit a polarisation P, a quantity denoting the dipole moment per unit volume, v, as in Equation 2.3 [15].

$$P = \frac{\mu}{v} \tag{2.3}$$

When discussing dielectric materials, it is useful to discuss capacitors. When a potential difference (V) is applied between parallel electrodes, each with a surface area A, and separated by a distance d, the electric field strength (E) and capacitance (C_0) as shown in Equation 2.4 and 2.5 can combine to give an expression for the amount of stored charge (q_0) as shown in Equation 2.6 [15].

$$E = \frac{V}{d} \tag{2.4}$$

$$C_0 = \frac{A\epsilon_0}{d} \tag{2.5}$$

$$q_0 = C_0 V = A\epsilon_0 E \tag{2.6}$$

Where ϵ_0 is the permittivity of free space (8.85×10^{-12} F.m^{-1}) [15].

If a dielectric material is placed between the parallel electrodes, the amended charge stored, q_1, changes by a factor of ϵ:

$$q_1 = A\epsilon_0\epsilon E \tag{2.7}$$

Where ϵ is the permittivity of the dielectric material. The difference in charge storage can then be expressed through Equation 2.8 [15]:

$$\Delta q = q_1 - q_0 = A\epsilon_0 E(\epsilon - 1) \tag{2.8}$$

Equation 2.8 can be substituted into Equation 2.2 to find the electric dipole moment and therefore the polarisation of the dielectric as in Equation 2.9 [15]:

$$P = \frac{\mu}{v} = \epsilon_0(\epsilon - 1)E = \eta\epsilon_0 E \tag{2.9}$$

Where η (=ϵ-1) represents the susceptibility of the medium. However due to many oxide perovskites possessing relative permittivities much larger than one, $\epsilon >> 1$, quite often the susceptibility will be considered equal to the permittivity, $\eta = \epsilon$ [15]. The four main mechanisms in which a material can become polarised under the application of an external field are shown in Figure 2.5 [1]:

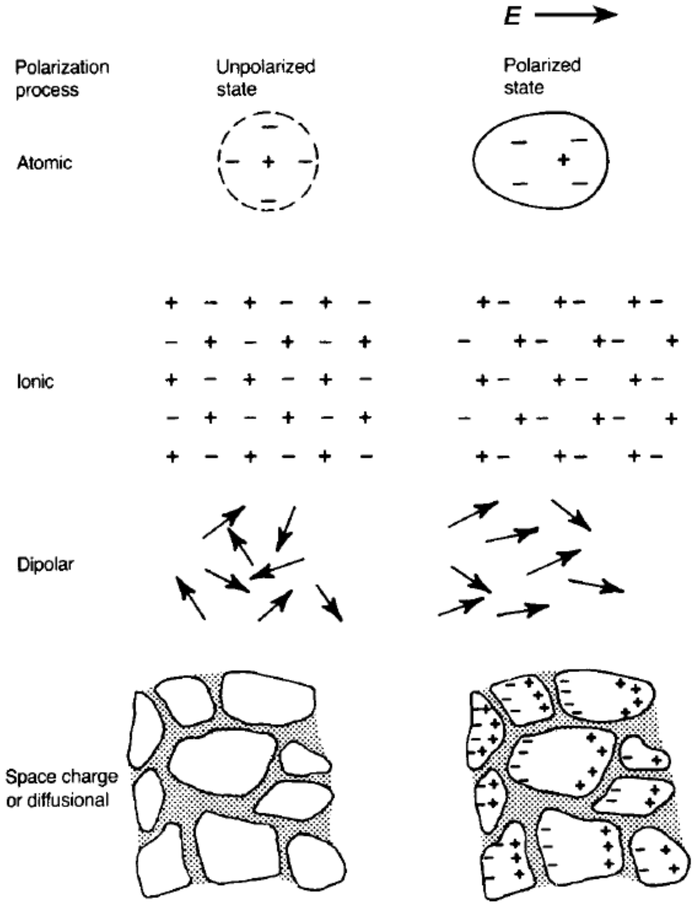

Figure 2.5: The four main polarisation mechanisms [1]

Atomic polarisation refers to displacement of the electron cloud within an atom to behave like a dipole. Ionic polarisation refers to the relative displacements between cations and anions within an ionic material. A dipolar polarisation is used to describe a material in which permanent dipoles are already present. When no electric field is applied, the dipoles are randomly orientated such that no net polarisation is observed. When an electric field is applied the dipoles will rotate to become parallel to the external field and a non-zero net polarisation is observed. Finally space charge polarisation arises when defect sites and grain boundaries form a potential barrier giving rise to dipole moments within a material [1].

Due to the non-idealistic nature of dielectrics, the permittivity is expressed as a complex value consisting of a real and an imaginary part as shown in Equation 2.10:

$$\epsilon^* = \epsilon' - j\epsilon'' \tag{2.10}$$

Where $j = \sqrt{-1}$, ϵ^*, ϵ', and ϵ'' are the complex, real and imaginary permittivity, respectively. The imaginary component is associated with lossy mechanisms such as conduction or rotation of charges and atoms [1]. A useful figure of merit to both material scientists and device engineers is the dissipation factor ($tan\delta$) which is mathematically defined as the ratio between the imaginary and real components of dielectric permittivity as shown in Equation 2.11. The larger the value of $tan\delta$, the more lossy the material.

$$tan\delta = \frac{\epsilon''}{\epsilon'} \tag{2.11}$$

Both the real and imaginary components of the permittivity are frequency dependent. At certain frequencies of alternating field polarisation mechanisms will 'freeze out' and its contribution to the real permittivity is eliminated. This 'freezing out' mechanism can also be characterised by a peak in the imaginary permittivity [1].

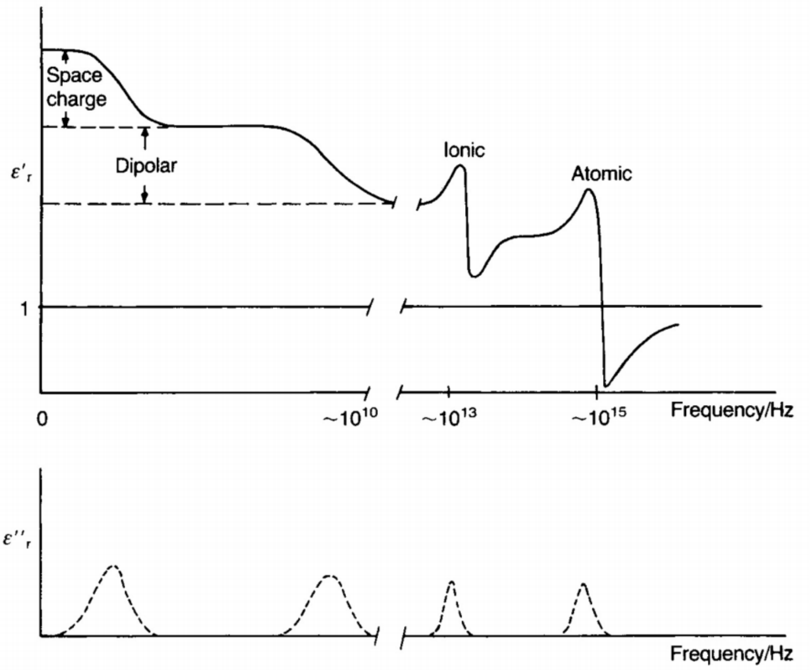

Figure 2.6: Real (ϵ') and imaginary (ϵ'') permittivity as a function of frequency illustrating the contributions and relations of different polarisation mechanisms [1]

2.2.2 Ferroelectricity

Ferroelectricity is a subgroup of pyroelectricity, which in turn is a subgroup of piezoelectricity. The most general description of a ferroelectric is a material that has reversible spontaneous polarisation under the application of an applied field [16].

2.2.2.1 Ferroelectric Phase Transitions

When a ferroelectric is heated above a critical temperature, it becomes paraelectric in which it adopts a centrosymmetric structural phase and no polarisation and piezoelectric behaviour can be observed. The threshold temperature in which this ferroelectric-paraelectric transition occurs is known as the Curie temperature [17] and is material dependent with BaTiO3 and PbTiO3 possessing Curie temperatures of ≈130°C [17] and ≈490°C [18], respectively.

The two forms of phase transition are first order and second order. A first order (discontinuous) transition is accompanied by a release of latent heat and discontinuity in internal energy, enthalpy, entropy and volume. In a second order transition, the phase changes continuously to zero and thermodynamic properties are all continuous, however their first derivatives are discontinuous [19].

Below the Curie temperature a ferroelectric can still experience phase transitions. However instead of a loss in polarisation the preferred polarisation orientation changes as a result of a change in structural phase [20]. Using barium titanate as an example (Figure 2.7), on cooling below 0°C the structural phase changes from a tetragonal state with polarisation along the ⟨001⟩ to an orthorhombic phase with preferred polarisation along the ⟨011⟩ direction, to finally a rhombohedral phase below -90°C with polarisation along the ⟨111⟩ axes [1].

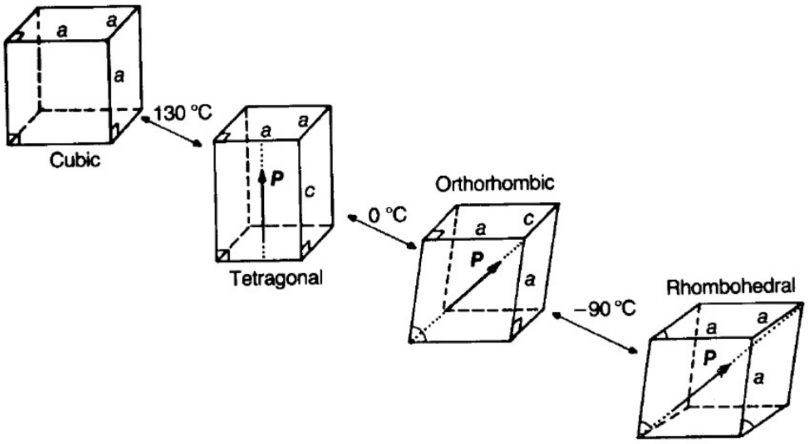

Figure 2.7: Structural phase changes of BaTiO3 from a high symmetry cubic paraelectric states above 130°C to a lower symmetry rhombohedral phase below -90°C [1]

2.2.2.2 Ferroelectric Domains

As a ferroelectric must possess at least two stable polarisation states, there are regions within the material that possess a polarisation vector that differs from another region. These regions are known as domains and are separated by domain walls [21]. Domains form in an attempt to reduce the elastic and electrostatic energy associated with the transformation from a paraelectric to ferroelectric state, and the number of possible orientations and direction of these domains are structurally dependent. In a tetragonal system there are 6 different orientations located along the ⟨001⟩; 180° domains form to reduce the electrostatic energy and 90° ferroelastic domains form to reduce the elastic energy associated with the distortion along the perpendicular (Figure 2.8). However a rhombohedral structure possesses 8 possible orientations located along the body diagonals ⟨111⟩ of the unit cell, therefore 71° and 109° domains form as well as 180° domains, however no 90° domains are present [22].

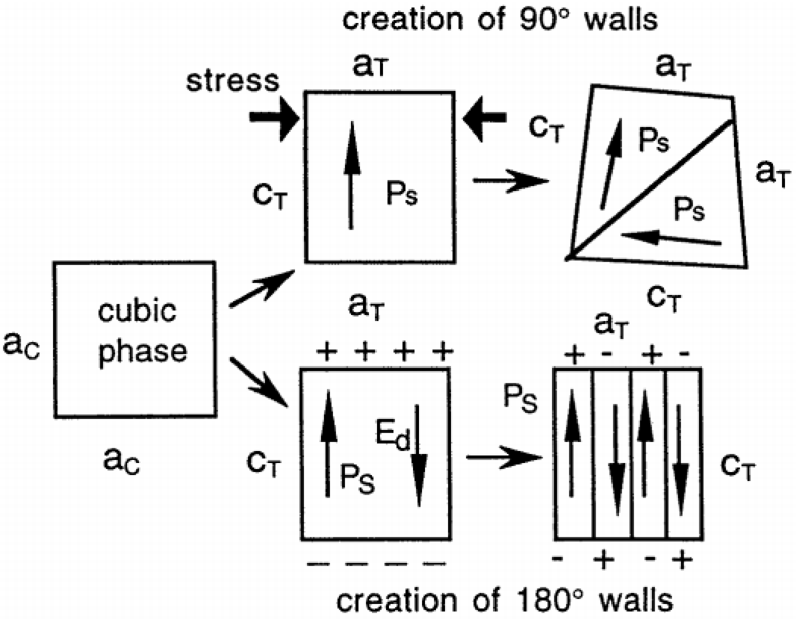

Figure 2.8: 90° and 180° formation in tetragonal materials [23]. a and c represent the crystallographic lattice parameters within the tetragonal (T) and cubic (C) phase. P_S is the spontaneous polarisation and E_d is the depoling field which acts opposite to the polarisation and originates from the difference in charge at each electrode

Although the formation of domains aids the reduction of the electrostatic energy, there is an energy cost to the formation of domain walls. The most energetically favourable domain configuration will occur when there is a balance between the energy saved from the formation of domains and the energy cost of domain wall formation [20].

Initially the domains will arrange themselves such that no macroscopic polarisation will be observed. The material can be altered in order to show a non-zero polarisation through the application of a DC field. This process is known as 'poling'. When poling occurs, the domains reorient themselves into a metastable state to reduce the angle between the dipole and applied electric field. When the applied field is removed, the domains will often relax into a more stable configuration whilst retaining a non-zero macroscopic polarisation. However the material can be returned to a state of zero net polarisation either through the application of stress or by heating above the Curie temperature. Poling is often carried out at temperatures above room temperature in order to increase domain wall mobility, a phenomenon that plays a significant role in the poling process, and achieve larger piezoelectric properties [24].

2.2.2.3 Hysteresis Loops

A common characterisation tool in ferroelectricity is a hysteresis loop shown in Figure 2.9. An increasing field is applied to the material and the resultant polarisation is measured until the material reaches a saturation point at which no further reorientation of domains can occur. The field is then switched until saturation in the opposite direction is achieved and finally reversed again to complete the cycle. Key features of a hysteresis loop are displayed in Figure 2.9. The saturation polarisation, P_{sat}, is the maximum achievable polarisation; the remanent polarisation, P_r, is the amount of polarisation at zero field; the coercive field, E_c, is the field at zero polarisation; and the electric field breakdown, E_b, is the point at which the material becomes electrically conductive [25].

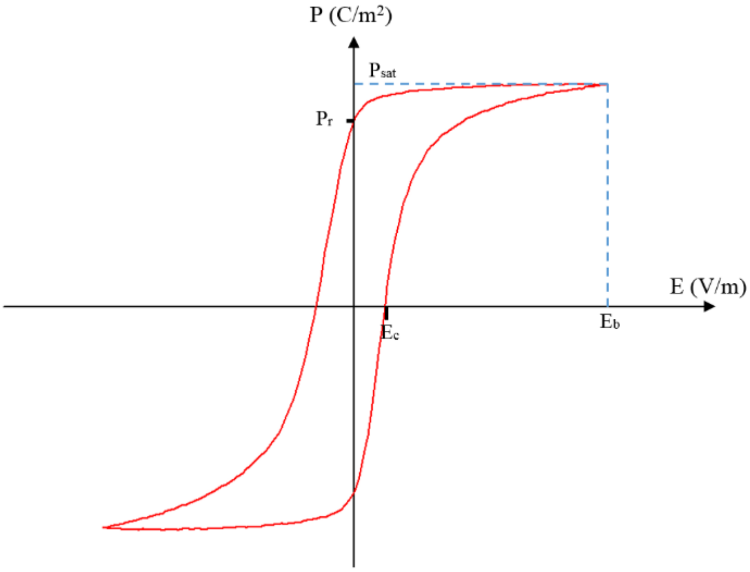

Figure 2.9: Polarisation, P vs. electric field, E for a ferroelectric material. P_{sat} is saturated polarisation, P_r is remanent polarisation, E_c, is coercive field, and E_b is the breakdown field

2.2.3 Piezoelectric Properties

2.2.3.1 Electrostriction

Electrostriction describes the strain induced in a material under applied field and is a phenomenon that occurs in all non-conducting materials. Its existence occurs due to the displacement of charges within a crystal lattice under a static field, however the material response if often infinitesimal. The equation that describes electrostriction can be seen in Equation 2.12.

$$x_{ij} = Q_{ijkl} P_k P_l \tag{2.12}$$

Where x_{ij} is a second-rank strain tensor, P_k and P_l are first-order polarisation vectors and Q_{ijkl} is the fourth rank electrostriction tensor.

2.2.3.2 Piezoelectricity

A material that has the ability to convert mechanical energy into electrical energy, or vice versa, is known as a piezoelectric material [1]. This phenomenon is known as the direct piezoelectric effect when an external pressure induces an electric response, and is known as the converse piezoelectric effect when a mechanical strain is induced from the application of an electric field [1]. The equations that describe the direct and converse piezoelectric effect are shown in Equation 2.13 and 2.14, respectively [26].

$$P_i = d_{ij} X_j \tag{2.13}$$

$$x_i = d_{ij} E_j \tag{2.14}$$

Where P is polarisation, X is stress, x is strain and E is electric field. Both Equation 2.13 and 2.14 show a linear dependency between the magnitude of polarisation and stress for the direct piezoelectric effect and between the strain and electric field for the converse piezoelectric effect which can be described by a constant, d_{ij} [26]. This constant is known as the piezoelectric charge constant and is a hugely important parameter for applications in SONAR and ultrasonic transducers [26].

Although both electrostriction and the converse piezoelectric effect relate polarisation to strain, the distinction is that this relationship is linear in the latter whereas the former exhibits a quadratic relationship as shown in Equation 2.12.

2.2.3.3 Material Properties in Piezoelectricity

Piezoelectric Charge Coefficient, d_{ij}

As mentioned previously the piezoelectric charge coefficient (d_{ij}) is one of the most important material properties in piezoelectricity and describes the amount of surface charge generated per pascal for the direct piezoelectric effect, or the amount of strain developed per unit electric field for the converse piezoelectric effect [20]. The subscripts, i and j, are used to determine the direction of the electric field and mechanical deformation with respect to the polarisation direction. For example, the d_{33} is the piezoelectric charge coefficient when the electric field and mechanical deformation are both parallel to the direction of polarisation. Alternatively, the d_{31} is the piezoelectric coefficient when the polarisation is along the 3-axis and mechanical deformation is perpendicular to the direction of polarisation [20].

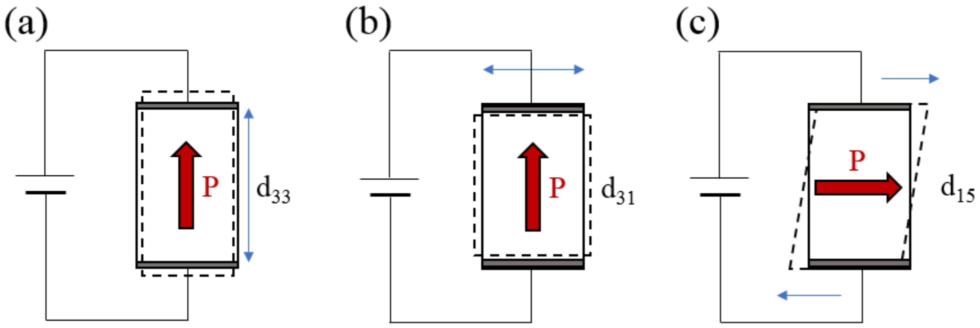

Figure 2.10: Schematic of the (a) longitudinal, (b) transverse, and (c) shear piezoelectric modes denoting the d_{33}, d_{31} and d_{15}, respectively

The hydrostatic piezoelectric charge coefficient, d_h describes the surface charge per Pascal when in an immersed surrounding such as oil or resin, and is calculated using Equation 2.15.

$$d_h = d_{33} + d_{32} + d_{31} \tag{2.15}$$

Piezoelectric Voltage Coefficient, g_{ij}

Another important material property which relates to the sensitivity of a device is the piezoelectric voltage coefficient (g_{ij}), otherwise known as the piezovoltage coefficient, which is defined as the amount of electric field generated per unit pressure (Vm/N) [27]. Similarly to the piezoelectric charge coefficient, the piezovoltage coefficient can be described using the subscripts i and j. The g_{33} coefficient can be calculated using Equation 2.16 [27].

$$g_{33} = \frac{d_{33}}{\epsilon_0 \epsilon_{33}} \tag{2.16}$$

Where d_{33} is the piezoelectric charge coefficient, ϵ_0 is the permittivity of free space, and ϵ_{33} is permittivity. A more in depth understanding of the g_{ij} coefficient both mathematically and physically is provided in Chapter 3. Furthermore the need for large g_{ij} coefficients is explained in Section 2.4.

Electromechanical coupling factor, k_{ij}

The electromechanical coupling factor (k) is described as 'possibly the best single measurement of a strength of a piezoelectric effect' [20]. It is defined as being the square root of the ratio between the amount of converted energy and the total input energy. The value for k can vary greatly from material to material, with typical values of 0.1 achieved for quartz and values of 0.9 for Rochelle salts [20]. Equation 2.17 and 2.18 show the k^2 calculations for the direct and converse piezoelectric effect, respectively.

$$k^2 = \frac{\textit{mechanical energy converted into electrical energy}}{\textit{input mechanical energy}} \tag{2.17}$$

$$k^2 = \frac{\textit{electrical energy converted into mechanical energy}}{\textit{input electrical energy}} \tag{2.18}$$

2.2.3.4 Morphotropic Phase Boundary (MPB)

The boundary between a rhombohedral phase and a tetragonal phase is known as a morphotropic phase boundary (MPB) and gives rise to enhanced piezoelectric and dielectric properties. The combination of possible polarisation orientations from the tetragonal and rhombohedral phases results in the increased sensitivity to external fields and stress [28]. As shown in Figure 2.11, the rhombohedral phase has eight possible polarisation directions along the body diagonal of the unit cell, whereas the tetragonal phase has six polarisation directions along the $\langle 001 \rangle$. Near the MPB, the degeneracy in energy states for both structural phases results in the ease of reorientation to external effects [28].

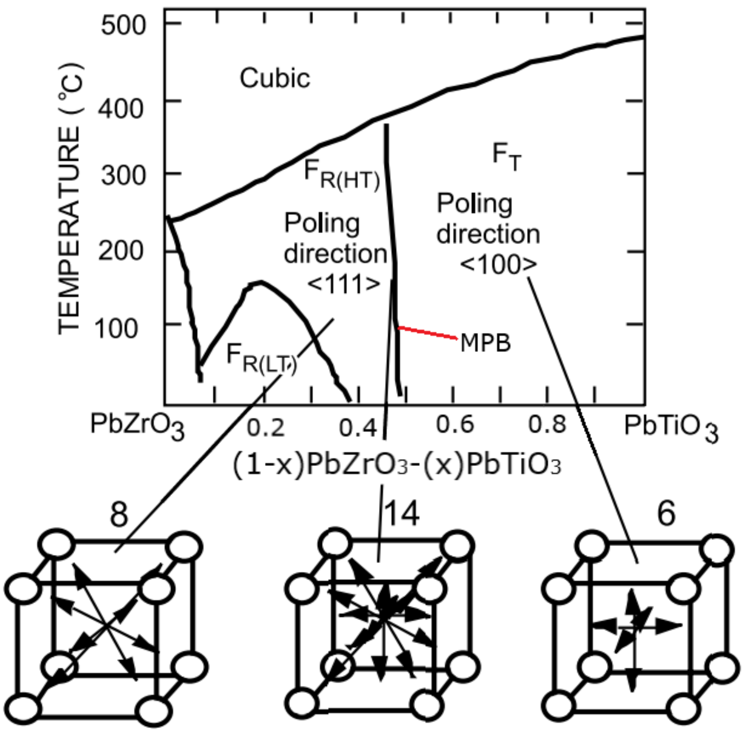

Figure 2.11: Phase diagram of Pb(Zr$1-x$Tix)O3 and a schematic of possible polarisations in the rhombohedral and tetragonal phases and near the MPB [29]. The number above each unit cell represents the number of possible polarisation directions

2.2.4 Doping

The introduction of foreign ions possessing a higher or lower valence state to that which it is replacing can have significant implications on the electrical properties of piezoelectric perovskite materials. The two resulting terms for the effects of doping are 'hard' and 'soft'. To illustrate, the example of isovalent and aliovalent doping will be applied to Pb(Zr,Ti)O_3.

When an undoped PZT sample undergoes sintering, PbO loss occurs resulting in the formation of oxygen and lead vacancies within the lattice as shown in Equation 2.19.

$$PbO_s \rightarrow PbO_V \uparrow + V_{Pb}'' + V_O^{\cdot\cdot} \tag{2.19}$$

Where PbO_s and PbO_V represent lead oxide in solid and vapour form, respectively and ↑ represents a species leaving the system, V_{Pb}'' is a vacancy located on a Pb-site resulting in a 2- relative charge, $V_O^{\cdot\cdot}$ is a vacancy on an oxygen site resulting in a 2+ relative charge.

More generally to electroceramics, similar behaviour in bismuth containing materials results in the formation of A-site and oxygen vacancies shown in Equation 2.20.

$$Bi_2O_{3s} \rightarrow Bi_2O_{3V} \uparrow + 2V_{Bi}^{'''} + 3V_O^{\cdot\cdot} \tag{2.20}$$

Where Bi_2O_{3s} and Bi_2O_{3V} represent bismuth oxide in solid and vapour form, respectively. $V_{Bi}^{'''}$ is a vacancy on a bismuth site resulting in a 3- relative charge, and $V_O^{\cdot\cdot}$ is as above.

One method to reduce the concentration of lead (and/or bismuth) vacancies is the excess of PbO (and/or Bi_2O_3), either within the ceramic or through controlled atmospheric conditions. However oxygen vacancy formation can still occur independent to other vacancy formation mechanisms as shown in Equation 2.21.

$$O_O^X \rightarrow \frac{1}{2}O_2 \uparrow + V_O^{\cdot\cdot} + 2e^{'} \tag{2.21}$$

Where O_O^X is an oxygen ion located on an oxygen site showing no change in relative charge, $\frac{1}{2}O_2 \uparrow$ is half an O_2 molecule leaving the system, $V_O^{\cdot\cdot}$ is an oxygen vacancy showing 2+ relative charge, and $e^{'}$ is an electron.

When a foreign ion with a higher or lower valence state is introduced at the expense of the original ion, vacancies will be formed in order to retain charge neutrality. When an acceptor ion such as Fe^{3+} is substituted for a Ti^{4+} ion on the B-site, the charge difference is compensated through the formation of oxygen vacancies as shown in Figure 2.22:

$$Fe_2O_3 \rightarrow 2Fe_{Ti}^{'} + 3O_O^X + V_O^{\cdot\cdot} \tag{2.22}$$

Where $Fe_{Ti}^{'}$ is an iron ion located on a titanium site resulting in a 1- relative charge. O_O^X and $V_O^{\cdot\cdot}$ are defined as above.

It is suggested that a complex defect dipole moment is formed between the acceptor and oxygen vacancy whose orientation is parallel to that of the local P_S, therefore inhibiting domain wall motion [30]. This increasing difficulty in poling results in the piezoelectric material becoming ‘hard’. This associated restriction in domain wall motion results in a decrease in the piezoelectric, dielectric and elastic properties. However due to the internal friction and associated heat generation through domain wall motion being restricted, the mechanical quality factor increases therefore making acceptor doping appropriate for materials used in high-power applications where stability to external stimuli is desired [30].

When a donor ion such as Nb^{5+} is substituted for either Ti^{4+} or Zr^{4+} in PZT, the concentration of oxygen vacancies is reduced and the charge difference is compensated through the formation of Pb-site vacancies as shown in Figure 2.23:

$$Nb_2O_5 \rightarrow 2Nb^{\cdot}_{Ti} + 5O_O^X + V_{Pb}^{''} \tag{2.23}$$

Where $Nb^{\cdot}_{Ti}$ is a niobium ion on a titanium site and a resulting 2+ relative charge. O_O^X and $V_{Pb}^{''}$ are defined as above.

The reduction in oxygen vacancy concentration results in increased domain wall mobility and therefore increased piezoelectric, dielectric and elastic properties [30]. However the internal friction associated with domain wall motion results in an increase in mechanical and dielectric losses and a decrease in the mechanical quality factor. Furthermore, the introduction of acceptor ions often results in the destabilisation of ferroelectric domain structure resulting in a decrease in the Curie temperature [31]. The increased sensitivity to changes in stimuli such as electric field results in donor doped piezoceramics being referred to as ‘soft’ and are more suitable candidates for actuator applications.

2.3 Relevant Materials

2.3.1 Lead Titanate, PbTiO3

The ferroelectric properties of lead titanate were first reported by Shirane et al. in 1950 [32]. Whilst other oxide perovskites can be observed to undergo multiple structural phase transitions below T_C, PbTiO3 exhibits no phase transitions to symmetries lower than tetragonal [33]. It possesses a much larger spontaneous strain with room temperature X-ray analysis showing a tetragonality of 6.3% [34,35] compared with that of barium titanate (1.1%) [20] . A theory for this behaviour is that it is due to the hybridisation of the Pb 6s and O 2p orbitals resulting in enhanced covalence and therefore spontaneous strain compared with that of similar oxide perovskites [34]. The large spontaneous strain also results in highly anisotropic piezoelectric and ferroelectric properties, i.e. the d_{33}/d_{31} and g_{33}/g_{31} are greater than other materials due to the intrinsic decoupling between the 33 and 31 modes [36].

The synthesis of pure lead titanate in polycrystalline form and in large single crystal form is difficult due to the tendency to fracture due the large lattice strain experienced when cooling through the cubic-tetragonal phase boundary. In order to alleviate this and enhance piezoelectric functionality A-site doping has been carried out in order to reduce the tetragonal strain, a strategy that will be discussed in greater depth in Chapter 3.

2.3.2 Bismuth Ferrite, $BiFeO_3$

Bismuth ferrite was first discovered in 1957 by Rowan and Swars [37]. It adopts a $R3c$ space group and has gathered much attention over the decades for a number of reasons [38]. Firstly it is a promising candidate as a lead-free alternative for some applications, a current challenge facing the ferroelectrics community. Secondly it possesses a very large Curie temperature of ≈830°C becoming useful for applications in harsh environments such as high temperature. Finally, the ability to exhibit multiferroic behaviour at room temperature promises a significant number of multifunctional device applications [38].

A disadvantage associated with bismuth ferrite is the difficulty in forming a pure single phase in the bulk form. This is due to the volatile nature of bismuth oxide during sintering creating unwanted secondary phases and undesirables such as Bi_2O_3, $Bi_2Fe_4O_9$ and $Bi_{25}FeO_{39}$ [38]. Furthermore $BiFeO_3$ exhibits significant conductivity which is attributed to the reduction of Fe^{3+} ions to Fe^{2+} and the generation of free charge carriers as in Equation 2.24 and oxygen vacancy conductivity through loss of volatiles as in Equation 2.20 and 2.21 [39].

$$Fe^{3+} \rightarrow Fe^{2+} + e' \tag{2.24}$$

Ionic substitution on both the Bi site and Fe site have been attempted in order to combat this issue. Substitution of bismuth with rare earth elements such as samarium [40] and neodymium [41] and substitution on the Fe site with dopants such a zinc [42] and manganese [43] have all been successful in improving the resistivity.

A method to overcome unwanted secondary phases of bismuth ferrite and the significant leakage current is to alloy with other ABO_3 perovskite oxides. Examples of this include $BaTiO_3$ [44], $SrTiO_3$ [45] and as will be discussed further in Section 2.3.3, $PbTiO_3$. The fabrication of a solid solution has allowed for the formation of a morphotropic phase boundary and also a decrease in the leakage current [38].

2.3.3 Bismuth Ferrite Lead Titanate, $(x)BiFeO_3-(1\text{-}x)PbTiO_3$

$(x)BiFeO_3-(1\text{-}x)PbTiO_3$ (BFPT) is a solid solution of the rhombohedrally distorted $BiFeO_3$ and tetragonally distorted $PbTiO_3$. Similarly to lead zirconate titanate, BFPT possesses a morphotropic phase boundary at which an increase in piezoelectric response is observed [46]. However the exact location of the MPB is still unclear. Fedulov [47] in 1964 observed a rhombohedral-tetragonal mixed phase region spanning from $0.66 \leq x \leq 0.73$ as shown in Figure 2.12 and additional studies by Woodward et al. [48] confirmed the existence of a rhombohedral-tetragonal mixed phase structure at $x=0.70$ using electron diffraction. A rhombohedral-orthorhombic-tetragonal MPB was discovered between $0.72 \leq x \leq 0.80$ by Ye et al. [49] using X-ray diffraction; an orthorhombic phase is also observed by Bhattacharjee through refinement methods [50]. The discrepancy in the location of the MPB is a result of the significant internal stresses which vary with processing conditions and therefore influences the compositional dependence [51]. Although the location and compositional width of the MPB is unclear, the almost exclusive spontaneous strain behaviour of this solid solution is widely accepted and is shown in Figures 2.13. Whilst many other solid solutions with a lead titanate end member observe a decrease in spontaneous strain from 6% with decreasing lead titanate content within the tetragonal region, the opposite is observed in BFPT with spontaneous strains being reported up to 18.7% [36].

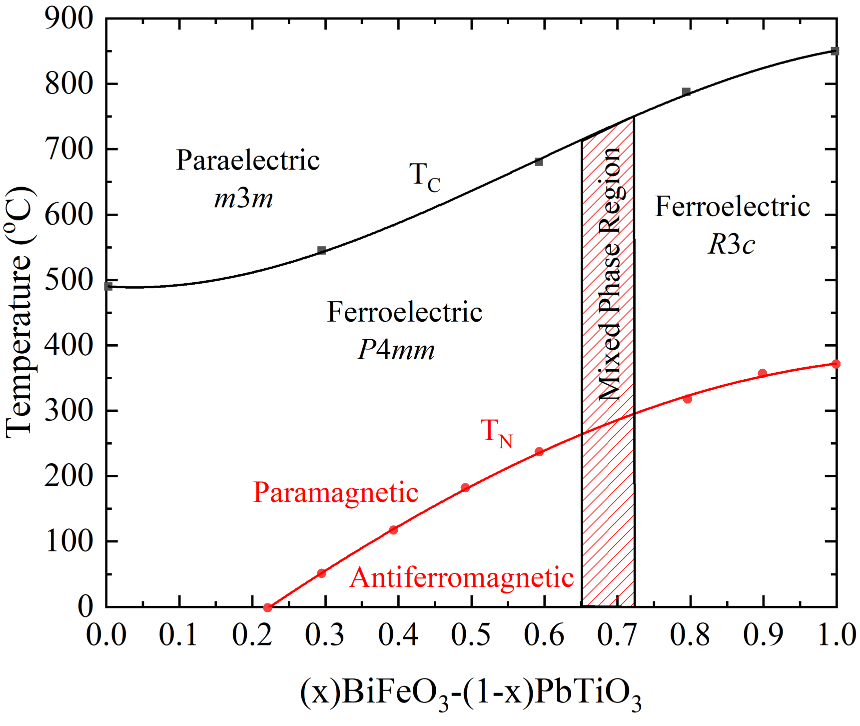

Figure 2.12: Ferroelectric and magnetic phase diagram of the (x)BiFeO3−(1-x)PbTiO3 solid solution. Adapted from [47] to show composition in molar fraction. The red line represent the Néel temperature where a antiferromagnetic-paramagnetic transition occurs. Ferroelectric behaviour is present from 0°C to T_C where a ferroelectric-paraelectric phase transition is observed. The compositional space between $0.65 \leq x \leq 0.72$ represents a *P4mm*+*R3c* mixed phase region; the left and right hand side of this region represents a tetragonal and rhombohedral phase, respectively.

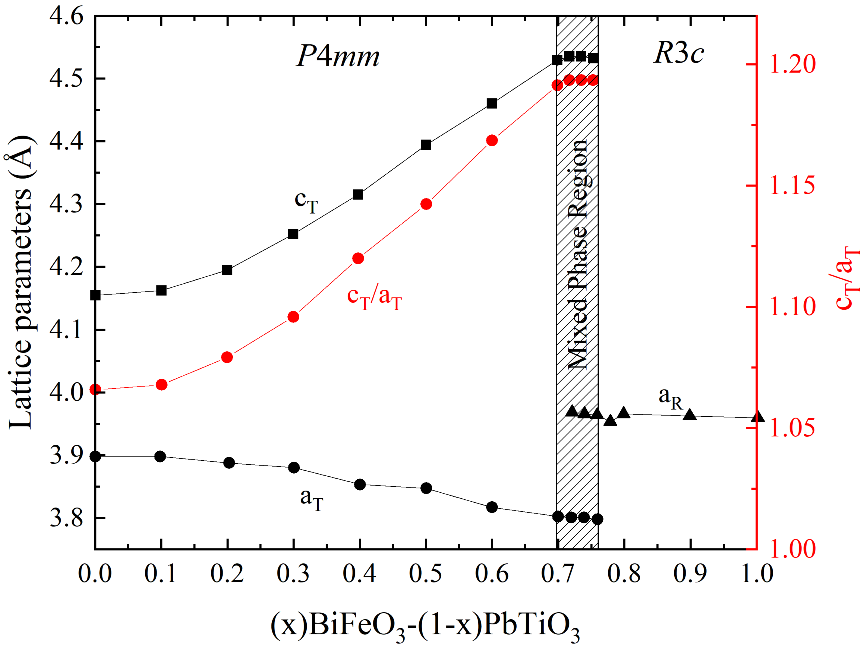

Figure 2.13: Lattice parameters and tetragonality, c_T/a_T, as a function of composition in a (x)BiFeO3 – (1-x)PbTiO3 solution (values taken from [52])

It is this large spontaneous strain that results in processing difficulties associated with this material. The dwell times and cooling rates associated with sintering regimes familiar to other materials result in either severe macro-cracking or full disintegration of the sample. In order to form well-sintered dense ceramics, a time-costly controlled grain growth and cooling regime have to be adopted. Another issue is that BFPT possesses a large coercive field [53], which results in poling difficulties. Unlike poling regimes for other 'hard' piezoelectric materials such as PZT-4 which can adopt a hot-poling system, BFPT shows significantly large electrical conductivity facilitated by Fe^{2+} / Fe^{3+} hopping at elevated temperatures. This significant conductivity also makes electrical characterisation of BFPT samples difficult [54] and it is due to these issues that characterisation data on BFPT is limited.

It was proposed by Bell et al. [55] that two conduction mechanisms are present in BFPT ceramics. The first is Fe^{2+}/Fe^{3+} hopping which generates free charge carriers as shown in Equation 2.24 that can contribute significantly to leakage and the second is oxygen vacancy conductivity which arises from the loss of volatiles such as Bi and Pb during fabrication and can also arise independently.

In order to alleviate the problem of conductivity, BFPT has been subject to A-site and B-site substitution similarly to studies on pure BiFeO3. Studies that involve A-site substitution with a Bi^{3+} ion include La^{3+} [51,53,56] and Nd^{3+} [57,58], both showing an increase in resistivity compared to undoped BFPT. Furthermore B-site substitution with the Fe^{3+} has been carried out using Ti^{4+} [55,59], Mn^{4+} [55], Sm^{3+} [60], Gd^{3+} [61,62], and Nb^{5+} [63] again showing improved insulative properties.

Not only does doping reduce the conductivity of BFPT, but also improves the ferroelectric and piezoelectric properties for two reasons. Firstly the substitution of A-site ions disturbs the covalence therefore reducing the tetragonality and the associated domain clamping, secondly the reduction in conductivity allows for more aggressive poling regimes to be carried out such as poling under high temperatures for ease of domain switching or higher poling fields without dielectric breakdown occurring both of which can result in improved piezoelectric performance. Table 2.3 lists structural, piezoelectric and dielectric properties of some doped BFPT polycrystalline ceramics.

Table 2.3: Piezoelectric, dielectric and structural data for a range of pure and modified $BiFeO_3$–$PbTiO_3$ polycrystalline ceramics from throughout literature

Material	d_{33} (pC/N)	ϵ_{33}	c/a	T_C (°C)	g_{33} (mVm/N)	tanδ	Ref.
0.70 $BiFeO_3$ – 0.30 $PbTiO_3$	11	148	1.178	477	8.4		[58]
0.70 $(Bi_{0.95}Nd_{0.05})FeO_3$ – 0.30 $PbTiO_3$	18	198	1.174	476	10.3		[58]
0.70 $(Bi_{0.90}Nd_{0.10})FeO_3$ – 0.30 $PbTiO_3$	34	158	1.170	450	24.3		[58]
$(Bi_{0.48}Nd_{0.08})FeO_3$ – 0.44 $PbTiO_3$	72	374	1.064	353	21.8	0.0186	[57]
$(Bi_{0.50}Nd_{0.08})FeO_3$ – 0.42 $PbTiO_3$	76	383	1.050	373	22.4	0.0201	[57]
$(Bi_{0.52}Nd_{0.08})FeO_3$ – 0.40 $PbTiO_3$	142	388		389	41.4	0.0255	[57]
$(Bi_{0.54}Nd_{0.08})FeO_3$ – 0.38 $PbTiO_3$	72	405		390	20.1	0.0145	[57]
$(Bi_{0.56}Nd_{0.08})FeO_3$ – 0.36 $PbTiO_3$	70	423		405	18.7	0.0189	[57]
$(Bi_{0.58}Nd_{0.08})FeO_3$ – 0.34 $PbTiO_3$	59	479		412	13.9	0.0208	[57]
$(Bi_{0.14}Nd_{0.20})FeO_3$ – 0.66 $PbTiO_3$	50	898	1.016	253	6.3	0.0376	[57]
$(Bi_{0.16}Nd_{0.20})FeO_3$ – 0.66 $PbTiO_3$	102	910	1.016	260	12.7	0.0210	[57]
$(Bi_{0.18}Nd_{0.20})FeO_3$ – 0.66 $PbTiO_3$	111	1240	1.013	286	10.1	0.0223	[57]
$(Bi_{0.20}Nd_{0.20})FeO_3$ – 0.66 $PbTiO_3$	135	1583	1.012	301	9.6	0.0269	[57]
$(Bi_{0.22}Nd_{0.20})FeO_3$ – 0.66 $PbTiO_3$	55	1689		324	3.7	0.0312	[57]
0.60 $(Bi_{0.9}La_{0.1})FeO_3$ – 0.40 $PbTiO_3$	112	580	1.100	460	21.8	0.0250	[56]
0.60 $(Bi_{0.9}La_{0.1})(Fe_{0.99}Ti_{0.01})O_3$ – 0.40 $PbTiO_3$	115	619	1.080	454	21.0	0.0270	[56]
0.60 $(Bi_{0.9}La_{0.1})(Fe_{0.98}Ti_{0.02})O_3$ – 0.40 $PbTiO_3$	117	682	1.070	450	19.4	0.0320	[56]
0.60 $(Bi_{0.9}La_{0.1})(Fe_{0.96}Ti_{0.04})O_3$ – 0.40 $PbTiO_3$	115	703	1.070	447	18.5	0.0410	[56]
0.40 $Bi(Fe_{0.60}Ga_{0.40})O_3$ – 0.60 $PbTiO_3$	52	207	1.090	540	28.4	0.0200	[62]
0.65 $BiFeO_3$ – 0.35 $PbTiO_3$	10	370	1.104	632	3.0		[51]
0.61 $(Bi_{0.975}La_{0.025})FeO_3$ – 0.39 $PbTiO_3$	11	313	1.093		4.0		[51]
0.60 $(Bi_{0.950}La_{0.05})FeO_3$ – 0.40 $PbTiO_3$	17	433	1.058		4.5		[51]
0.59 $(Bi_{0.925}La_{0.075})FeO_3$ – 0.41 $PbTiO_3$	21	375	1.045		6.4		[51]
0.585 $(Bi_{0.90}La_{0.10})FeO_3$ – 0.415 $PbTiO_3$	107	563	1.043	386	21.4		[51]
0.57 $(Bi_{0.85}La_{0.15})FeO_3$ – 0.43 $PbTiO_3$	170	838	1.038		22.9		[51]
0.56 $(Bi_{0.80}La_{0.20})FeO_3$ – 0.44 $PbTiO_3$	229	1865	1.023	264	13.8		[51]
0.54 $(Bi_{0.70}La_{0.30})FeO_3$ – 0.46 $PbTiO_3$	96	1912	1.012	189	5.7		[51]
0.70 $Bi(Fe_{0.95}Ga_{0.05})O_3$ – 0.30 $PbTiO_3$	48	337		638	16.2	0.0310	[64]
0.65 $(Bi_{0.70}La_{0.30})(Fe_{0.95}Ga_{0.05})O_3$ – 0.35 $PbTiO_3$	51	572		614	10.2	0.0310	[64]
0.60 $(Bi_{0.90}La_{0.10})(Fe_{0.95}Ga_{0.05})O_3$ – 0.40 $PbTiO_3$	163	878		382	21.0	0.0370	[64]
0.57 $(Bi_{0.80}La_{0.20})(Fe_{0.95}Ga_{0.05})O_3$ – 0.43 $PbTiO_3$	296	1755		263	19.0	0.0489	[64]
0.70 $(Bi_{0.8}La_{0.2})(Fe_{0.95}Ga_{0.05})O_3$ – 0.30 $PbTiO_3$	58	771		429	8.5	0.0541	[65]
0.65 $(Bi_{0.8}La_{0.2})(Fe_{0.95}Ga_{0.05})O_3$ – 0.35 $PbTiO_3$	119	858		353	15.7	0.0424	[65]
0.60 $(Bi_{0.8}La_{0.2})(Fe_{0.95}Ga_{0.05})O_3$ – 0.40 $PbTiO_3$	183	1362		284	15.2	0.0529	[65]
0.575 $(Bi_{0.8}La_{0.2})(Fe_{0.95}Ga_{0.05})O_3$ – 0.425 $PbTiO_3$	293	1754		261	18.9	0.0506	[65]
0.55 $(Bi_{0.8}La_{0.2})(Fe_{0.95}Ga_{0.05})O_3$ – 0.45 $PbTiO_3$	237	1226		266	21.8	0.0353	[65]
0.525 $(Bi_{0.8}La_{0.2})(Fe_{0.95}Ga_{0.05})O_3$ – 0.475 $PbTiO_3$	86	964			10.1	0.0248	[65]
0.50 $(Bi_{0.8}La_{0.2})(Fe_{0.95}Ga_{0.05})O_3$ – 0.50 $PbTiO_3$	101	722		315	15.8	0.0265	[65]
0.45 $(Bi_{0.8}La_{0.2})(Fe_{0.95}Ga_{0.05})O_3$ – 0.55 $PbTiO_3$	78	616		335	14.4	0.0353	[65]

Table 2.3 shows the general research trends with regards to the doping of $BiFeO_3$-$PbTiO_3$ polycrystalline ceramics, showing a popularity for rare-earth doping. It is also

seen that relatively high d_{33} values can be achieved compared to undoped $BiFeO_3$-$PbTiO_3$ with significant doping levels, mainly due to the decrease in the tetragonality facilitated through A-site substitution which will be discussed further in Section 3.5. Table 2.3 also shows that a significant proportion of doping regimes are isoelectronic, most likely due to the desire to improve piezoelectric properties rather than reducing the conductivity. The studies mentioned previously where aliovalent B-site doping has occurred, show a reduction in the conductivity through conventional donor-doping mechanisms which result in the elimination of oxygen vacancies. However these studies focus purely on reducing the conductivity and no piezoelectric or crystallographic properties are measured and hence are not listed in Table 2.3.

Taking into account these considerations, the choice of Nb for the donor-doping of $BiFeO_3$-$PbTiO_3$ in Chapter 5 are for the following reasons. The use of Nb^{5+} for donor-doping and the elimination of oxygen vacancies is a widely-accepted, fundamental mechanism within the field of ferroelectrics. So much so that the example of Nb-doping is taught in undergraduate lectures and published in textbooks [66–68] which cover the fundamental scientific concepts in the field. Although niobium doping of $BiFeO_3$-$PbTiO_3$ polycrystalline ceramics has been carried out previously by Zuo et al. [63], only 1mol% was studied as part of a wider range of dopants and no piezoelectric properties were measured, therefore still providing scope for an original and more thorough study.

The second consideration is a from a potentially industrial perspective. Niobium pentoxide (Nb_2O_5) is a relatively cheap metal oxide (2kg - £770 + VAT [69]) which is advantageous from a business perspective where high-throughput, large-batch ceramic processing may be taking place.

2.4 Piezoelectric Materials in Sonar Applications

Piezoelectric materials are used in a wide range of areas from engine knock sensors to inkjet printing and fuel injection systems to medical and military transducers and in 2015, Amcite Market Intelligence valued the demand for piezoelectric devices at approximately \$21.6bn [70]. Although the diversity of applications of piezoelectric materials are relatively broad, this section primarily focusses on the use of piezoelectric materials for sonar applications. The application of piezoelectric materials can be broken down into active and passive applications, both which will be discussed in the following sections.

2.4.1 Applications in Active Sonar

Active sonar systems rely on the projection of sound using acoustic transducer which are then detected either by a separate hydrophone located away from the projector or self-detection of reflected signals [71]. The performance criteria for piezoelectric materials in this particular application involve a high efficiency and high power output and are usually operated at resonant frequencies in order to magnify the output motion [72]. The power density, Γ, for a piezoelectric ceramic can be calculated using Equation 2.25:

$$\Gamma = \omega Q_m k^2 \epsilon^T E^2 / 2 \tag{2.25}$$

Where ω is the angular frequency, Q_m is the mechanical quality factor, k is the electromechanical coupling factor, ϵ^T is the permittivity at constant tensile stress and E is the electric field strength.

2.4.2 Applications in Passive Sonar

In many applications the active sonar system will act as a projector and hydrophone. However there are cases in which the use of a separate hydrophone is required. Examples of these are towed arrays which are towed from a ship at a distance to remove the self-noise generated, surveillance sonar, passive search and ranging sonars and sonobuoys [72].

As the human ear is a poor receiver of sound underwater the main aim of the hydrophone is to act as ears by detecting or ‘hearing’ pressure variations created by acoustic signals and comparing them to the background noise of the water. When an incident acoustic signal reaches a hydrophone, a voltage is generated that is proportional to the pressure. The major difference between the projectors and hydrophones is the operating conditions. Projectors tend to be used at resonance to maximise the power output whilst hydrophones are operated over a wider range of frequencies below resonance and favour a high open circuit output voltage and a low signal-to-noise. The difference in the intended usage of the device results in a difference in performance criteria and different figure of merits compared to that of active sonar systems that fundamentally stem to the performance criteria of the piezoelectric ceramic [72].

Whilst projectors can be found to have reasonably complicated set-ups, hydrophones can possess a humbler schematic where the most basic set-up is a piezoelectric material with electrodes, relevant wiring and waterproofing means.

The electric field experienced at the electrodes of a piezoelectric that have been applied parallel to the polar axis, E_3, can be defined by Equation 2.26.

$$E_3 = g_{31}X_1 + g_{32}X_2 + g_{33}X_3 + \zeta_{33}^T D_3 \tag{2.26}$$

Where g_{ij} are the piezoelectric voltage coefficients, X_i is stress, ζ_{33}^T is the impermittivity at constant stress and D_3 is the electric displacement along the polar axis.

The electric field intensity can be integrated to determine the voltage as shown in Equation 2.27:

$$V = \int_{-t/2}^{t/2} E_3 dz = E_3 d \tag{2.27}$$

Where z is the polar direction and d is the thickness of the sample.

Combining Equation 2.26 and 2.27 for an open circuit condition where D=0 results in Equation 2.28.

$$V = g_{31}dX_1 + g_{32}dX_2 + g_{33}dX_3 \tag{2.28}$$

If the 3 face is exposed, and 1 and 2 are shielded from the incident signal then X_1=X_2=0 and X_3 is equal to the pressure amplitude of the signal, p_i, and the hydrophone sensitivity, M_{33}, can be calculated using Equation 2.29.

$$M_{33} = V/p_i \tag{2.29}$$

Where V is voltage and p_i is the pressure of an incident acoustic wave.

This similar treatment can be applied to cases where the 2 or 1 face are exposed and the resulting two faces are both shielded giving equations for M_{31} and M_{32}, respectively.

When all faces are exposed to the incident acoustic wave, X_1, X_2 and X_3 are all non-zero, the hydrostatic sensitivity, M_h, can be calculated as shown in Equation 2.30.

$$M_h = g_h d \tag{2.30}$$

Where g_h is the hydrostatic voltage coefficient which similarly to the hydrostatic charge coefficient described in Section 2.2.3.3 represents the voltage coefficient is submerged in oil or resin.

Calculated values for the hydrophone sensitivities are referenced to 1V per micropascal and are therefore multiplied by 10^{-6} to convert from Pa. The receiving voltage sensitivity (RVS) is then quoted on a logarithmic scale as shown in Equation 2.31.

$$RVS = 20log_{10}|M| \tag{2.31}$$

From a materials science point of view, the equations above highlight the importance of the piezoelectric voltage coefficient and hence the motivation for this work.

Chapter 3

An Investigation into the Piezoelectric Voltage Coefficient

Many applications which monitor changes of the local environment are carried out through the measurement of voltage which is then converted to the desired digital format. An example of this is temperature monitoring with a thermocouple. When two dissimilar metals are joined at each end and a temperature gradient is introduced, a voltage is generated due to the thermoelectric effect or Seebeck effect [73], the size of which is material dependent. In knowing the metals used in the thermocouple and measuring the voltage, a digital conversion to temperature can be made [74]. Another example is a humidity monitor where two conductive films are separated by an insulative layer. When moisture collects on the insulative layer, a voltage difference is experienced between the electrodes which is digitally converted into grams per cubic meter or more commonly relative humidity [75]. As shown in section 2.4.2 this principle of voltage measurement is similar for electroacoustic pressure sensors in sonar applications where the voltage generated from an incident wave is converted in decibels [72].

Over the decades commercially dominant lead zirconate titanate has been the cornerstone of piezoelectric ceramics in device applications. Its tailorability offers a wide range of piezoelectric and dielectric variation with some formulations achieving d_{33} values of <750pC/N [2]. The drive for enhanced piezoelectric performance has resulted in much attention being paid to Generation I, II and III piezoelectric single crystals with commercially available PMN-PT single crystals achieving d_{33} of up to 2000pC/N [3]. Whilst the use of single crystals has revolutionised medical and military transducers, the improvement in piezoelectric performance is often coupled with the enhancement of the relative permittivity as shown in Figure 3.1 which ultimately limits the voltage generated (V=q/C).

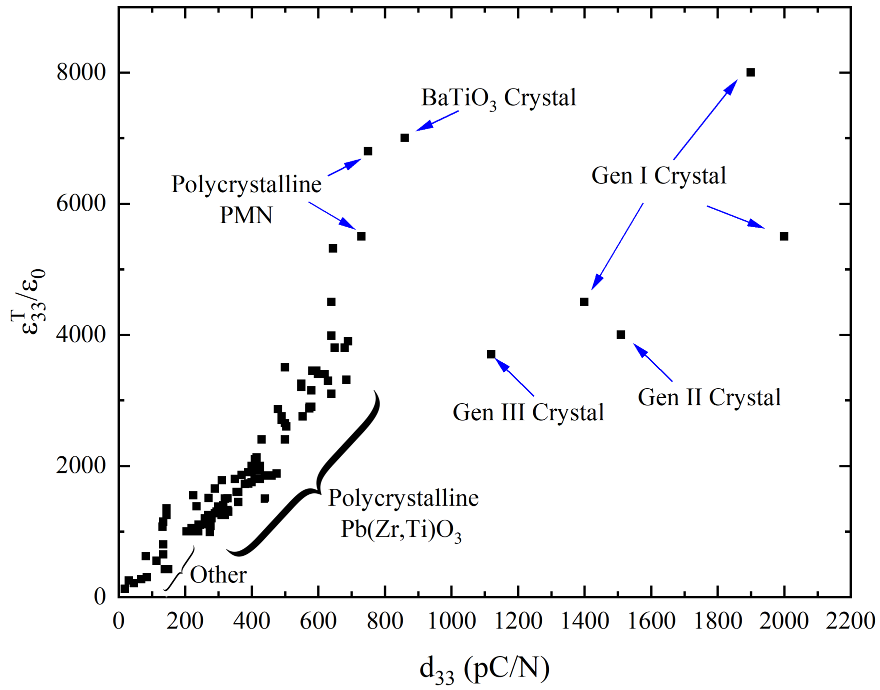

Figure 3.1: The relative permittivity as a function of d_{33} for a range of commercially available polycrystalline and single crystal materials. All datapoints taken from [76], except values for Gen II and III single crystals which are taken from Ref. [77]. “Other” materials include modified lead titanate, barium titanate and bismuth titanate polycrystalline ceramics.

The relationship between piezoelectric charge coefficient (d_{ij}), piezoelectric voltage coefficient (g_{ij}) and permittivity at constant tensile stress (ϵ^T_{ij}) is analogous to the relationship between voltage, charge and capacitance (V=q/C) as shown in Equation 3.1 - 3.4:

$$g_{33} = \frac{d_{33}}{\epsilon^T_{33}\epsilon_0} \tag{3.1}$$

$$g_{31} = \frac{d_{31}}{\epsilon^T_{33}\epsilon_0} \tag{3.2}$$

$$g_{15} = \frac{d_{15}}{\epsilon^T_{11}\epsilon_0} \tag{3.3}$$

$$g_h = \frac{d_h}{\epsilon^T_{33}\epsilon_0} \tag{3.4}$$

Where d_{33}, d_{31}, d_{15}, and d_h are the longitudinal, lateral, shear and hydrostatic charge coefficients, ϵ^T_{33} and ϵ^T_{11} are the parallel and perpendicular components of the permittivity at constant tensile stress, and ϵ_0 is the permittivity of free space.

Figure 3.1 suggests that improving the voltage coefficient which is represented by the inverse gradient is self-limiting and that significant improvement cannot be achieved as the trend shows the relative permittivity scales with d_{33}. However the advancement of processing capabilities with single crystals and textured ceramics, the development of new materials and tuning of current materials either compositionally or through doping has resulted in the successful enhancement of the voltage coefficient.

Much attention has been focussed on the demonstration of high g_{33} and g_h values in polymer-ceramic (PC) composites and current reviews about high g_{33} materials focus mainly on the development of new PC devices using commercially available PZT and/or the use of Pb-free materials in current PC devices [78–81]. A limiting factor is the relatively low working temperature range in which it can be used until the polymer begins to warp and buckle. Applications requiring a high throughput of piezoceramics such as piezoelectric arrays drive the need for readily available 'plug-in-and-play' materials that share similar processing to PZT.

It is the aim of material scientists to correlate a materials physical property with that of their functional properties and therefore this chapter aims to shed light on the fundamental mechanisms that drive high g_{ij} coefficients for single crystal and polycrystalline materials. Comparisons to literature are made and the limiting factors considered. Finally materials both past and present possessing an enhanced g_{ij} compared to PZT are discussed.

3.1 Single Crystals and Single Domains

The Landau-Devonshire derived piezovoltage coefficients in the tetragonal, orthorhombic and rhombohedral phases are expressed as [82]:

$$Tetragonal \begin{pmatrix} 0 & 0 & 0 & 0 & Q_{44}P_3 & 0 \\ 0 & 0 & 0 & Q_{44}P_3 & 0 & 0 \\ 2Q_{12}P_3 & 2Q_{12}P_3 & 2Q_{11}P_3 & 0 & 0 & 0 \end{pmatrix}$$

$$Orthorhombic\begin{pmatrix} 0 & 0 & 0 & 0 & Q_{44}P_3 & Q_{44}P_3 \\ 2Q_{12}P_3 & 2Q_{11}P_3 & 2Q_{12}P_3 & Q_{44}P_3 & 0 & 0 \\ 2Q_{12}P_3 & 2Q_{12}P_3 & 2Q_{11}P_3 & Q_{44}P_3 & 0 & 0 \end{pmatrix}$$

$$Rhombohedral\begin{pmatrix} 2Q_{11}P_3 & 2Q_{12}P_3 & 2Q_{12}P_3 & 0 & Q_{44}P_3 & Q_{44}P_3 \\ 2Q_{12}P_3 & 2Q_{11}P_3 & 2Q_{12}P_3 & Q_{44}P_3 & 0 & Q_{44}P_3 \\ 2Q_{12}P_3 & 2Q_{12}P_3 & 2Q_{11}P_3 & Q_{44}P_3 & Q_{44}P_3 & 0 \end{pmatrix}$$

Where Q_{ij} are the electrostriction coefficients and P_3 is the polarisation along the [001] when the spontaneous polarisation is broken down into 3 orthogonal components.

For all structural phases, the expressions above identify the need for large polarisation along the [001] (P_3) as the electrical driving force for high g_{ij}. For tetragonal materials, the spontaneous polarisation (P_S) $=P_3$, whereas for the orthorhombic and rhombohedral phase it is $=P_3/\sqrt{2}$ and $=P_3/\sqrt{3}$, respectively. Whilst this means that large g_{ij} coefficients are attainable from orthorhombic and rhombohedral materials, it implies that the most significant enhancement is observed in tetragonal materials.

The intimate relationship between macroscopic polarisation, tetragonality (c/a) and ionic displacement has been studied by Qi et al. [83] using density functional theory calculations of single domain systems. Two methods for achieving large [001] polarisation are presented. The first is based on the rattling ion model where the use of B-site ions with small radii results in large ionic displacements and therefore its contribution to the polarisation. The presence of B-site ions with small radii can also result in structural stability due to the ease of forming short A-O bonds. The second method is doping with a small quantity of large B-site ions which increases ionic displacement due to volume expansion of the unit cell. The tolerance factor suggests that a large B-site ion results in the most stable structural phase being rhombohedral facilitated by the rotation of the octahedral oxygen cage. However, providing small concentrations of large B-site ions such that the TiO_6 octahedra can retain rigidity and [001] orientation, A-site displacement is preferred in order to achieve the desirable A-O bond which in turn elongates the unit cell and increasing the polarisation.

Cohen [84] has given insight into the atomic nature of tetragonal materials by observing the electronic structures of $BaTiO_3$ and $PbTiO_3$ through density functional theory.

Whilst both materials are tetragonal at room temperature, there is a vast discrepancy in the spontaneous strain. Cohen found through calculations of the electronic density of states that whilst both materials show hybridisation of Ti 3d and O 2p, a characteristic imperative to ferroelectric behaviour, $PbTiO_3$ also exhibits A-O hybridisation between the Pb 6s and O 2p orbitals. This additional bonding contribution along with the relatively small ionic radius of Pb (1.49Å [85]) compared to Ba (1.61Å [85]) results in some shorter A-O bonds in $PbTiO_3$ and hence leads to larger c/a ratio and polarisation [84]. Similar A-O covalence has also been observed in Bi-based materials with hybridisation between Bi 6s and O 2p sites [86]. Li- [87] and K-based [88] perovskites show mostly ionic bonding between A-site and oxygen ions, similar to $BaTiO_3$ and therefore lack the chemical, structural and electrical mechanisms behind high g_{ij} coefficients. Despite the current drive within the ferroelectrics community for lead-free alternatives, evidence suggests that the need for highly polarisable A-site ions such as Pb are highly desirable along with Bi for large tetragonality, polarisation and therefore g_{ij} coefficients in single crystal form.

Figure 3.2 shows the g_{33}, g_{31}, g_{15} and g_h as a function of tetragonality from experimental and theoretical work of $P4mm$ single crystals. Material properties of tetragonal crystals are scarce for two reasons. Firstly the drive for materials possessing high d_{ij} coefficients has resulted in the preferred growth of [001] domain engineered rhombohedral crystals, making the motivation for the growth of tetragonal crystals low. Secondly the significantly large spontaneous strain of materials particularly with a tetragonality exceeding 1.5% results in processing difficulties, with samples often possessing significant macro-cracking or small sample size which limits characterisation ability. Despite these factors, Figure 3.2 shows a general increase in g_{33}, $|g_{31}|$, g_{15} and g_h with increasing tetragonality.

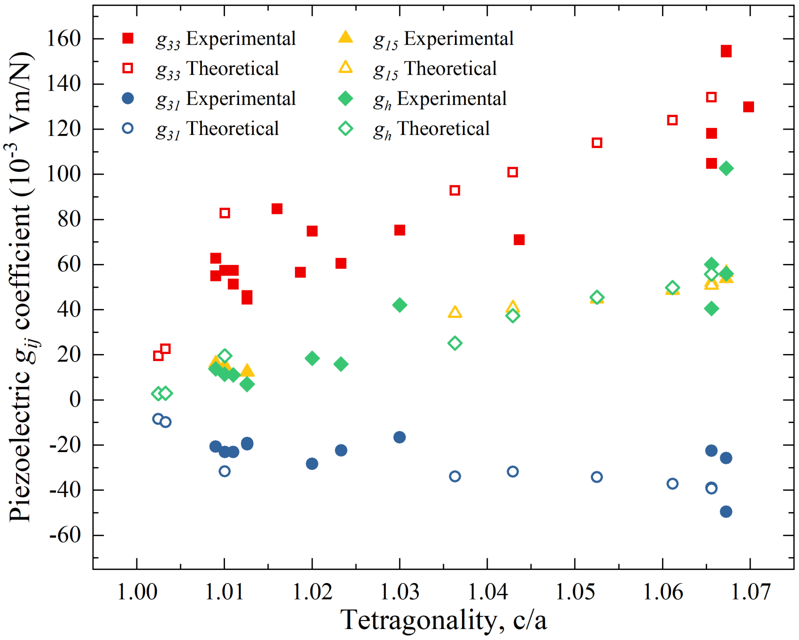

Figure 3.2: Piezoelectric g_{33}, g_{31}, g_{15} and g_h coefficients as a function of tetragonality, c/a for *P4mm* single crystals throughout literature. Material properties listed in Table A.1

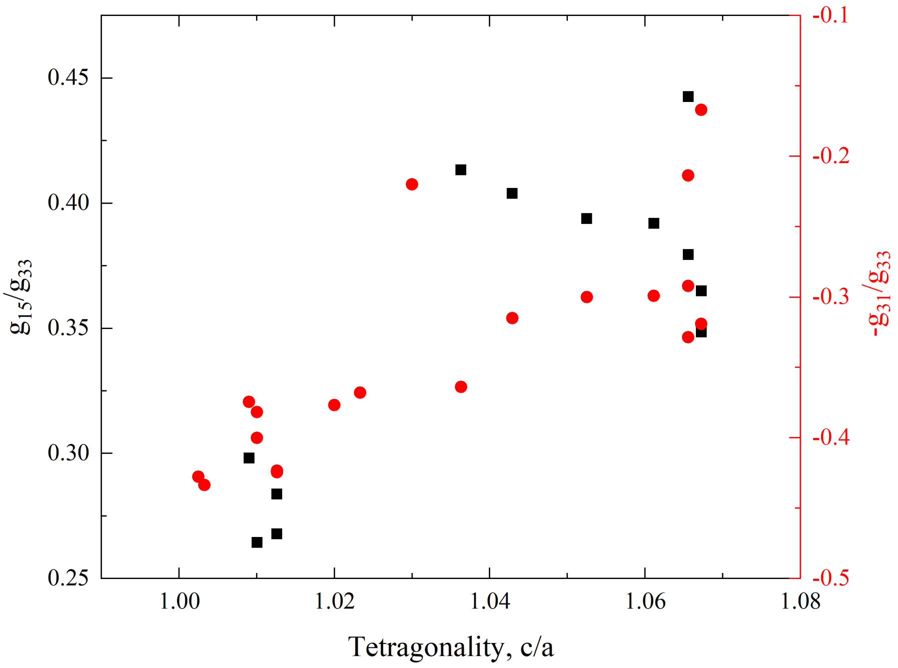

Figure 3.3: Piezoelectric anisotropy between the shear-longitudinal modes (g_{15}/g_{33}) and lateral-longitudinal (g_{31}/g_{33}) for tetragonal single crystals from literature

The increase in tetragonality also results in an increase in piezoelectric anisotropy between both the lateral-longitudinal g_{31}/g_{33} modes and shear-longitudinal modes g_{15}/g_{33} as shown in Figure 3.3. An explanation for the increasing anisotropy is the enhanced covalence between the B-site and axial oxygen ion which may electrically clamp ions and increase the preferential polarisation longitudinally rather than laterally.

It is useful to calculate the piezoelectric properties as a function of angle away from the polar axis to observe whether a ferroelectric material exhibits ‘extender’ or ‘rotator’ behaviour. Rotator ferroelectrics arise when the piezoelectric properties are enhanced through the application of an electric field away from the polar axis. These types of ferroelectrics also possess higher d_{15}/d_{33} ratios with the large shear component contributing to d_{31} values which reduces the hydrostatic properties. Extender ferroelectrics possess smaller d_{15}/d_{33} ratios and show the largest d_{33} along the polar axis, and therefore contribution to the d_{31} from the shear component is substantially lower resulting in larger piezoelectric anisotropy and hydrostatic coefficients.

If all piezoelectric properties are known, the orientational dependence can be calculated by converting to alternative coordinate systems. The longitudinal charge coefficient (d_{33}^{*}) and relative permittivity ($\epsilon_{33}^{T*}/\epsilon_0$) as function of angle away from the polar axis (Θ) can be calculated using Equation 3.5 and 3.6, respectively.

$$d_{33}^{*} = cos\Theta(d_{31}sin^2\Theta + d_{15}sin^2\Theta + d_{33}cos^2\Theta) \tag{3.5}$$

$$\epsilon_{33}^{T*}/\epsilon_0 = (\epsilon_{11}^{T}/\epsilon_0)sin^2\Theta + (\epsilon_{33}^{T}/\epsilon_0)cos^2\Theta \tag{3.6}$$

Figure 3.4 shows the polar plots of (a) d_{33}^{*}, (b) $\epsilon_{33}^{T*}/\epsilon_0$, and (c) g_{33}^{*} at different tetragonalities. The d_{33}^{*} shows clear distinguishability between the rotator and extender behaviour of tetragonal materials. Electrically the critical value of d_{15}/d_{33} at which a rotator ferroelectric converts into an extender ferroelectric is approximately 1.5 [89]. Whilst the lack of d_{15} and $\epsilon_{11}^{T}/\epsilon_0$ values results in significant gaps between each c/a ratio, Figure 3.4 (a) shows the critical value of tetragonality for a rotator-extender transition occurs within 1.013 and 1.036. For $\epsilon_{33}^{T*}/\epsilon_0$, all materials show a similar trend showing a maximum perpendicular to the polar axis. The dielectric anisotropy is largest at low tetragonalities which exhibits a more defined ‘donut’ shape with larger indentation along the polar axis. As tetragonality decreases the dielectric anisotropy decreases, gradually replacing the well-defined donut shape with an elongated sphere however still showing a maximum perpendicular to the polar axis. The g_{33}^{*} is observed to increase continuously along the [001] with tetragonality similar to Figure 3.2. Whilst the piezoelectric d_{33}^{*} coefficient clearly distinguishes between extender and rotator ferroelectrics, the piezoelectric g_{33}^* coefficient shows extender ferroelectric behaviour for all tetragonal materials.

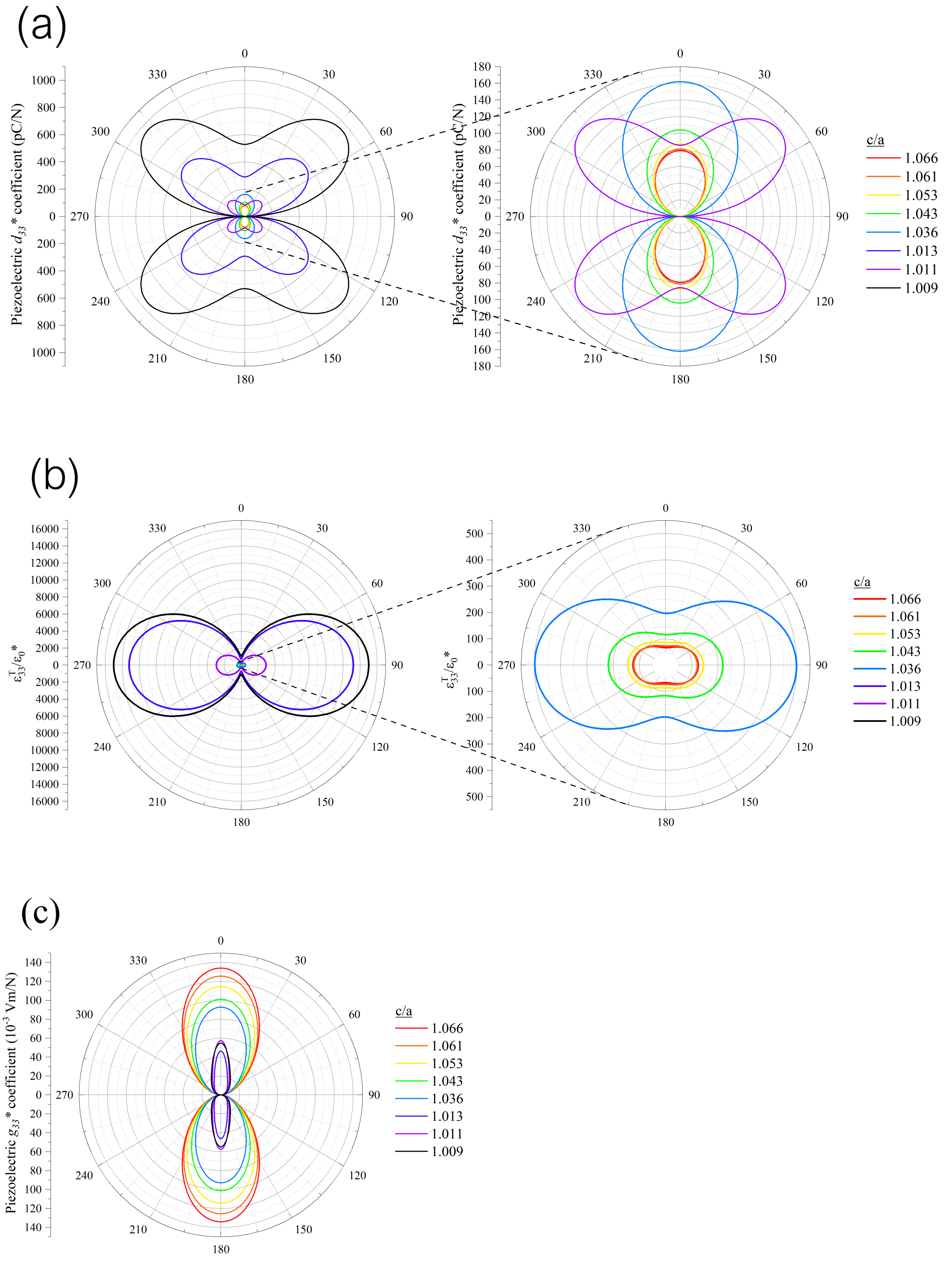

Figure 3.4: Polar plots of (a) piezoelectric charge coefficient, d_{33}^* (b) relative permittivity, $\epsilon_{33}^{T*}/\epsilon_0$, and (c) piezoelectric voltage coefficient, g_{33}^* as a function of angle away from the polar axis. d_{33}^* was calculated using Equation 3.5 and $\epsilon_{33}^T/\epsilon_0$ calculated using Equation 3.6 using d_{33}, d_{31}, d_{15}, $\epsilon_{33}^T/\epsilon_0$ and $\epsilon_{11}^T/\epsilon_0$ values for tetragonal single crystals and single domains from literature.

3.2 Polycrystalline Ceramics

Figure 3.5 shows the g_{33}, g_{31} and g_h for polycrystalline materials as a function of tetragonality. Whilst for single crystals the tetragonality appears to be the significant driving force (Figure 3.2), for polycrystalline samples the relationship is more complicated. A wide distribution for g_{33} can be observed with peak values achieved at tetragonalities between 1.015 and 1.030. The initial increase in g_{33} may be attributed to the increasing polarisation similar to behaviour for single crystals, however above 3% tetragonality the g_{33} continuously decreases. The distribution of g_{31} is much smaller and remains relatively unchanged compared to g_{33} with values ranging from -0.3x10^{-3} to -5.9x10^{-3}Vm/N. A combination of the distributions in the g_{ij} coefficients also results in a wide distribution of g_h.

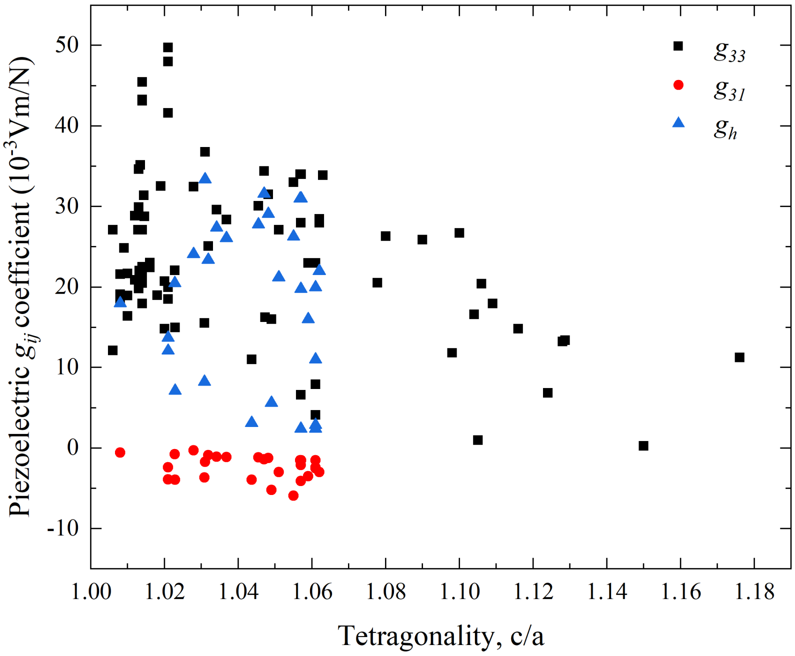

Figure 3.5: Piezoelectric g_{33}, g_{31}, and g_h as a function of tetragonality for polycrystalline ceramics from throughout literature. Material properties listed in Table A.2

The significant difference between polycrystals and single crystals is microstructure, with polycrystalline samples made up of many grains which lack any long range orientation, whilst single crystals consist of one grain with long range translational symmetry. It is most likely that the more complex microstructure in polycrystals and the subsequent intergranular effects have drastic effects on electrical properties similar to behaviour observed for the piezoelectric d_{ij} coefficient.

Leist et al. [51] used the case study of La-doped $BiFeO_3$-$PbTiO_3$ polycrystalline ceramics to study the effect of tetragonality on the piezoelectric and dielectric properties. It was found that above a critical tetragonality of 1.045 the suppression of domain switching resulted in d_{33} values of 10-20pC/N, whereas below the critical tetragonality d_{33} values of up to 10 times greater were measured. It was also postulated that the nucleation of new domains through the application of an external electric field is energetically unfavourable due to the enormous elastic energy for highly tetragonal materials. Li et al. [90] showed an increase in domain wall density with increasing La content for La-doped BFPT. Although not explicitly stated by the author that this was a result of decreasing domain wall strain energy through decreasing tetragonality, it may be a likely cause. Yoon et al. [91] have also investigated the influence of tetragonality on piezoelectric properties of (1-x)$BaTiO_3$-(x)$Bi_{0.5}Na_{0.5}TiO_3$ polycrystalline ceramics. It was found through transmission electron microscopy and polarisation-electric field loops that an increase in tetragonality reduces reversible domain wall contributions to piezoelectricity and reduces irreversible domain wall mobility. Furthermore, high-energy X-ray diffraction studies have also shown a decrease in 90° domain wall motion at increasing tetragonalities [92]. As domain wall density and motion heavily influence the piezoelectric properties, the suppression of domain walls though intergranular stress leads to low d_{33} and therefore low g_{33} values in polycrystalline samples.

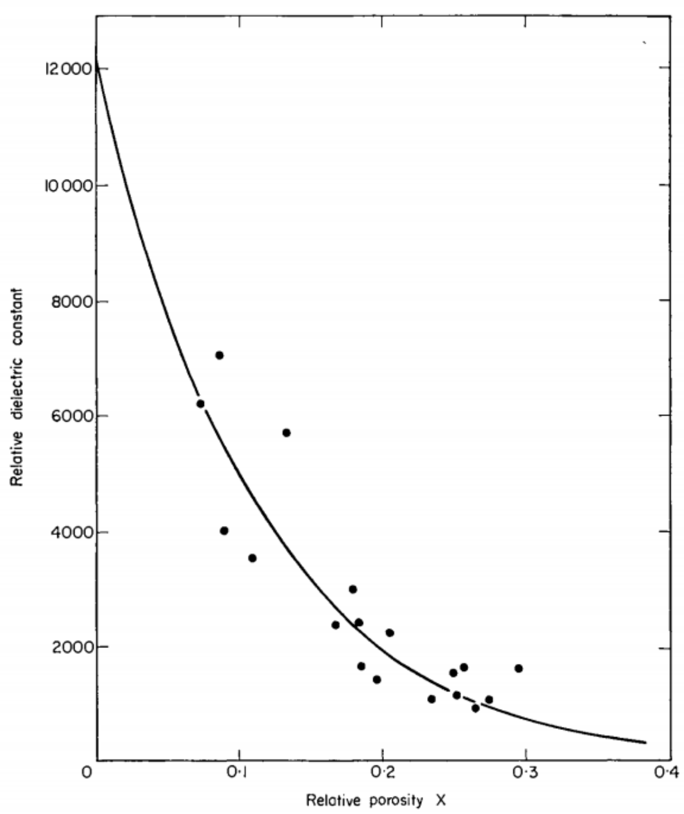

Figure 3.6: Relative permittivity against relative porosity for $Ba_{0.76}Sr_{0.24}TiO_3$ Ceramics. Taken from [20]

The effect of intergranular stress can be alleviated with the introduction of pores within the piezoceramics. The presence of pores in a material can reduce the intergranular stress, and the elastic constraints from neighbouring grains are reduced therefore reorientation of individual grains is easier and backswitching is less likely to occur. Not only do porous ceramics aid in the reorientation of individual grains but the dilution of the permittivity as shown in Figure 3.6 can also dramatically increase the piezovoltage coefficients. Bowen et al. [93] showed that the hydrostatic g_h can be significantly improved through the introduction of porosity into PZT with values for g_h increasing from $\approx$5x10^{-3}Vm/N for highly dense piezoceramics to $>$150x10^{-3}Vm/N at 40% relative density. Although the reduction in relative density compared to conventionally processed PZT reduces the piezoelectric d_{33} simply through the shear lack of piezoceramic present, the degradation of the relative permittivity due to the replacement of ceramic within the sample which typically can possess ϵ_{rel}>100 with air (ϵ_{rel}=1) results in improved g_{33}. Furthermore the effect of porosity also reduces the d_{31} at a much quicker rate than the d_{33} resulting in greater hydrostatic properties.

Another consideration is the coercivity of polycrystalline ceramics compared to single crystals. Polycrystalline samples typically possess a higher coercive field than their single crystal counterparts as shown in Figure 3.7, due to ferroelastic domain wall pinning at grain boundaries which in turn requires higher fields to overcome [20, 94–96]. For materials possessing low tetragonality or materials that are ferroelectrically soft, the amount of electric field required is practically achievable, however for materials with high tetragonality the amount of field required exceeds practical capabilities therefore results in low d_{ij} and g_{ij} values through insufficient poling.

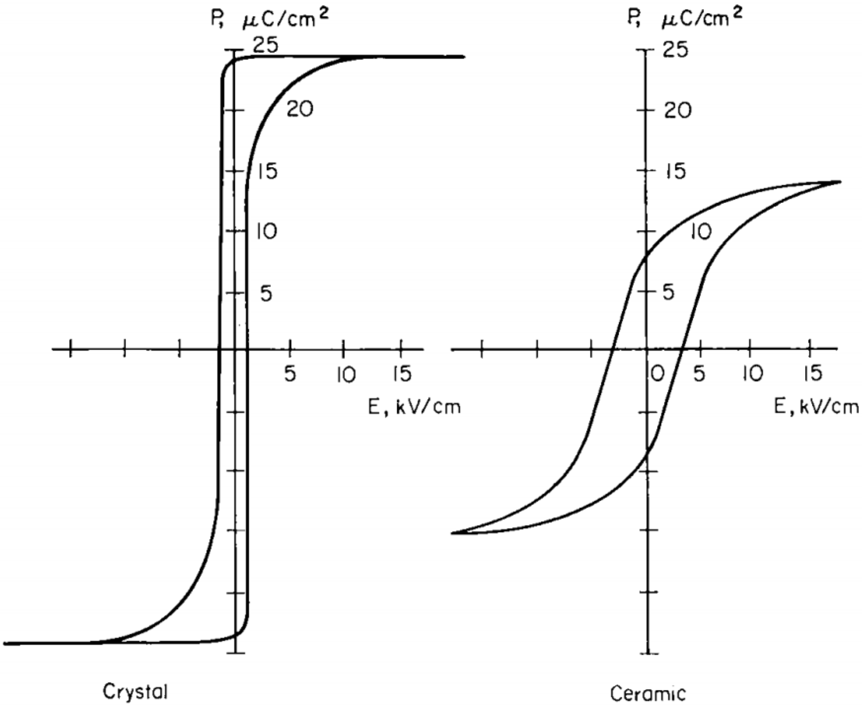

Figure 3.7: PE loops for single crystal and polycrystalline BaTiO3. Taken from [20]

It is interesting to note that KNN-based ferroelectric materials show relatively large g_{33} values with relatively low values for the tetragonality [97]. Whilst this could simply be coincidental that KNN-based materials occupy the region where the polarisation contribution from tetragonality is at a maximum before microstructural effects begin to suppress the g_{33}, Ahn et al. [98] proposed that the electronegativity of these materials could be considered a key factor. The authors constructed a function , F_t shown in Equation 3.7, that not only considers the tolerance factor but also the average electronegativity (Equation 3.8) and found a correlation between the F_t and g_{33} shown in Figure 3.8.

$$F_t = \Delta(t_G + \Delta\chi)/\Delta x \tag{3.7}$$

$$\Delta\chi = (\chi_{A-O} + \chi_{B-O})/2 \tag{3.8}$$

Where t_G is the Goldschmidt tolerance factor as shown in Equation 2.1, χ_{A-O} is the difference between A-site and oxygen-ion electronegativity, and χ_{B-O} is the difference between B-site and oxygen-ion electronegativity, Δx is the required dopant mole fraction in order to induce an orthorhombic-tetragonal phase transition.

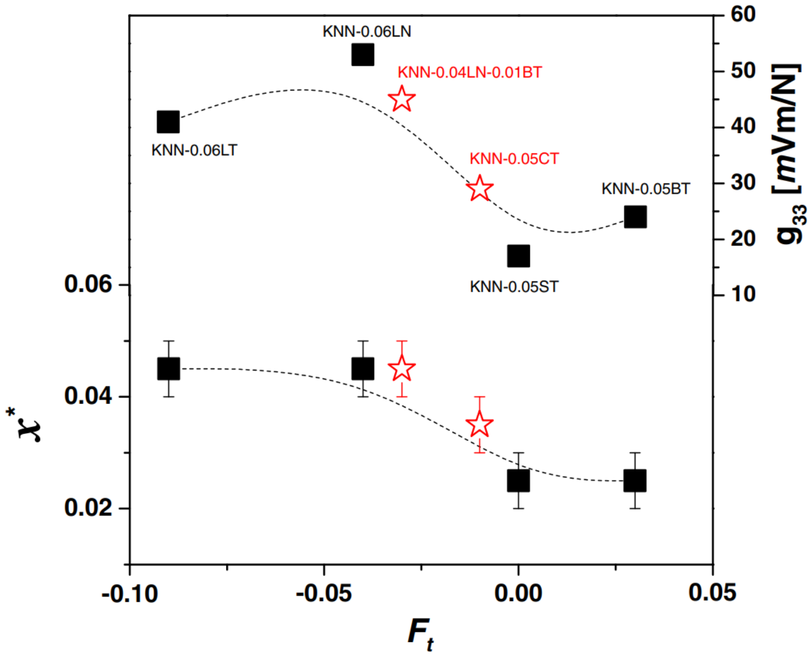

Figure 3.8: The orthorhombic-tetragonal transition doping level, x^* and g_{33} as a function of F_t (Equation 3.7) for modified KNN polycrystalline ceramics. Taken from [98]

Equation 3.7 cannot be applied generally as many materials do not require a doping regime in order to create a tetragonal phase and therefore x=0. However the idea that electronegativity may have a significant role on the piezovoltage coefficient is one to be explored. Figure 3.9 shows g_{33}, g_{31} and g_h values against the average electronegativity $\bar{\chi}$ (Equation 3.8) and the difference between electronegativity of A and B ions compared to oxygen $\Delta\chi$ $(= [\chi_{A-O} - \chi_{B-O}]/2)$. In both cases no clear relationship can be observed and therefore any potential relationship between the electronegativity and g_{ij} is still unclear.

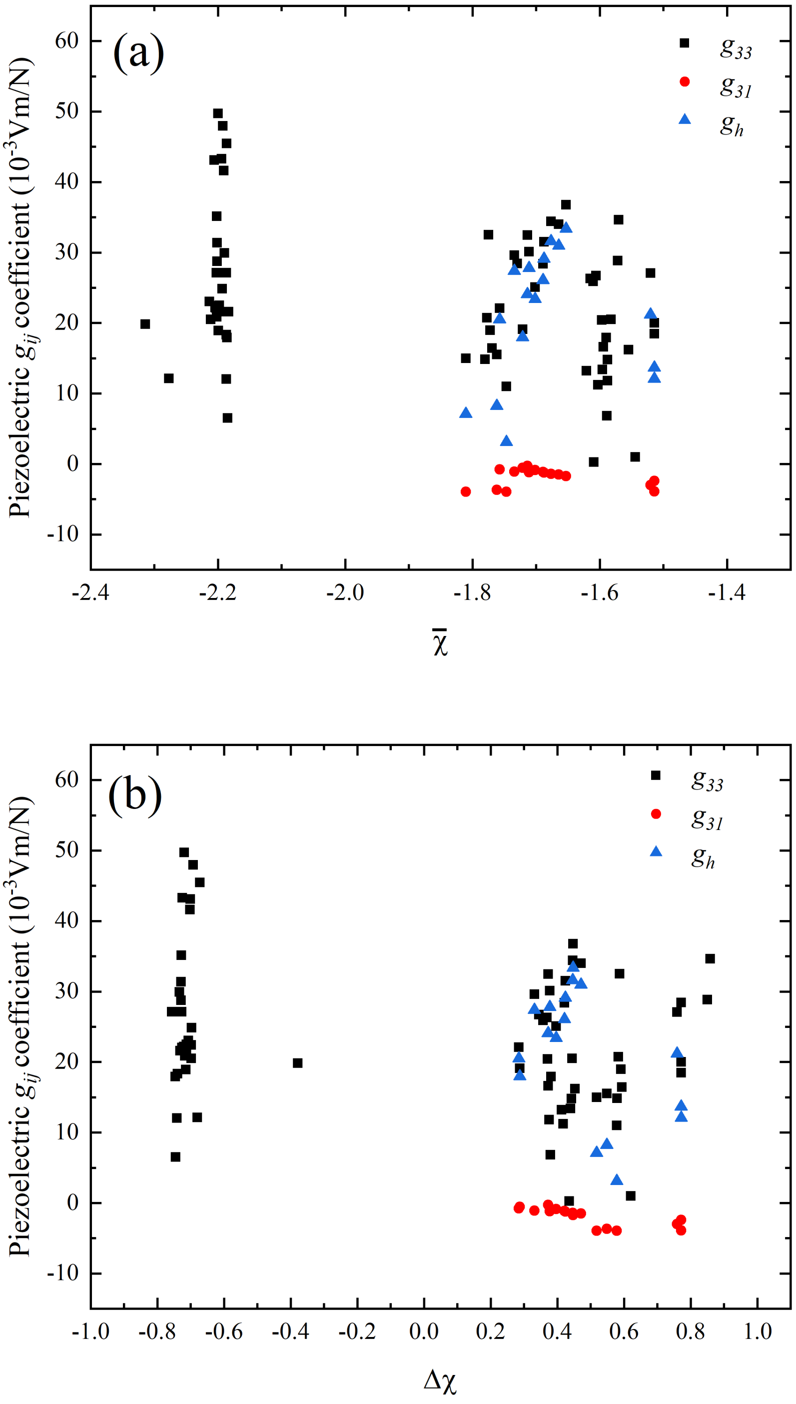

Figure 3.9: Piezoelectric g_{33}, g_{31}, and g_h coefficients vs (a) average compound electronegativity ($[\chi_{A-O} + \chi_{B-O}]/2$), and (b) difference in electronegativity between A-site and B-site ions relative to the oxygen ion ($[\chi_{A-O} - \chi_{B-O}]/2$)

Finally the relative atomic weights between A and B site ions has also been postulated to give good correlation between material properties and g_{33}. As shown in Figure 3.10 the g_{33} is relatively unchanged for lead based materials due to the coupling between the permittivity and d_{33} as shown previously in Figure 3.1. For B-site heavy materials such as the modified KNN family, the inverse relative atomic weight shows that whilst the d_{33} shows a similar trend to lead based materials the permittivity follows the inverse trend and therefore the g_{33} is drastically improved to twice that of lead based materials [99]. As mentioned by the authors, the reason for this phenomenon is still unknown.

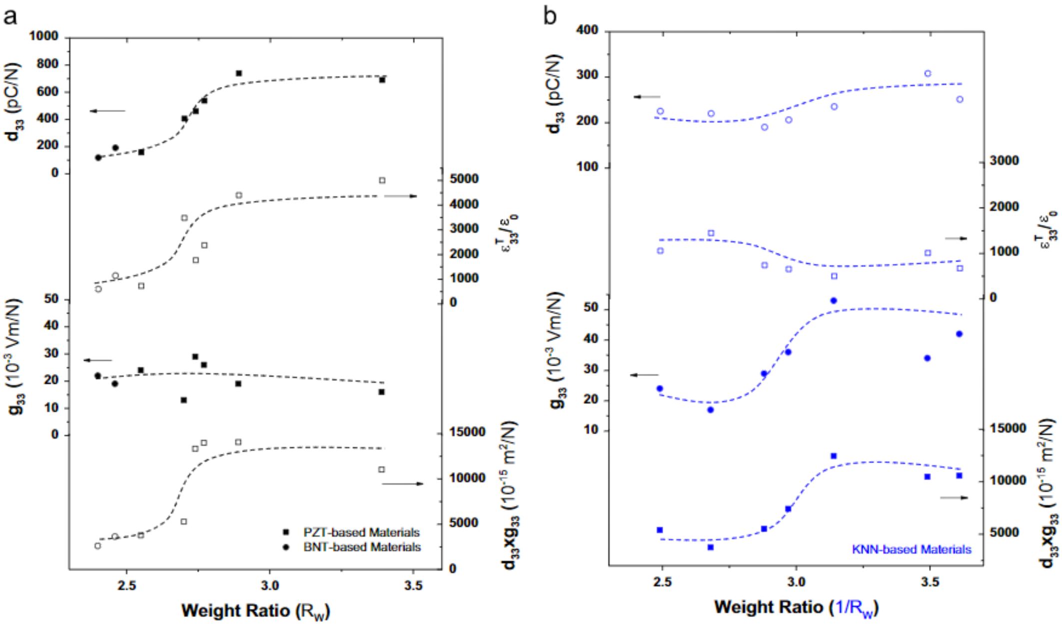

Figure 3.10: The d_{33}, $\epsilon_{33}^T/\epsilon_0$, g_{33}, and d_{33}xg_{33} (a) as a function of relative atomic weight between A-site and B-site ions in A-site heavy PZT and BNT based materials and (b) as a function of the reciprocal of relative atomic weight for B-site heavy KNN-based materials. Taken from [99]

3.3 Material candidates for high g_{ij}

3.3.1 Lead Titanate, $PbTiO_3$

The use of lead titanate in hydrophone applications is not recent. However to overcome the issue of processing, the lead titanate polycrystalline ceramics are heavily modified to reduce the spontaneous strain. Table 3.1 shows the reported piezoelectric and dielectric properties of some modified lead titanate polycrystalline ceramics. Similarly to the doping of $BiFeO_3$-$PbTiO_3$ polycrystalline ceramics shown in Table 2.3, rare-earth doping of $PbTiO_3$ has been a popular choice for the enhancement of piezoelectric properties. Although the values for the d_{33} and d_{31} are inferior to that of PZT, the lower values for the d_{31} due to the intrinsic decoupling of 33-31 modes through significant tetragonality, results in higher hydrostatic properties that compared to PZT. Furthermore, the reduced permittivity which is another product of increased tetragonality also results in higher g_{33} and g_h coefficients compared to PZT, making these materials more suitable for passive sonar device applications. Due to industry confidentiality with regards to the chemical formulations of these materials, it is difficult to say exactly what modifications modified lead titanate ceramics have been undertaken. However the author suspects that the materials used in device applications are $(Pb_{0.72}Ca_{0.24})(Co_{0.5}W_{0.5})_{0.04}Ti_{0.96}O_3$ polycrystalline ceramics, based on the similarity in material properties between those quoted in Ref. [100], and the material properties that are quoted for hydrophone devices in Ref. [101].

Table 3.1: Piezoelectric, dielectric and structural data for a range of pure and modified PbTiO3 polycrystalline ceramics from throughout literature

Material	d_{33} (pC/N)	d_{31} (pC/N)	d_h (pC/N)	g_{33} (mVm/N)	g_{31} (mVm/N)	g_h (mVm/N)	Ref.
$Pb[(Y_{0.5}Nb_{0.5})_{0.07}(Ti_{0.5}Zr_{0.5})_{0.93}]O_3$	330	-146	38	23.8	-10.5	2.7	[102]
$Pb_{0.85}La_{0.15}Ti_{0.96}Mo_{0.02}Fe_{0.02}O_3$			64			20.2	[103]
$Pb_{0.76}Ca_{0.24}Ti_{0.98}Mn_{0.02}O_3$	50	-4.1	41.8	34.0	-2.7	28.5	[104]
$Pb_{0.73}Sm_{0.02}Ca_{0.24}Ti_{0.98}Mn_{0.02}O_3$	52	-3.5	45.0	28	-1.9	24.2	[104]
$Pb_{0.70}Sm_{0.04}Ca_{0.24}Ti_{0.98}Mn_{0.02}O_3$	65	-3.4	58.2	31	-1.6	27.7	[104]
$Pb_{0.67}Sm_{0.06}Ca_{0.24}Ti_{0.98}Mn_{0.02}O_3$	75	-3.2	68.6	28	-1.2	25.6	[104]
$Pb_{0.64}Sm_{0.08}Ca_{0.24}Ti_{0.98}Mn_{0.02}O_3$	78	-2.5	73.0	23	-0.8	21.5	[104]
$Pb_{0.75}La_{0.02}Ca_{0.24}Ti_{0.98}Mn_{0.02}O_3$	48	-2.2	43.6	33.5	-1.5	30.4	[105]
$Pb_{0.76}Ca_{0.24}Ti_{0.955}Ta_{0.02}Mn_{0.02}O_3$	33	-1.1	30.8	29.8	-0.1	27.8	[105]
$Pb_{0.76}Ca_{0.24}Ti_{0.98}Mn_{0.02}O_3$	45	-2.0	41	34	-1.5	31	[106]
$Pb_{0.74}La_{0.02}Ca_{0.24}Ti_{0.98}Mn_{0.02}O_3$	54	-2.2	49.6	34.4	-1.4	31.6	[106]
$Pb_{0.72}La_{0.04}Ca_{0.24}Ti_{0.98}Mn_{0.02}O_3$	60	-2.4	55.2	28.4	-1.1	26.1	[106]
$Pb_{0.70}La_{0.06}Ca_{0.24}Ti_{0.98}Mn_{0.02}O_3$	75	-2.6	69.8	25.1	-0.9	23.4	[106]
$Pb_{0.68}La_{0.08}Ca_{0.24}Ti_{0.98}Mn_{0.02}O_3$	85	-3.0	79	32.5	-0.3	24.1	[106]
$(Pb_{0.76}Ca_{0.24})(Co_{0.5}W_{0.5})_{0.04}Ti_{0.96}O_3$	68.2	-3.2	61.9	36.8	-1.7	33.4	[100]
$PbTiO_3 + 0.05Bi_{2/3}TiO_3$	9.1	-3.1	2.9	6.6	-2.1	2.4	[107]
$PbTiO_3 + 0.025PbZn_{1/3}Nb_{2/3}O_3$	20	-1.5	17.0	11	-0.8	9.3	[107]
$PbTiO_3 + 0.05PbZn_{1/3}Nb_{2/3}O_3$	47	-7	33	23	-3.5	16	[107]
$PbTiO_3 + 0.05PbNb_{4/5}O_3$	37	-10	17	16	-5.2	5.6	[107]
$PbTiO_3 + 0.025Bi(Zn_{0.5}Ti_{0.5})O_3$	43	-2.5	38	23	-1.5	20	[107]
$PbTiO_3 + 0.05Bi(Zn_{0.5}Ti_{0.5})O_3$	37	-3.9	29	28	-3	22	[107]
$PbTiO_3 + 0.025Bi_{2/3}Zn_{1/3}Nb_{2/3}O_3$	15	-4.4	6	8	-2.5	2.9	[107]
$PbTiO_3 + 0.05Bi_{2/3}Zn_{1/3}Nb_{2/3}O_3$	47	-7.4	32	28	-4.1	19.8	[107]
$Pb_{0.975}La_{0.025}Ti_{0.99}Mn_{0.01}O_3$	52.8	-5.8	41.3	27.1	-3.0	21.2	[108]
$Pb_{0.985}La_{0.015}Ti_{0.99}Mn_{0.01}O_3$	62	-8.0	45.9	18.5	-2.4	13.7	[108]
$Pb_{0.985}La_{0.015}TiO_3$	83.8	-16.5	50.8	20	-3.9	12.1	[108]

The growth of $PbTiO_3$ in single crystal form aims to improve g_{ij} coefficients by exploiting the larger degree of translational symmetry. Despite the large spontaneous strain and volatile nature of reagents, high quality lead titanate single crystals have been grown and tested possessing g_{33} values from 104.9-154.3x10^{-3} Vm/N, $|g_{31}|$ values between 22.4-49.4x10^{-3} Vm/N and g_h values from 40.5-102.8x10^{-3} Vm/N [109–111]. The large variation in material properties can stem from sample quality, differences in chemistry and quantity of flux, and method of testing and associated errors of characterisation. Generally these values are found to be in agreement with theoretical calculations made by Haun et al. [112].

The growth of large pure lead titanate crystals has been attempted using a number of crystal growing techniques such as the flux method, float-zone method and top-seeded solution growth method. Table 3.2 lists the techniques used for growing lead titanate crystals and achieved dimensions and the piezoelectric and dielectric properties of characterised lead titanate single crystals are shown in Table A.1.

Table 3.2: Achieved crystal dimensions for a range of growth techniques from throughout literature for $PbTiO_3$

Growth Technique	Dimensions (mm^3)	Ref.
Top-seeded solution growth	32 x 32 x 6	[113]
Flux growth	4 x 3 x 2	[114]
Float-zone growth	5 x 2 x 2	[115]
Self-flux growth	5 x 5 x 5	[116]
Flux growth	3 x 2 x 1	[117]
Flux growth	20 x 12 x 3	[118]
Flux growth	2.5 x 1.5 x 1.5	[119]
Flux growth	2 x 2 x 0.2	[120]
Flux growth	3 x 2.8 x 1.1	[121]
Flux growth	4.5 x 4.5 x 1.7	[122]
Self-flux growth	4 x 4 x 2	[123]
Flux growth	10.1 x 10.1 x 2.9	[124]
Czochralski	20⌀ x 3 (circular)	[125]
Flux growth	4.5 x 2.5 x 0.6	[126]
Flux growth	5 x 3 x 1	[127]
Flux growth	<10	[128]

It is obvious to see from Table 3.2 that the scalability in growing highly tetragonal crystals is a major issue for commercialisation. Arguably the most scalable method of growing ferroelectric single crystals is by modified Bridgman method where single crystals of PMN-PT with 3"⌀ have been achieved and are commercially available [129]. In this method material is placed into a platinum crucible which is in turn placed into a dual-zone vertical furnace. The material is melted in the 'hot' zone and is then slowly lowered into the 'cold' zone which is below the melting point to induce crystallisation [130]. This method is well suited for growing rhombohedral crystals where the volume expansion when cooling through the Curie temperature is <1% and thus the only limitations are the size of furnace and crucible. The physical constraints of the platinum crucible wall and the volume expansion of the material when cooling through T_C results in intense cracking or even complete disintegration of samples. The practical limit of tetragonality for using the modified Bridgman method is unclear, however Li et al. [131] observed significant cracking at the top of a Bridgman grown PIN-PMN-PT single crystal with c/a ratio of 1.016, whereas regions within the same crystal where c/a=1.009 and 1.011 showed no signs of cracking. Although growing crystals possessing c/a=1.011 may be the most commercially scalable option, this would limit the g_{33},

g_{31}, g_{15} and g_h to approximately 80, -30, 20 and 20×10^{-3}Vm/N according to Figure 3.2. Whilst these values for g_{33}, g_{31}, and g_{15} exceed that of many other materials, the hydrostatic voltage coefficient is lower than that of modified $PbTiO_3$ polycrystalline ceramics [100,104–106,132]. Commercial barium titanate with a tetragonality of approximately 1.1% is processed using top seeded solution growth (TSSG) which overcomes the issue of crucible constraints [133–135]. Whilst this method may be suitable for barium titanate, the extreme loss of volatiles for bismuth and lead based materials results in exposure time limitation and therefore crystal size.

Another crystal growth technique that may be considered is solid state crystal growth [136]. Whilst this technique is very much still in its infancy, it may be the future of commercially grown single crystals due to its low costs relative to other techniques and similar to TSSG overcomes the issue of the physical constraint of the crucible walls for highly tetragonal materials.

Another possibility of fabricating high g_{ij} piezoelectric materials that may be commercially viable are textured ceramics. Textured ceramics offer an intermediate between polycrystalline ceramics and single crystals. Although the presence of grains and grain boundaries is similar to polycrystalline ceramics, the microstructure is designed in order to provide a degree of crystallographic and polarisation alignment similar to single crystals [137,138]. Liu et al. [139] have fabricated <001> textured tantalum and antimony co-doped 0.99KNN-0.01$CaZrO_3$ with texturing degrees varying from 71.5-88.8%. Comparisons to non-textured samples of identical composition showed an average increase in the g_{33} of 85.0%. Furthermore, work on textured BCTZ [140] showed an increase in the g_{33} from 12.5x10^{-3}Vm/N for nontextured ceramics to 34.3x10^{-3}Vm/N for 96% textured ceramics. However the most significant g_{33} has been measured for textured lead titanate ceramics. Yan et al. [141] were able to fabricate textured Sm and Mn co-doped $PbTiO_3$ ceramics using templated grain growth method. It was found that as the degree of texturing was increased, the piezoelectric d_{33} increases from 53pC/N for non-textured ceramics to 95pC/N and 127pC/N for 82% textured and 95% textured, respectively. The relative permittivity decreases with increasing texture giving values of 202, 146 and 124 for non-textured, 85% and 95% textured, respectively. The reasons for the enhancement of the d_{33} and suppression of the dielectric permittivity are analogous with those of single crystals. As the texturing degree increases, the angle between crystallite polarisations and the polar axis, where a maximum d_{33} for an extender ferroelectric and a minimum relative permittivity is observed, decreases. The simultaneous increase in the piezoelectric d_{33} coefficient and decrease in the relative permittivity results in the significant increase in g_{33} from 30x10^{-3} Vm/N for polycrystalline $PbTiO_3$ ceramics to 74x10^{-3}Vm/N for 82% textured ceramics and 115x10^{-3}Vm/N for 95% textured samples.

3.3.2 Bi(Me)O3 – PbTiO3 Single Crystals

High quality single crystals of tetragonal $BiScO_3$-$PbTiO_3$ have been grown using the solution growth method (or flux method). Initial results reported in 2002 by Zhang et al. [142] showed that single crystal 0.66$BiScO_3$-0.34$PbTiO_3$ possessed a g_{33} and g_h 75.3x10^{-3} Vm/N and 42.2x10^{-3} Vm/N, respectively, and later in 2004 grew and characterised modified $BiScO_3$-$PbTiO_3$ [143]. Although it is unclear what modification was made and the stoichiometry of the crystals, a g_{33} and g_h of 60.6x10^{-3} Vm/N and 18x10^{-3} Vm/N were reported.

Liu et al. [144] have grown and characterised Bi(Zn,Ti)O_3-$PbTiO_3$ and Bi(Zn,Nb)O_3-$PbTiO_3$ crystals using top-seeded solution method. Although the nominal stoichiometry was calculated to be 0.4BZT-0.6PT and 0.3BZN-0.7PT, energy dispersive X-ray analysis indicated stoichiometry of the crystals to be approximately 0.14BZT-0.86PT (BZTPT14) and 0.38BZN-0.62PT (BZNPT38). The tetragonality was reported as being 1.069982 and 1.04363 for BZPTPT14 and BZNPT38 crystals, respectively, and it was reported that BZTPT14 crystals possess a d_{33} of 138pC/N and relative permittivity of 120 resulting in a g_{33} of approximately 130x10^{-3} Vm/N, and BZNPT38 crystals possess a d_{33} of 157pC/N, a relative permittivity of 250 and g_{33} of 71x10^{-3} Vm/N.

The extremely large tetragonality reported for $BiFeO_3$-$PbTiO_3$ [36, 48, 49, 145, 146] also raises the notion of this solid solution being a potential candidate as a high g_{ij} material. Burnett et al. [147] have grown 0.5$BiFeO_3$-0.5$PbTiO_3$ crystals using the flux method possessing a relative permittivity of 200 and tetragonality of 1.11. Furthermore Zhu et al. [148] have also grown tetragonal BFPT single crystals again using the flux method with stoichiometry 0.67$BiFeO_3$-0.33$PbTiO_3$. The tetragonality of these crystals was found to be 1.1778 which resulted in significant cracking of the samples. However no piezoelectric properties were measured in either study.

Chapter 4

Phenomenological Theory of the BiFeO3–PbTiO3 Solid Solution

A clear correlation between the tetragonality of a piezoelectric single crystal and the g_{ij} coefficients was shown in Chapter 3. Section 2.3.3 highlighted the almost exclusive spontaneous strain behaviour of the (x)BiFeO$_3$-(1-x)PbTiO$_3$ solid solution which can exceed 18% at x=0.7 [35]. Using this information it is necessary to look at BiFeO3–PbTiO3 as a possible candidate for high g_{ij} piezoelectric ceramics.

There is limited data on single crystal BiFeO3–PbTiO3 due to significant conductivity and large spontaneous strain on cooling through the Curie temperature leading to significant fracturing and potentially full disintegration. Theoretical and mathematical studies can be powerful tools for explaining phenomena behind experimental data, or as a predictive tool bridging gaps between current understanding and expected properties and trends of materials.

Here, Landau-Devonshire (LD) theory has been applied to BiFeO3–PbTiO3 using two methods. Initially a linear coefficient method has been employed, however this fails to replicate the experimentally observed spontaneous strain behaviour. By using experimental X-ray diffraction data and modelling the spontaneous strain as an external tensile stress on the unit cell, the dielectric and piezoelectric properties have been investigated. Although Park et al. [149] have previously used phenomenological theory to study the evolution of Curie temperature with BiFeO3 content in BiFeO3–PbTiO3, this study explores the dielectric and piezoelectric properties as a function of composition and temperature.

4.1 Introduction to Landau Theory

Landau theory is a powerful mathematical tool used for describing phase transitions by considering the free energy of a system transforming from a high-symmetry state to a lower symmetry state. An appropriate order parameter is employed to describe the transition through a critical point and is chosen in order to satisfy the criteria that it is zero in the high-symmetry phase and a non-zero value in the low-symmetry state [150]. The Gibbs free energy ,G, takes the form of an expanded power series, eliminating odd power terms to satisfy symmetry conditions, as a function of external influences such as temperature, stress and field, as well as an order parameter as shown in Equation 4.1.

$$G(X, E, T) = G_0 + \alpha_1\psi^2 + \alpha_2\psi^4 + \alpha_3\psi^6 + \alpha_4\psi^8 + ... \tag{4.1}$$

Where G_0 is the equilibrium value of the free energy at the critical transition point, α_i are Landau coefficients, T is temperature, X_i is stress, E_i is electric field strength and ψ is the order parameter [150].

In 1949 and 1951 Alfred Frederick Devonshire [82, 151] applied Landau theory to describe the transitions and properties of ferroelectrics using the macroscopic spontaneous polarisation, P, as the order parameter. In the high symmetry centrosymmetric cubic phase the polarisation is zero and upon transformation to a lower symmetry non-centrosymmetric state the polarisation becomes a non-zero value therefore making it an appropriate order parameter.

Often the temperature dependence is embedded with the first Landau coefficient which takes the form $\alpha_1 = \alpha_0(T - T_C)$, where α_0 is a temperature independent term and T_C is the Curie temperature [150]. By expanding the free energy of the system as a function of the order parameter, external influences such as temperature, pressure and field, truncating to the 6th order gives Equation 4.2.

$$\Delta G(X, E, T) = \alpha_0(T - T_C)P^2 + \alpha_2P^4 + \alpha_3P^6 \tag{4.2}$$

Where as mentioned previously α_0, α_2 and α_3 are known as the Landau coefficients and contain all the dielectric information of the material. These coefficients are determined through experimental data however the validity of individual sets of coefficients can be scrutinised. For example there are multiple publications each possessing new Landau coefficients for barium titanate as shown in Table 4.1. The deviation of Landau coefficients over time can be due to:

- Increased computing capabilities giving the values of Landau coefficients for high order terms such as P^8.
- Each set of coefficients are most likely to have been taken from different sets of experimental data and therefore differences in property values and sample quality can lead to differences in coefficients.

Table 4.1: Reported Landau coefficients for $BaTiO_3$ over time from throughout literature. Taken from [152]

α_1, α_{11}, α_{111}	α_{12}, α_{112}, α_{123}	α_{1111}, α_{1112}. α_{1122}, α_{1123}	Ref.
$3.3 \times 10^5(T-368.5)$	-	-	[153]
1.37×10^8	-	-	
2.76×10^9	-	-	
$3.3 \times 10^5(T-381)$	3.23×10^8	-	[154]
$4.69 \times 10^6(T-393)$	4.36×10^9	-	
$-5.38 \times 10^7(T-393) + 2.68 \times 10^9$	-	-	
$3.34 \times 10^5(T-381)$	3.23×10^8	-	
$4.69 \times 10^6(T-393) - 2.02 \times 10^8$	4.47×10^9	-	[155]
$-5.52 \times 10^7(T-393) + 2.76 \times 10^9$	4.91×10^9	-	
$3.33 \times 10^5(T-383)$	4.9×10^8	-	
$3.6 \times 10^6(T-448)$	2.9×10^9	-	
6.6×10^9	$7.6 \times 10^7(T-393) + 4.4 \times 10^{10}$	-	[156]
$4.124 \times 10^5(T-388)$	7.974×10^8	3.863×10^{10}	[157]
-2.097×10^8	-1.950×10^9	2.529×10^{10}	
1.294×10^9	-2.500×10^9	1.637×10^{10}	
		1.367×10^{10}	
$3.61 \times 10^5(T-391)$	$-2.24 \times 10^9 + 6.7 \times 10^6 T$	4.84×10^{10}	[158]
$-1.83 \times 10^9 + 4 \times 10^6 T$	-2.2×10^9	2.53×10^{11}	
$1.39 \times 10^{10} - 3.2 \times 10^7 T$	5.51×10^{10}	2.80×10^{11}	
		9.35×10^{10}	

For materials such as barium titanate, obtaining high quality single crystals has become more convenient over the years and hence there has been an abundance of Landau-Devonshire related work towards barium titanate. However there are a large number of materials in which experimental data for single crystals is either scarce or non-existent, therefore phenomenological theories adopt assumptions and methods to describe these materials.

The previous description of Landau-Devonshire is a very fundamental description and considers a single component of the order parameter. For ferroelectrics it is more useful to break down the single-component polarisation into three orthogonal components labelled P_1, P_2 and P_3 which represent the polarisation components along the [100], [010] and [001] vectors, respectively [150].

By applying the multi-component order parameter, the full Gibbs free energy of a stress-free crystal, again truncated to the 6th order power term becomes:

$$\begin{aligned}\Delta G = {} & \alpha_1(P_1^2 + P_2^2 + P_3^2) + \alpha_{11}(P_1^4 + P_2^4 + P_3^4) \\ & + \alpha_{12}(P_1^2P_2^2 + P_2^2P_3^2 + P_1^2P_3^2) + \alpha_{111}(P_1^6 + P_2^6 + P_3^6) \\ & + \alpha_{112}(P_1^4[P_2^2 + P_3^2] + P_2^4[P_3^2 + P_1^2] + P_3^4[P_1^2 + P_2^2]) + \alpha_{123}P_1^2P_2^2P_3^2\end{aligned} \tag{4.3}$$

It is important to note that as the polarisation breaks down into three orthogonal components, additional Landau coefficients (α_{ijk}) have been introduced in order to describe the coupling between each orthogonal component.

The lowest energy value for each polarisation component can be determined by minimising the free energy with respect to each polarisation component:

Cubic	$P_1 = P_2 = P_3 = 0$
Tetragonal	$P_1 = P_2 = 0; P_3 \neq 0$
Orthorhombic	$P_1 = 0; P_2 = P_3 \neq 0$
Rhombohedral	$P_1 = P_2 = P_3 \neq 0$

$$\frac{\partial G}{\partial P_1} = 0 \qquad \frac{\partial G}{\partial P_2} = 0 \qquad \frac{\partial G}{\partial P_3} = 0$$

By using the appropriate structurally dependent conditions, the values for the polarisation components can be determined using the quadratic relation:

$$P^2 = \frac{-b \pm \sqrt{b^2 - 4ac}}{2a} \tag{4.4}$$

Tetragonal	$a = 3\alpha_{111}$	$b = 2\alpha_{11}$	$c = \alpha_1$
Orthorhombic	$a = 3\alpha_{111} + 3\alpha_{112}$	$b = 2\alpha_{11} + \alpha_{12}$	$c = \alpha_1$
Rhombohedral	$a = 3\alpha_{111} + 6\alpha_{112} + \alpha_{123}$	$b = 2\alpha_{11} + 2\alpha_{12}$	$c = \alpha_1$

So far the free energy has mainly been considered as a function of the order parameter, however other contributions to the free energy can arise from the application of external influences such as stress, electric field and the electrostrictive contributions [150]. The total free energy of the system considering all these contributions can be written as:

$$\Delta G_{total} = G_L + G_{EL} + G_{COUP} + G_{ES} \tag{4.5}$$

Where G_L is the Landau contribution which takes the form of Equation 4.3. G_{EL} is the elastic contribution, G_{COUP} is the contribution from electrostriction and G_{ES} the electrostatic contribution:

$$\begin{aligned} G_{EL} = &-\frac{1}{2}s_{11}^{P}(X_1^2 + X_2^2 + X_3^2) - s_{12}^{P}(X_1X_2 + X_2X_3 + X_3X_1) \\ &-\frac{1}{2}s_{44}^{P}(X_4^2 + X_5^2 + X_6^2) \end{aligned} \tag{4.6}$$

$$\begin{aligned} G_{COUP} = -Q_{11}(X_1P_1^2 + X_2P_2^2 + X_3P_3^2) + Q_{12}[(X_1(P_2^2 + P_3^2) + X_2(P_1^2 + P_3^2) \\ + X_3(P_1^2 + P_2^2))] - Q_{44}(X_4P_2P_3 + X_5P_1P_3 + X_6P_1P_2) \end{aligned} \tag{4.7}$$

$$G_{ES} = -E_1P_1 - E_2P_2 - E_3P_3 \tag{4.8}$$

Where s_{ij} is elastic compliance, X_i is external stress, Q_{ij} are the electrostriction coefficients, E_i is the external field, and P is polarisation.

Similarly to the polarisation components the external stress has been deconstructed into multi-component values where X_1, X_2, X_3 represent the orthogonal tensile or compressive components and X_4, X_5, X_6 are the shear stress components.

By substituting Equations 4.3 and 4.6 – 4.8 into Equation 4.5, the free energy of a ferroelectric system can be given by:

$$\begin{aligned} \Delta G_{total} = &\alpha_1(P_1^2 + P_2^2 + P_3^2) + \alpha_{11}(P_1^4 + P_2^4 + P_3^4) + \alpha_{12}(P_1^2P_2^2 + P_2^2P_3^2 + P_1^2P_3^2) \\ &+ \alpha_{111}(P_1^6 + P_2^6 + P_3^6) + \alpha_{112}(P_1^4[P_2^2 + P_3^2] + P_2^4[P_3^2 + P_1^2] + P_3^4[P_1^2 + P_2^2]) \\ &+ \alpha_{123}P_1^2P_2^2P_3^2 - \frac{1}{2}s_{11}^{P}(X_1^2 + X_2^2 + X_3^2) - s_{12}^{P}(X_1X_2 + X_2X_3 + X_3X_1) \\ &- \frac{1}{2}s_{44}^{P}(X_4^2 + X_5^2 + X_6^2) - Q_{11}(X_1P_1^2 + X_2P_2^2 + X_3P_3^2) \\ &+ Q_{12}[(X_1(P_2^2 + P_3^2) + X_2(P_1^2 + P_3^2) + X_3(P_1^2 + P_2^2))] \\ &- Q_{44}(X_4P_2P_3 + X_5P_1P_3 + X_6P_1P_2) - E_1P_1 - E_2P_2 - E_3P_3 \end{aligned} \tag{4.9}$$

By applying the same structurally dependent conditions as mentioned earlier to the free energy of a stress-free crystal (X_i=0), in the absence of an electric field (E_i=0), and truncated to the 6th order power gives the following:

$$\begin{aligned} \Delta G_{Cubic} = \quad & 0 \\ \Delta G_{Tetra} = \quad & \alpha_1P_3^2 + \alpha_{11}P_3^4 + \alpha_{111}P_3^6 \\ \Delta G_{Ortho} = \quad & \alpha_1(P_2^2 + P_3^2) + \alpha_{11}(P_2^4 + P_3^4) + \alpha_{12}(P_1^2P_2^2 + P_2^2P_3^2 + P_3^2P_1^2) \\ & +\alpha_{111}(P_2^6 + P_3^6) + \alpha_{112}(P_2^4P_3^2 + P_3^4P_2^2) \\ \Delta G_{Rhom} = \quad & \alpha_1(P_1^2 + P_2^2 + P_3^2) + \alpha_{11}(P_1^4 + P_2^4 + P_3^4) + \alpha_{12}(P_1^2P_2^2 + P_2^2P_3^2 + P_1^2P_3^2) \\ & +\alpha_{111}(P_1^6 + P_2^6 + P_3^6) + \alpha_{112}(P_1^4[P_2^2 + P_3^2] + P_2^4[P_3^2 + P_1^2] + P_3^4[P_1^2 + P_2^2]) \\ & +\alpha_{123}P_1^2P_2^2P_3^2 \end{aligned}$$

By simultaneously solving the free energy for each structural phase the most likely structure at a particular temperature can be studied. Figure 4.1 show the free energy as a function of temperature for barium titanate and lead titanate using Landau coefficients from [155] and [112], respectively. For barium titanate it is initially shown that the lowest free energy is the rhombohedral phase below 200K. From 200K to 282K the lowest energy phase is orthorhombic, from 282K to 395K it is tetragonal and finally above 395K the system becomes cubic. For lead titanate the lowest energy structural phase from 0K to the Curie temperature at approximately 765K is always tetragonal. The example for lead titanate and barium titanate as well as other unary perovskites is unsurprising as the coefficients have been derived from experimental data and therefore reapplying them should result in the correct transition temperatures. However for solid solutions this technique may be a useful tool in determining the most likely structural phase at particular temperatures and compositions.

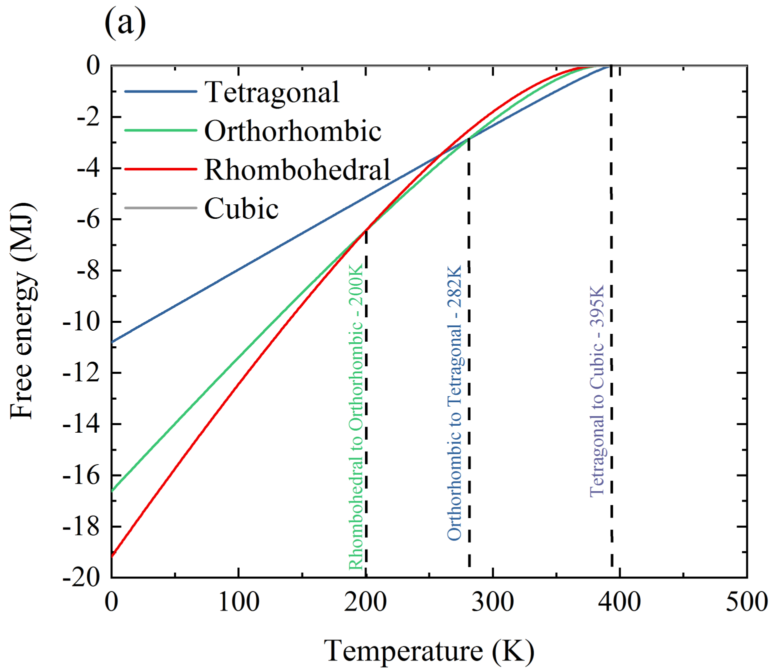

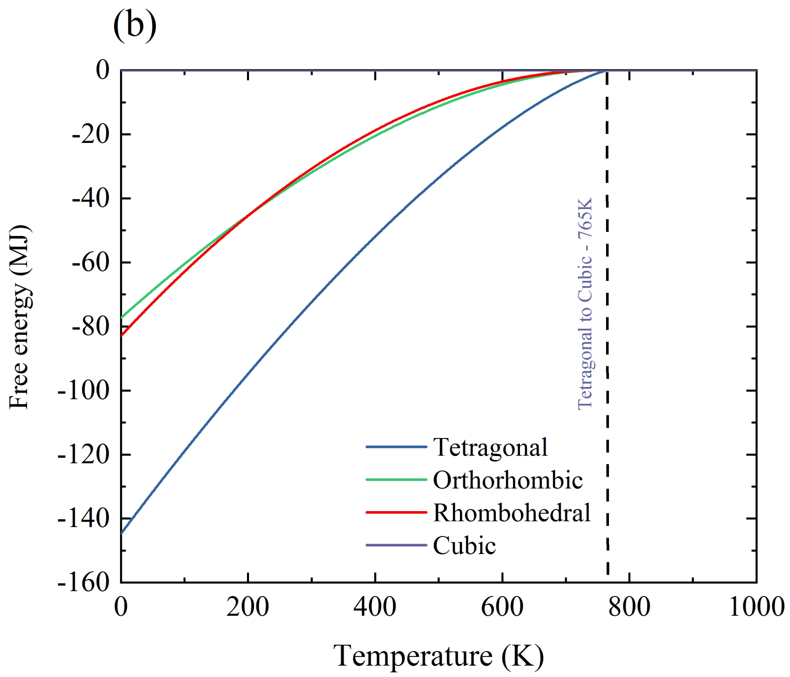

Figure 4.1: Landau-Devonshire derived free energy versus temperature for (a) BaTiO3 and (b) PbTiO3

The elastic spontaneous strain is calculated by differentiating the free energy as a function of stress ($\partial \Delta G / \partial X_i$):

Cubic - $x_1 = x_2 = x_3 = x_4 = x_5 = x_6 = 0$
Tetragonal - $x_1 = x_2 = Q_{12} P_3^2$; $x_3 = Q_{11} P_3^2$; $x_4 = x_5 = x_6 = 0$
Orthorhombic - $x_1 = 2Q_{12} P_3^2$; $x_2 = x_3 = (Q_{11} + Q_{12}) P_3^2$; $x_4 = Q_{44} P_3^2$; $x_5 = x_6 = 0$
Rhombohedral - $x_1 = x_2 = x_3 = (Q_{11} + 2Q_{12}) P_3^2$; $x_4 = x_5 = x_6 = Q_{44} P_3^2$

The double partial derivative of the free energy with respect to polarisation gives rise to dielectric stiffness values ($\xi_{ij} = \partial^2 \Delta G / \partial P_i \partial P_j$). By multiplying by the permittivity of free space (ϵ_0) the relative dielectric stiffness can be calculated:

Cubic - $\xi_{11} = \xi_{22} = \xi_{33} = \epsilon_0 \alpha_1 (T - T_C)$; $\xi_{12} = \xi_{23} = \xi_{31} = 0$

Tetragonal -
$$\xi_{11} = \xi_{22} = \epsilon_0 [\alpha_1 (T - T_C) + \alpha_{12} P_3^2 + \alpha_{112} P_3^4]$$
$$\xi_{33} = \epsilon_0 [\alpha_1 (T - T_C) + 3\alpha_{11} P_3^2 + 5\alpha_{111} P_3^4]$$
$$\xi_{12} = \xi_{23} = \xi_{31} = 0$$

Orthorhombic -
$$\xi_{11} = \epsilon_0 [\alpha_1 (T - T_C) + 2\alpha_{12} P_3^2 + 2\alpha_{112} P_3^4 + \alpha_{123} P_3^4]$$
$$\xi_{22} = \xi_{33} = \epsilon_0 [\alpha_1 (T - T_C) + 3\alpha_{11} P_3^2 + \alpha_{12} P_3^4 + 5\alpha_{111} P_3^4 + 7\alpha_{123} P_3^4]$$
$$\xi_{12} = \xi_{31} = 0,\ \xi_{23} = \epsilon_0 [2\alpha_{12} P_3^2 + 8\alpha_{112} P_3^4]$$

Rhombohedral -
$$\xi_{11} = \xi_{22} = \xi_{33} =$$
$$\epsilon_0 [\alpha (T - T_C) + 3\alpha_{11} P_3^2 + 2\alpha_{12} P_3^4 + 5\alpha_{111} P_3^4 + 14\alpha_{112} P_3^4 + \alpha_{123} P_3^4]$$
$$\xi_{12} = \xi_{23} = \xi_{31} = \epsilon_0 [2\alpha_{12} P_3^2 + 8\alpha_{112} P_3^4 + 2\alpha_{123} P_3^4]$$

The dielectric stiffness coefficients given here for the orthorhombic and rhombohedral phase are given as the values along the P_3 axis. It is possible to convert these such that the direction of vector is along the [011] and [111], i.e. rotating such that P_3 becomes the polar axis.

Orthorhombic - $\xi'_{11} = \xi_{11};\ \xi'_{22} = \xi_{33} - \xi_{23}; \xi'_{33} = \xi_{33} + \xi_{23}; \xi'_{12} = \xi'_{23} = \xi'_{31} = 0$

Rhombohedral - $\xi'_{11} = \xi'_{22} = \xi_{11} - \xi_{12}; \xi'_{33} = \xi_{11} = 2\xi_{12}.\xi'_{12} = \xi'_{23} = \xi'_{31} = 0$

The dielectric susceptibility (η_{ij}) can be calculated using the reciprocal of the dielectric stiffness:

Cubic - $\eta_{11} = \eta_{22} = \eta_{33} = \frac{1}{\xi_{11}};\ \eta_{12} = \eta_{23} = \eta_{31} = 0$

Tetragonal - $\eta_{11} = \eta_{22} = \frac{1}{\xi_{11}};\ \eta_{33} = \frac{1}{\xi_{33}}$

Orthorhombic - $\eta_{11} = \frac{1}{\xi_{11}}; \eta_{22} = \eta_{33} = \frac{\xi_{33}}{(\xi_{33}^2 - \xi_{23}^2)}; \eta_{12} = \eta_{31} = 0$
$\eta_{23} = \frac{-\xi_{23}}{(\xi_{33}^2 - \xi_{23}^2)}; \eta'_{11} = \frac{1}{\xi'_{11}}; \eta'_{33} = \frac{1}{\xi'_{33}}; \eta'_{12} = \eta'_{23} = \eta'_{31} = 0$

Rhombohedral - $\eta_{11} = \eta_{22} = \eta_{33} = (\xi_{11}^2 - \xi_{12}^2)/(\xi_{11}^3 - 3\xi_{11}\xi_{12}^2 + 2\xi_{12}^3)$
$\eta_{12} = \eta_{31} = \eta_{23} = (\xi_{11}^2 - \xi_{11}\xi_{12})/(\xi_{11}^3 - 3\xi_{11}\xi_{12}^2 + 2\xi_{12}^3)$

Determining the piezoelectric g_{ij} coefficients ($\partial^2\Delta G/\partial P_i \partial X_j$) for the rhombohedral and tetragonal phase gives:

Tetragonal - $g_{33} = 2Q_{11}P_3; g_{31} = g_{32} = 2Q_{12}P_3$
$g_{15} = g_{24} = Q_{44}P_3; g_{11} = g_{12} = g_{13} = g_{14} = g_{16} = 0$
$g_{21} = g_{22} = g_{23} = g_{25} = g_{26} = g_{34} = g_{35} = g_{36} = 0$

Rhombohedral - $g_{11} = g_{22} = g_{33} = 2Q_{11}P_3; g_{14} = g_{25} = g_{36} = 0$
$g_{12} = g_{13} = g_{21} = g_{23} = g_{31} = g_{32} = 2Q_{12}P_3$
$g_{15} = g_{16} = g_{24} = g_{26} = g_{34} = g_{35} = Q_{44}P_3$

The piezoelectric charge coefficient can then be calculated ($d_{ij} = g_{kj}\eta_{ik}$):

Tetragonal - $d_{33} = 2\epsilon_0\eta_{33}Q_{11}P_3; d_{31} = d_{32} = 2\epsilon_0\eta_{33}Q_{12}P_3$
$d_{15} = d_{24} = \epsilon_0\eta_{11}Q_{44}P_3; d_{11} = d_{12} = d_{13} = d_{14} = d_{16} = 0$
$d_{21} = d_{22} = d_{23} = d_{25} = d_{26} = d_{34} = d_{35} = d_{36} = 0$

Rhombohedral - $d_{11} = d_{22} = d_{33} = 2\epsilon_0(\eta_{11}Q_{11} + 2\eta_{12}Q_{12})P_3$
$d_{14} = d_{25} = d_{36} = 0$
$d_{12} = d_{13} = d_{21} = d_{23} = d_{31} = d_{32} = 2\epsilon_0[\eta_{11}Q_{12} + \eta_{12}(Q_{11} + Q_{12})]P_3$
$d_{15} = d_{16} = d_{24} = d_{26} = d_{34} = d_{35} = \epsilon_0(\eta_{11} + \eta_{12})Q_{44}P_3$

4.2 Landau-Devonshire Theory of Ferroelectric Solid Solutions

Over the decades Landau-Devonshire theory has been applied to ferroelectric solid solutions using different methods in an attempt to replicate the compositional dependence of the system. Arguably the most comprehensive application of Landau-Devonshire theory of a ferroelectric solid solution is for the phenomenological description of the commercially dominant $Pb(Zr, Ti)O_3$ by Haun et al. [159–163] and of Generation I and II single crystal materials by Heitmann and Rossetti [164]. In the former the authors use high temperature X-ray diffraction data on sol-gel derived PZT at multiple compositions in order to determine the spontaneous strains, x_3 and x_1 as both a function of temperature and composition and combined with previously published electrostriction coefficients allowed for the construction of polarisation values as a function of temperature and composition. Combining this data with low temperature dielectric data on poled and unpoled polycrystalline ceramics and using the Bruggeman relation to evaluate the effective single domain dielectric values the Curie-Weiss constants could be calculated. Combining the two experimental data values to determine the compositional dependence of the Landau coefficients allowed for a fully comprehensive thermodynamic description of PZT in which the free energy, phase diagram, spontaneous polarisation, spontaneous octahedral tilt angle, dielectric and piezoelectric properties were calculated for single domain PZT over all temperatures and compositions. Other similar examples of using the heavy dependence on experimental data include a phenomenological description of solid solutions between $Ba(Zr, Ti)O_3$ [165] and $(Ba, Ca)TiO_3$ [166].

Although the previous work on PZT is arguably the most comprehensive analysis of a ferroelectric solid solution, alternative methodologies have been employed. Heitmann and Rossetti used a linear coefficient relation in which the Curie-Weiss constant, Curie temperature and fourth order power terms were linearly related between each end member. This novel method was applied to binary solid solutions such as PZT and PMN-PT as well as the ternary solid solution PIN-PMN-PT, again constructing phase diagrams that are concordant with experimental observations and allowing for a comprehensive description of the dielectric and piezoelectric properties [164].

4.3 Application of the Linear Coefficient Method

Landau coefficients listed in Table 4.2 have been taken from [112] and [167, 168]. Whilst the coefficients for PbTiO3 are an established set, the coefficients of BiFeO3 are relatively new and to the author's knowledge at the time of writing have not been used in any other studies since publication.

Table 4.2: Landau coefficients used for PbTiO3 and BiFeO3

Coefficient	PbTiO3	BiFeO3
T_C (°C)	492.2	827
C_{CW} (10^5 $°C^{-1}$)	1.50	2.04*
α_{11} ($10^7 m^5/[C^2.F]$)	-7.252	22.9
α_{12} ($10^8 m^5/[C^2.F]$)	7.5	3.06
α_{111} ($10^8 m^9/[C^4.F]$)	2.606	0.599
α_{112} ($10^8 m^9/[C^4.F]$)	6.1	-0.000334
α_{123} ($10^9 m^9/[C^4.F]$)	-3.66	-0.178
Q_{11} ($10^{-2} m^4/C^2$)	0.089	0.032
Q_{12} ($10^{-2} m^4/C^2$)	-0.026	-0.016
Q_{44} ($10^{-2} m^4/C^2$)	0.0675	0.02
Ref.	[112]	[167], * [168]

In order to assign a value of α_0, the Curie-Weiss constant was extrapolated using Ref. [168] where a linear relationship has been established between the Curie temperature of materials and their corresponding Curie-Weiss constant (Figure 4.2). Using the accepted Curie temperature of BiFeO3 of 827°C [167] a Curie-Weiss constant of 2.04x10^5 °C^{-1} was adopted. The established value of the Curie-Weiss constant for lead titanate 1.50x10^5 °C^{-1} was used [112]. All other Landau coefficients and electrostriction coefficients were given a linear correlation to represent the variation in composition as shown in Equation 4.10.

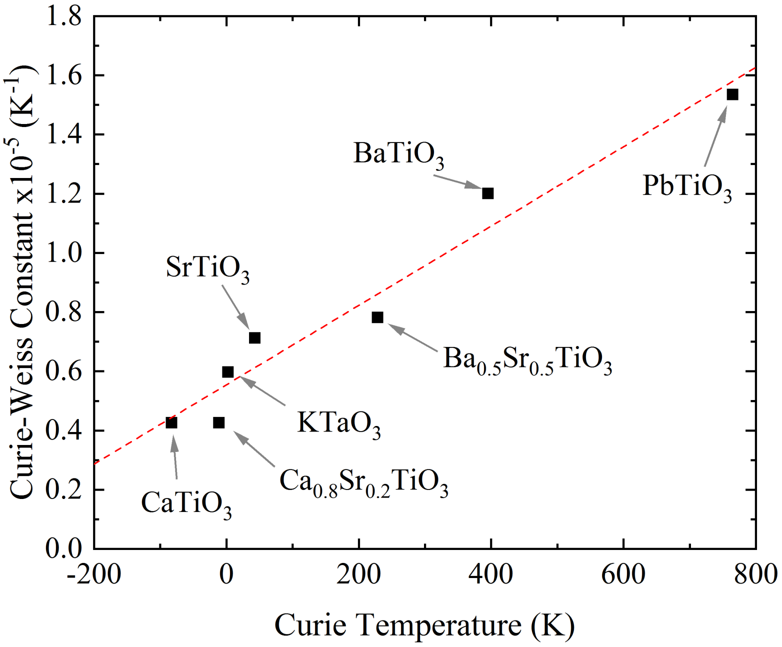

Figure 4.2: Curie-Weiss constant versus Curie temperature for a range of unary and binary perovskites. Adapted from [168]

$$
\begin{aligned}
T_C^{BFPT} &= (1-x)T_C^{PT} + (x)T_C^{BF} \\
C_{CW}^{BFPT} &= (1-x)C_{CW}^{PT} + (x)C_{CW}^{BF} \\
\alpha_{11}^{BFPT} &= (1-x)\alpha_{11}^{PT} + (x)\alpha_{11}^{BF} \\
\alpha_{12}^{BFPT} &= (1-x)\alpha_{12}^{PT} + (x)\alpha_{12}^{BF} \\
\alpha_{111}^{BFPT} &= (1-x)\alpha_{111}^{PT} + (x)\alpha_{111}^{BF} \\
\alpha_{112}^{BFPT} &= (1-x)\alpha_{112}^{PT} + (x)\alpha_{112}^{BF} \\
\alpha_{123}^{BFPT} &= (1-x)\alpha_{123}^{PT} + (x)\alpha_{123}^{BF} \\
Q_{11}^{BFPT} &= (1-x)Q_{11}^{PT} + (x)Q_{11}^{BF} \\
Q_{12}^{BFPT} &= (1-x)Q_{12}^{PT} + (x)Q_{12}^{BF} \\
Q_{44}^{BFPT} &= (1-x)Q_{44}^{PT} + (x)Q_{44}^{BF} \qquad (4.10)
\end{aligned}
$$

The free energy for a tetragonal, orthorhombic and rhombohedral system was simultaneously calculated to determine the most likely structural phase over all temperatures at selected compositions. Figure 4.3 shows that at no point is the most likely structure orthorhombic for (x)$BiFeO_3$–(1-x)$PbTiO_3$ where x=0.60, 0.65, 0.675, 0.70, 0.75 and 0.80. For compositions where x=0.60, 0.65 and 0.675 the most stable structural phase is always tetragonal with no intermediate ferroelectric-ferroelectric phase transitions occurring between 0°C and T_C. For x=0.7 a rhombohedral-tetragonal phase transition occurs at approximately 50°C and remains tetragonal until T_C. At compositions x=0.75 and x=0.80, this transition occurs at higher temperatures which suggests a compositionally dependent morphotropic phase boundary. It is worth noting that the monoclinic phase has not been considered in this study due to limitations in the available Landau coefficients. In order to consider the monoclinic phase Landau coefficients up to P^8 must be provided. As this is not the case for the coefficients of each end member the monoclinic phase cannot be assessed.

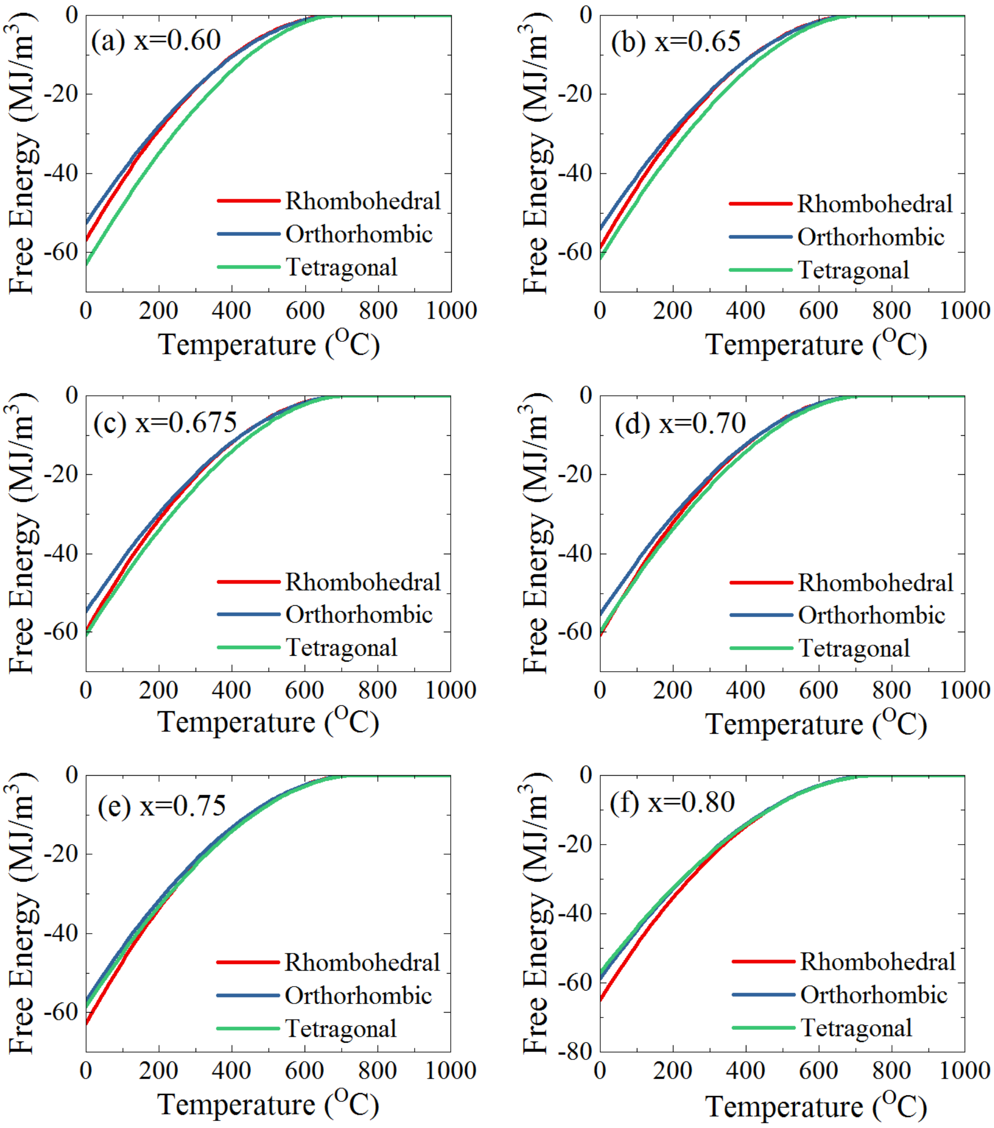

Figure 4.3: Landau-Devonshire derived free energy versus temperature for the (x)BiFeO$_3$-(1-x)PbTiO$_3$ solid solution at x= (a) 0.60, (b) 0.65, (c) 0.675, (d) 0.70, (e) 0.75, and (f) 0.80

The preliminary results shown in Figure 4.3 show that the only structural phases to be considered are rhombohedral and tetragonal. By comparing the magnitude of the free energies of the tetragonal and rhombohedral phase at each composition and temperature a phase diagram can be constructed. As the composition moves towards BiFeO3 the difference in free energy will decrease until there is a degeneracy in energy levels in which case the two structural phases are equal and represents the tetragonal-rhombohedral transition giving rise to a morphotropic phase boundary when ΔG=0. The total free energy decreases below zero as the magnitude of G_{rhom} becomes greater than G_{tet}.

$$\Delta G_{total} = |G_{tet}| - |G_{rhom}| \tag{4.11}$$

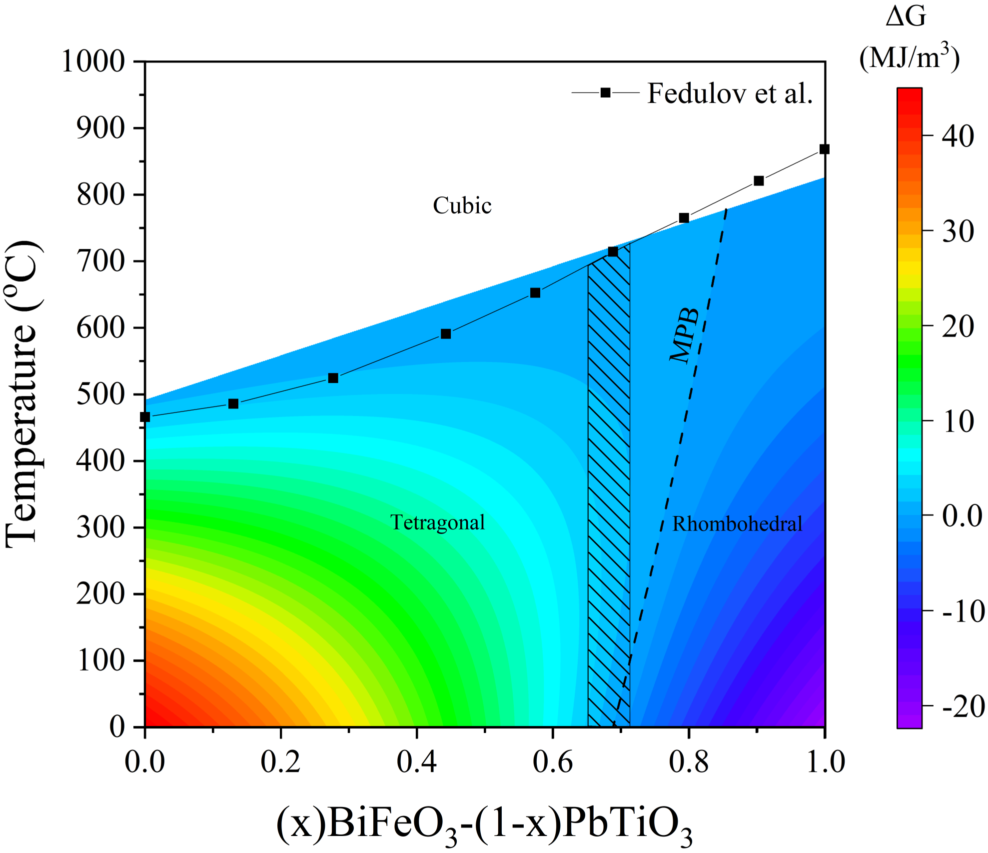

Figure 4.4: Landau-Devonshire derived structural phase diagram for the (x)$BiFeO_3$-(1-x)$PbTiO_3$ solid solution using a linear coefficient relation. The original phase diagram constructed by Fedulov et al. [47] has been superimposed for comparison, with the shaded region representing the area of tetragonal-rhombohedral coexistence

As mentioned previously, a large mixed phase region can be observed in BFPT polycrystalline ceramics and for a while it was suggested that whilst many tetragonal materials form 90° ferroelectric domains in order to relieve the internal stress associated with elongation along an axis, the tetragonality and internal stress is so large in BFPT that it is more energetically favourable to create a significant volume fraction of rhombohedral phase [145]. Kothai et al. [169] found however that the coexistence of structural phases was a phenomenon related to the grain size, with samples possessing grains $\approx 1\mu$m showing $P4mm$+$R3c$ coexistence whereas samples with grains of $\approx 10\mu$ms showed pure $P4mm$ phase. It is postulated that when small grains are present a self-generated compressive stress created through the capillary action of the surface energy results in the presence of a rhombohedral phase. As the grain size increases the compressive stress is reduced and therefore discourages the formation of a rhombohedral phase. Therefore although many reported polycrystalline samples possess a coexistence of phases, single crystal samples will be most likely single $P4mm$ or $R3c$ phase depending on the composition as shown mathematically in Figure 4.4 and experimentally both for tetragonal BFPT crystals [147] and rhombohedral crystals [170].

As mentioned in Section 2.3.3, since the development of BFPT in the 1960s, the exact location of the MPB in (x)BiFeO3 – (1-x)PbTiO3 has been ambiguous, with values between 0.60≤x≤0.80 being reported [47–50]. Bell et al. [145] suggest that this is due to the large stresses at the surface of the sample that can heavily influence diffraction patterns, the degree of which is sensitive to processing conditions [171]. Grain size effects, crushing, annealing, grinding regimes and sample form all have an influence on the degree of the surface stresses and therefore distort the location of the MPB. The findings in Figure 4.4 provide a thermodynamically derived location of x=0.696 for the MPB at 25°C to be considered along with the catalogue of experimental findings.

As Landau coefficients are often extrapolated from a single experimental set of data they can be limited for general use. For example coefficients that are interpolated from experimental data obtained from a BiFeO3 thin film may be suitable for the individual experiment and potentially to other BiFeO3 thin films. However they may not be suitable for describing other systems such as polycrystalline and single crystal systems. The agreement between experimental and theoretical $BiFeO_3$-$PbTiO_3$ phase diagram highlights the validity of the BiFeO3 coefficients derived from experimental work on mesocrystals and the Curie-Weiss constant obtained from [168] and [167], respectively.

Figure 4.5 shows the spontaneous strain as a function of composition at 25°C, calculated by differentiating the free energy as a function of stress ($\partial\Delta G/\partial X_i$):

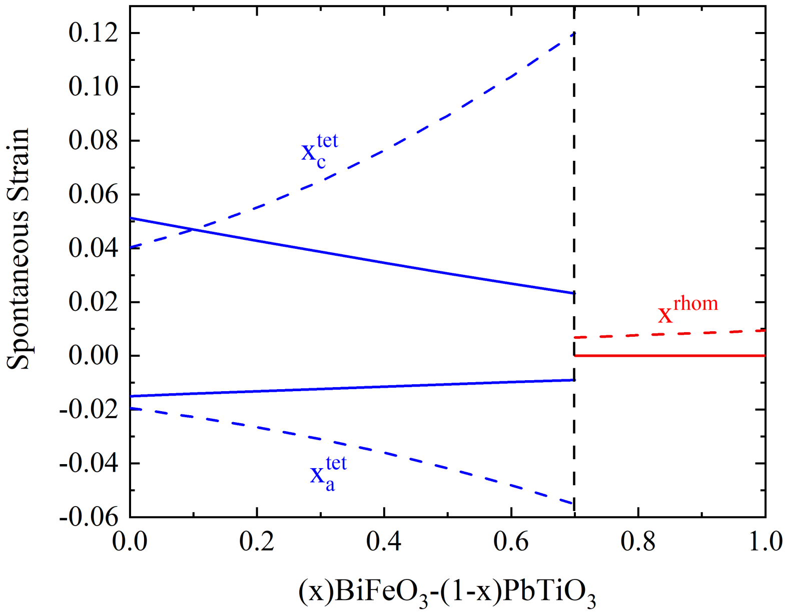

Figure 4.5: Spontaneous strain for the (x)BiFeO3 – (1-x)PbTiO3 solid solution. The solid lines represent the calculated strain values from Landau-Devonshire theory and the dashed lines represent experimental measurements from [172]

The calculated spontaneous strain in Figure 4.5 is common in many ferroelectric solid solutions which reduces with decreasing PbTiO3 content until the MPB at which point the lattice parameters 'collapse' and become equal as the system becomes pure $R3c$ phase. However as mentioned previously the solid solution between BiFeO3 and PbTiO3 exhibits almost exclusive spontaneous strain behaviour which increases with decreasing lead titanate content. To the author's knowledge the only other binary solid solution in which this phenomenon occurs is Bi(Zn, Ti)O3 – PbTiO3. However in this system both end members are tetragonal with pure Bi(Zn, Ti)O3 possessing a tetragonality of 22% [83]. The dashed line in Figure 4.5 is experimental data for the spontaneous strain calculated on bulk polycrystalline samples from [172]. Although the calculated phase diagram in Figure 4.4 may be useful consideration when arguing the 'true' MPB location at x=0.696 BiFeO3, this discrepancy between theoretical and experimental data for the spontaneous strain highlights the limitation of the linear coefficient method for describing this solid solution and limits the validity of any resultant dielectric and piezoelectric properties calculated. Essentially, *if a method cannot tell us what we already know about a material, how valid will it be for telling us what we do not?*

4.4 The External Tensile Stress Model

To overcome the issue of incorrectly describing the spontaneous strain behaviour as a function of composition, the system has been treated as an external tensile stress within the tetragonal region. This tensile stress acts to 'pull' the unit cell along the [001] such that the spontaneous strain along the c-axis is increased from ≈4% at pure lead titanate to ≈12% at the MPB within the tetragonal region. Similar methodology is adapted in density functional theory of tetragonal materials such as BaTiO3 and PbTiO3 where the *c* lattice parameter is fixed to match experimental observed values using a positive pressure within the unit cell. The *a* and *b* lattice parameters are then allowed to relax and find a minimum free energy position [173]. Within the rhombohedral phase the stress is a shear stress that is acting to reduce the angle between the polarisation along the [111] and P_3 along the [001] when approaching the MPB.

Whilst the linear coefficient method models the compositional change of the solid solution through variation of the Landau coefficients, the external tensile stress method fixes the Landau coefficients for lead titanate and bismuth ferrite in the tetragonal and rhombohedral regions respectively, and the compositional dependence is modelled as the change in tensile or shear stresses.

To calculate the tensile stress required to result in the subsequent spontaneous strain shown in Figure 4.5 the experimental data was fitted empirically to construct a relationship between strain and composition. A polynomial fit was adopted to describe this relationship within the tetragonal region and a tangential relation was employed to replicate the rotation of the polarisation away from the [111] towards the [001] within the rhombohedral region. The empirical equations used are shown in Equation 4.12 and 4.13:

$$strain_{tet} = 0.07892x^2 + 0.05842x + 0.04029 \tag{4.12}$$

$$strain_{rhom} = tan(90 - (-0.51x + 89.956)) \tag{4.13}$$

Where x is the $BiFeO_3$ content.

A temperature dependence was constructed by using the normalised strain against normalised temperature for each end member. By normalising both variables it is possible to create a general relation that can be applied to a range of compositions where the strain and Curie temperature vary.

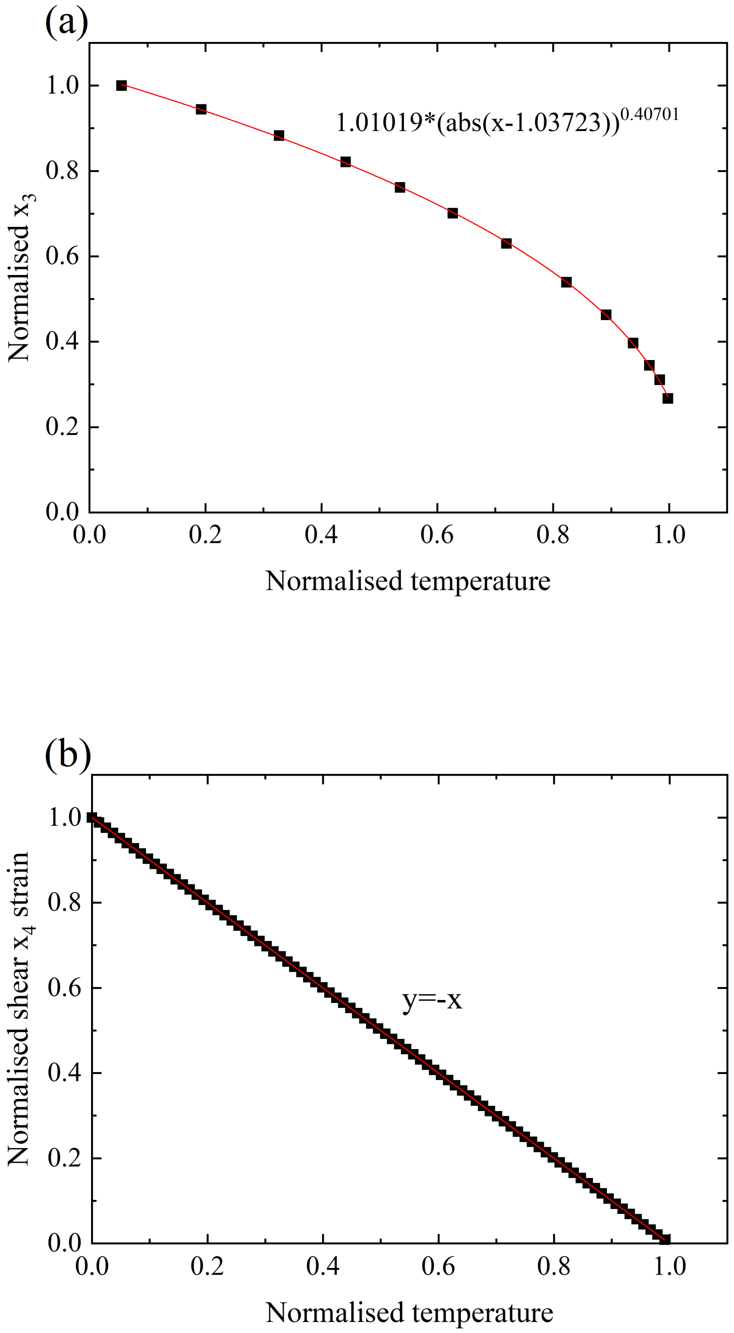

Figure 4.6: Normalised strain vs normalised temperature (T/T_C) for (a) PbTiO3 and (b) BiFeO3

Combining the normalised trends in Figure 4.6, the linear relationship between the Curie temperature of each end member and the expression describing the relationship between strain and composition shown in Equations 4.12 and 4.13 gives the spontaneous strain across all compositions and temperatures within the tetragonal and rhombohedral region given by Equation 4.14 and 4.15, respectively.

$$\begin{aligned} strain_{tet} &= (0.07892x^2 + 0.05842x + 0.04029) \\ &\quad \times (1.01019 \times (|\frac{y}{492[1-x] + 827[x]}| - 1.03723)^{0.40701}) \end{aligned} \tag{4.14}$$

$$strain_{rhom} = tan(90 - (-0.51x + 89.956)) \times (1 - |\frac{y}{492[1-x] + 827[x]}|) \tag{4.15}$$

Where x is $BiFeO_3$ content and y is temperature in degrees Celsius.

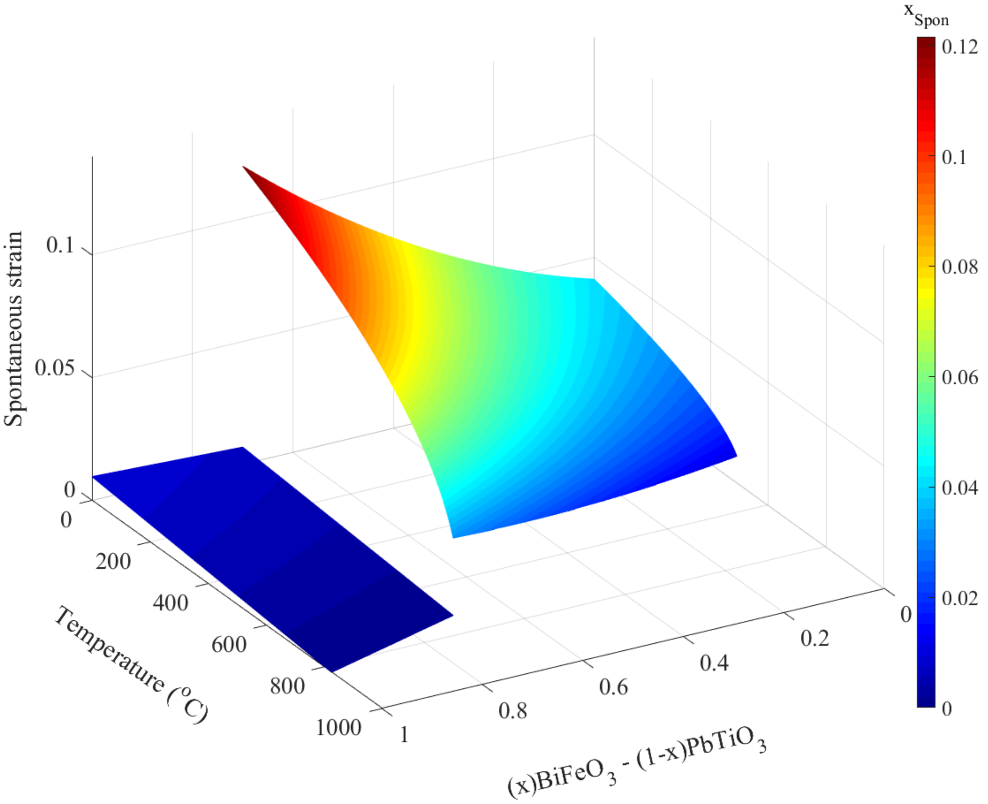

Figure 4.7: Empirically derived spontaneous strain along the [001] calculated for the (x)$BiFeO_3$-(1-x)$PbTiO_3$ solid solution across all compositions and temperatures using Equation 4.14 and 4.15

It can be seen from Figure 4.7 that an immediate limitation to this method is the lack of reproducibility describing the temperature dependence of the morphotropic phase boundary. The phase diagram constructed using the linear coefficient model showed a natural temperature dependence where at 25°C the MPB is located at x=0.7 but at 400°C is located at x=0.8 whereas in Figure 4.5 the MPB remains at x=0.7 throughout. This is due to the tensile stress method extending the compositional dependence of spontaneous strain measured at room temperature across all temperatures. This may be overcome by considering the temperature dependence of the lattice parameters across a range of compositions similar to work carried out by Haun et al. for PZT [160].

Using values for spontaneous strain calculated using Equation 4.14 and 4.15 the polarisation can be calculated using the electrostriction relation as shown in Equation 4.16 and 4.17 and is shown in Figure 4.8.

$$P_{tet} = \sqrt{\frac{strain_{tet}}{Q_{11}}} \tag{4.16}$$

$$P_{rhom} = \sqrt{\frac{strain_{rhom}}{Q_{44}}} \tag{4.17}$$

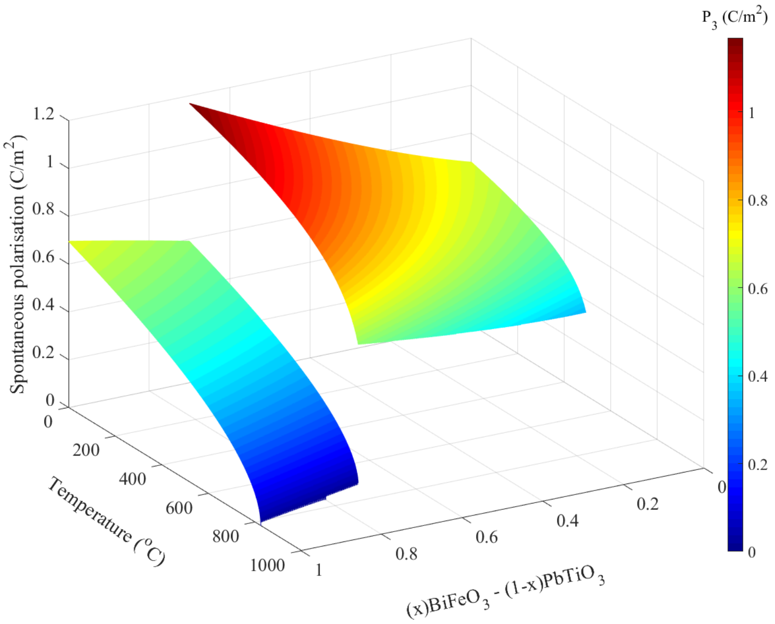

Figure 4.8: Empirically derived spontaneous polarisation along the [001] for the (x)$BiFeO_3$-(1-x)$PbTiO_3$ solid solution across all compositions and temperatures using Equation 4.16 and 4.17

It is worth noting the nature of the phase transitions of this material. Within the tetragonal region, a first-order phase transition occurs. This is characterised by the discontinuity in the polarisation at the Curie temperature and within the rhombohedral phase a second order transition occurs characterised by the lack of discontinuity. This phenomenon occurs due to the initial nature of the Landau coefficient α_{11} which describes a first order transition if <0 and describes a second order transition if >0.

By applying the same structural phase conditions for the values of P_1, P_2 and P_3 and introducing phase dependent values for external stress, the total Gibbs free energy becomes:

Cubic	$P_1 = P_2 = P_3 = 0$	$X_1 = X_2 = X_3 = X_4 = X_5 = X_6 = 0$
Tetragonal	$P_1 = P_2 = 0; P_3 \neq 0$	$X_1 = X_2 = X_4 = X_5 = X_6 = 0; X_3 \neq 0$
Rhombohedral	$P_1 = P_2 = P_3 \neq 0$	$X_1 = X_2 = X_3 = 0; X_4 = X_5 = X_6 \neq 0$

$$\begin{aligned}
\Delta G_{Cubic} = {} & 0 \\
\Delta G_{Tetra} = {} & \alpha_1 P_3^2 + \alpha_{11} P_3^4 + \alpha_{111} P_3^6 - \tfrac{1}{2} s_{11}^P X_3^2 - Q_{11} X_3 P_3^2 \\
\Delta G_{Rhom} = {} & 3\alpha_1 P_3^2 + 3\alpha_{11} P_3^4 + 3\alpha_{12} P_3^4 + 3\alpha_{111} P_3^6 + 6\alpha_{112} P_3^6 + \alpha_{123} P_3^6 \\
& -\tfrac{3}{2} s_{44}^P X_{4,5,6} P_3^2 - 3Q_{44} X_{4,5,6} P_3^2
\end{aligned}$$

Minimising the free energy ($\partial \Delta G / \partial P_3$) gives the following:

$$Tetragonal : \alpha_1 + 2\alpha_{11} P_3^2 + 3\alpha_{111} P_3^4 - Q_{11} X_3 = 0 \tag{4.18}$$

$$Rhombohedral : \alpha_1 + 2\alpha_{11} P_3^2 + 2\alpha_{12} P_3^2 + 3\alpha_{111} P_3^4 + 6\alpha_{112} P_3^4 + \alpha_{123} P_3^4 - Q_{44} X_{4,5,6} = 0 \tag{4.19}$$

Using values for the polarisation obtained by Equation 4.16 and 4.17 the external tensile stress was calculated as follows:

$$X_3 = \frac{\alpha_1 + 2\alpha_{11} P_3^2 + 3\alpha_{111} P_3^4}{Q_{11}} \tag{4.20}$$

$$X_{4,5,6} = \frac{\alpha_1 + 2\alpha_{11} P_3^2 + 2\alpha_{12} P_3^2 + 3\alpha_{111} P_3^4 + 6\alpha_{112} P_3^4 + \alpha_{123} P_3^4}{Q_{44}} \tag{4.21}$$

The partial derivative of the free energy with respect to stress gives rise to dielectric stiffness values ($\xi_i = \partial \Delta G / \partial X_i$). By multiplying by the permittivity of free space (ϵ_0) the relative dielectric stiffness can be calculated:

Cubic - $\xi_{11} = \xi_{22} = \xi_{33} = \epsilon_0 \alpha_1 (T - T_C); \xi_{12} = \xi_{23} = \xi_{31} = 0$

Tetragonal -
$$\begin{aligned}
&\xi_{11} = \xi_{22} = \epsilon_0 [\alpha_1 (T - T_C) + \alpha_{12} P_3^2 + \alpha_{112} P_3^4 - 2Q_{12} X_3] \\
&\xi_{33} = \epsilon_0 [\alpha_1 (T - T_C) + 3\alpha_{11} P_3^2 + 5\alpha_{111} P_3^4 - 2Q_{11} X_3] \\
&\xi_{12} = \xi_{23} = \xi_{31} = 0
\end{aligned}$$

Rhombohedral -
$$\begin{aligned}
&\xi_{11} = \xi_{22} = \xi_{33} = \\
&\epsilon_0 [\alpha (T - T_C) + 3\alpha_{11} P_3^2 + 2\alpha_{12} P_3^4 + 5\alpha_{111} P_3^4 + 14\alpha_{112} P_3^4 + \alpha_{123} P_3^4] \\
&\xi_{12} = \xi_{23} = \xi_{31} = \epsilon_0 [2\alpha_{12} P_3^2 + 8\alpha_{112} P_3^4 + 2\alpha_{123} P_3^4] - Q_{44} X_6
\end{aligned}$$

The equations given for the dielectric susceptibility, piezoelectric voltage coefficient and piezoelectric charge coefficient are consistent with those mentioned previously.

4.4.1 Dielectric Properties

Figure 4.9 (a) shows the dielectric susceptibility versus temperature for various compositions within the tetragonal region ($0<x<0.7$), and Figure 4.9 (b) show the dielectric relative permittivity versus temperature for compositions within the rhombohedral region ($0.7<x<1$). In both cases the typical dielectric behaviour is observed as a function of temperature. In the absence of any intermediate ferroelectric-ferroelectric phase transitions the dielectric permittivity is observed to show an accelerated increase until the Curie temperature, in which a proper ferroelectric begins to follow the Curie-Weiss law. This increase with temperature is due to the increased mobility of ions that comes with the associated thermal energy. In Slater's rattling ion model the polarisability of the B-site ion will increase rapidly with increasing temperature and hence increasing both the piezoelectric and dielectric properties. The most significant finding is the decrease of the relative permittivity as a function of lead titanate content within the tetragonal region. It is shown in Figure 4.10 that when approaching the MPB the value for the permittivity decreases. This is contrary to most ferroelectric solid solution possessing an MPB in which the dielectric and piezoelectric properties are enhanced around the MPB due to the increased number of possible polarisation directions [28]. This unusual behaviour may be attributed to the increased spontaneous strain and covalence within the unit cell. As the spontaneous strain increases so too does the covalence between the Fe and Ti atoms and the axial oxygen ions. The increased B-O covalence leads to reduced mobility, polarisability and therefore permittivity. Within the rhombohedral region, the opposite and more traditional trend is observed where the permittivity increases from pure $BiFeO_3$ towards to the MPB.

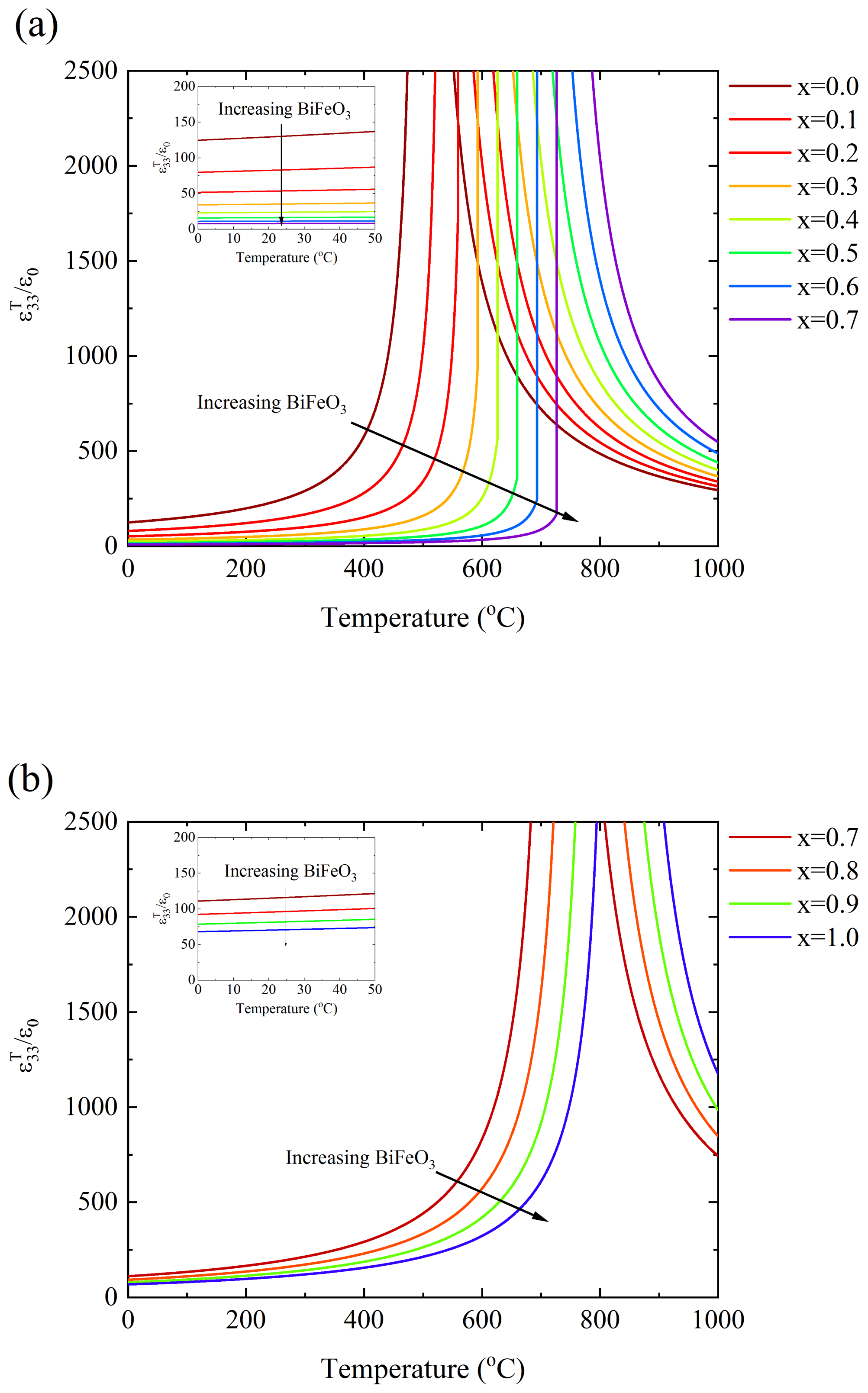

Figure 4.9: Relative permittivity versus temperature for (x)BiFeO3 – (1-x)PbTiO3 solid solution within (a) the tetragonal region and (b) the rhombohedral region

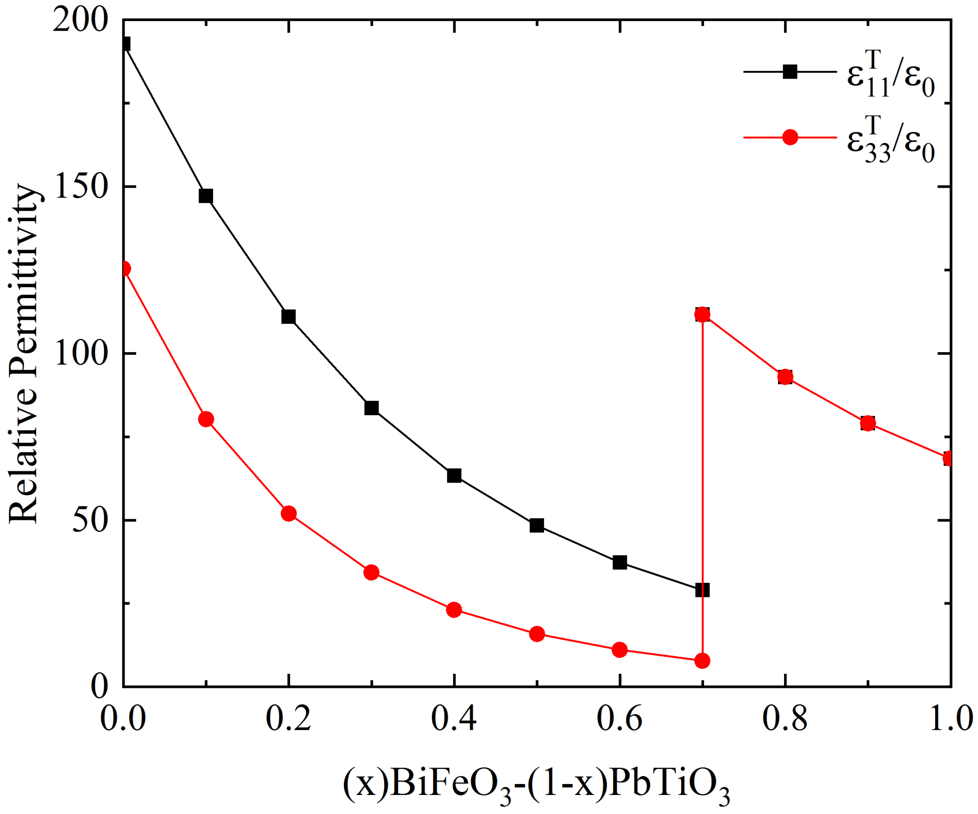

Figure 4.10: Relative permittivity versus composition for (x)BiFeO3 – (1-x)PbTiO3 at 25°C for the 11 (■) and 33 (●) modes

4.4.2 Piezoelectric Properties

Figures 4.11 - 4.14 show the piezoelectric charge coefficients in 33, 31 and 15 mode and the hydrostatic coefficient as a function of temperature. Figure 4.15 shows all the coefficients as a function of composition at 25°C. The piezoelectric properties are analogous to the dielectric properties and similar explanations can be made for the observed behaviour. All modes of the piezoelectric coefficient are seen to decrease when approaching the MPB within the tetragonal region with d_{33} decreasing from 135.2pC/N at pure lead titanate to 16.2pC/N at 0.70 $BiFeO_3$. Once again this could be attributed to the increasing B-O covalence within the unit cell. As the intrinsic strain and covalence increase, the mobility of the B-site ion is reduced and therefore reducing the polarisability and consequently its piezoelectric activity. Furthermore the piezoelectric coefficients show typical temperature dependent behaviour by increasing when approaching the Curie temperature, at which point the d_{ij} becomes zero and the sample depoles as the system converts from a non-centrosymmetric system to a centro-symmetric system. Again this can be explained through the increasing mobility of ions within the unit cell at elevated temperatures.

Stevenson et al. [46] showed that high field d_{33} values of polycrystalline $BiFeO_3$-$PbTiO_3$ follows a more traditional ferroelectric solid solution behaviour and increases towards the MPB. Although this behaviour goes against the behaviour predicted in this study by Landau Devonshire theory, the discrepancy could be due to the enhanced significance of extrinsic effects or the presence of an $P4mm+R3c$ coexistence both of which contribute to larger piezoelectric charge response. As this work treats the system as a single-crystal, single-domain, extrinsic contributions are not considered and also due to the fact that Landau-Devonshire theory only sheds light on the single most energetically favourable structural phase, it does not consider a coexistence of phases.

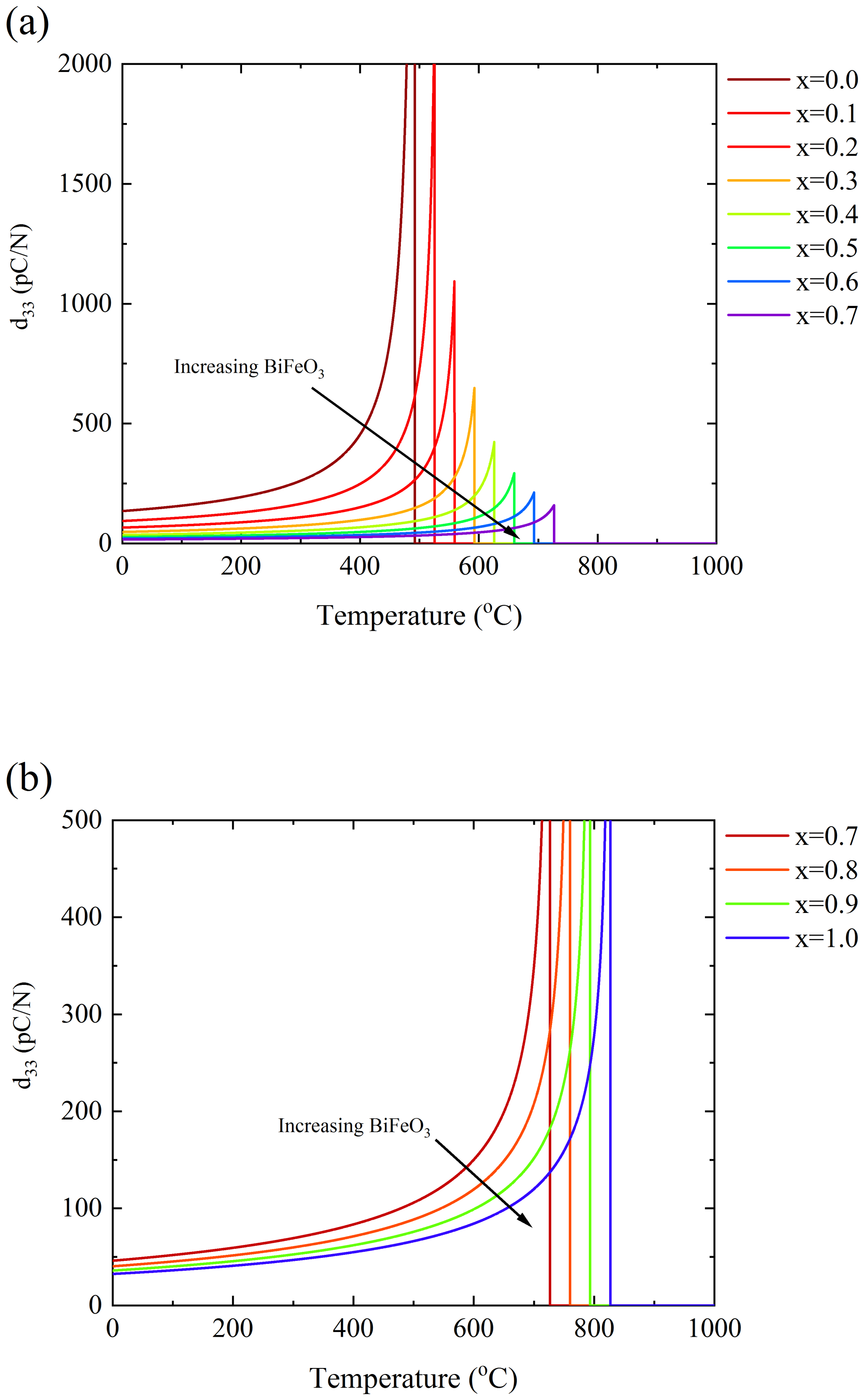

Figure 4.11: Piezoelectric d_{33} coefficient versus temperature for (x)BiFeO3 – (1-x)PbTiO3 solid solution within (a) the tetragonal region and (b) the rhombohedral region

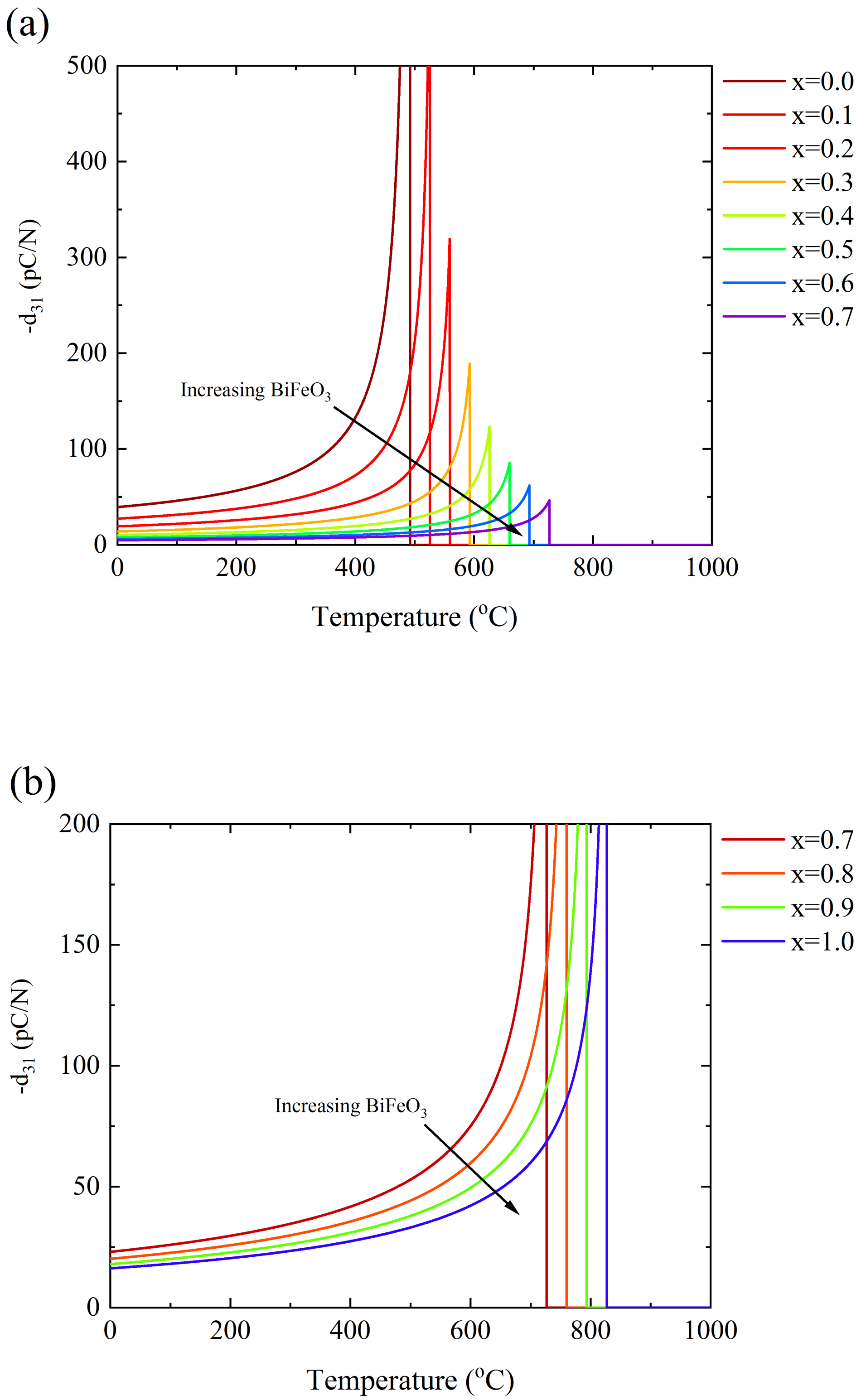

Figure 4.12: Piezoelectric -d_{31} coefficient versus temperature for (x)BiFeO3 – (1-x)PbTiO3 solid solution within (a) the tetragonal region and (b) the rhombohedral region

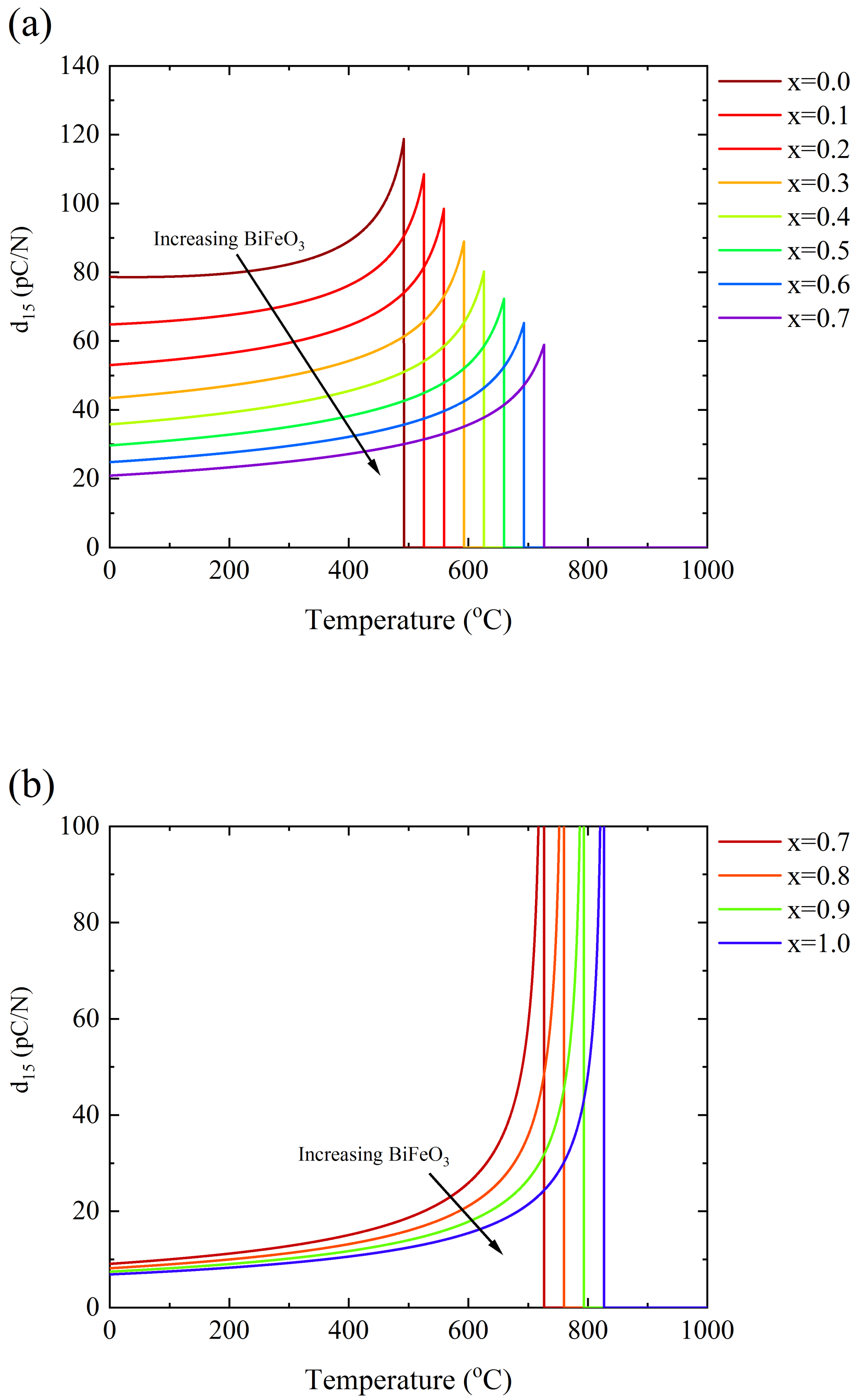

Figure 4.13: Piezoelectric d_{15} coefficient versus temperature for (x)BiFeO3 – (1-x)PbTiO3 solid solution within (a) the tetragonal region and (b) the rhombohedral region

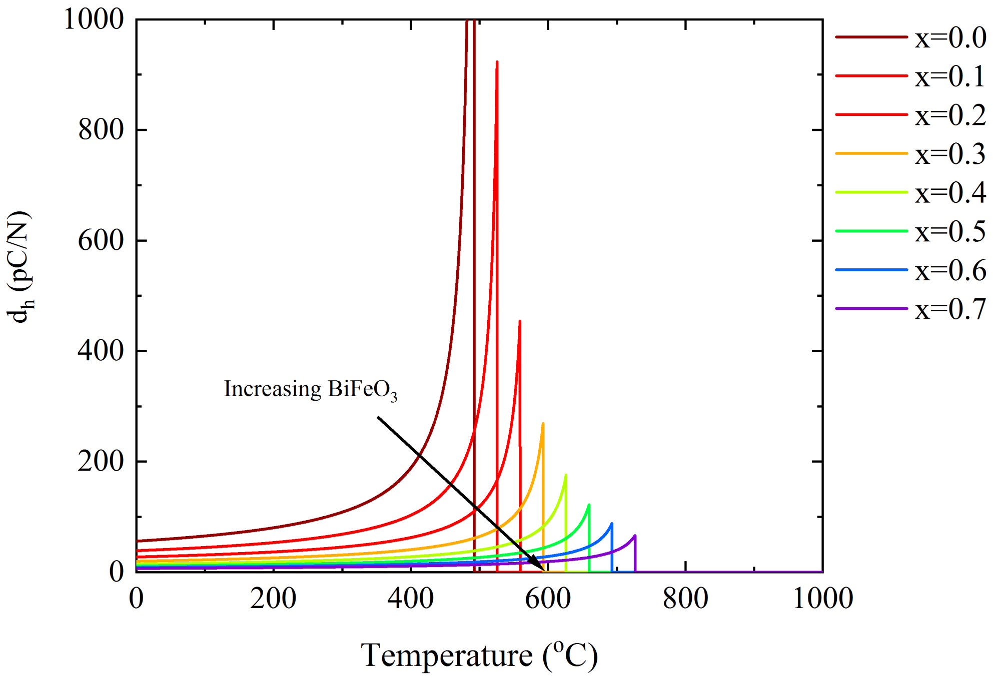

Figure 4.14: Hydrostatic piezoelectric d_h coefficient versus temperature for (x)BiFeO3 – (1-x)PbTiO3 solid solution within the tetragonal region. Rhombohedral hydrostatic values are calculated as being zero and are therefore omitted

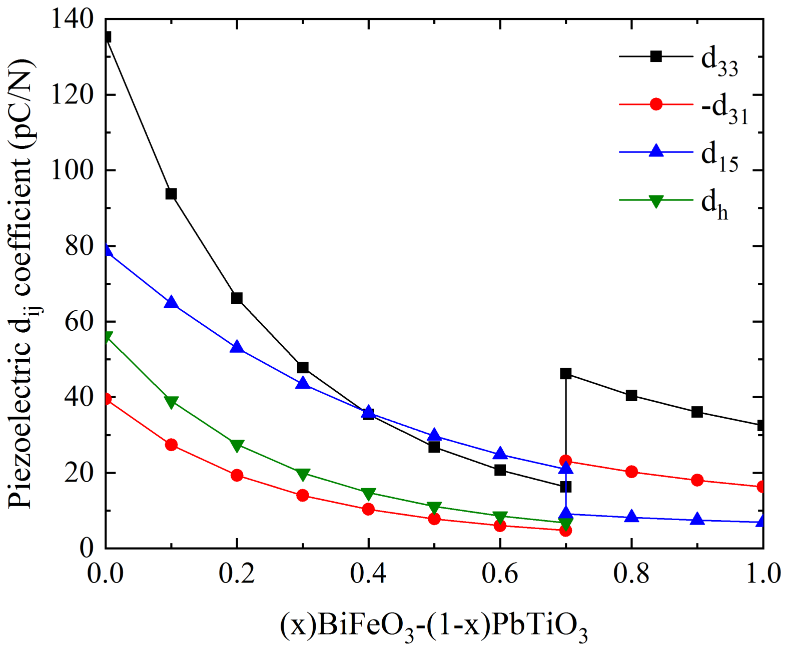

Figure 4.15: Piezoelectric d_{ij} coefficient versus composition for (x)BiFeO3 – (1-x)PbTiO3 solid solution at 25°C

Figures 4.16 to 4.19 show values for the piezoelectric voltage coefficient along the 33, 31 and 15 mode as well as values for the hydrostatic coefficient as a function of temperature and Figure 4.20 shows all piezoelectric voltage coefficient modes as a function of composition at 25°C. Unsurprisingly the trend is similar to the polarisation which for tetragonal compositions is highest at low temperatures and decreases gradually until T_C at which point a discontinuous first order transition results in a sudden drop and the sample depoles and no piezoelectric activity is observed. For rhombohedral compositions the largest g_{ij} is similarly found at low temperature. However a second order transition is observed in this case and a continuous decrease in the g coefficients occurs until T_C.

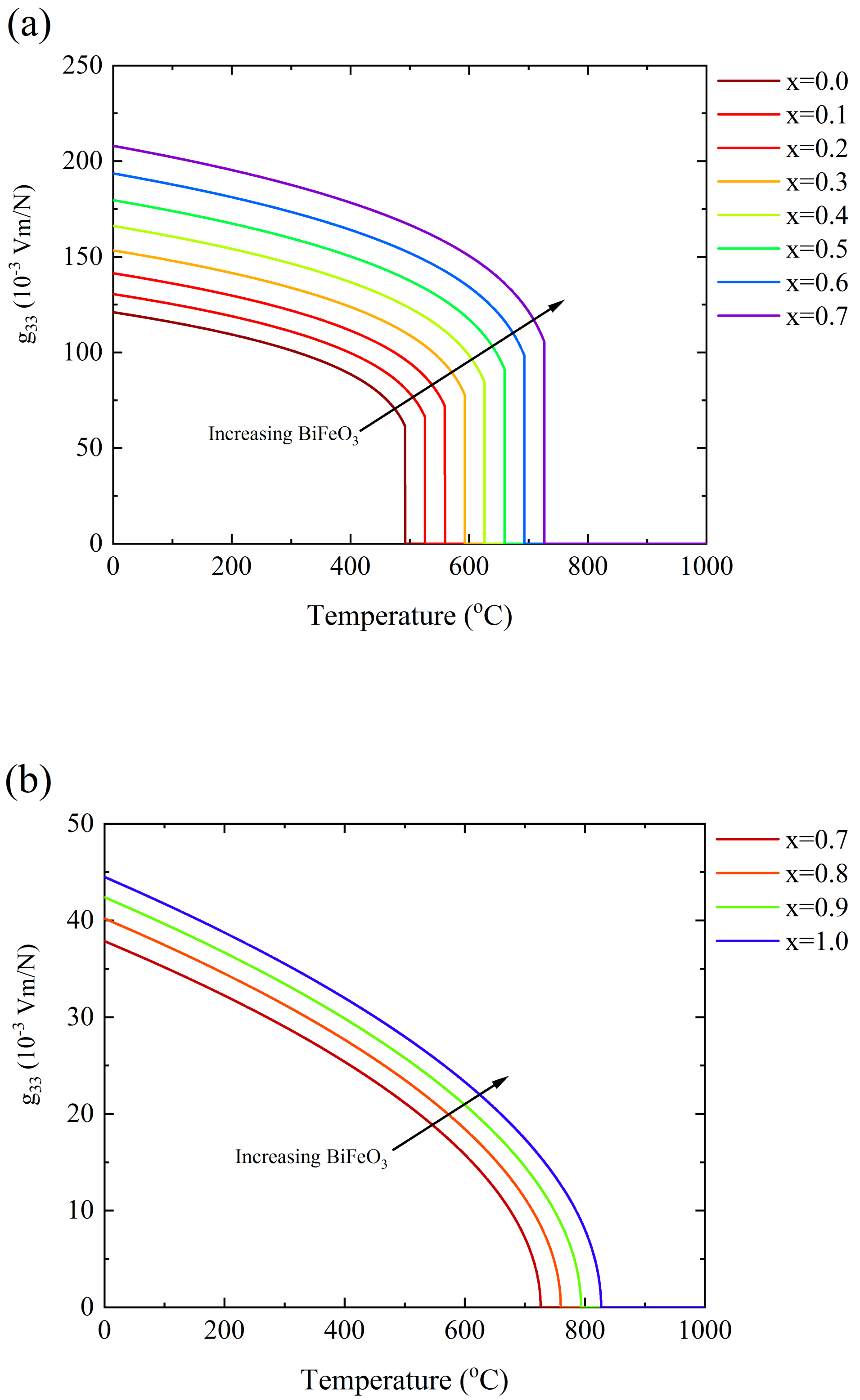

Figure 4.16: Piezoelectric g_{33} coefficient versus temperature for (x)BiFeO3 – (1-x)PbTiO3 solid solution within (a) the tetragonal region and (b) the rhombohedral region

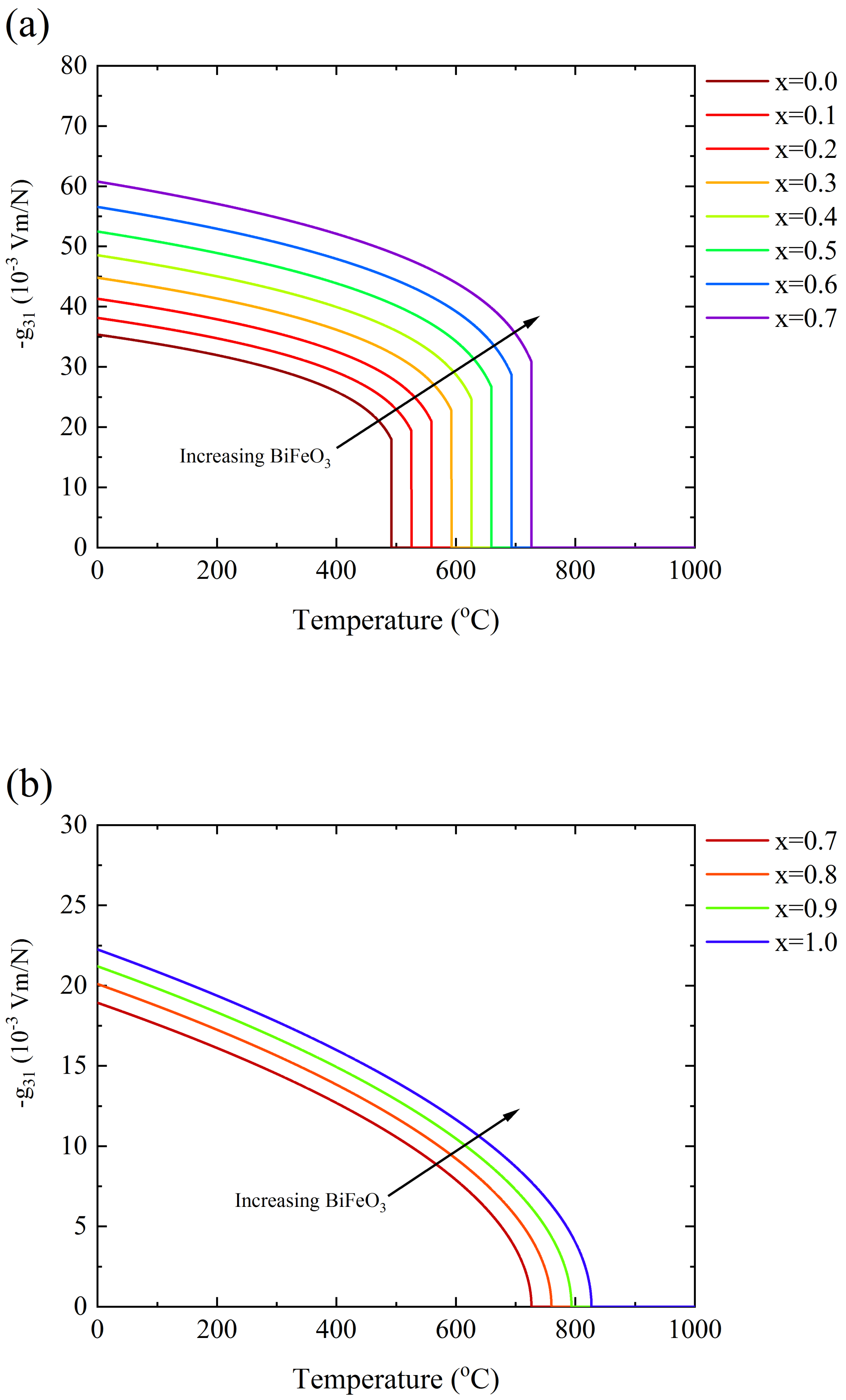

Figure 4.17: Piezoelectric $-g_{31}$ coefficient versus temperature for (x)BiFeO3 – (1-x)PbTiO3 solid solution within (a) the tetragonal region and (b) the rhombohedral region

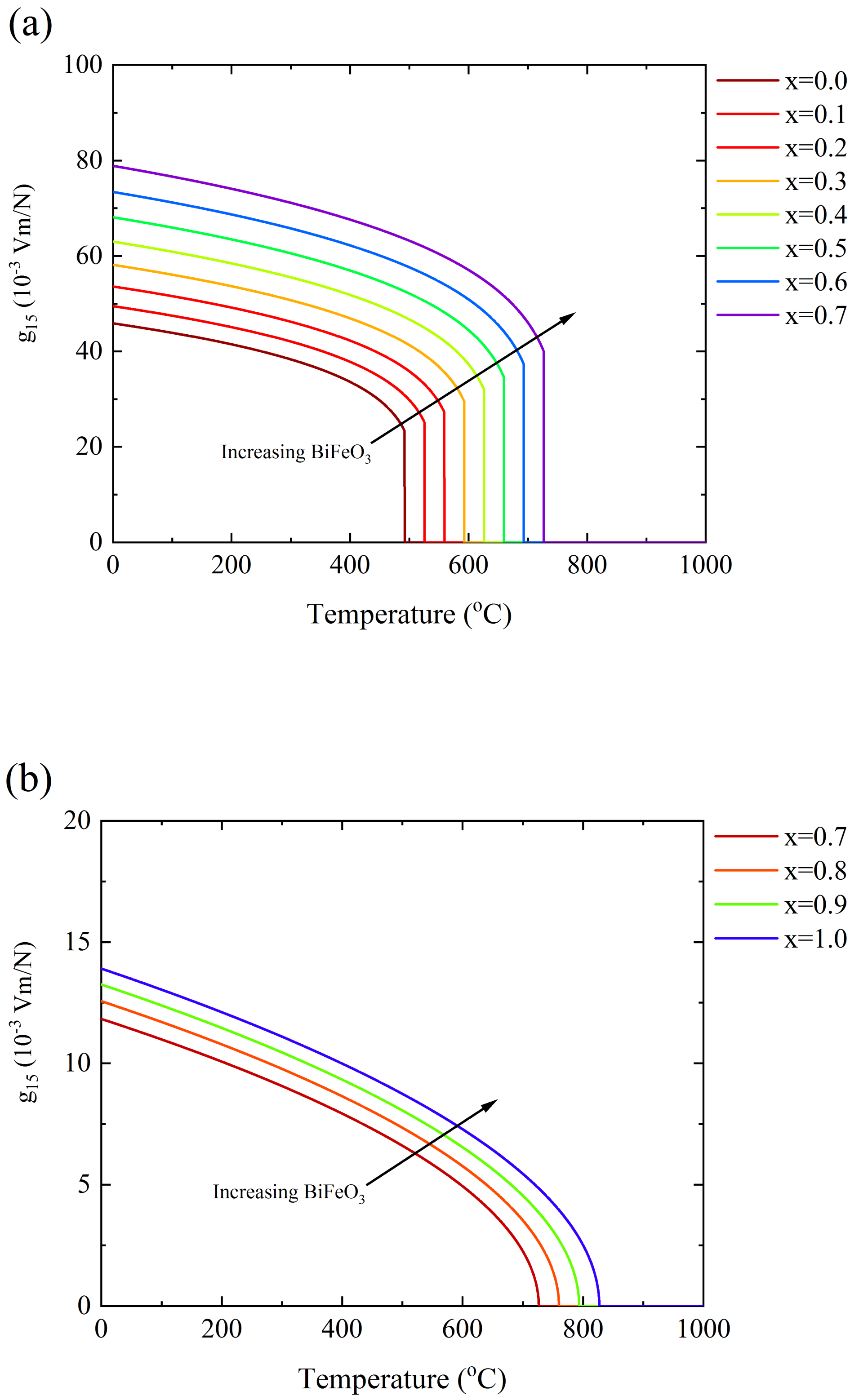

Figure 4.18: Piezoelectric g_{15} coefficient versus temperature for (x)BiFeO3 – (1-x)PbTiO3 solid solution within (a) the tetragonal region and (b) the rhombohedral region

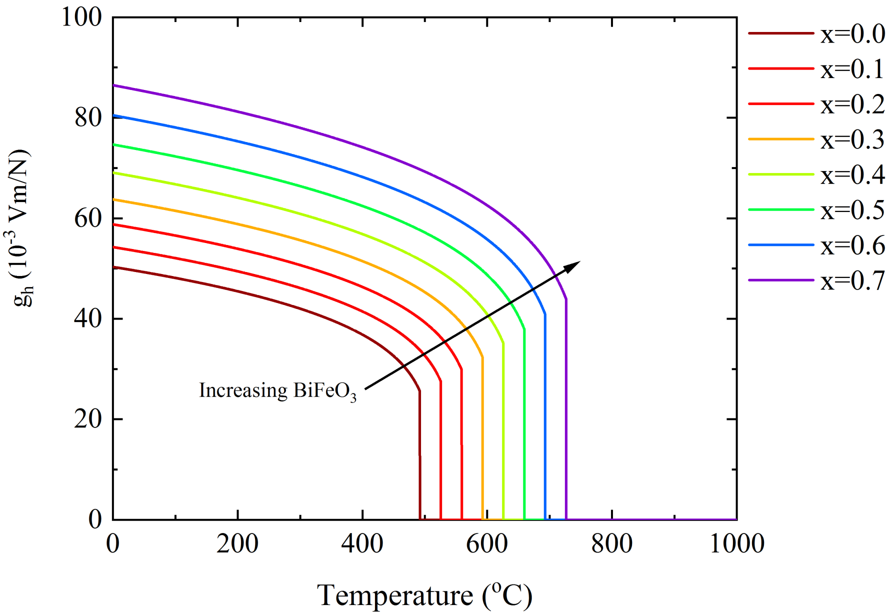

Figure 4.19: Hydrostatic piezoelectric g_h coefficient versus temperature for (x)BiFeO3 – (1-x)PbTiO3 solid solution within the tetragonal region. Rhombohedral hydrostatic values are calculated as being zero and are therefore emitted

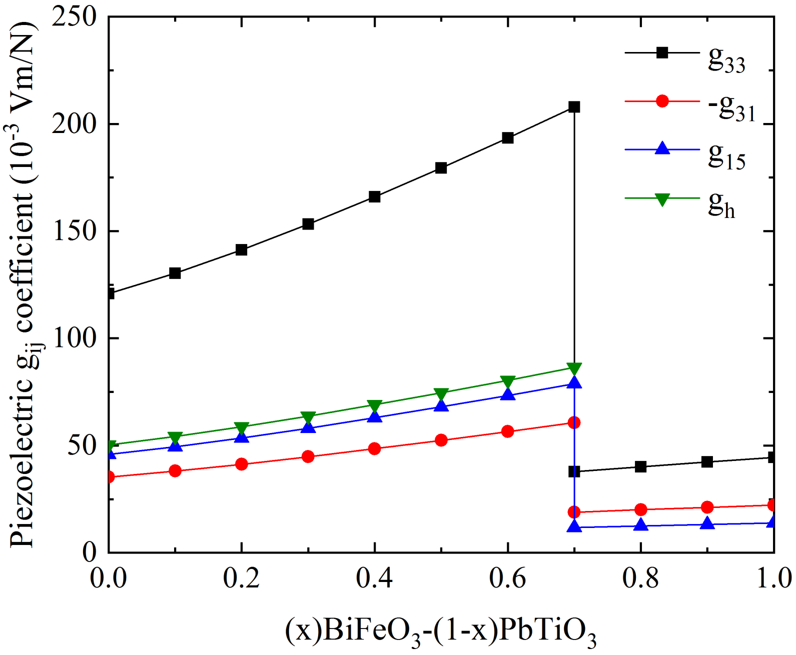

Figure 4.20: Piezoelectric g_{ij} coefficient versus composition for (x)BiFeO3 – (1-x)PbTiO3 solid solution at 25°C

It is clear from Figure 4.20 that BiFeO3 – PbTiO3 single domains possess exceptionally large g_{ij} coefficients when compared to previously reported materials both experimentally and theoretically and current military grade devices listed in Table 4.3. Although both the piezoelectric charge coefficients and relative permittivity decrease with tetragonality as shown in Table 4.4 and are lower than other materials listed in Table 4.3, the faster rate of decay in the relative permittivity compared to the charge coefficient results in an enhancement of the g_{ij} coefficient. Although both are heavily dependent on the change in polarisation with electric field, which decreases with tetragonality due to increasing degree of electrical clamping, the d_{ij} coefficient is also dependent on the absolute value of polarisation (d_{33}=$2Q_{11}P\epsilon_{33}$) which increases with tetragonality and therefore slows the rate of decay. This results in the enhancement of the g_{ij} coefficient with tetragonality.

Similar dielectric and piezoelectric trends were observed by Rossetti et al. [174] when studying the effect of stresses on lead titanate single crystals. Compressive stresses were seen to result in increased dielectric susceptibility for both 33 and 11 modes and the piezoelectric charge properties also increased with compressive stress. The rate of increase of susceptibility exceeds the charge coefficient and therefore all piezovoltage coefficients decrease with compressive stress. For tensile stresses the opposite was observed with both susceptibility and charge coefficients decreasing and the piezovoltage coefficients increasing similar to observations in this study. It is important to note that the work by Rossetti et al. treats the application of stresses as hydrostatic stress, whilst in this work the tensile stress is applied uniaxially and therefore values differ.

All dielectric and piezoelectric properties at 25°C as a function of composition are listed in Table 4.4.

Table 4.3: Dielectric and piezoelectric properties of high g_{ij} piezoceramics from throughout literature compared with Landau-Devonshire derived properties calculated for 0.70 BiFeO3 – 0.30 PbTiO3 in this work

Material	$\epsilon^T_{33}/\epsilon_0$	d_{33} (pC/N)	d_{31} (pC/N)	d_h (pC/N)	g_{33} mVm/N	g_{31} mVm/N	g_h mVm/N	Ref.
Tetragonal BiScO3 – PbTiO3	820	440	-162	116	60.6	-22.3	16.0	[143]
0.34 BiScO3 – 0.66 PbTiO3	300	200	-44	112	75.3	-16.6	42.2	[142]
PbTiO3 Single Crystal (I)	80	83.7	-27.5	28.7	118.2	-38.8	40.5	[111]
PbTiO3 Single Crystal (II)	170	51.0	-4.4	42.2	33.9	-2.9	36.4	[111]
PbTiO3 Single Crystal (III)	126	117	-25.0	67.0	104.9	-22.4	60.1	[111]
Tetragonal 0.14BZT-0.86PT	120	138			129.9			[144]
Tetragonal 0.38BZN-0.62PT	250	157			71.0			[144]
Textured PbTiO3 82%	146	95	-8.6	77.8	74.0	-6.7	60.6	[141]
Textured PbTiO3 95%	124	127	-26.8	73.4	115.0	-24.4	66.2	[141]
PZT Navy Type I	3195	315	-132	51	25.5	-10.7	4.1	[175]
PZT Navy Type II	1800	409	-176	57	25.7	-11.0	3.7	[176]
PZT Navy Type III	1105	260	-93	74	28.8	-9.5	9.8	[175]
Generation I Crystals	8200	2800			38.5			[77]
Generation II Crystals	4000	1510			42.7			[77]
Generation III Crystals	3700	1120			34.2			[77]
0.70 BiFeO3 – 0.30 PbTiO3	7.8	16.2	-4.7	6.7	207.9	-60.7	86.5	This work

Figure 4.22 shows the d_{33}, $\epsilon^T_{33}/\epsilon_0$ and g_{33} in spherical coordinates as a function of angle away from the polar axis for 0.7 BiFeO3 – 0.3 PbTiO3 single domain. Although the general trend is similar to tetragonal PZT and PbTiO3 shown in Figure 3.4, subtle differences can be observed. The orientational dependence of the d_{33} of materials in Figure 3.4 shows elongated spheres along the [001], whilst for BFPT70 the orientational dependence is less elliptical and more spherical. This is most likely due to the change in d_{33}/d_{15} ratio with increasing BiFeO3 content as the d_{33}/d_{31} ratio is constant for all compositions within the tetragonal region. Furthermore the smaller $\epsilon_{33}/\epsilon_{11}$ ratio of BFPT70 compared to previous materials results in a more exaggerated 'donut' shape in which the impression along the [001] is far more defined. A combination of these two factors results in a more elongated trend for the g_{33} coefficient along the [001] and as mentioned previously results in giant piezovoltage response.

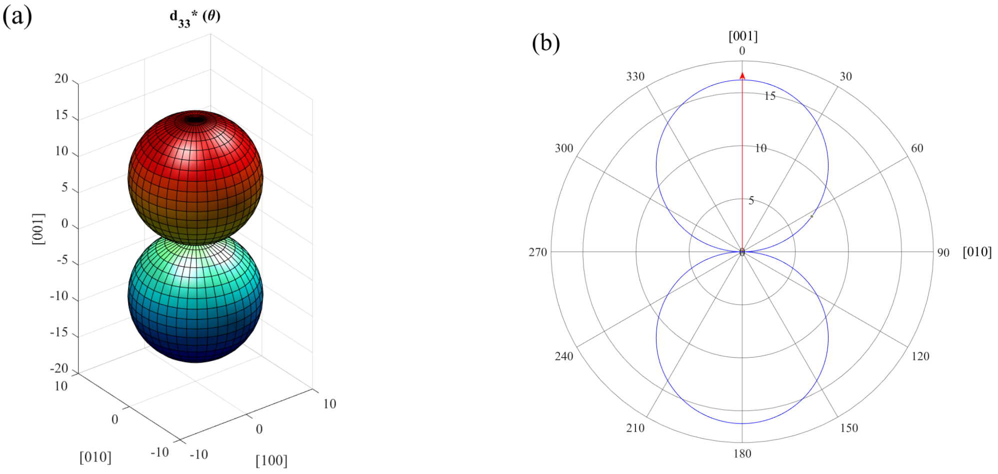

Table 4.4: Landau-Devonshire derived dielectric and piezoelectric properties for the solid solution at 25°C in this work. Nomenclature BFPT(x) = (x)BiFeO3 – (1-x)PbTiO3

	PbTiO3	BFPT10	BFPT20	BFPT30	BFPT40	BFPT50	BFPT60	BFPT70Tet	BFPT70Rhom	BFPT80	BFPT90	BiFeO3
$\epsilon_{11}^T/\epsilon_0$	192.8	147.2	110.9	83.5	63.3	48.3	37.2	29.0	111.6	92.8	79.0	68.4
$\epsilon_{33}^T/\epsilon_0$	125.4	80.2	51.9	34.3	23.1	15.9	11.1	7.8	111.6	92.8	79.0	68.4
d_{33} (pC/N)	135.2	93.7	66.2	47.8	35.4	26.8	20.7	16.2	46.2	40.5	36.0	32.5
d_{31} (pC/N)	-39.5	-27.4	-19.3	-14.0	-10.3	-7.8	-6.0	-4.7	-23.1	-20.2	-18.0	-16.3
d_{15} (pC/N)	78.6	64.8	53.1	43.5	35.8	29.7	24.8	20.9	9.1	8.2	7.5	6.9
d_h (pC/N)	56.2	39.0	27.5	19.9	14.7	11.1	8.6	6.7	0.0	0.0	0.0	0.0
g_{33} mVm/N	120.9	130.4	141.3	153.2	166.0	179.5	193.5	207.9	37.8	40.1	42.3	44.4
g_{31} mVm/N	-35.3	-38.1	-41.3	-44.8	-48.5	-52.4	-56.5	-60.7	-18.9	-20.1	-21.2	-22.2
g_{15} mVm/N	45.9	49.5	53.6	58.1	63.0	68.1	73.4	78.8	11.8	12.5	13.2	13.9
g_h mVm/N	50.3	54.2	58.7	63.7	69.0	74.6	80.4	86.4	0.0	0.0	0.0	0.0

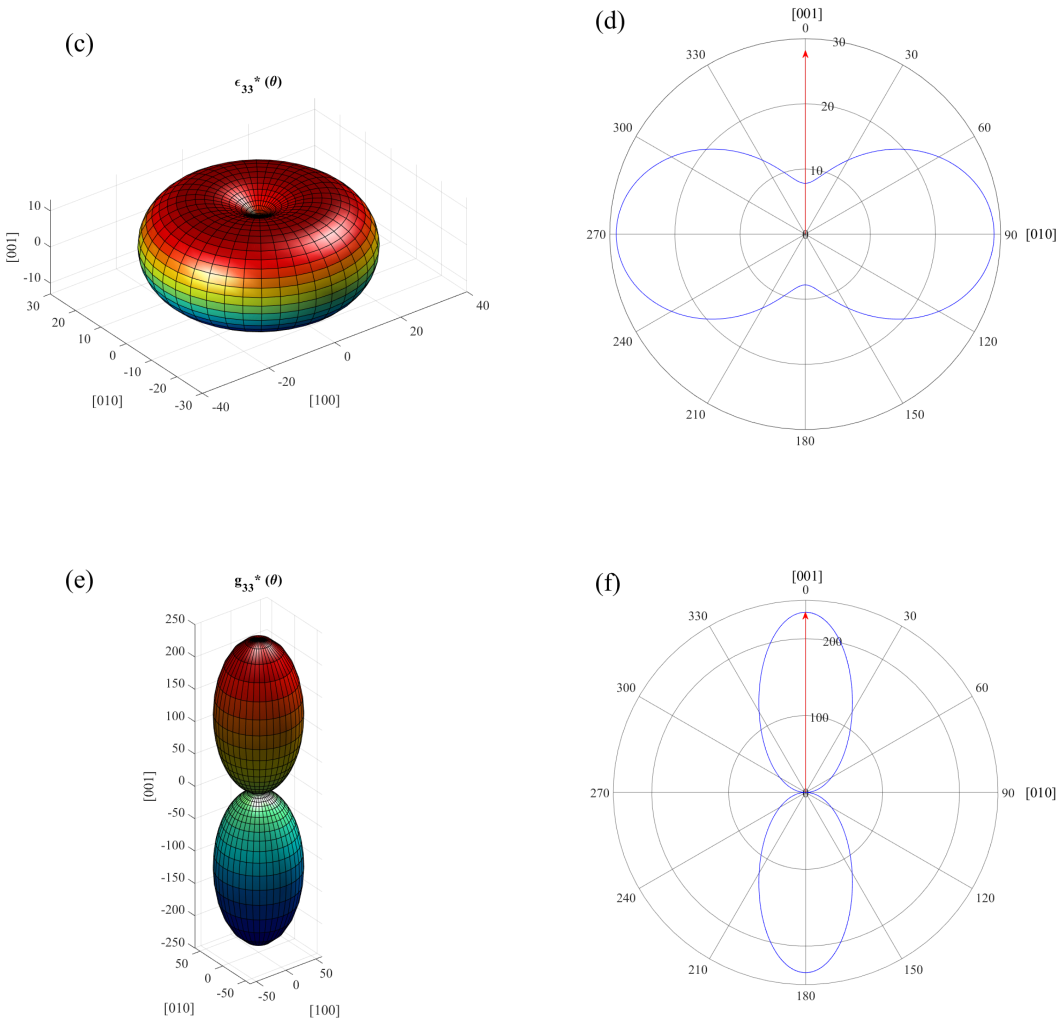

Figure 4.21: (a) Spherical and (b) cross-sectional polar coordinates of d_{33}. (c) Spherical and (d) cross-sectional polar coordinates of ϵ_{33}. (e) Spherical and (f) cross-sectional polar coordinates of g_{33}. All coefficients are as function of angle away from the polar axis for 0.7 BiFeO3 – 0.3 PbTiO3 at 25°C

Figure 4.22 shows the receiving voltage sensitivity (RVS) calculated using Equation 2.31 for materials listed in Table 4.4 with the addition of current military grade modified $PbTiO_3$ polycrystalline ceramics taken from [101]. For all modes $0.70BiFeO_3$-$0.30PbTiO_3$ is found to exhibit the highest sensitivity (lowest magnitude) and highlights the potential for this material in underwater passive sonar transducer applications.

It is worth noting that Landau-Devonshire theory treats the system as ideal and non-lossy, therefore $tan\delta$ values which dictate the level of signal-to-noise in the hydrophone cannot be calculated.

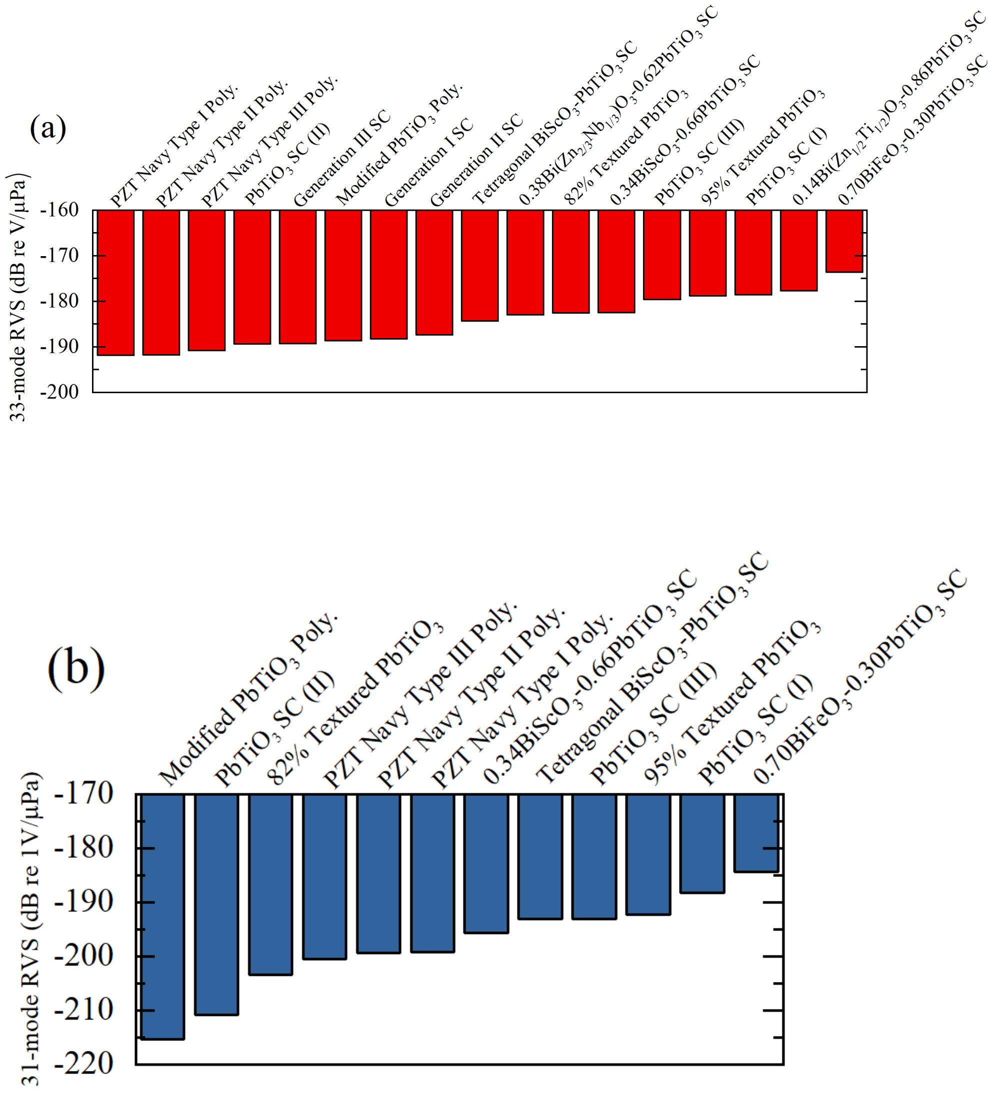

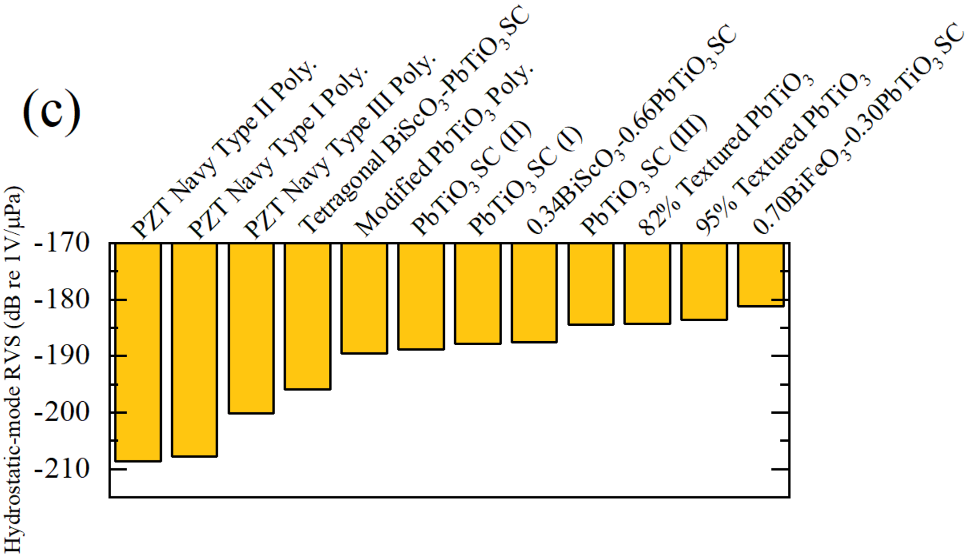

Figure 4.22: Receiving voltage sensitivity (RVS) values calculated using Equation 2.31 using the (a) 33 mode, (b) 31/32 mode, and (c) hydrostatic mode for materials listed in Table 4.4 with the addition of current military grade modified $PbTiO_3$ polycrystalline ceramics. SC = single crystal, poly.=polycrystalline ceramic. Sample thicknesses have been fixed to 1mm for the sake of Equation 2.31

Chapter 5

Characterisation of Heavily Nb-Doped $BiFeO_3$-$PbTiO_3$ Ceramics

As mentioned in the previous chapter and Section 2.3.3, the solid solution of rhombohedral bismuth ferrite and tetragonal lead titanate is of great scientific and technological interest. However this solid solution is plagued by enormous spontaneous strain when cooling through the Curie temperature making fabrication difficult, high conductivity facilitated by Fe^{2+}/Fe^{3+} hopping and oxygen vacancies, and substantial ferroelectric hardness making functionality difficult.

In this chapter $0.65Bi_{1-\frac{2x}{3}}Fe_{1-x}Nb_xO_3$-$0.35PbTiO_3$ (x=0.00, 0.01, 0.02, 0.05, 0.10, 0.20, 0.30) polycrystalline ceramics have been fabricated to overcome the issue of conductivity and improve the functionality of this solid solution. Initially Nb-doping appears to ferroelectrically harden the material reducing the d_{33} at doping levels x<0.20 at which point some piezoelectric activity is restored. However upon annealing the d_{33} is observed to drastically improve.

X-ray diffraction and scanning electron microscopy has been carried out to understand the structural and microstructural properties, Berlincourt measurements and permittivity vs temperature have been used to observe the effect of annealing on electrical properties. Impedance spectroscopy, X-ray photoelectron spectroscopy and polarisation/strain v electric field loops have been used in order to gain a deeper understanding of the defect chemistry dynamics.

5.1 Characterisation Techniques

5.1.1 X-Ray Diffraction

X-ray diffraction (XRD) is a powerful and commonly used tool in the structural characterisation of materials. The significance of using X-rays rather than other forms of electromagnetic radiation is the similarity between the X-ray wavelength and the interatomic distances within the crystal lattice.

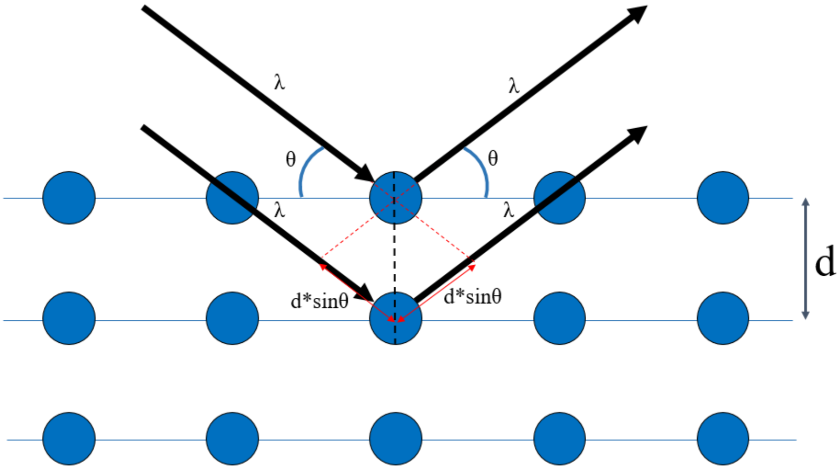

Figure 5.1: Schematic of X-ray diffraction and derivation of Bragg's law. Adapted from [177]

In 1919 William Henry Bragg and William Lawrence Bragg received a Nobel prize for "their services in the analysis of crystal structure by means of X-rays" and the conditions required for the diffraction of X-rays were determined. As shown in Figure 5.1 when incident X-rays are targeted at planes of atoms, one beam will diffract from the top plane of atoms whereas the second beam will continue to travel through the material to the plane of atoms below which is separated by an interatomic distance, d. Constructive interference will occur when the two X-rays that leave the crystal are in phase and therefore the additional distance of the second beam must be an integer number of wavelengths, nλ. Using trigonometry it is clear that the second beam must travel $2dsin\Theta$ distance further as shown in Equation 5.1 [177].

$$n\lambda = 2dsin\Theta \tag{5.1}$$

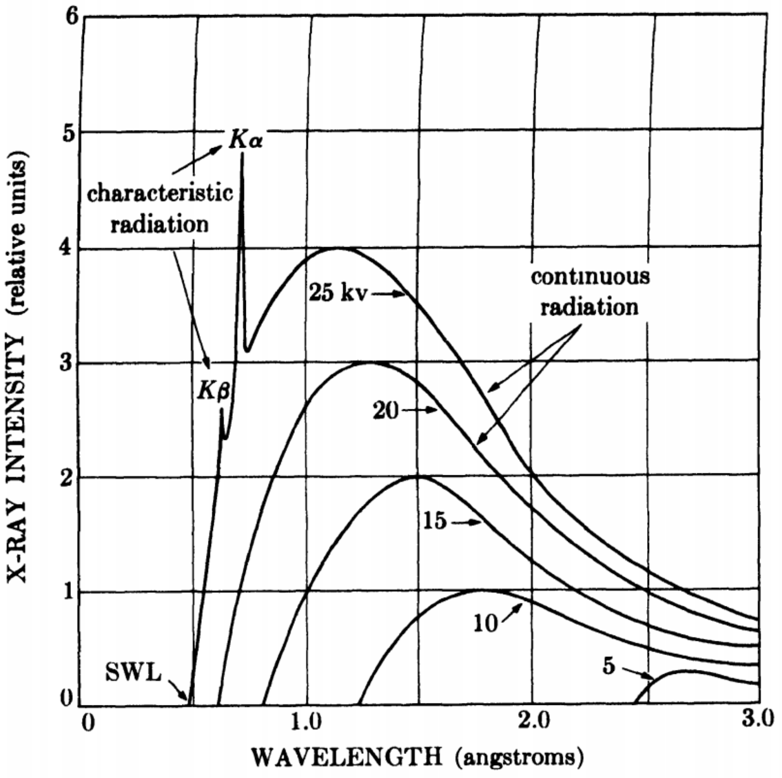

Figure 5.2: Characteristic spectrum of molybdenum target at varying accelerating voltages. Taken from [177]

The production of X-rays is often carried out using X-ray tubes in which there is a source of electrons, an accelerating voltage and metal target. Electrons are generated through thermionic emission and accelerated using high voltages in the order of 30-60kV towards a metal target of high purity. X-rays are produced when the high energy electrons hit the metal target and the energy associated with the sudden deceleration of the electrons results in the conversion to radiation consisting of a mixture of X-ray wavelengths in all directions. When direct detection of X-rays from the metal target are analysed (Figure 5.2) a wide range of wavelengths can be observed with the intensity also related to the accelerating voltage. The wide range of X-ray wavelengths originates since all electrons will not decelerate in the same way. Electrons which hit the target and are stopped in one impact will give up their energy in one go and give rise to photons with maximum energy, whereas some electrons may gradually lose their energy as they collide with multiple atoms within the metal target. These scans are referred to as *bremsstrahlung* derived from the German for “braking radiation” [177].

Figure 5.2 also shows that above a certain accelerating voltage, sharp peaks are formed at particular wavelengths. These peaks are characteristic of the target metal and are consequently named characteristic lines, with the whole combination of peaks known as the characteristic spectrum. The characteristic lines are categorised into sets labelled K, L and M in order of increasing wavelength. In the case of molybdenum, the K-lines are located around 0.7Å, L-lines at around 5Å and M-lines at much higher wavelengths. Within the characteristic line sets multiple K-lines are present, however only some of these peaks can be detected. These are known as $K\alpha_1$, $K\alpha_2$ and $K\beta_1$ with each having a characteristic wavelength. The $K\alpha_1$ and $K\alpha_2$ peaks may sometimes be indistinguishable due to the small difference in wavelengths and therefore only appear as one larger peak simply known as the $K\alpha$ peak [177].

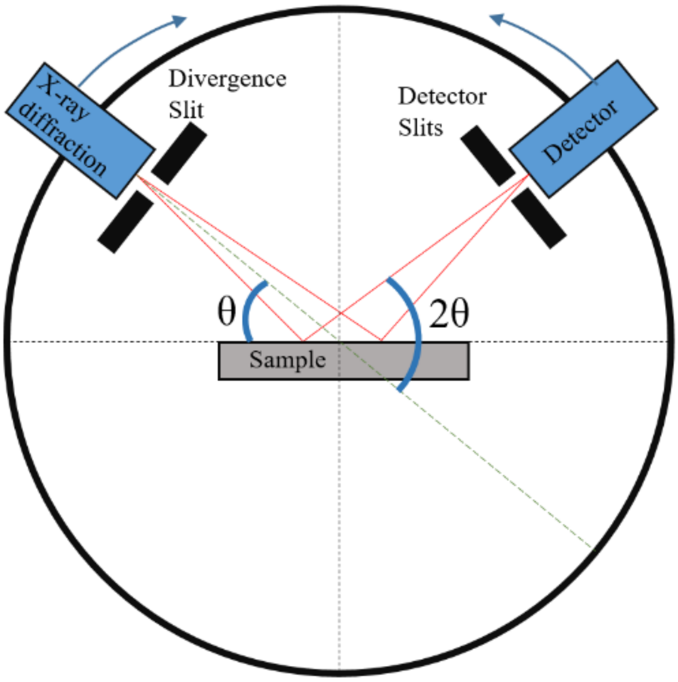

Figure 5.3: Illustration of a Bragg-Brentano set-up during X-ray diffraction data collection. Adapted from [177]

In this study a Bragg-Brentano goniometer set-up was used throughout and is shown in Figure 5.3. In this setup the X-ray source and detector rotate around a focusing circle allowing for constant distance from the sample throughout. Furthermore the Bragg-Brentano set-up also means that the diffraction vector is always perpendicular to the surface of the sample.

5.1.1.1 Peak Broadening

Figure 5.4 shows an X-ray diffraction pattern for an ideal crystal and for a material exhibiting peak broadening effects. An X-ray diffraction pattern from a perfect arrangement of unit cells within a lattice will produce vertical lines representing the exact d-spacings. Particle size, defects which can disrupt the continuity of atomic planes and strain can all give rise to peak broadening in which the d-spacing is given over a range of values.

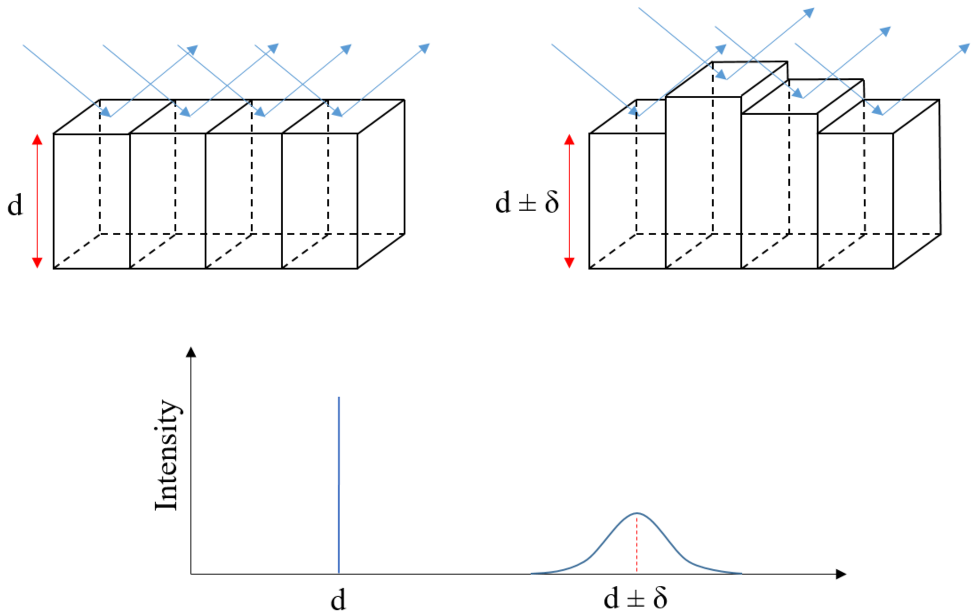

Figure 5.4: A demonstration of how imperfections in a crystal lattice can result in peak broadening. Adapted from [178]

5.1.2 Scanning Electron Microscopy

Scanning electron microscopy (SEM) has become an extremely useful imaging technique for the analysis of particles, surface topography and microstructures. SEM is similar to conventional light microscopy however it can achieve much higher resolution due to the much shorter wavelength compared to optical light. The Rayleigh criterion describes the limit of resolution between two points and the wavelength. For optical microscopy, the resolution limit is approximately 0.4 microns for blue light and approximately 0.2 microns for UV light. For electron microscopy, the wavelength of the incident electrons can be calculated using the De Broglie wavelength and ignoring relativistic effects results in a theoretical resolution limit of 0.2nm. In reality the resolution limit is dictated by other factors such as the accelerating voltage, working distance and stigmation, as well as sample quality and preparation [179].

Figure 5.5 shows a schematic of an SEM and illustrates the main components. Firstly an electron gun usually consisting of a tungsten filament is used to generate electrons which are then accelerated using voltages between 1kV-30kV. The chamber is evacuated to avoid interactions between the electrons and air. Using a series of condenser lenses, objective lenses and apertures, the electron beam can be focussed and spot size modified. The focussed beam is then scanned across the sample surface in a two-dimensional raster and an appropriate detector is used to monitor electrons as they are emitted from the surface. The two main detectors and therefore two main imaging techniques that are used in SEM are secondary electron imaging and backscattered electron imaging. In secondary electron imaging an Everhart-Thornley detector is positioned to the side of the sample stage which by using a small positive bias can attract low energy electrons towards it. Backscattered electron imaging uses much higher energy electrons compared to secondary electron imaging. These detectors are placed above the sample and only measure electrons that are travelling in line-of-sight of the detector without any positive bias being used hence a low yield, and therefore this results in darker images compared to images obtained using secondary electrons [180].

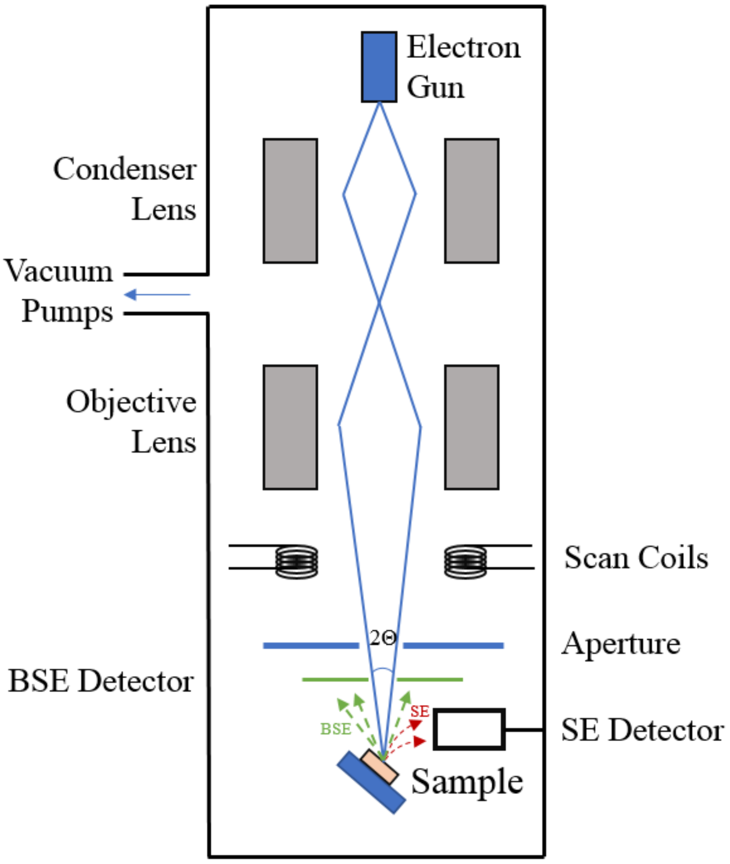

Figure 5.5: Schematic of a scanning electron microscope. SE=secondary electron, BSE=backscattered electron. Adapted from [180]

5.1.3 Permittivity vs Temperature

The plotting of relative permittivity vs temperature is a fundamental technique used to analyse the general dielectric properties and to determine the Curie point of a material. Usually this setup mimics a parallel plate capacitor using a high-conducting wire such as silver or platinum. The sample is placed within these wires and an inductor-capacitor-resistor (LCR) meter is used to determine the capacitance which if the sample dimensions are known can be used to calculate the relative permittivity. The dissipation factor (tanδ) can also be determined by comparing the phase difference between the input and output signal which can again be mapped as a function of temperature.

5.1.4 Berlincourt Measurements

The Berlincourt method is arguably the most straight forward method of measuring the d_{33} of a piezoelectric material. Unlike resonance methods in which the sample geometries must be modified in order to isolate the desired resonance mode, the Berlincourt method provides a much easier route.

The simplest definition of the piezoelectric d_{33} coefficient can be shown in Equation 5.2 and represents the change in electric displacement along the 3-direaction (δD_3) with the change in applied stress also in the 3-direction (δX_3) whilst maintaining constant field [181].

$$d_{33} = \left[\frac{\delta D_3}{\delta X_3}\right]_E \tag{5.2}$$

This equation can be re-written as:

$$d_{33} = \frac{q/A}{F/A} = \frac{q}{F} \tag{5.3}$$

Where q is the developed charge, A is the area that the force, F, is applied over and the area of charge accumulation on the electrode. A Berlincourt meter consists of a force head and the control electronics. A force head schematic is shown in Figure 5.6. The sample is placed in between two contact probes which can be modified to accommodate different sized samples. The top probe is often controlled by a thread and is lowered onto the top electrode of the sample and applies a constant static force. The lower probe provides an oscillating force at a frequency defined by the user which in turn is connected to a reference sample such as PZT which measures the applied force. The charge is then measured, and a readout is given [181].

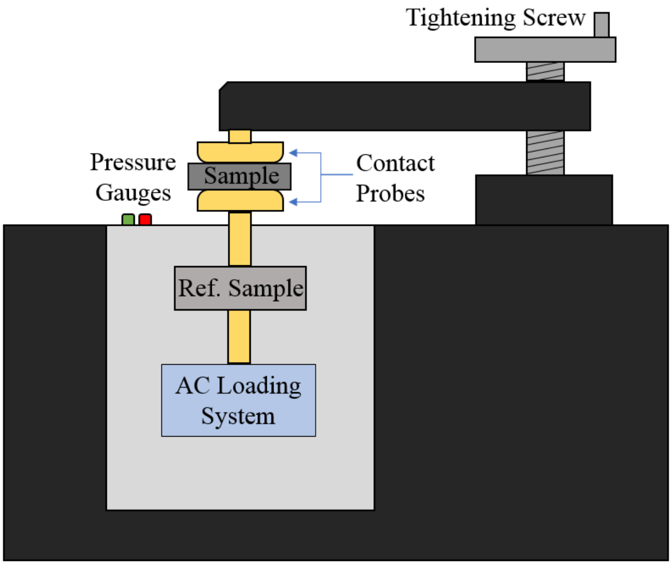

Figure 5.6: Schematic of Berlincourt piezoelectric meter set-up. Adapted from [181]

5.1.5 Polarisation vs Electric Field

The measurement of polarisation against electric field is fundamental in the characterisation of ferroelectric materials. It involves the switching of the two metastable states of the sample by the application of an electric field. The technique is based on the modified Sawyer-Tower circuit shown in Figure 5.7.

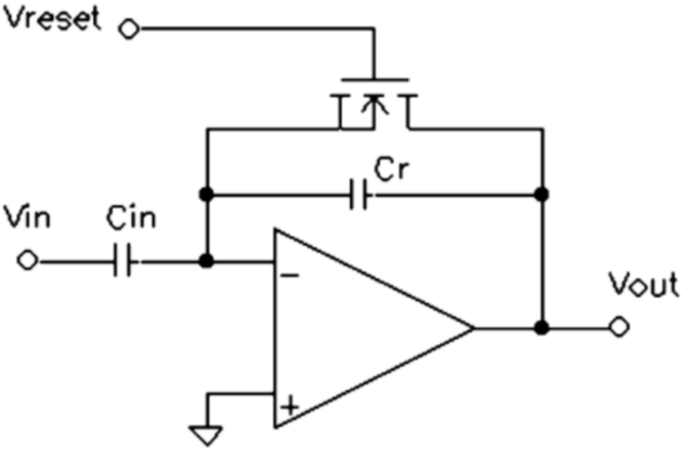

Figure 5.7: Circuit diagram of a Sawyer-Tower circuit used to calculate P-E loops. Taken from [182]

With known sample dimensions, the polarisation (P) and electric field (E) are calculated using Equations 5.4 and 5.5, respectively.

$$E = \frac{V_{IN}}{d} \tag{5.4}$$

$$P = \frac{q}{A} = \frac{C_R V_{OUT}}{A} \tag{5.5}$$

Where P is the polarisation, q is the charge, A is the electrode area of the sample, C_R is the capacitance of a reference, and V_{OUT} is the voltage across the capacitor.

5.1.6 Strain vs Electric Field

A typical strain-field measurement set-up can be shown in Figure 5.8. The sample is placed in between two copper contacts which in turn is submerged in oil as to avoid arcing and a fibre optic probe consisting of a light transmitting filament and light receiving filament is placed above the upper contact. A high voltage signal of frequency between 0.1-100Hz is applied to the sample resulting in deformation of the sample and displacement of the upper copper contact. This displacement is related to the intensity of the reflected light and therefore can be accurately determined when calibrated.

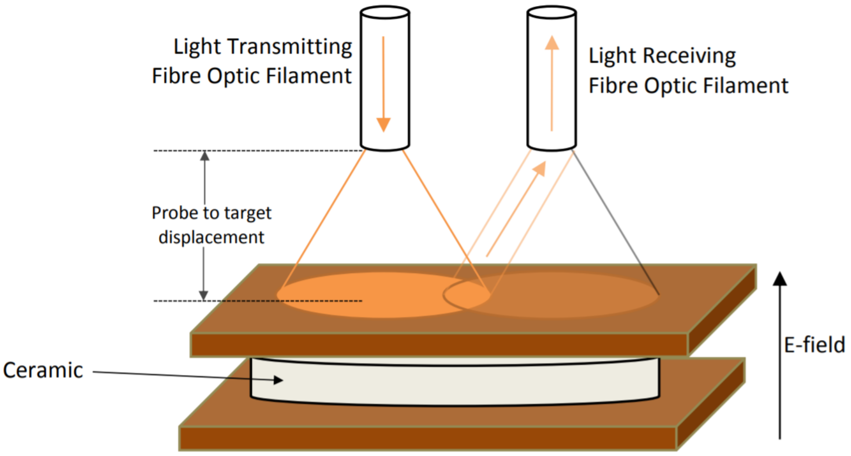

Figure 5.8: Typical strain-field measurement set-up. Taken from [183]

5.1.7 Impedance Spectroscopy (IS)

The most fundamental description for impedance is that it is a measure of an electrical circuit's ability to resist the flow of current. Whilst this is analogous to resistance, the main difference is that resistance is independent of frequency whereas impedance is frequency dependent [184].

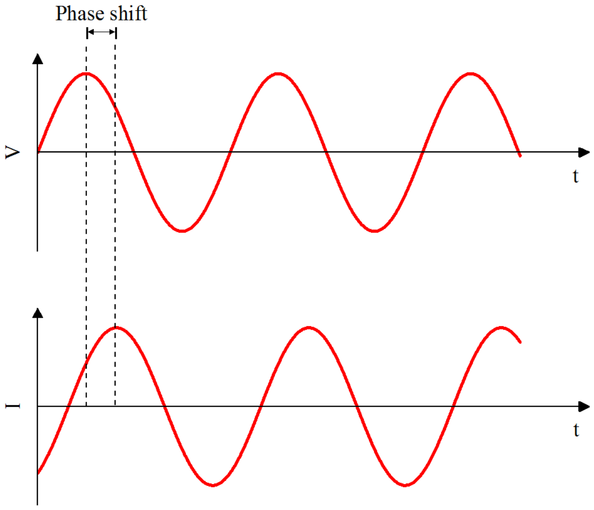

Figure 5.9: AC voltage and current as a function of time and demonstration of phase shift between the them.

Impedance is measured by applying an AC signal of known voltage to a sample and measuring the current response. The known signal can be expressed as a function of time as shown in Equation 5.6 and graphically in Figure 5.9.

$$V_t = V_0 sin(\omega t) \tag{5.6}$$

Where V_t is the voltage at time t, V_0 is the voltage amplitude, and ω is the angular frequency of the signal. The sample will then cause a shift in the response signal and a drop in the amplitude which can be expressed as:

$$I_t = I_0 sin(\omega t + \phi) \tag{5.7}$$

Where I_t is the current at time t, I_0 is the amplitude of the current, ω is the angular frequency and ϕ is shift in the response signal.

The impedance, Z, is then calculated by dividing to input signal by the response signal similar to Ohm's law:

$$Z_t = \frac{V_t}{I_t} = \frac{V_0 sin(\omega t)}{I_0 sin(\omega t + \phi)} = Z_0 \frac{sin(\omega t)}{sin(\omega t + \phi)} \tag{5.8}$$

An alternative method of mathematically describing the impedance is as a complex value using the Euler's relationship in Equation 5.9 and expressing the input and response signal as follow:

$$exp(j\phi) = cos\phi + jsin\phi \tag{5.9}$$

$$V_t = V_0 exp(j\omega t) \tag{5.10}$$

$$I_t = I_0 exp(j\omega t - \phi) \tag{5.11}$$

Where $j = \sqrt{-1}$. The alternative expression for the constructed impedance can then be expressed using similar treatment as before.

$$Z(\omega) = \frac{V_t}{I_t} = \frac{V_0 exp(j\omega t)}{I_0 exp(j\omega t - \phi)} = Z_0 exp(j\phi) = Z_0(cos\phi + jsin\phi) = Z' + jZ'' \tag{5.12}$$

The ability to analyse the impedance of a sample as a function of frequency allows for much more information to be collected compared to DC analysis particularly in the characterisation of ferroelectrics. As discussed in Chapter 2, the polarisation of a material can be broken down into different contributions which "freeze out" at different frequencies. This description of mechanism relaxations is highly simplified as many more relaxations can take place within these frequency ranges. These originate from separate conduction mechanisms from either A-site vacancies, oxygen vacancies, B-site vacancies or free charge carriers. Furthermore these relaxations can also take place within different regions of the ceramic such as within the grain, at grain boundaries, or at the ceramic-electrode interface. The power of impedance spectroscopy comes with the ability to deconvolute these different contributions to the overall impedance as shown in Equation 5.13 and allows the user to probe different areas within the ceramic [185].

$$Z_{total} = Z_{grain} + Z_{grainboundary} + Z_{electrode} \tag{5.13}$$

Although this characterisation technique is named dielectric *impedance* spectroscopy, there are other important electrical quantities that must be considered to gain a fuller understanding of the test sample. The first is admittance (Y^*) which in complex form relates to the complex impedance (Z^*) as shown in Equation 5.14.

$$Y^* = \frac{1}{Z^*} \tag{5.14}$$

And the second is electric modulus (M^*) which can be expressed in complex form according to Equation 5.15.

$$M^* = j\omega C Z^* \tag{5.15}$$

Where $j = \sqrt{-1}$, ω is the angular frequency, and C is capacitance.

It is important to analyse these other quantities, particularly the electric modulus function as it allows for the observation of responses that may not be obvious when considering only impedance measurements as shown in Figure 5.10. This is due to the different weightings of the data. For example, in an average ferroelectric material the impedance is dominated by the grain boundary contribution and thus will dominate the impedance spectrum and may hide any contributions from the bulk. Whereas the electric modulus will highlight the smallest capacitance since the M$''$ maximum will be $=\epsilon_0/2$C which will usually come from the bulk response [186].

The two most common plots in impedance spectroscopy are Bode plots (Figure 5.10), in which the imaginary parts of the quantities are plotted as a function of frequency and provide a general overview of the material's response to the stimulus giving an indication as to the number of relaxation mechanisms. The second plot is a complex plot shown in Figure 5.11 in which the real and imaginary part of a quantity are plotted against each other. By constructing an equivalent circuit which can accurately model the raw data, values for the resistance and capacitance can be extracted.

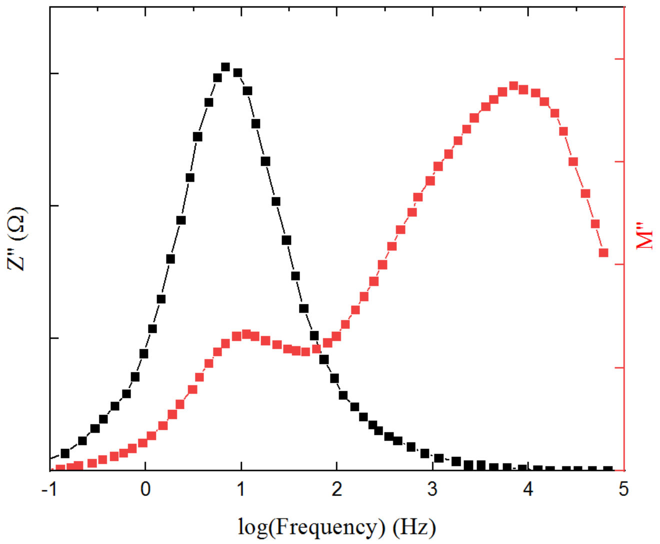

Figure 5.10: Imaginary impedance Z$''$ and imaginary modulus M$''$ versus frequency for barium titanate polycrystalline ceramics as an example of a Bode impedance plot. Taken from [187]

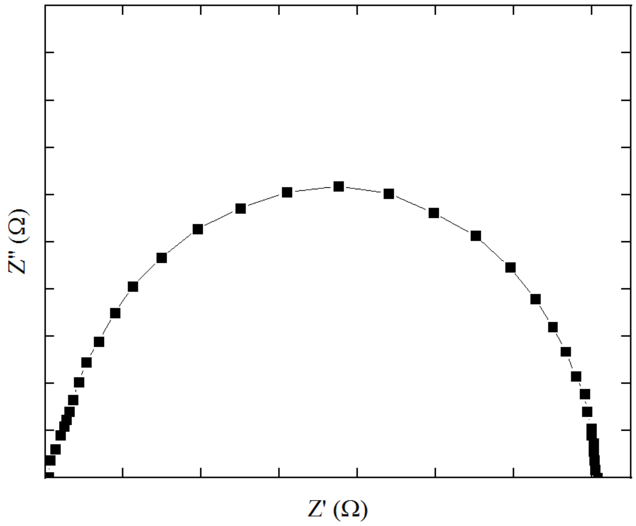

Figure 5.11: Z″ v Z′ for barium titanate polycrystalline ceramic as an example of a complex impedance plot. Taken from [187]

5.1.7.1 The Constant Phase Element

A material that exhibits ideal capacitive behaviour will have one relaxation time and can be demonstrated in the Bode plots as a single vertical line and in a complex plot as a perfect semicircle. In reality a material will not act as an ideal capacitor and a distribution of relaxation times occurs which can be shown in the Bode plot through broadening of the relaxation peak and in the complex plot as a rotated semicircle where the centre lies below the x-axis. In order to model this non-ideal behaviour, a constant phase element (CPE) is often included in the equivalent circuit along with a resistor and capacitor [186]. The impedance of the CPE (Z^*_{CPE}) is defined as shown in Equation 5.16.

$$Z^*_{CPE} = [B(j\omega)^m]^{-1} \tag{5.16}$$

Where $B = \gamma/cos(m\pi/2)$, γ is a constant, $j = \sqrt{-1}$ and m is a constant between 0 and 1. At m=1, the CPE acts as an ideal capacitor and at m=0 acts as an ideal resistor.

5.1.8 X-Ray Photoelectron Spectroscopy (XPS)

XPS is a chemical analysis surface technique which was first developed by Kai Siegbahn and the research group at the University of Uppsala, Sweden, in the 1960's. A spectrometer is used to measure the kinetic energy of electrons that have been emitted from the surface of a material through excitation of an incident photon [188]. Usually the graph of choice to present this data is counts or intensity vs the binding energy which is calculated using Equation 5.17.

$$E_{binding} = hf - E_{kinetic} - \kappa \tag{5.17}$$

Where hf is the known energy of the incident photon, $E_{kinetic}$ is the measured kinetic energy and κ is the spectrometer work function. Although the experimental dependent variable is the kinetic energy, the binding energy signifies the more intrinsic nature of the samples and is therefore preferred during analysing and plotting.

XPS is based on the photoelectric effect which is shown in Figure 5.12. An incident photon excites an electron in the core levels which in turn is emitted and contributes to the photoelectron spectrum. As the energy of the incident photon is changed, so does the measured kinetic energy of the emitted electrons. The obtained spectrum accurately replicates the electronic structure of the atom as shown in Figure 5.13.

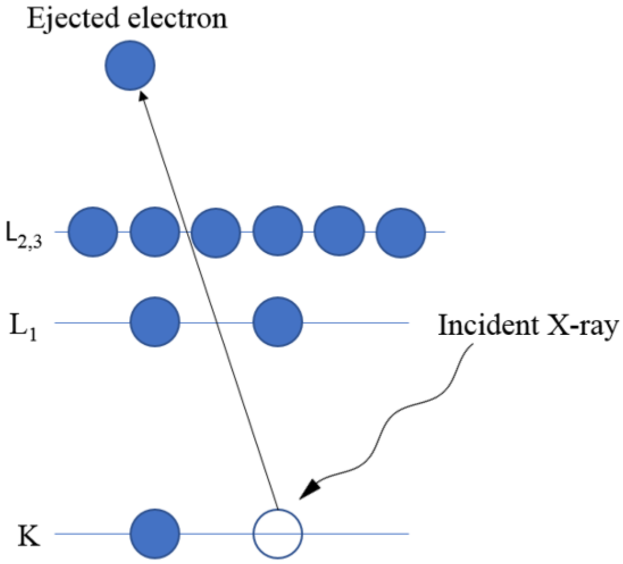

Figure 5.12: Schematic showing the process of the photoelectric effect. Adapted from [188]

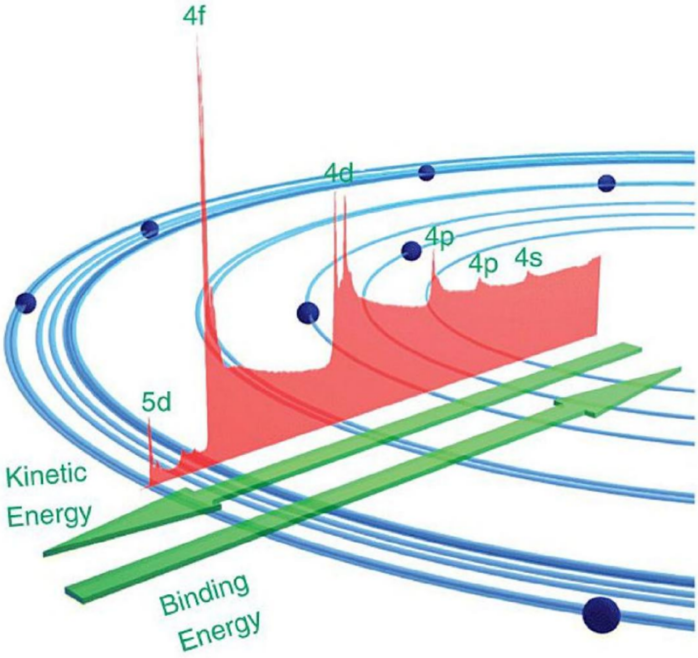

Figure 5.13: Illustration demonstrating a typical XPS spectrum (red) and how the peak locations and background are related to the fundamental electronic structure of the atom (blue). Taken from [189]

When electrons of a core level are emitted without loss of energy, characteristic lines in the spectra are generated whereas electrons that undergo inelastic scattering form the background of the spectrum. An atom that has emitted a core electron can relax in two ways, through the emission of an X-ray or the emission of a secondary electron (more commonly known as an Auger electron). When a vacancy is formed after the emission of an electron through the photoelectric effect, an electron from a higher energy level will drop to fill the vacancy. The energy from this relaxation of a higher energy electron leads to the emission of this second electron from the atom [188].

Due to the difference in fundamental chemical environment of each atom such as number of protons and electrons and the differences in electronegative and electropositive nature, each element has a unique binding energy. For materials with multiple elements, the characteristic spectra overlap each other. Software can then be used to identify these elements by using a database containing these ‘fingerprint’ binding energy values. Furthermore the binding energies deviate slightly and arise from the differences in chemical environments, e.g. a carbon bonded with an oxygen atom will have a different binding energy to that of a carbon bonded to a hydrogen atom. This chemical shift is a useful tool in analysing chemical information such as the oxidation state of an element. XPS is a purely surface sensitive technique and arises from the short distances that electrons can travel before losing their characteristic energy through inelastic collisions. Therefore, the technique is limited to approximately 1-10nm in depth [189].

5.2 Experimental Procedure

5.2.1 Synthesis of Powder

Commercially available reagent powders of Bi_2O_3 (99.9%), PbO (99.9%), Fe_2O_3 (>99%), TiO_2 (99.9%) and Nb_2O_5 (99.99%) (Sigma Aldrich) were dried overnight at 120°C in order to dehydrate the powder and allow for more accurate chemical weights. Non-stoichiometric mixtures were weighed to form $0.65Bi_{1-\frac{2x}{3}}Fe_{1-x}Nb_xO_3$-$0.35PbTiO_3$ (x=0.00, 0.01, 0.02, 0.05, 0.10, 0.20, 0.30). The choice of 0.65:0.35 ($BiFeO_3$:$PbTiO_3$) ratio was to be close enough to the morphotropic phase boundary (MPB) as to exhibit large spontaneous strain but far enough away from the MPB such that a $P4mm$ phase is retained on the introduction of dopants. Bell et al. [55] found that the introduction of even small quantities of Mn^{4+} (x=0.0025) resulted in a significant shift in the MPB such that a pure $R3c$ phase was observed. Furthermore, the choice of Nb^{5+} as a dopant is explained in Section 2.3.3. The reason for the non-stoichiometric calculation of Bi is as follows. Considering only the Nb-doping of $BiFeO_3$, there are four potential compensation mechanisms for donor doping: I - electron compensation, II - oxygen vacancy annihilation, III - A-site vacancies, and IV - B-site vacancies as shown in Equations 5.18-5.21:

$$\text{I} \qquad Nb_2O_5 \leftrightarrow 2Nb^{\cdot\cdot}_{Fe} + 3O^X_O + O_2 \uparrow +4e^{'} \tag{5.18}$$

$$\text{II} \qquad Nb_2O_5 + 2V^{\cdot\cdot}_O \leftrightarrow 2Nb^{\cdot\cdot}_{Fe} + 5O^X_O \tag{5.19}$$

$$\text{III} \qquad 3Nb_2O_5 \leftrightarrow 6Nb^{\cdot\cdot}_{Fe} + 4V^{'''}_{Bi} + 15O^X_O \tag{5.20}$$

$$\text{IV} \qquad 3Nb_2O_5 \leftrightarrow 6Nb^{\cdot\cdot}_{Fe} + 4V^{'''}_{Fe} + 15O^X_O \tag{5.21}$$

Mechanisms I and III are expected to dominate under heat treatment in air, mechanism II may dominate in oxidising conditions, and mechanism IV may occur, although it may be unlikely, resulting in the precipitation of Fe_2O_3 although it is unlikely. To avoid the deleterious effects of mechanism I and IV, and in order to avoid the experimental complexities of sintering or annealing in pure or high pressure oxygen, mechanism III is chosen as the means of electrical neutrality. Equation 5.20 shows that for every quantity x of Nb, $2x/3$ amount of Bi must be removed in order to acheive electrical neutrality.

Reagents were ball milled in iso-2-propanol with yttria-stabilised zirconia (YSZ) beads (Tosoh, Japan) for 24 hours allowing for the thorough mixing and breaking down of powders. Dried and sieved powders were then placed inside an alumina crucible with an alumina tile lid and calcined at 800°C for 4 hours in air using a heating and cooling rate of 200°C/hour. Once calcined, powders were sieved again to break up large agglomerates and ball milled for another 24 hours in deionised water and 2wt% Optapix ceramic binder (Ceramco, Italy). The resultant slurry was dried initially using a Kenwood kitchen chef induction heated mixing bowl and placed into an oven at >120°C overnight. Powders were then sieved for a final time.

5.2.2 Synthesis of Pellets

Powders were uniaxially pressed at 125MPa into 10mm diameter pellets and buried in a powder bed of identical composition within an alumina crucible set-up. An initial binder burnout stage involved gradual heating up to 600°C at 60°C/hour and dwelling for 1 hour, followed by heating to 1000°C (x=0.00, 0.01, 0.02 & 0.05) or 1050°C (x=0.10, 0.20 & 0.30) at 300°C/hour for 0.5 hours. Pellets were then cooled at 20°C/hour down to room temperature. The slow cooling is imperative to the survival of the samples when cooling through the cubic-tetragonal phase transition and the formation of dense, uncracked samples. The choice of sintering temperature was determined through optimisation, in which samples were sintered from 900°C-1100°C at 50°C intervals and the geometric and archimedes density were measured to find the sintering temperature which resulted in the highest values of absolute and relative density. All other parameters such as binder burnout stage, heating and cooling rates, and dwell times were taken from Ref. [190].

In an ideal experiment in which only the effect of Nb-doping on $BiFeO_3-PbTiO_3$ was being studied, a coherent maximum sintering temperature would have been used. However it was decided that optimising the density would help eliminate the significant distraction of the effect of porosity and therefore it was preferential to characterise the electrical properties of dense ceramics rather than porous ceramics, hence x=0.10, 0.20 and 0.30 samples were sintered 50°C higher. Final samples possessed relative densities between 95.8%-96.8% for low Nb-contents (x<0.05) and 95.7% to 92.2% for highly doped Nb-samples.

This set-up and sintering regime resulted in material losses of <1wt%. Samples initially showed a dull grey consistency due to the loss of volatiles from the surface. The depleted layer was removed using silicon carbide paper before any density measurements resulting in samples appearing more shiny and metallic-like as shown in Figure 5.14.

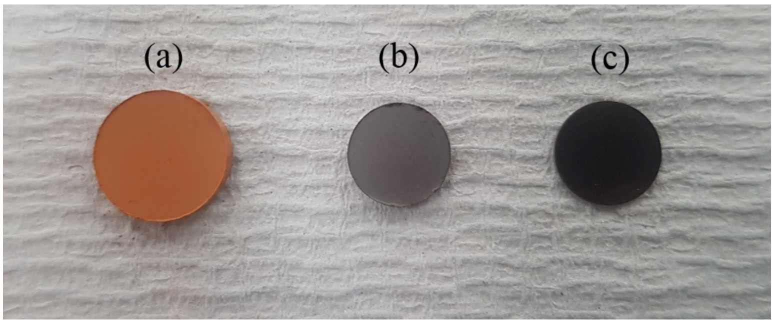

Figure 5.14: $BiFeO_3-PbTiO_3$ polycrystalline pellets in (a) green form (b) sintered form and (c) polished form.

For electrical analysis, samples were ground to 1mm in thickness using a Beuhler Metaserv Motopol 12 (Beuhler, USA). The samples were then electroded using fire-on silver paste (Gwent group, UK) on opposing faces carefully so as to not create a short circuit around the edge of the sample and fired at 550°C for 15 minutes.

For the annealing study samples were placed in an alumina crucible and covered with an alumina tile to reduce the loss of volatiles. Samples were then annealed at 750°C for 0.5 hours with a heating and cooling rate of 200°C/hour and 50°C/hour, respectively.

All characterisation and results in this thesis were carried out using the same batch of powder. A second collection of samples were fabricated to test repeatability showing concordancy in crystallography, and general agreement in the dielectric and piezoelectric measurements. Slight variation in the dielectric and piezoelectric properties from batch-to-batch were due to the nature of ceramic processing however identical trends were observed. For the case of x=0.01 and 0.02, a third set was fabricated and tested in order to confirm the anomolous behaviour of x=0.01 samples.

5.2.3 X-Ray Diffraction

X-ray diffraction was carried out on a PANalytical X'Pert Diffractometer (Phillips, The Netherlands) using a Cu target and a Bragg-Brentano set-up. The voltage and current used to generate the X-rays were 40kV and 40mA throughout. A standard step size of 0.033° was used from 15°-60° 2Θ and a scan time of 30 minutes was employed. All characterisation was carried out on pellets that had been crushed using a pestle and mortar and annealed.

5.2.3.1 Refinement

Rietveld refinement is a highly established method for detailed structural characterisation of ferroelectric materials. It involves the creation of a model structural system which is then compared to raw data by adjusting parameters such as unit cell dimensions, atomic positions and scale factors. Typically a weighted R-profile (R_{wp}) value is used to quantify the degree of coherence between the two by analysing the difference in height, width and peak position between the model and the data. Another value that is often quoted to quantify goodness of fit is chi^2 which mathematically is represented as R_{wp}/R_{exp} where R_{exp} is the expected R factor and considers the quality of the raw data and represents the best possible value of R_{wp} that can be achieved. When chi^2 approaches 1, the goodness of fit increases [191]. Once the user has reached a point either where no more justifiable refinements can be made and/or further parameter refinement results in the decrease in goodness of fit values, then detailed crystallographic data can be extracted such as unit cell parameters, atomic positions and occupancies, and structural phase percentage weights in ferroelectric solid solutions.

Rietveld refinement is an important part of crystallographic analysis of materials and is therefore important to have a basic understanding of how it works. It is also important to understand its limitations, one of which is the inability to analyse materials with significant peak broadening and anisotropy. Although peak broadening and anisotropic effects have refineable parameters within Rietveld analysis, this phenomenon is too large to be accountable in $BiFeO3-PbTiO3$. As shown in Figure 5.15 when the peak broadening and anisotropy are refined in order to match the pattern of the tetragonal (001) peak, a large discrepancy between the model and experimental data of the tetragonal (100) becomes obvious and vice versa. This issue is repeated across multiple tetragonal peaks and therefore the best weighted R-profile that could be achieved in this study was ≈25. The inability to sufficiently fit the Rietveld model has been observed previously [178,190] and leads to the inability to accurately refine the bismuth ferrite – lead titanate solid solution and similar anisotropic materials using standard laboratory X-ray diffraction facilities and therefore the validity of the refined parameters obtained.

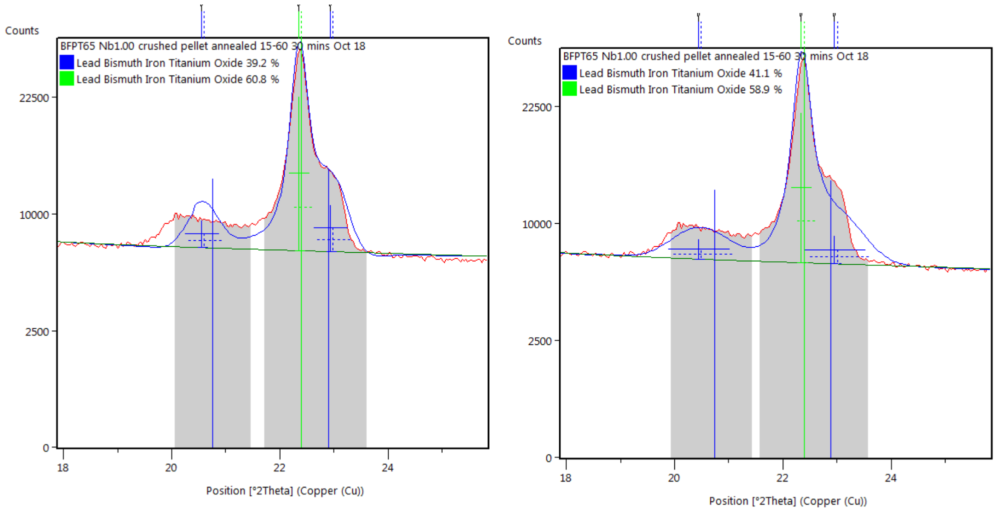

Figure 5.15: Rietveld refinement fitting results for x=0.01 Nb:BFPT65 demonstrating severe anisotropic effects of the tetragonal {001} peaks

For this study, a HighScore Plus (Malvern Panalytical, UK) least-square fitting method was used and data was compared to the International Centre of Diffraction Data (ICDD) database in order to determine the structural phases present. Once the appropriate ICDD files were chosen, and combining the goodness of fit to experimental data, relative peak intensities and scale factors, HighScore Plus is able to provide a semi-quantitative value for the percentage weights of each component.

5.2.4 Scanning Electron Microscopy

In order for detailed analysis of the microstructure of samples, a high level of polishing was carried out. Whilst the pellets for previous studies had been mechanically ground so as to remove material and reduce the thickness of the sample, here the process involves using far less aggressive abrasives in order to remove scratches and create a flat surface.

Samples were fixed to the bottom of a grinding plate with laboratory grade bees wax. Once mounted the samples would be initially ground with 800 grade SiC abrasive paper, and then polished using a series of diamond suspension sprays gradually reducing in particle size. A regular top-up of diamond suspension spray was applied during each polishing step in order to maintain a sufficient level of lubrication and avoid smearing across the sample surface. Between each route, the samples were cleaned using distilled water and detergent. Table 5.1 gives details on the polishing route used in this study.

Table 5.1: Polishing route used for preparing samples for scanning electron microscopy

Step No.	Surface	Abrasive	Lubricant	Force (per specimen)	Time (min:sec)	Platen Speed (rpm)	Head Speed (rpm)	Relative Rotation
1	SiC	800	Water	4 lbs	0:40	150	60	Comp
2	SiC	1200	Water	4 lbs	1:20	150	60	Comp
3	TexMet P	9μm Metadi Supreme		4 lbs	5:00	150	60	Contra
4	TexMet P	3μm Metadi Supreme		4 lbs	5:00	150	60	Comp
5	Trident	1μm Metadi Supreme		4 lbs	3:00	150	60	Comp
6	ChemoMet	MasterMet Colloidal Silica		4 lbs	1:20	100	60	Contra

Samples were then chemical etched using a solution of 50mL water, 3mL HCl and 3 drops of HF. This solution was initially formulated by Professor Bell and has since been used by previous students at the University of Leeds [178,192] for $BiFeO_3$-$PbTiO_3$ or similar materials. The samples were submerged in etchant for 10 seconds, bathed in water for 10 minutes and thoroughly washed with detergent and methanol. The samples were then placed in an oven $>$100°C for 5 minutes to thoroughly dry the sample and remove any moisture that may have become trapped in pores.

An etched sample was then stuck onto a carbon adhesive pad which in turn was stuck onto a stainless steel SEM stub. Carbon paint was spread around the edges of the sample in order to create a sufficient conductive path for electrons and prevent charge build-up on the surface of the sample which can severely distort the SEM image. A 5nm layer of carbon was sputtered onto the sample to increase the conductivity across the sample surface.

SEM was carried out using a Hitachi SU8230. The electron beam settings were kept at 5kV accelerating voltage and 22.3μA current throughout all samples.

Grain size analysis was carried out using ImageJ software (National Institutes of Health, USA) using the grain boundary intercept method. In this method a line of known length is drawn across the SEM image and the number of grain boundary interceptions is counted carefully by eye. The average grain size is taken as the length of the known line divided by the number of boundary interceptions. This number is further multiplied by a correction factor of 1.56 which takes into account the overlapping of grains which can make grains seem smaller than they are and also overcomes the issue of uncertainty which can arise when measuring possibly anisotropic individual grains [193]. For each sample 10 lines were drawn and the intercepts counted for each and averaged, the error was calculated using the standard deviation between average grain sizes across each line.

5.2.5 Permittivity vs Temperature

The capacitance and tanδ were measured on unpoled samples using an Agilent 4284A LCR meter (Agilent, USA) connected using a GPIB interface (IEEE) which, using the sample dimensions measured using a micrometer and inputted into the software by the user, were automatically converted to relative permittivity. Samples were placed in between two silver wires and placed inside a tube furnace. A heating and cooling rate of 3°C/min and a maximum temperature of 750°C was employed. A K-type thermocouple was located within the vicinity of the sample and recorded using a USB-TC01 device (National Instruments, UK).

5.2.6 Poling & Berlincourt Measurements

A short poling study was carried out in order to determine the optimum poling conditions. This step involved poling samples over a range of temperatures and fields and the ideal poling parameters were taken as the conditions that resulted in the largest d_{33}. Table 5.2 shows that the point at which the highest d_{33} was achieved is at 75°C with a poling field of 8kV/mm. A poling time of 5 minutes was implemented for all samples. Although this poling regime was determined using undoped BFPT samples, it was used across all Nb content samples for consistency.

Table 5.2: d_{33} values for undoped $0.65\,BiFeO_3 - 0.35\,PbTiO_3$ for a range of temperatures and DC electric fields, poled for 5 minutes. (BD=breakdown)

	5kV/mm	6kV/mm	7kV/mm	8kV/mm	9kV/mm
50°C	15.8pC/N	17.8pC/N	26.9pC/N	37.6pC/N	BD
75°C	18.0pC/N	32.1pC/N	38.1pC/N	**49.2pC/N**	BD
100°C	BD	BD	BD	BD	BD
125°C	BD	BD	BD	BD	BD

After poling, samples were allowed to rest for 24 hours and then d_{33}, capacitance and tanδ measurements were tested using a Piezotest PM300 Berlincourt meter (Piezotest, Singapore) with a dynamic force 0.25N at 110Hz.

For d_{31} measurements, samples were cut using a diamond saw into 5mm x 3mm x 1mm cuboids, electroded across the 5mm x 3mm large faces, poled, and left for 24 hours before measurement. Figure 5.16 shows the schematic of the d_{31} measurement set-up. The d_{31} was measured by placing the rectangle in between the Berlincourt meter probes along the long axis such that the electrode face was perpendicular to the probes. Alumina tiles were placed in between the probe and sample so that the equipment did not short circuit along the electrode and wires were used to connect the probes to each face of the sample. The reading from the Berlincourt meter was then recorded and divided by the aspect ratio of the rectangle to give the d_{31}.

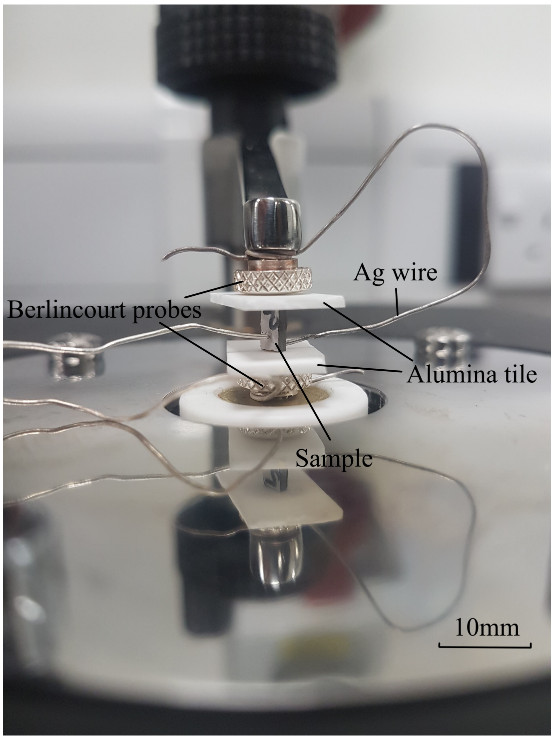

Figure 5.16: Photograph of the appropriate d_{31} setup using a d_{33} meter

Using the d_{33}, d_{31}, capacitance and dimensions of the samples, the hydrostatic piezoelectric charge coefficient d_h and piezoelectric voltage coefficients were calculated using Equations 5.22 - 5.25.

$$d_h = d_{33} + 2d_{31} \tag{5.22}$$

$$g_{33} = \frac{d_{33}}{\epsilon_0 . \epsilon_{33}} \tag{5.23}$$

$$g_{31} = \frac{d_{31}}{\epsilon_0 . \epsilon_{33}} \tag{5.24}$$

$$g_h = \frac{d_h}{\epsilon_0 . \epsilon_{33}} \tag{5.25}$$

The error bars in all piezoelectric properties were calculated through the standard deviation of 5 samples from the same batch. Occurances where no error bars can be observed are due to the error being hidden by the datapoint and therefore show little deviation.

5.2.7 Polarisation vs Electric Field Loops

P-E loops were carried out on a Precision LC Analyser (Radiant, USA) connected to a Trek 5/80 high voltage amplifier (Trek, USA). Samples were ground down to $<500\mu$m in order to maximise the amount of available electric field whilst still retaining structural integrity, electroded as before, and placed between two contacts within a PTFE chamber. The samples were submerged in silicone oil in order to increase the dielectric breakdown voltage and prevent arcing around the edges of the pellet. All measurements were carried out at room temperature.

A high voltage AC signal of 1Hz was cycled 3 times and averaged for each sample with a pre-loop delay of 1s.

5.2.8 Strain vs Electric Field Loops

x-E loops were carried out using a high precision MTI-2100 fotonic sensor placed above the top contact within the PTFE chamber. Calibration of the fibre optic sensor was carried out before each sample was tested. As the equipment is all interconnected with the P-E loop apparatus, the x-E loops were carried out using the same electric field stimulus and data recording parameters mentioned in Section 5.2.7.

5.2.9 Dielectric Impedance Spectroscopy

Impedance spectroscopy was done using a Modulab XM MTS (Solartron Analytical, UK). Sample and thermocouple setup within the tube furnace was identical to that mentioned in Section 5.2.5. A heating rate and cooling rate was set to 2°C/min between 250°C-650°C. This heating regime was cycled twice such that the first cycle would characterise the unannealed samples and second cycle the annealed samples. A 1V sweeping AC signal from 1Hz – 1MHz was used resulting in each measurement taking approximately 20 seconds. Rapid measurements were needed in order to avoid warping of the impedance spectra from rapid changes in temperature during the measurement. 20 second measurements combined with a 2°C/min heating and cooling rate resulted in approximately 0.67°C variation between the start and end of measurement. Equivalent circuit fitting was done using ZView (Scribner Associates, USA).

5.2.10 X-Ray Photoelectron Spectroscopy

X-ray photoelectron spectroscopy was carried out using a SPECS UHV system with high performance XR50M dual Al/Al X-ray anodes and a PHOIBOS 150 analyser

(Specs, Germany). Sample surface preparation was similar to that for scanning electron microscopy outlined in Table 5.1. The anode parameters were set to 400W power and accelerating voltage of 15kV. The iris diameter was set to 60mm. Samples were stuck to aluminium plates and placed into an ultrahigh vacuum ($7x10^{-10}$Pa) and the lateral and height positions calibrated. An FG 500-A flood gun was used throughout with energy of 3eV and a filament current of 0.25μA in order to replenish any generated holes in the samples throughout data collection. Scans were taken from -5eV to 1400eV with a step size of 0.343101eV and acquisition time of 0.1s.

Data analysis was carried out using CasaXPS (Casa Software Ltd, UK). The spectrum was calibrated using the carbon 1s peak (284.4eV) and a ‘Shirley’ background setting was adopted throughout. Peak position values for valence states of each element were compared to values stated in [194]. Due to time restraints, XPS analysis was only carried out on unannealed samples.

5.3 Results & Discussion

5.3.1 X-Ray Diffraction

Figure 5.17 shows XRD patterns from 15°-60° 2Θ for all compositions. A pure perovskite consisting of *R*3*c* and *P*4*mm* space groups can be observed for samples up to x=0.02 Nb content showing no evidence of undesirable secondary phases. Ceramics containing x=>0.05 Nb show the introduction of a pyrochlore phase which increases with higher Nb content. This suggests that between x=0.02-0.05 Nb content, the solid solution solubility limit has been reached in which the perovskite becomes unstable and begins to adopt a more energetically favourable pyrochlore phase.

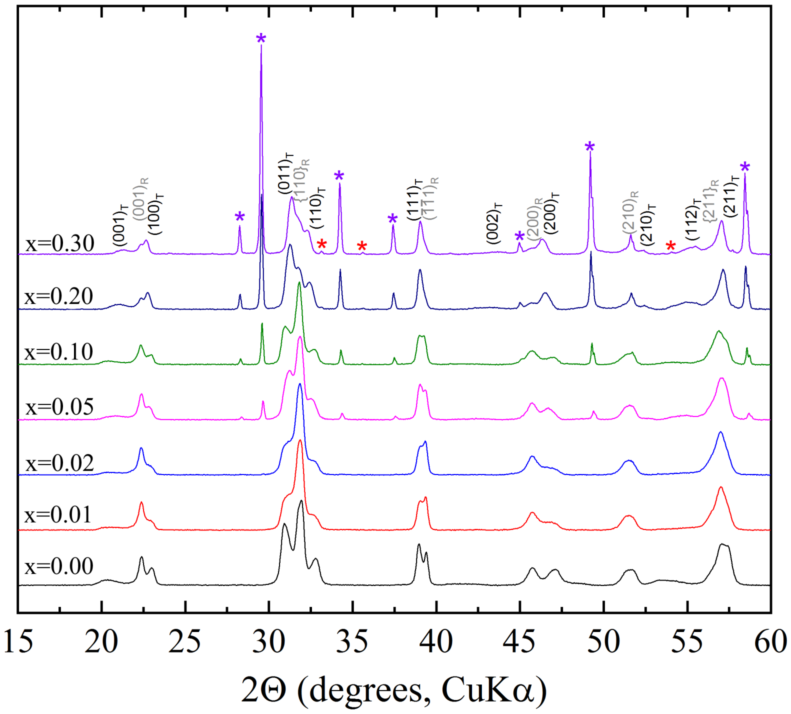

Figure 5.17: XRD scans from 15°-60° 2Θ for $0.65Bi_{1-\frac{2x}{3}}Fe_{1-x}Nb_xO_3$ - $0.35PbTiO_3$ (x=0.00, 0.01, 0.02, 0.05, 0.10, 0.20, 0.30) crushed and annealed polycrystalline ceramics. Peak indexing has been carried out using *P*4*mm* and *R*3*c* space groups in the pseudo-cubic context. Purple asterisks represent peaks originating from the pyrochlore phase and red asterisks from pure Fe_2O_3

The increasing instability of the perovskite phase with Nb content can be demonstrated by using a modified Goldschmidt tolerance factor to describe a solid solution by taking the average A-site and B-site radii based on stoichiometry. As shown in Figure 5.18, the tolerance factor diverges away from 1 implying that the stability of the perovskite decreases with increasing Nb content. This is most likely due to the difference in ionic radius of the host Fe^{3+} (0.55Å [85]) ions and the foreign Nb^{5+} (0.64Å [85]) ion. The larger size of the Nb^{5+} means that the ion cannot comfortably occupy the B-site, disrupting the local chemistry and crystallography and increasing instability.

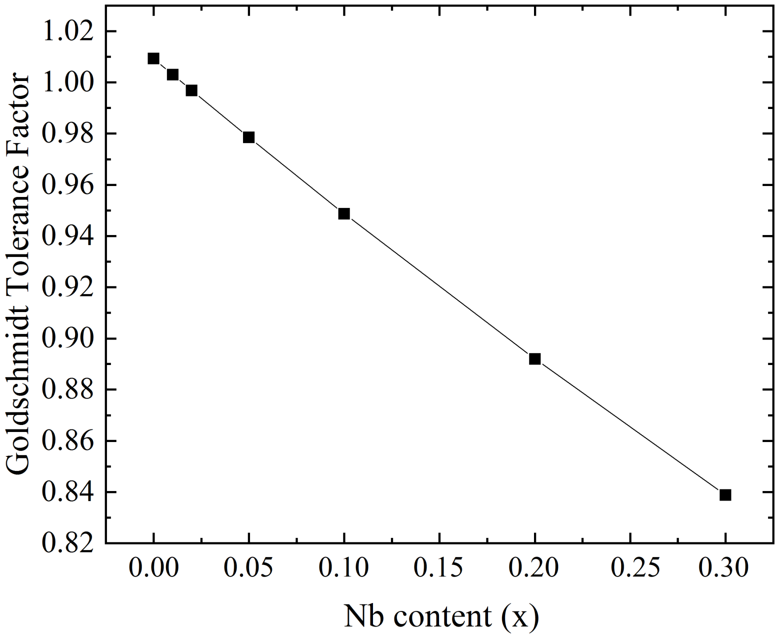

Figure 5.18: Goldschmidt tolerance factor vs Nb content for $0.65Bi_{1-2x/3}Fe_{1-x}Nb_xO_3$-$0.35PbTiO_3$ (x=0.00, 0.01, 0.02, 0.05, 0.10, 0.20, 0.30)

Another explanation for this instability is the increasing amount of bismuth vacancies as a function of Nb content. Whilst the formation of undesirable pyrochlore phases are often attributed to excessive loss of volatiles during processing [195–198], the purposeful removal of bismuth ions for charge balance in this study and the subsequent creation of A-site vacancies also disrupts the perovskite stability to a point in which a pyrochlore phase is more favourable.

By undergoing a search and match profile, ICDD files determined that the most appropriate match for the undesirable pyrochlore phase is $Pb_{1.7}Ti_{0.8}Nb_{1.2}O_{6.3}$. In reality it is more likely to consist of many different formulations with a mixture of all atomic components with Pb and Bi occupying the A-sites and Fe, Ti and Nb occupying B-sites, similar to the perovskite phase. Conventional wisdom suggests that Pb will dominate the A-sites of the pyrochlore phase as at high Nb contents, a significant amount of bismuth is stoichiometrically removed for charge compensation.

At x=0.20 and x=0.30 Nb, a small quantity of Fe_2O_3 becomes present suggesting that in heavily doped samples, another solid solubility limit is reached in which reagent segregation occurs.

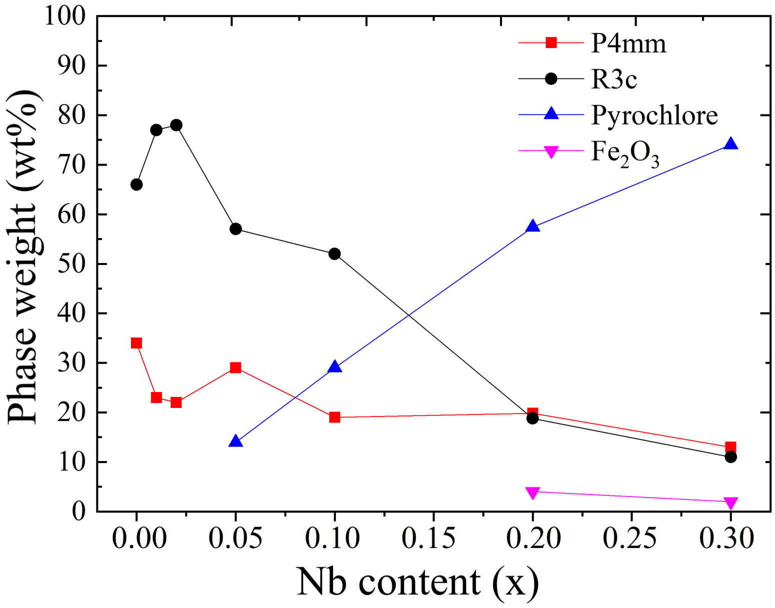

Figure 5.19: Relative phase weights as a function of Nb content calculated semi-quantitively using HighScore Plus and ICDD files for *P4mm* BFPT (ICDD:01-079-9997), *R3c* BFPT (ICDD: 01-082-9790), pyrochlore (ICDD: 00-066-0193) and pure iron oxide (ICDD: 01-089-0596)

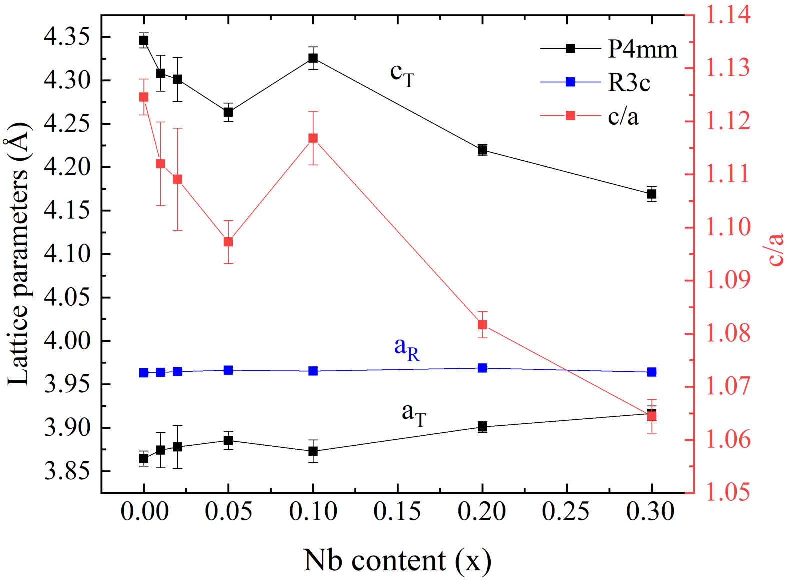

Figure 5.20: Rhombohedral lattice parameters, tetragonal lattice parameters and the tetragonality (c/a) as a function of niobium content

Figure 5.20 shows tetragonal and rhombohedral lattice parameters and tetragonality with Nb content. From x=0.00-0.05 the tetragonality reduces from approximately 12.5% to 9.9% which is predominantly dictated by the decrease in c_T. This is most likely due to the introduction of the foreign Nb^{5+} ion and the discrepancy in ionic size. It is possible that the large Nb ion may disrupt the A-O and B-O covalence which is responsible for the large tetragonality in undoped BFPT. At x=0.10, there is a large increase in the tetragonality and c_T-axis lattice parameter and a small decrease in the a_T-axis lattice parameter. Although more foreign Nb ions are present, this trend is more likely linked to an increase in grain size as a result of a higher sintering temperature. As mentioned previously, the tetragonality of $BiFeO_3$-$PbTiO_3$ solid solution is closely related to the grain size with larger grains producing a more tetragonally pure material [169]. From x=0.10-0.30, the tetragonality continues to reduce down to 6.5%. Again this is most likely due to the decrease in A-O covalence due to the increase in concentration of A-site vacancies and also the B-O bonding. The lattice parameters of the rhombohedral phase (a_R) remain almost constant over all Nb contents.

5.3.2 Scanning Electron Microscopy

The microstructure of each composition was analysed using both secondary electrons and backscattered electron imaging. Average grain size and perovskite-pyrochlore ratios were determined only using backscattered images shown in Figure 5.21 as these provided more clearly defined grain boundaries using ImageJ (National Institutes of Health, USA).

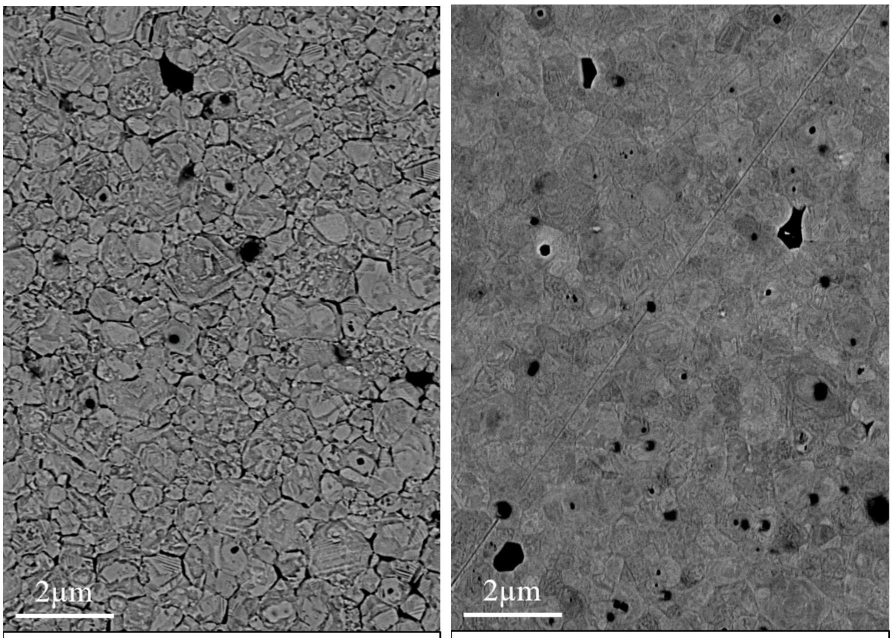

(a) x=0.00 BSE 5kV

(b) x=0.01 BSE 5kV

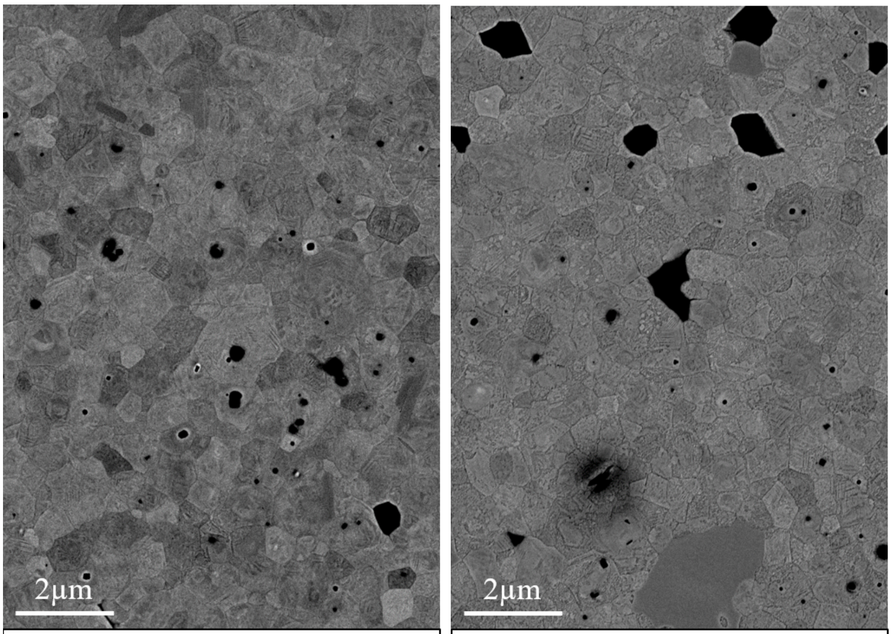

(c) x=0.02 BSE 5kV

(d) x=0.05 BSE 5kV

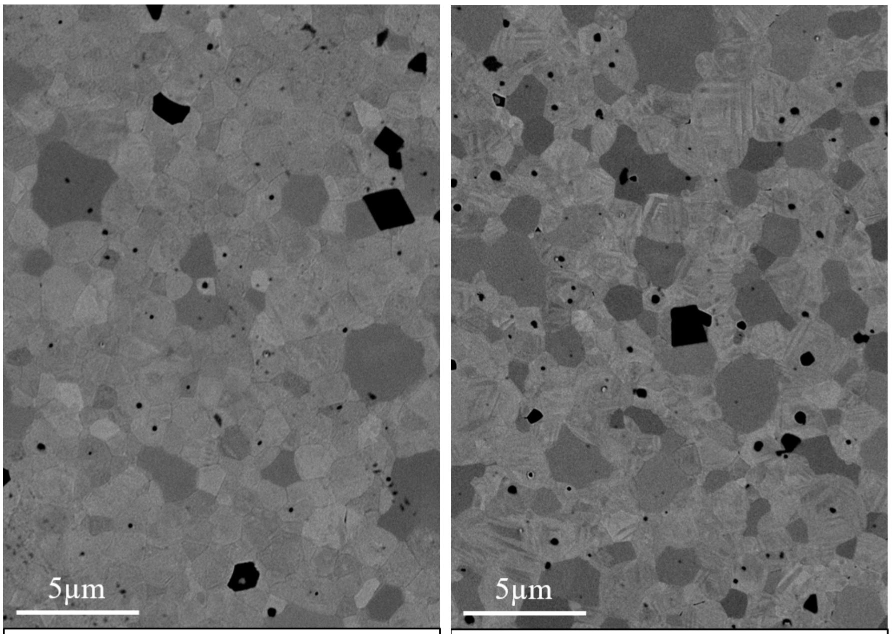

(e) x=0.10 BSE 5kV

(f) x=0.20 BSE 5kV

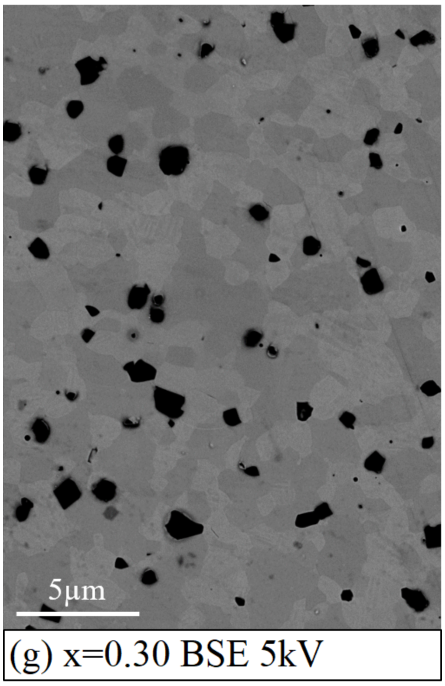

Figure 5.21: Backscattered electron images for x=(a) 0.00, (b) 0.01, (c) 0.02, (d) 0.05, (e) 0.10, (f) 0.20, and (g) 0.30 Nb:BFPT65 polycrystalline ceramics with 5kV accelerating voltage

Figure 5.21 a) – g) show the general microstructure of polished polycrystalline ceramics that have been etched for 10 seconds. Initial observations of low Nb containing samples show dense polycrystalline ceramics with minimal porosity. Despite the enormous tetragonality of $BiFeO_3$-$PbTiO_3$, no micro or macro cracking is observed for any samples highlighting the importance of a slow cooling program during fabrication. The images also highlight the suitability of the polishing route with very few scratches observed and even showing ferroelectric domain structures.

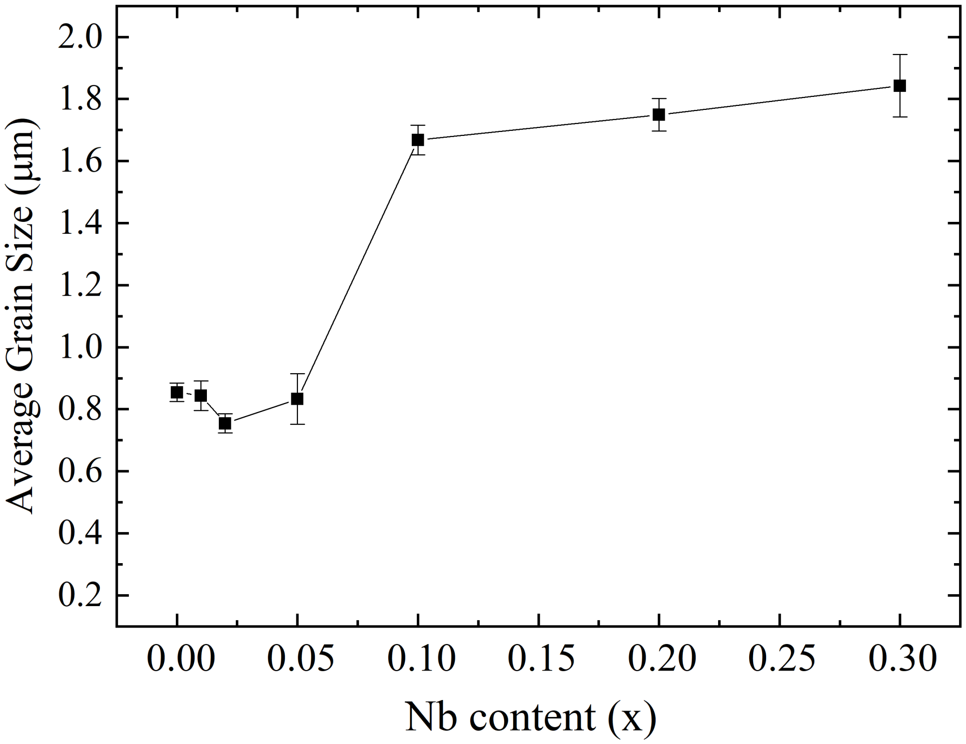

Figure 5.22: Average grain size vs Nb content

Figure 5.22 shows the average grain size calculated using the interception method as a function of Nb content. Initially the average grain size is measured to be approximately 0.85μm. This is larger than the grain sizes reported for undoped BFPT65 by Stevenson [190], however the discrepancy is due to the different methods of milling. In this study, powders were ball milled for 24 hours using 1cm sized YTZ media whereas Stevenson used attrition milling which has been shown to result in smaller grains due to the increased agitation of the powder and milling media resulting in smaller initial powders [190].

For x=0.01, no significant change in grain size can be observed with average grain size decreasing only slightly to 0.83μm, and at x=0.02 Nb content the grain size drops again to 0.75μm before increasing again to 0.8μm at x=0.05. For samples containing x=0.10, 0.20 and 0.30 Nb, the grain size increases to 1.7μm, 1.72μm and 1.8μm, respectively. Similarly to the tetragonality, this dramatic increase is most likely due to the increase in the sintering temperature used during fabrication. When the sintering temperature is increased, it provides more thermal energy to the ions and increases mobility, material transfer to the grain boundary is increased and therefore grain size also increases.

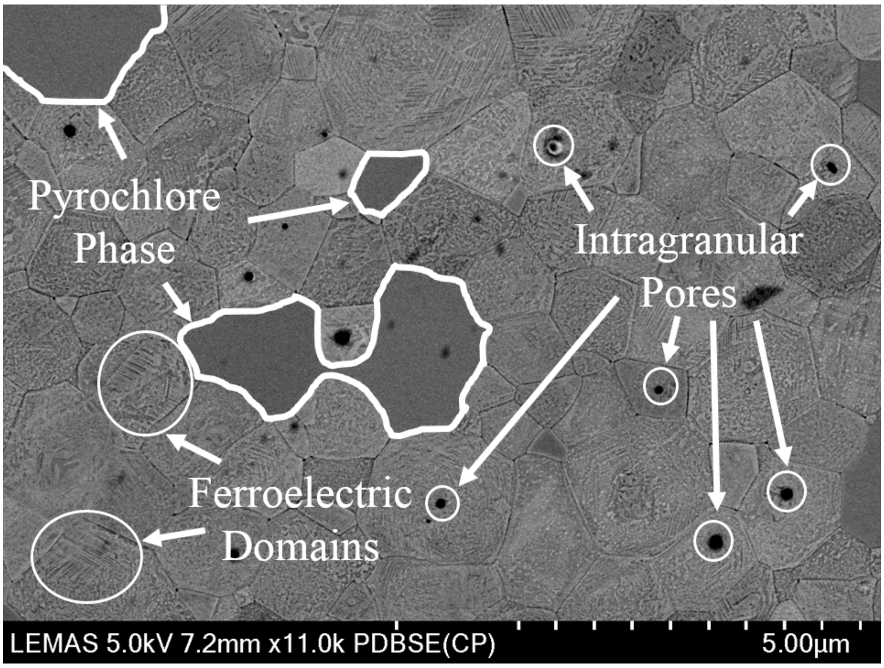

Figure 5.23: 11000x magnification 5kV BSE image of x=0.10 Nb:BFPT65. Features have been highlighted and annotated such as regions of pyrochlore phase showing no ferroelectric domain texturing, ferroelectric domains showing a typical herringbone structure and intragranular pores implying a core-shell structure

Figure 5.23 shows a 5kV BSE image of x=0.10 Nb:BFPT65 and is annotated to illustrate some SEM features observed in this study. One of these characteristics observed with the highly doped samples is the increasing presence of non-textured areas containing few grain boundaries between them and may represent the pyrochlore phase due to the lack of ferroelectric domains within the regions. Furthermore XRD showed that this pyrochlore phase becomes more prominent with increasing Nb content, a characteristic that is also observed with the non-textured regions. Figure 5.19 compares the semi-quantitative phase weight of pyrochlore phase calculated by HighScore Plus software and the area size of the non-textured regions using ImageJ. A clear correlation can be observed suggesting that the non-textured regions are indeed the pyrochlore phase. The difference in pyrochlore percentage may stem from the fact that XRD was carried out on crushed and annealed powders and is more representative of the bulk material, whereas the SEM analysis was carried out on a small area of the sample at the surface and may not necessarily represent the bulk material.

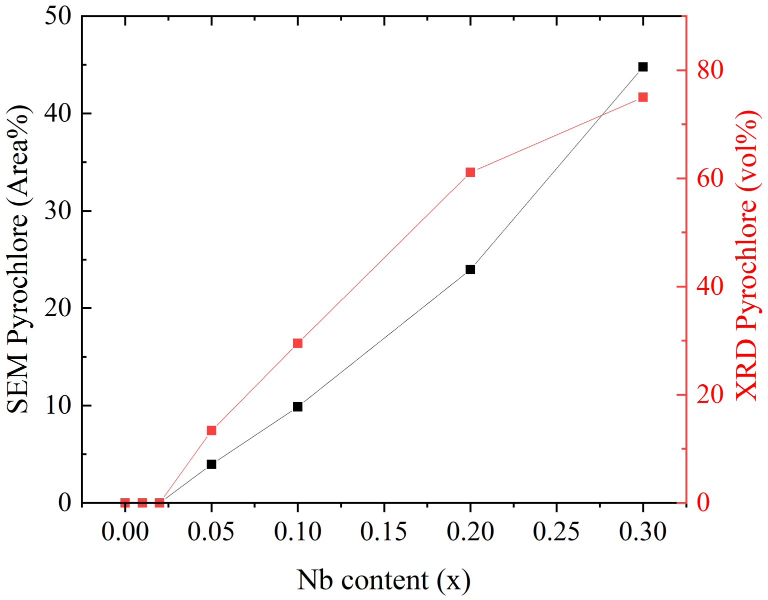

Figure 5.24: Relative presence of pyrochlore calculated from SEM using area mapping function in ImageJ software and XRD using semi-quantitative phase weight data

An interesting observation is the presence of small pores within the grains. These are shown in Figure 5.23 and imply the presence of a core-shell structure in which the chemistry of the centre of the grain (core) is different from the grain boundary (shell). This phenomenon occurs due to the segregation of ions and defects such that the concentration at the grain and grain boundary are different. The fact that pores are present instead of the core is most likely due to the aggressiveness of the etching process which appears to have etched away the centre material. The observation of a core-shell structure is useful for impedance spectroscopy discussed in Section 5.3.5.1, in which the appropriate model equivalent circuit is heavily influenced by these observations.

5.3.3 Permittivity vs Temperature

Figures 5.25 (a)-(g) show the relative permittivity at 100kHz as a function of temperature for all unpoled samples when both unannealed and annealed. For pure BFPT an initial bump is observed at approximately 450°C which may be attributed to the relaxation of oxygen vacancies before increasing to maximum relative permittivity at 672°C. For the annealed sample, a similar trend can be observed, however the temperature at maximum relative permittivity is below that of the unannealed sample.

For all Nb containing samples there is no coherence between the relative permittivity trend before and after annealing. Unannealed x=0.01 Nb-doped samples (Figure 5.25(b)) show that the initial bump at approximately 450°C for undoped BFPT has almost disappeared implying the elimination of oxygen vacancies. The relative permittivity then gradually increases towards T_C where a maximum value of approximately 6000 is measured at approximately 650°C. Above T_C a small hump can be observed. Although this feature implies that the relative permittivity does not follow Curie-Weiss law and therefore exhibits relaxor-like behaviour, it may be more likely that the observed trend is a result of large conductivity at high temperature which is more obvious when looking at the tanδ. For annealed, x=0.01 samples another bump may be observed at approximately 500°C, which again may be a result of defect relaxation. Similar observations can be made for x=0.02 (Figure 5.25(c)), x=0.05 (Figure 5.25(d)) and x=0.10 (Figure 5.25(e)) samples in which annealed samples show a characteristic hump between 450°C and 500°C.

For x=0.20 Nb-doped samples (Figure 5.25(f)), the opposite trend can be observed in the unannealed state where the relative permittivity shows two distinct peaks, the first again most likely representing a relaxation of defects and the second representing the Curie temperature. In the annealed state a single clear, broad peak is observed. This implies that there is a bimodal distribution of defects which when in an unannealed state have two distinct relaxation temperatures, however once annealed are more evenly distributed resulting in a more coherent relaxation temperature.

Finally for x=0.30 Nb-doped samples (Figure 5.25(g)), a single peak is observed in both unannealed and annealed state although the latter shows an increase in both the intensity and Curie temperature.

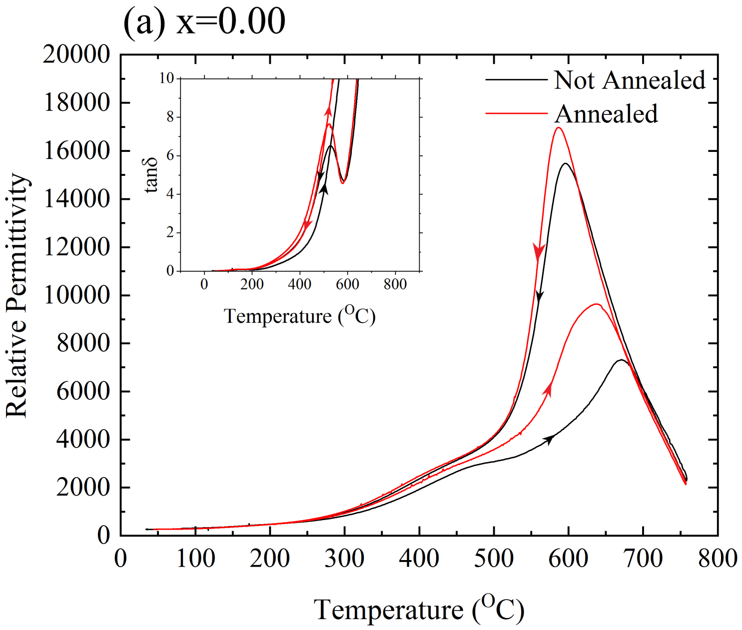

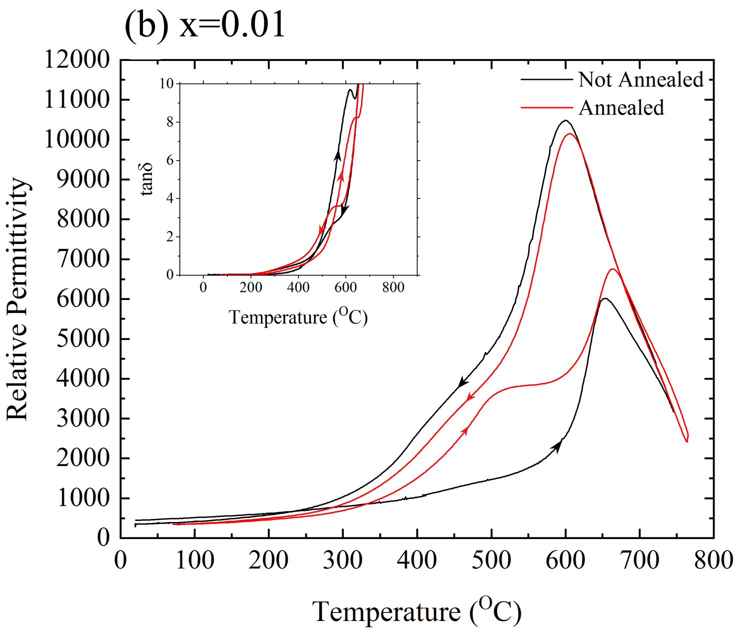
(b) x=0.01
Relative Permittivity
0
1000
2000
3000
4000
5000
6000
7000
8000
9000
10000
11000
12000
0
100
200
300
400
500
600
700
800
Temperature (^OC)
Not Annealed
Annealed
tanδ
0
2
4
6
8
10
0
200
400
600
800
Temperature (^OC)

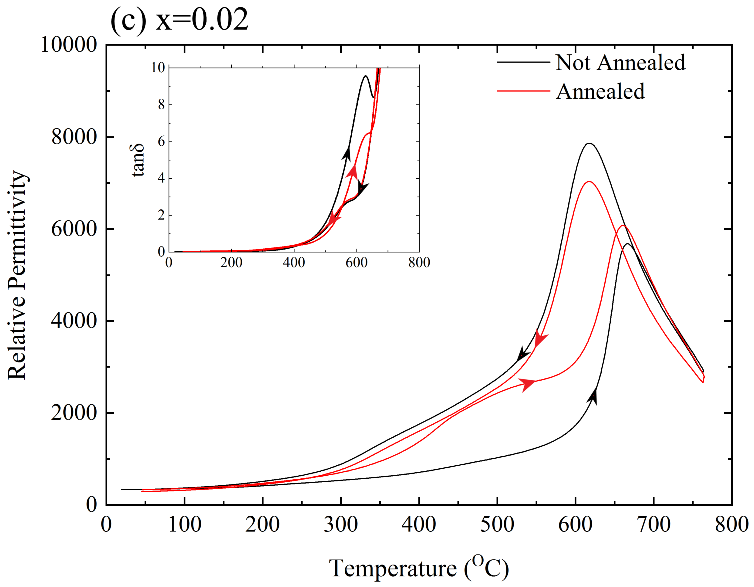
(c) x=0.02
Relative Permittivity
0
2000
4000
6000
8000
10000
0
100
200
300
400
500
600
700
800
Temperature (^OC)
Not Annealed
Annealed
tanδ
0
2
4
6
8
10
0
200
400
600
800

(d) x=0.05

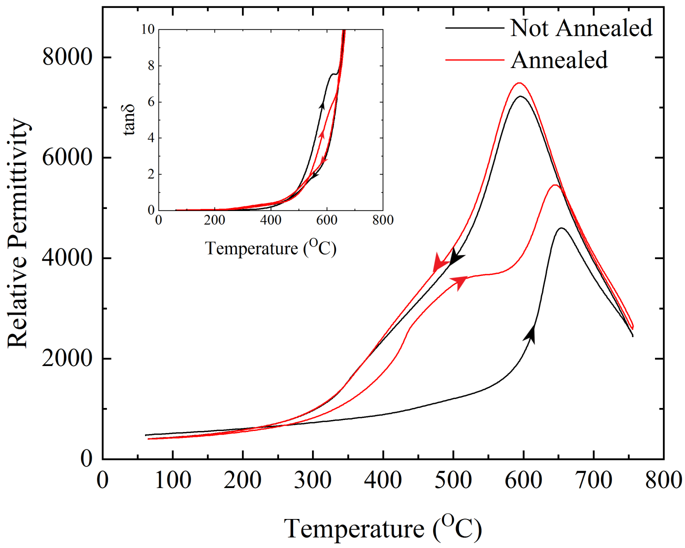
Not Annealed
Annealed
Relative Permittivity
0
2000
4000
6000
8000
0
100
200
300
400
500
600
700
800
Temperature (OC)
tanδ
0
2
4
6
8
10
0
200
400
600
800
Temperature (OC)

(e) x=0.10

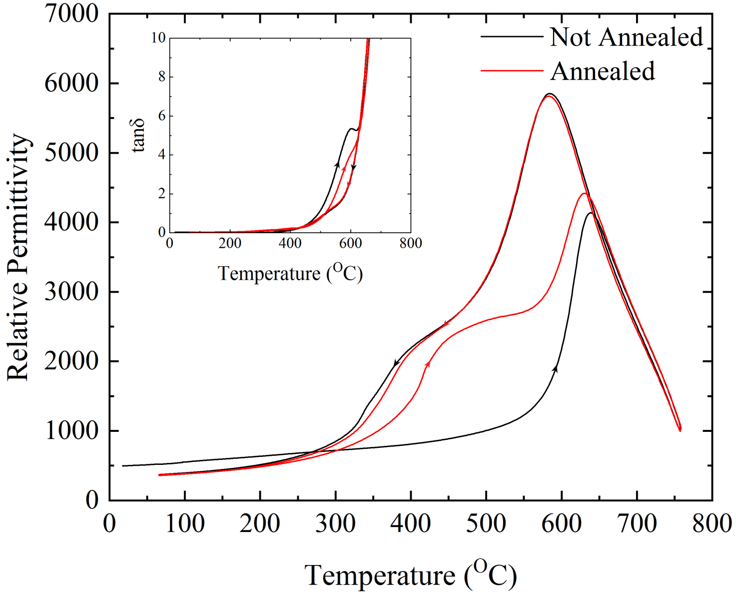
Not Annealed
Annealed
Relative Permittivity
0
1000
2000
3000
4000
5000
6000
7000
0
100
200
300
400
500
600
700
800
Temperature (OC)
tanδ
0
2
4
6
8
10
0
200
400
600
800
Temperature (OC)

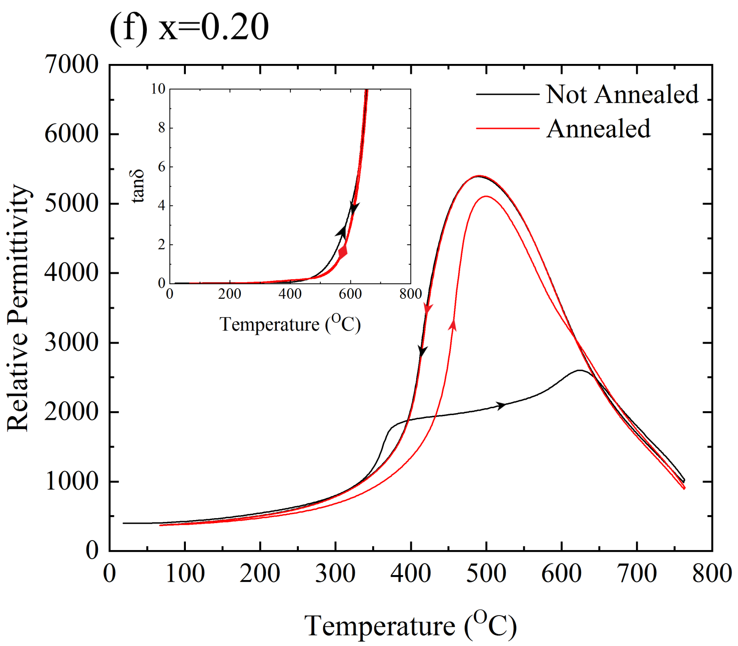

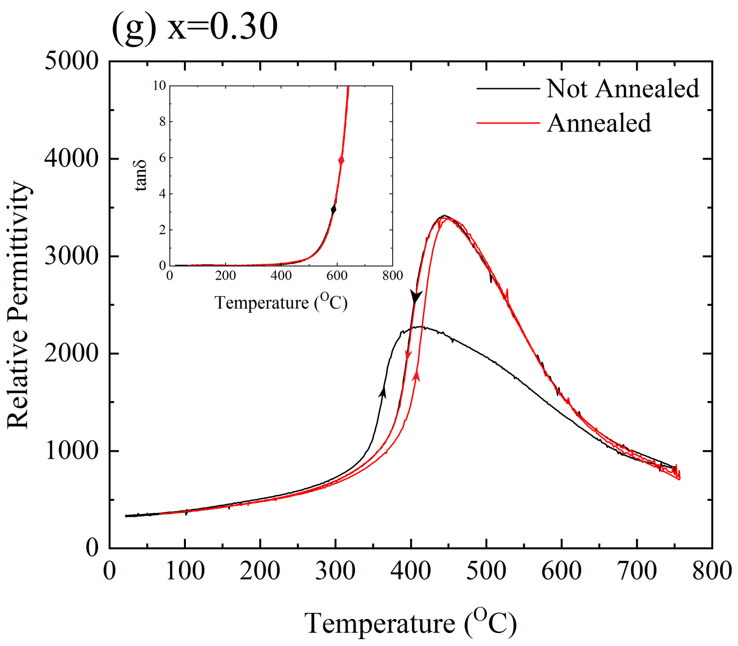

Figure 5.25: Permittivity vs temperature at 100kHz for x=(a) 0.00, (b) 0.01, (c) 0.02, (d) 0.05, (e) 0.10, (f) 0.20 and (g) 0.30 unpoled Nb:BFPT65. The black line represents scans of unannealed samples and red line represents scans of annealed samples

Figure 5.26 shows the temperature of maximum permittivity in degrees Celsius as a function of Nb content for both annealed and unannealed samples. In both cases, the introduction of Nb generally results in this value decreasing. Similarly to the observation in tetragonality as a function of Nb content (Figure 5.20), this may be due to the break in periodicity of the crystallographic lattice which may weaken the A-O and B-O covalence and therefore reduce the amount of thermal energy required to transform from a non-centrosymmetric to a centrosymmetric structure.

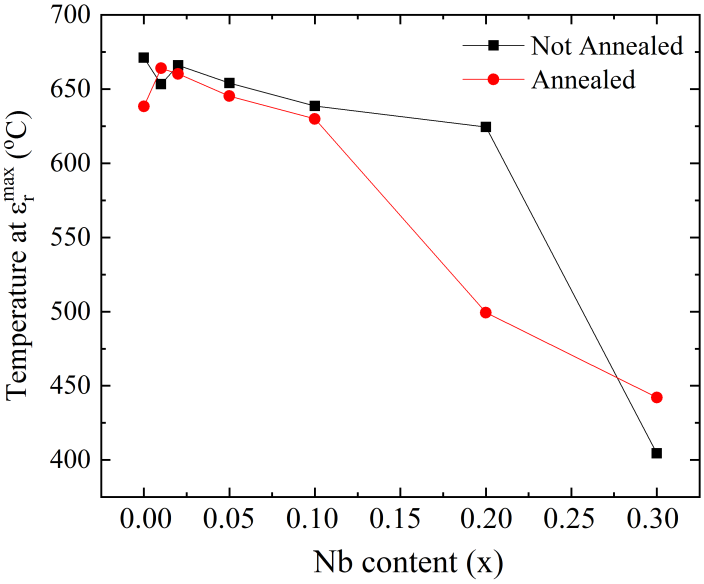

Figure 5.26: Temperature at maximum permittivity vs Nb content for unannealed (■) and annealed (●) samples

5.3.4 Berlincourt Measurements

Motivated by the observations in Section 5.3.3 that annealing has a significant effect on the relative permittivity v temperature scans, the piezoelectric properties of Nb-doped BFPT65 polycrystalline samples were measured before and after annealing using the Berlincourt method.

Figure 5.27 shows the relative permittivity as a function of Nb content before and after annealing. The lowest relative permittivity is measured for undoped BFPT which may be attributed to the inability to store charge due to a high concentration of free charge carriers and vacancies. x=0.01 Nb improves the dielectric performance with the relative permittivity increasing from 280 for undoped BFPT to 458. The permittivity then reduces to 411 for x= 0.02 Nb-doped samples and then increases again to 477 and 535 for x=0.05 and x=0.10, respectively. Whilst the reason for the decrease in relative permittivity at x=0.02 is unclear, the general increase from x=0.00-0.10 implies a reduction in free carrier density and oxygen vacancy concentration both of which would result in reduced permittivity. The significant reduction in relative permittivity for x=0.20 and x=0.30 may be due to the presence of a pyrochlore phase and/or the high number of A-site vacancies. Once annealed the permittivity reduces for x=0.00, 0.02, 0.05, 0.10 and 0.20, remains unchanged for x=0.01 and increases for x=0.30. Although the values for the relative permittivity vary before and after annealing the general trend as a function of Nb content is similar.

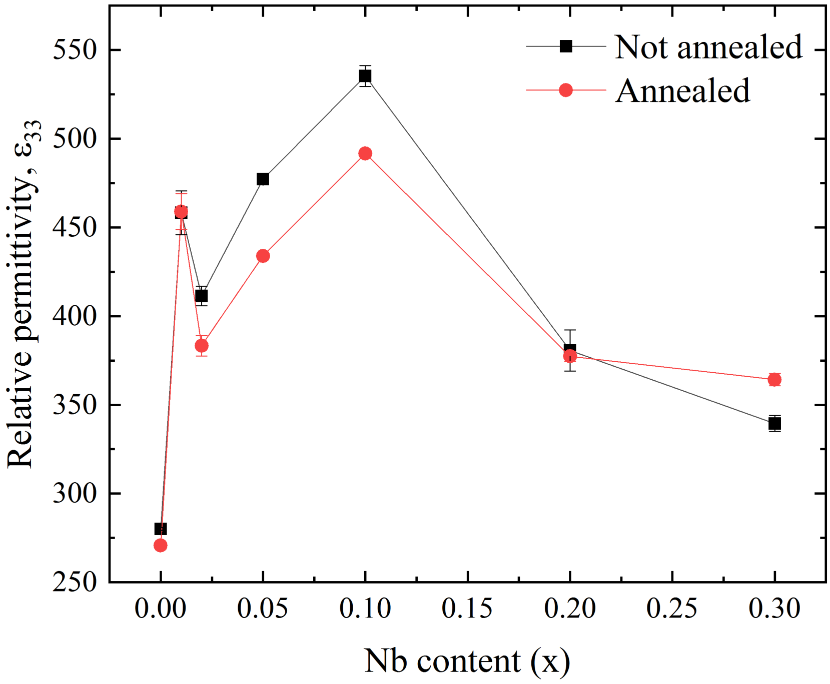

Figure 5.27: Relative permittivity values as a function of Nb content for unannealed (■) and annealed (●) samples

Figure 5.28 shows the dissipation factor (tanδ) as a function of Nb content before and after annealing. The general trend shows an initial decrease in losses for x=0.01 which increases again for higher Nb containing samples. The initial drop in tanδ could be attributed to the elimination of oxygen vacancies as evidenced in the permittivity v temperature graphs. The gradual increase in tanδ with increasing Nb content can either be related to the increasing number of vacancies such as bismuth and oxygen vacancies contributing to a higher conductivity or as evidence for lossy mechanisms such as domain wall motion increasing which implies higher piezoelectric properties. Similarly to the relative permittivity once annealed the general trend remains, however the tanδ increases for x=0.01, 0.02, 0.05, 0.10 and 0.20 after annealing again implying an increase in domain wall motion [199].

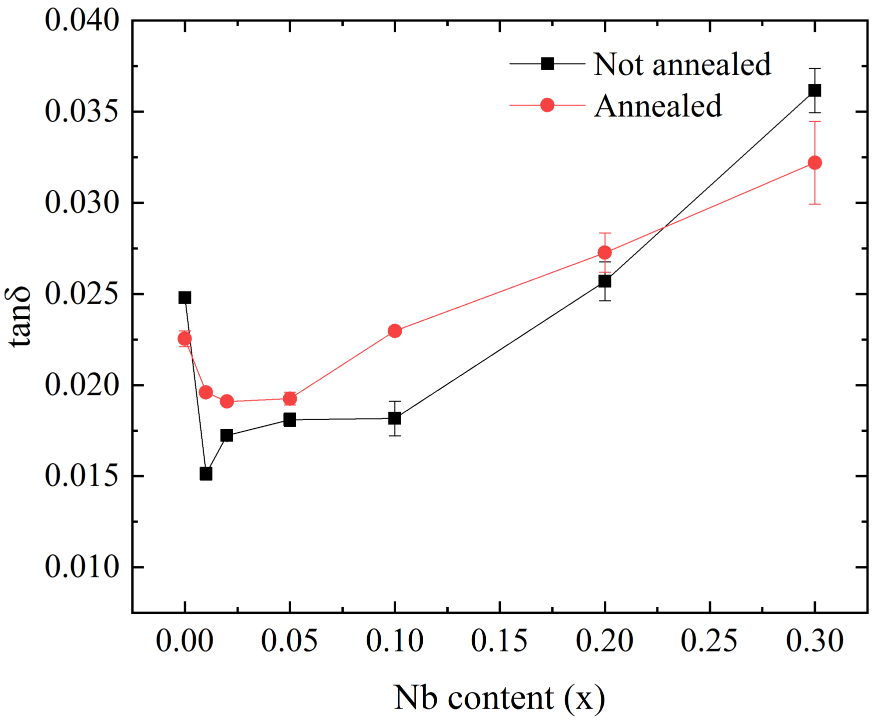

Figure 5.28: tanδ values as a function of Nb content for unannealed (■) and annealed (●) samples

Figure 5.29 shows the d_{33} as a function of Nb content for unannealed and annealed samples. Undoped BFPT65 is observed to have a d_{33} of 42.1pC/N. For unannealed samples, the d_{33} significantly drops for samples containing x<0.20 Nb with values ranging from a maximum of 17.6pC/N for x=0.02 Nb to a minimum of 2.6pC/N for x=0.10. This is contrary to previously reported studies of niobium doping in which the d_{33} increases due to the reduction in the concentration of oxygen vacancies, which in turn reduces the concentration of dipoles which can inhibit domain wall mobility and therefore the piezoelectric activity [200–203]. For samples containing x=0.20, the d_{33} increases to approximately the same as for pure $BiFeO_3-PbTiO_3$ and then decreases again due to the increasing concentration of non-piezoelectric phase in the system as shown by XRD studies in Section 5.3.1.

Once annealed, samples exhibit greater piezoelectric activity. Excluding x=0.01 Nb, a more conventional trend for Nb-doped ferroelectrics is observed in which the d_{33} increases from 46.3pC/N for undoped BFPT to 82.0pC/N for samples containing x=0.05 Nb. Above x=0.05 the d_{33} decreases in an almost linear manner. As mentioned previously, this is most likely due to the increasing concentration of the non-piezoelectric pyrochlore phase at high Nb contents.

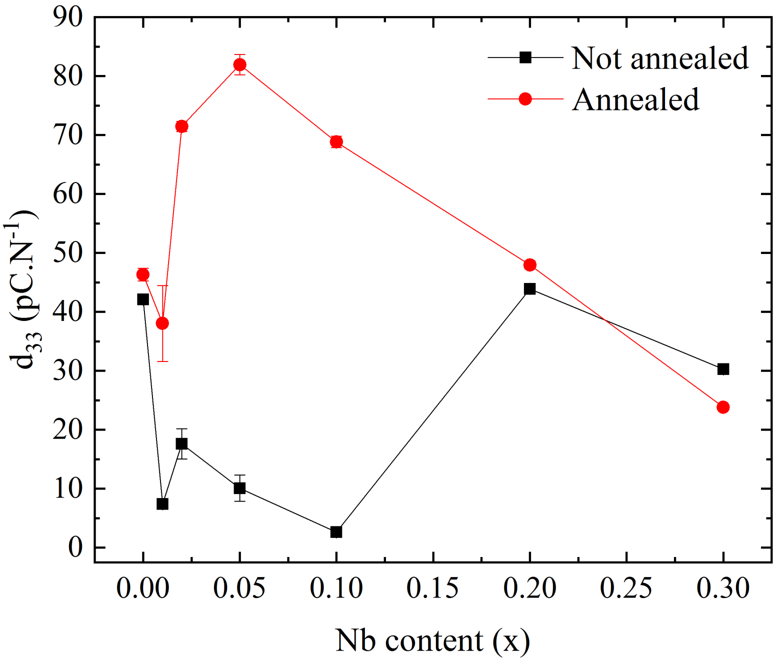

Figure 5.29: Piezoelectric d_{33} values as a function of Nb content for unannealed (■) and annealed (●) samples

Figure 5.30 shows the $-d_{31}$ values also measured by the Berlincourt method using rectangular plates. Similarly to the d_{33} measurements, unannealed samples show low values for the piezoelectric coefficient which is indicative of hard acceptor-doping with the -d_{31} decreasing from 9.9pC/N for undoped samples to 1.50, 3.2, 1.8 and 0.20pC/N for x=0.01, 0.02, 0.05, and 0.10 samples, respectively. The $|d_{31}|$ then increases to 7.2pC/N for x=0.20 and then reduces to 5.9pC/N at x=0.30, again due the increase in concentration of the non-piezoelectric pyrochlore phase. After annealing the $|d_{31}|$ shows significant improvement compared to its virgin state, in particular x=0.10 samples where the $|d_{31}|$ increases by more than 40 times.

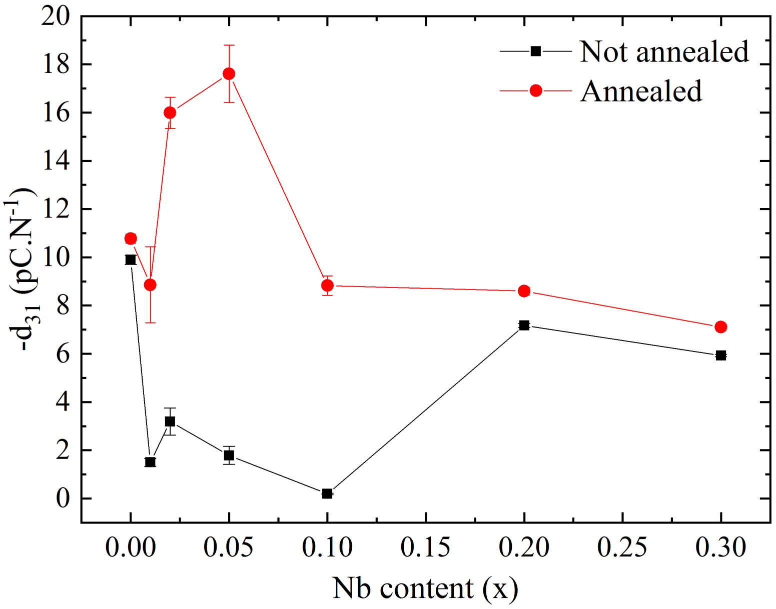

Figure 5.30: Piezoelectric $-d_{31}$ values as a function of Nb content for unannealed (■) and annealed (●) samples

The hydrostatic piezoelectric coefficient ($d_h = d_{33} + 2d_{31}$) is shown in Figure 5.31 and represents the piezoelectric response of a material when in an immersed surrounding. Unsurprisingly the results follow a similar trend to those shown in Figure 5.29 and Figure 5.30. It is interesting to note that although the d_{33} and d_{31} measurements show that the piezoelectric d_{33} and $|d_{31}|$ coefficients of commercially dominant PZT far exceeds that of the materials mentioned in this study, the hydrostatic coefficients of x=0.05 (46.7pC/N) and x=0.10 (51.2pC/N) Nb-doped BFPT65 are comparable to that of PZT401 (51.0pC/N [175]). This is because PZT has significant coupling between the 33 mode and 31 mode, therefore the d_{31} approaches $d_{33}/2$ and thus d_h approaches 0. For materials such as modified lead titanate [101] and Nb-doped BFPT65 considered here, the d_{31} is significantly less than $d_{33}/2$ and therefore the d_h is comparable to material considered to possess larger piezoelectric activity. This large difference between the $|d_{31}|$ and $d_{33}/2$ implies significant intrinsic decoupling between the 33 and 31 modes.

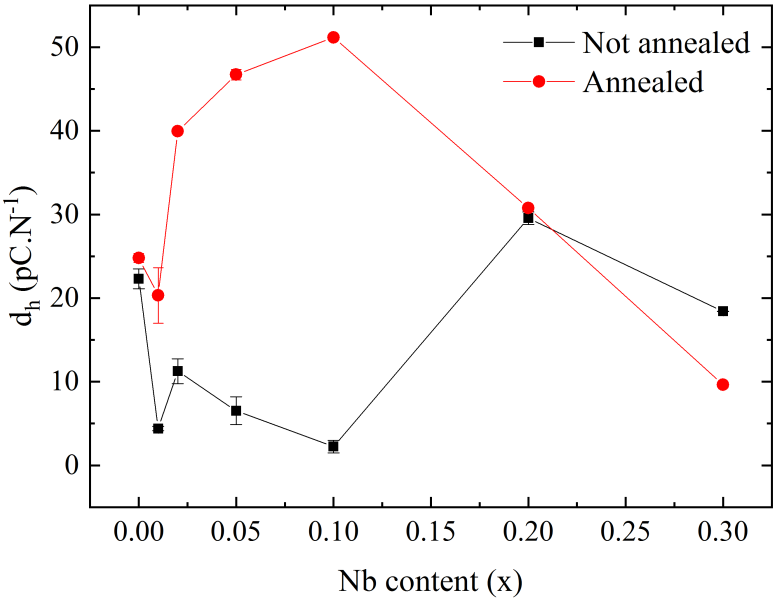

Figure 5.31: Piezoelectric d_h values as a function of niobium content for unannealed (■) and annealed (●) samples

Figure 5.32 shows the piezovoltage g_{33} ($=d_{33}/\epsilon_r\epsilon_0$) coefficient as a function of Nb content for annealed and unannealed samples showing almost identical trends to that of the charge coefficients. For undoped, unannealed 0.65$BiFeO_3$-0.35$PbTiO_3$ a g_{33} of 17.0×10^{-3}Vm/N is measured which decreases to 1.8×10^{-3}Vm/N for x=0.01 Nb. The measured g_{33} for unannealed x=0.02, 0.05, 0.10, 0.20 and 0.30 samples are 4.9, 2.4, 0.6, 13.0 and 10.1×10^{-3}Vm/N. respectively. Once annealed the g_{33} increases for all samples excluding x=0.30 measuring 19.3, 9.4, 21.1, 21.3, 15.8, 14.4, 7.4×10^{-3}Vm/N for x=0.00, 0.01, 0.02, 0.05, 0.10, 0.20 and 0.30, respectively. Whilst Figures 5.29 - 5.31 illustrated that undoped BFPT possessed lower values than many of the doped and annealed samples, the g_{33} of undoped BFPT is significantly larger than unannealed doped samples and comparable to annealed x=0.02 and x=0.05 samples. This is due to the low values for the capacitance and subsequently the relative permittivity compared to Nb-doped samples.

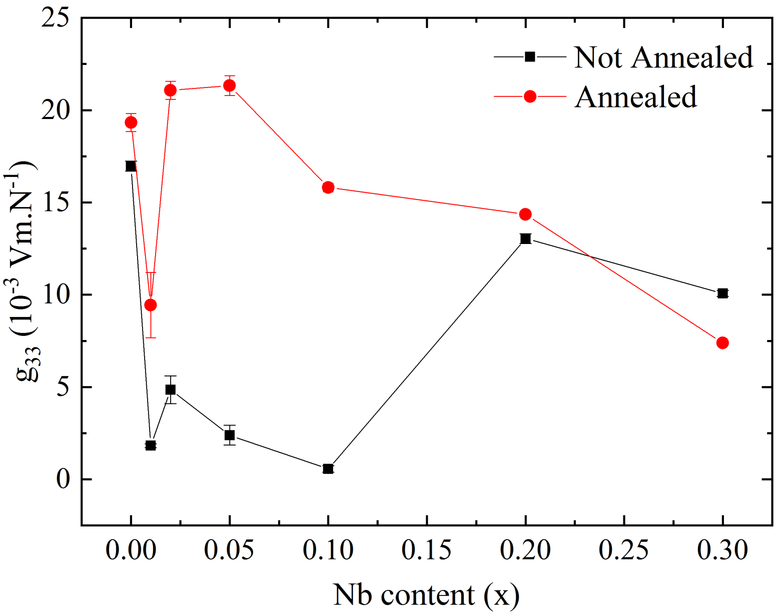

Figure 5.32: Piezoelectric g_{33} values as a function of Nb content for unannealed (■) and annealed (●) samples

Figure 5.33 shows values for -g_{31} ($=d_{31}/\epsilon_r\epsilon_0$) for each Nb doping regime and for annealed and unannealed samples and almost identical trends are observed to that of g_{33} (Figure 5.32). Whilst Figure 5.32 showed that values for the g_{33} coefficient in PZT401 (25.5×10^{-3} Vm/N [175]) are only slightly larger than undoped BFPT and x=0.02 and x=0.05 doped samples, Figure 5.33 shows that the $|g_{31}|$ of Nb-doped BFPT65 is much lower than that of PZT401 (10.7×10^{-3}Vm/N [175]) even after annealing. As the main determining factor of the value of the $|g_{31}|$ is the $|d_{31}|$, the reason for such low values is similar to the charge coefficient in that PZT401 has high coupling between the 33 and 31 modes resulting in large $|d_{31}|$ values whereas in doped and undoped BFPT, the coupling is very low and therefore low $|d_{31}|$ and $|g_{31}|$ values are measured.

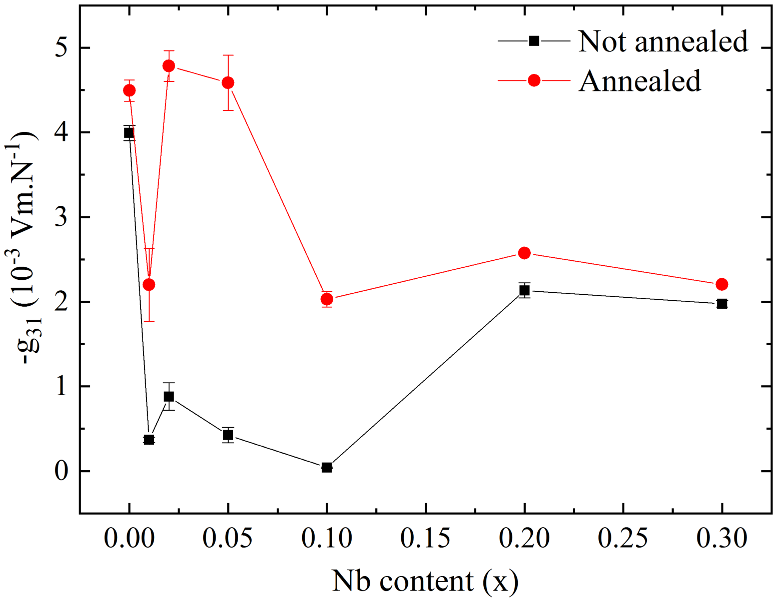

Figure 5.33: Piezoelectric $-g_{31}$ values as a function of niobium content for unannealed (■) and annealed (●) samples

Figure 5.34 shows the hydrostatic g_h coefficient as a function of Nb content for annealed and unannealed samples. Unannealed samples measured g_h values of 9.4, 1.1, 1.5, 1.5, 0.5, 8.8 and 6.1$\times 10^{-3}$Vm/N for x=0.00, 0.01, 0.02, 0.05, 0.10, 0.20 and 0.30, respectively. Similarly to g_{33}, the g_h of all samples excluding x=0.30 increase once annealed to 10.3, 5.0, 12.0, 12.2, 11.8, 9.2, 3.0$\times 10^{-3}$Vm/N for x=0.00, 0.01, 0.02, 0.05, 0.10, 0.20 and 0.30, respectively.

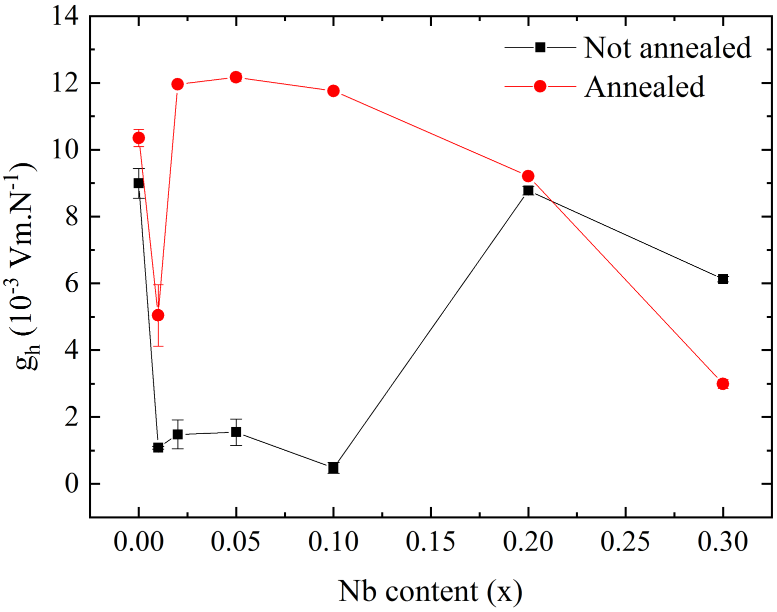

Figure 5.34: Piezoelectric g_h values as a function of Nb content for unannealed (■) and annealed (●) samples

A common occurrence in all piezoelectric coefficient measurements is the initial decrease in piezoelectric activity from undoped to x=0.01 Nb-doped samples. Whilst other samples show enhancement of the d_{33} after annealing resulting in piezoelectric activity exceeding that of pure BFPT, x=0.01 doped samples do not achieve values greater than undoped samples even after annealing. Although the reason for this phenomenon cannot be explained using Berlincourt measurements or permittivity vs. temperature plots, Section 5.3.7 shows that this behaviour is a result of high Ti^{3+} and oxygen vacancy concentration which form domain wall pinning dipoles and subsequently reduce the piezoelectric activity.

Another occurrence in these measurements is the enhancement of piezoelectric activity after annealing. It is interesting to note that the greatest enhancement of piezoelectric activity is observed in the defective perovskite states. Although the undoped BFPT samples will naturally contain A-site vacancies and oxygen vacancies due to the manner of high temperature fabrication, they are ideally defect-free for the sake of this study as the stoichiometry has been calculated in order to occupy all sites. Samples doped with x=0.20 and x=0.30 Nb could also arguably be considered defect free as they have transformed into a different structure in order to compensate for the defects. Alternatively the stoichiometry of x=0.01, 0.02, 0.05 and 0.10 samples have been calculated in order to force the formation of bismuth vacancies with the aim of controlling the introduction of defects into the lattice. This significant improvement in chemically defective samples and relatively unchanged performance of non-defective samples implies that the enhancement of the piezoelectric properties could be a result of a defect related phenomena as opposed to crystallographic or microstructural. Although aliovalent doping of ferroelectric materials has been a useful tool that has been utilised for decades in the tuneability of electrical and mechanical properties, understanding the dynamics of these defects through further heat treating in $BiFeO_3$-$PbTiO_3$ polycrystalline ceramics in this study, may aid the improved performance of other solid solutions.

Although the main objective of this chapter is to understand the conduction mechanisms in $BiFeO_3$-$PbTiO_3$ polycrystalline ceramics and attempt to reduce the conductivity through Nb doping, it is useful to compare the piezoelectric performance of materials in this study to others for relevance. Table 5.3 shows the piezoelectric and dielectric properties of Nb-doped BFPT65 alongside lead zirconate titanate and modified lead titanate. As mentioned earlier, the 33 and 31 piezoelectric coefficients and the hydrostatic charge coefficient for undoped and Nb-doped BFPT65 polycrystalline ceramics are inferior to that of commercially available hard PZT. However the hydrostatic voltage coefficient is superior with annealed x=0.05 samples exhibiting values almost three times larger than PZT401 and almost 25% greater than PZT807. This is attributed to the natural decoupling of these two modes due to the large tetragonality which results in low 31 values which results in a larger g_h.

However the piezoelectric voltage coefficients g_{33} and g_h of modified $PbTiO_3$ are far greater than those of the materials in this study. The main consideration is the coexistence of the rhombohedral and tetragonal structural phases in BFPT:Nb samples which enhances both piezoelectric and dielectric properties [28]. Although Table 5.3 confirms the enhancement of the d_{33} in BFPT:Nb, it is found to also enhance the relative permittivity to more than twice that of $PbTiO_3$ which in turn reduces the g_{33}. The coexistence of phases may also explain the relatively large values for the d_{31} compared to $PbTiO_3$ which results in larger values for g_{31} and ultimately limits the

g_h. The natural decoupling of 33 and 31 modes combined with the existence of a single tetragonal phase may explain the incredibly low values for the relative permittivity and the d_{31} for $PbTiO_3$ ceramics, resulting in larger g_{33} and g_h as shown in Table 5.3. Although the stoichiometry of this $BiFeO_3$-$PbTiO_3$ solid solution was chosen in order to achieve large tetragonality compared to many other ferroelectric solid solutions, it may be useful to explore compositions containing lower concentrations of $BiFeO_3$ in order to achieve a single tetragonal phase. A final consideration is the longevity in the use of modified $PbTiO_3$ polycrystalline ceramics and industrial demand driving marginal gains in piezoelectric properties. As mentioned in Chapter 1, the popularity of modified $PbTiO_3$ is mentioned as far back as the 1980s [4]. The decades of optimising chemical modifications and processing has ultimately led to material properties mentioned in Table 5.3. By exploring chemical modifications such as different $BiFeO_3$ to $PbTiO_3$ stoichiometries, studying Nb levels between x=0.02 and x=0.10 and introducing further dopants along with process optimisation such as investigating different poling conditions and the industrialisation of material fabrication may result in piezovoltage coefficients that are comparable or may even exceed those of traditional Ca-modified $PbTiO_3$. This may be possible despite the limitations that were proposed in Chapter 3 in which highly tetragonal polycrystalline ceramics display suppressed g_{33} values due to high coercivity and reduced domain wall densities.

Table 5.3: Piezoelectric and dielectric properties of annealed pure and Nb-doped BFPT65, lead zirconate titanate and modified lead titanate polycrystalline ceramics. *calculated from d_{33} and g_{33} values by thesis author

Material	d_{33} (pC/N)	d_{31} (pC/N)	d_h (pC/N)	g_{33} (10^{-3}Vm/N)	g_{31} (10^{-3}Vm/N)	g_h (10^{-3}Vm/N)	ϵ_{rel}	tanδ	Ref.
BFPT65	46.3	-10.8	24.8	19.3	-4.5	10.3	271	0.0225	This work
x=0.01 Nb:BFPT65	38.0	-8.9	20.3	9.4	-2.2	5.0	459	0.0196	This work
x=0.02 Nb:BFPT65	71.5	-16.0	40.0	21.1	-4.8	12.0	383	0.0191	This work
x=0.05 Nb:BFPT65	82.0	-17.6	46.7	21.3	-4.6	12.2	434	0.0193	This work
x=0.10 Nb:BFPT65	68.8	-8.8	51.2	15.8	-2.0	11.8	492	0.0230	This work
x=0.20 Nb:BFPT65	48.0	-8.6	30.8	14.4	-2.6	9.2	377	0.0273	This work
x=0.30 Nb:BFPT65	23.8	-7.1	9.6	7.4	-2.2	3.0	364	0.0322	This work
PZT401	315	-132	51	25.5	-10.7	4.1	1395	0.0020	[175]
PZT807	260	-93	74	28.8	-9.5	9.8	1105	0.0016	[175]
Modified $PbTiO_3$	68	-3.2	61.6	37.0	-1.7	33.6	208*		[101]

5.3.5 Dielectric Impedance Spectroscopy

As observed in the previous section, the annealing of Nb-doped $BiFeO_3$-$PbTiO_3$ results in improved piezoelectric properties. It is postulated that this may be a defect related phenomenon due to the compositions that showed significant improvement. Permittivity measurements as a function of temperature (Figure 5.25) showed the origin of a relaxation before maximum permittivity after annealing. To understand the defect chemistry further, dielectric impedance spectroscopy has been carried out from ≈300°C to ≈600°C for both unannealed samples and annealed samples to observe the differences between them.

The step-by-step analysis of impedance spectroscopy data was carried out using the method of Ref. [186].

5.3.5.1 Choice of Equivalent Circuit

An appropriate equivalent circuit was chosen using the following methods:

1. Using observations of the material's physical properties and construct an equivalent circuit that represents that system and resulting conduction mechanisms.
2. Analysis of fundamental spectra and observing the changes in the real and imaginary impedance and modulus.
3. Trial and error with multiple equivalent circuits and using a least squared fit method to calculate the best fit.

In Section 5.3.2, SEM observations showed that all compositions possessed a core-shell structure in which elemental segregation results in electrochemical differences between the grain and the grain boundary. This implies that the appropriate equivalent circuit should be made up of two sections, the first is a resistor-capacitor-constant phase element (R-C-CPE) in parallel to represent the conduction mechanism coming from the grain (core) and the second a resistor-capacitor (RC) in parallel but in series with the previous R-C-CPE to represent the conduction mechanism from the grain boundary (shell).

Bode plots of the impedance and modulus were carried out and the frequency response of the real and imaginary parts have been observed. Figures 5.35 to 5.36 show these spectra for x=0.05 Nb however the analysis is coherent with other compositions.

The impedance and modulus Bode plots for all other compositions can be found in Appendix B.

Figure 5.35 a) and b) show the real and imaginary parts of the impedance as a function of frequency over a range of temperatures for unannealed samples and Figure 5.35 c) and d) show the same for the annealed sample. The real impedance shows typical relaxation behaviour where a maximum value is observed at lower frequencies. However at the relaxation frequency the impedance drops to a minimum representing the freezing-out of a polarisation mechanism. The imaginary impedance response shows a well-defined peak representing the change from a short-range conduction mechanism at higher frequencies to a long-range conduction mechanism as the frequency tends towards a DC signal. The shift in peak relaxation frequency as a function of temperature also shows that the material possesses a negative temperature coefficient of resistance (NTCR) and that the relaxation process has a temperature dependence. The initial impedance response shows only one clearly defined peak suggesting that only one conduction mechanism is present and therefore only the R-C-CPE is required, contrary to what was postulated from SEM studies. However only consulting the frequency response of the impedance may not disclose all the information as discussed in Section 5.1.7.

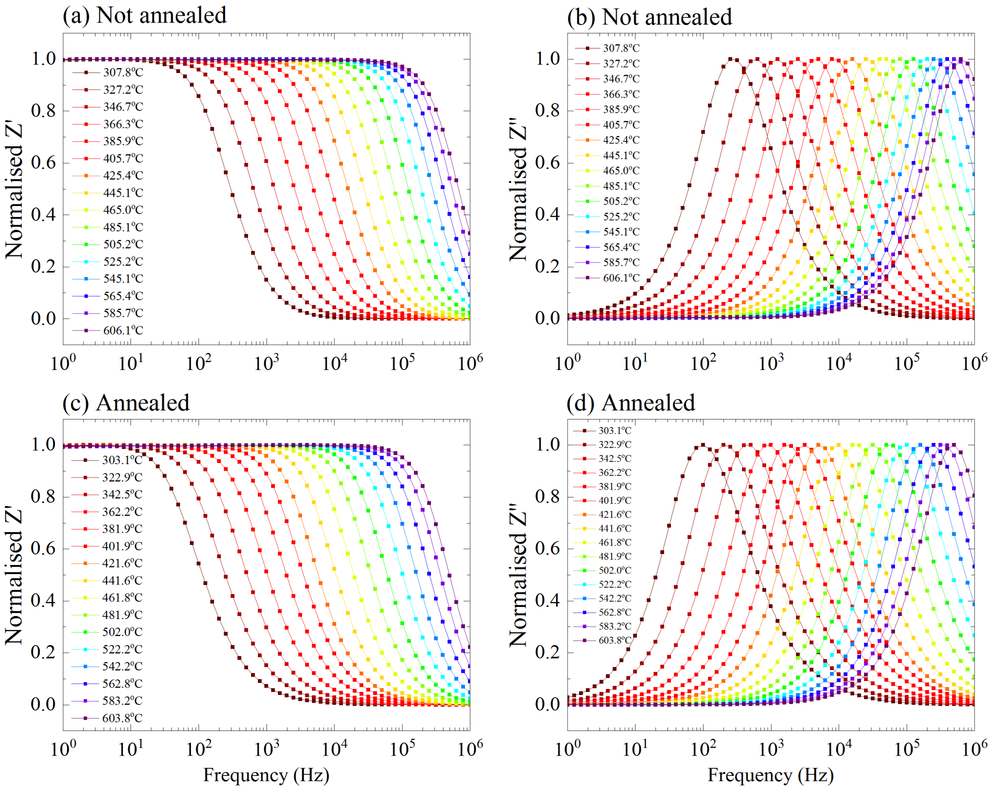

Figure 5.35: (a) Real and (b) imaginary impedance for x=0.05 Nb:BFPT65 before annealing, and (c) real and (d) imaginary impedance for x=0.05 Nb:BFPT65 after annealing

Figure 5.36 a) and b) show the real and imaginary modulus as a function of frequency between ≈310°C to ≈610°C for unannealed x=0.05 and Figure 5.36 c) and d) show the same for annealed samples. The real component of the modulus initially starts at a minimum in the low frequency region and increases at the relaxation frequency and continues to rise to a maximum at higher frequencies. Similarly to the imaginary part of the impedance, the imaginary modulus shows a relaxation peak representing the conversion from a long-range to a short-range conduction mechanism. Once again, the shifting of relaxation peak to higher frequencies with temperature indicates a temperature dependent conduction mechanism. Once annealed a clear shoulder can be observed in the imaginary modulus representing a relaxation of a second conduction mechanism. This implies the relevance of the second R-C contribution within the equivalent circuit. It is unclear whether the second relaxation peak is present in the unannealed state and simply dwarfed by the larger peak, in which case the second R-C should be present in the analysis of both unannealed and annealed state. It was decided that for consistency, the equivalent circuit for both the unannealed and annealed state should be fixed.

(a) Not annealed (b) Not annealed

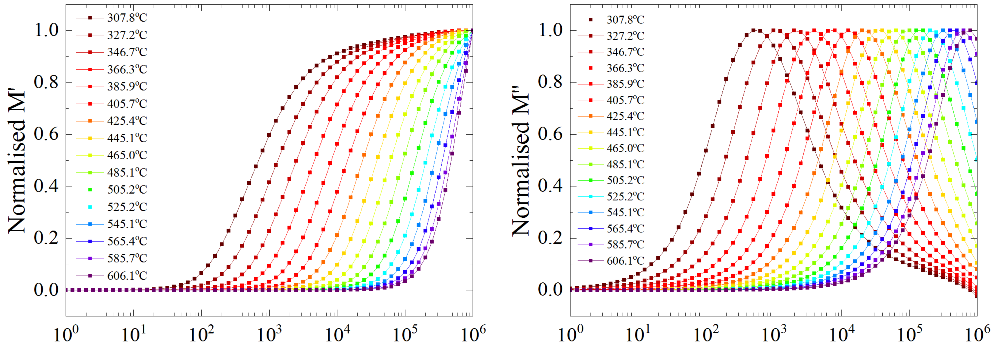

(c) Annealed (d) Annealed

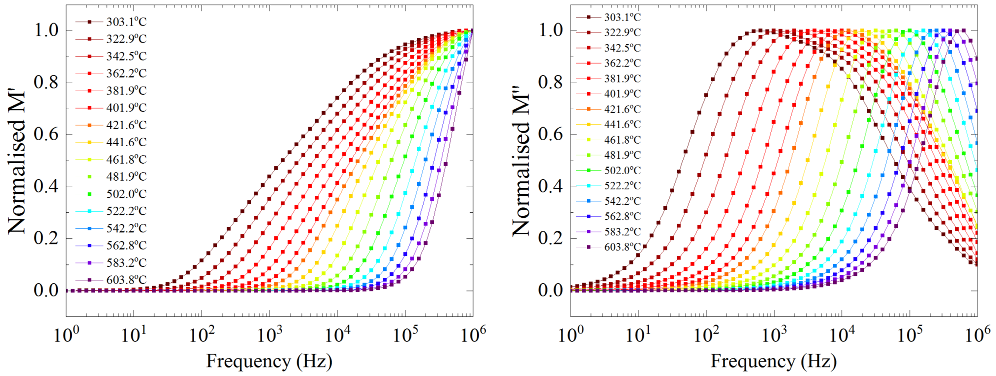

Figure 5.36: (a) Real and (b) imaginary modulus for x=0.05 Nb:BFPT65 before annealing, and (c) real and (d) imaginary modulus for x=0.05 Nb:BFPT65 after annealing

The final consideration is the quality of fit compared to experimental data. Four equivalent circuits were chosen and compared using the chi^2 values which are shown in Table 5.5. The four equivalent circuits can be seen in Table 5.4, circuit A is a simple R-C circuit in parallel, circuit B is similar to circuit A except it has the substitution of the capacitor with a CPE, circuit C is the same as circuit B but with both C and CPE in parallel, and the fourth circuit is the same as circuit C with the addition of another R-C in series. Figures 5.37 - 5.40 show the equivalent circuit impedance and modulus, Bode and complex fits for undoped BFPT65 at 308.0° for visual observations. chi^2 values of all annealed and unannealed compositions at ≈ 310°C are listed in Table 5.5.

Table 5.4: Trial equivalent circuits for best-fit analysis

Circuit A	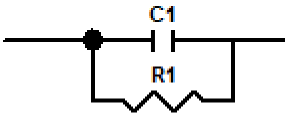
Circuit B	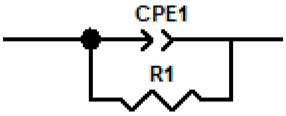
Circuit C	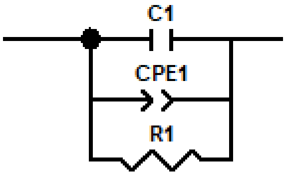
Circuit D	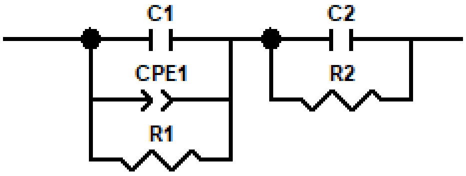

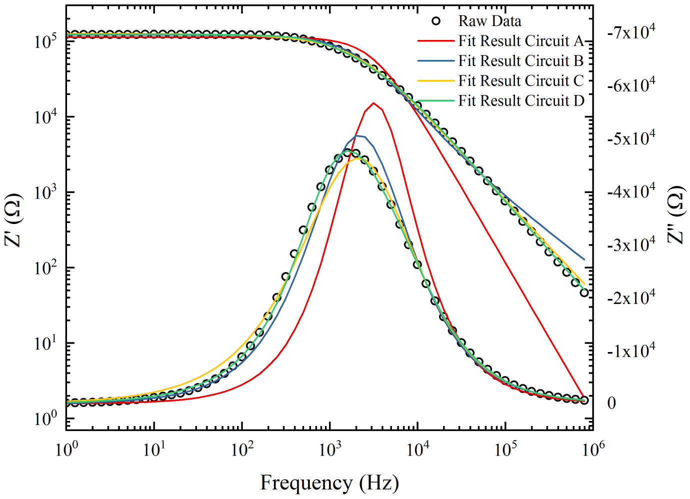

Figure 5.37: Real and imaginary impedance as a function of frequency for undoped and unannealed BiFeO3 – PbTiO3 at 308.0°C with fitting results for equivalent circuits A, B, C and D shown in Table 5.4

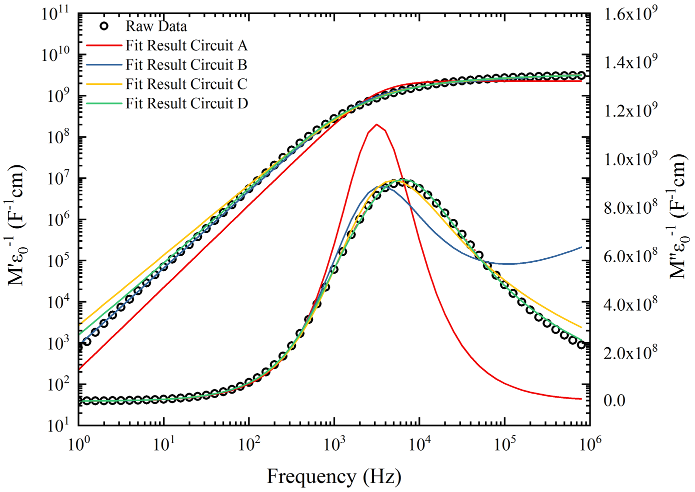

Figure 5.38: Real and imaginary modulus as a function of frequency for undoped and unannealed BiFeO3 − PbTiO3 at 308.0°C with fitting results for equivalent circuits A, B, C and D shown in Table 5.4.

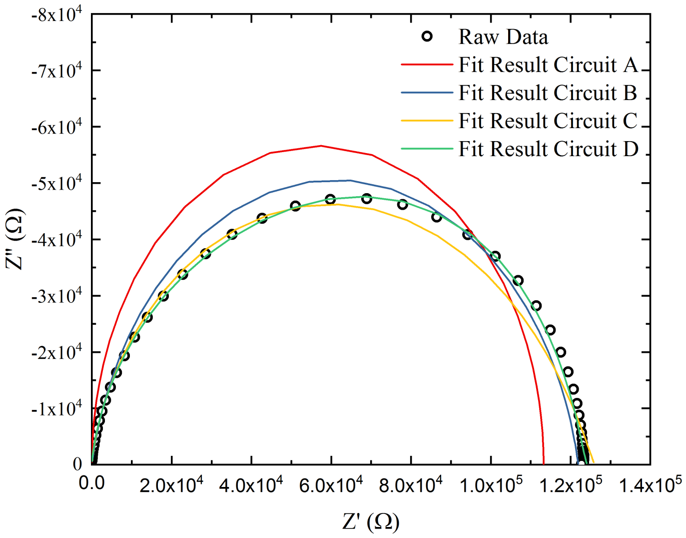

Figure 5.39: Impedance Cole-Cole plot for undoped and unannealed BiFeO3 − PbTiO3 at 308.0°C with fitting results for equivalent circuits A, B, C and D shown in Table 5.4

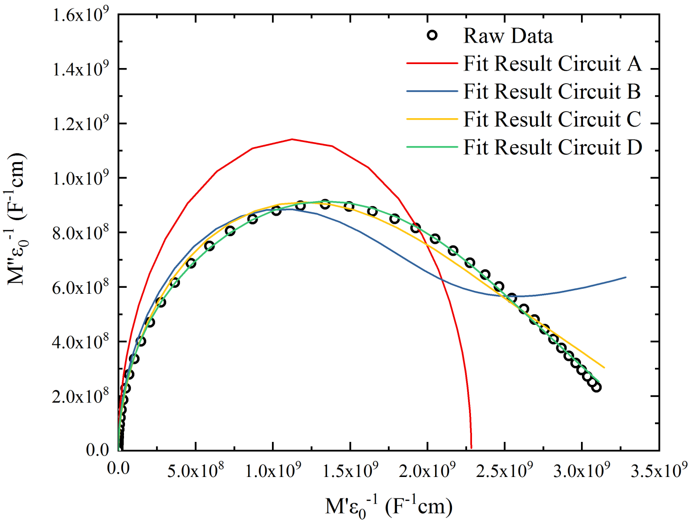

Figure 5.40: Modulus Cole-Cole plot for undoped and unannealed $BiFeO_3-PbTiO_3$ at 308.0°C with fitting results for equivalent circuits A, B, C and D shown in Table 5.4

Table 5.5: Sum of the squares for circuits A-D for each composition annealed and unannealed at ≈310°C

Nb content	Circuit A	Circuit B	Circuit C	Circuit D
x=0.00 - Not annealed	2.1431	0.20579	0.031947	0.00276
x=0.00 - Annealed	4.0965	0.35873	0.033241	0.009795
x=0.01 - Not annealed	1.8805	0.42036	0.058437	0.007019
x=0.01 - Annealed	7.2766	1.1530	0.098911	0.045495
x=0.02 - Not annealed	1.2257	0.29651	0.040307	0.005278
x=0.02 - Annealed	5.358	0.70206	0.074904	0.032107
x=0.05 - Not annealed	0.90663	0.22669	0.03237	0.004637
x=0.05 - Annealed	5.8983	0.78026	0.093954	0.037075
x=0.10 - Not annealed	0.18323	0.060993	0.010507	0.002667
x=0.10 - Annealed	4.5216	0.92878	0.091636	0.02834
x=0.20 - Not annealed	2.0859	0.52931	0.10291	0.013127
x=0.20 - Annealed	2.9604	0.65032	0.09989	0.021559
x=0.30 - Not annealed	1.0222	0.24261	0.036953	0.004975
x=0.30 - Annealed	2.3794	0.51266	0.068211	0.011485

Using all three appropriate measures to find the appropriate equivalent circuit, it was decided that circuit D is appropriate.

5.3.5.2 Determination of the Constant Phase Element Parameters

Like many characterisation techniques that require fitting of a model to raw data, an appropriate set of initial starting parameters must be made. As discussed previously in Section 5.1.7.1, the constant phase element is used to compensate for the non-ideal Debye behaviour of materials in which there is a broad range of relaxation times.

Initial parameters for B and m in Equation 5.16 were determined by considering the real component of the electric admittance, Y', shown in Equation 5.26, as a function of angular frequency shown in Figure 5.41.

$$Y' = R^{-1} - (1 + B(j\omega)^m cos(\frac{m\pi}{2})) \tag{5.26}$$

Where R is resistance, B is a pre-exponential factor, $j = \sqrt{-1}$, ω is angular frequency, and m is the exponent that describes the degree of unideal Debye relaxation.

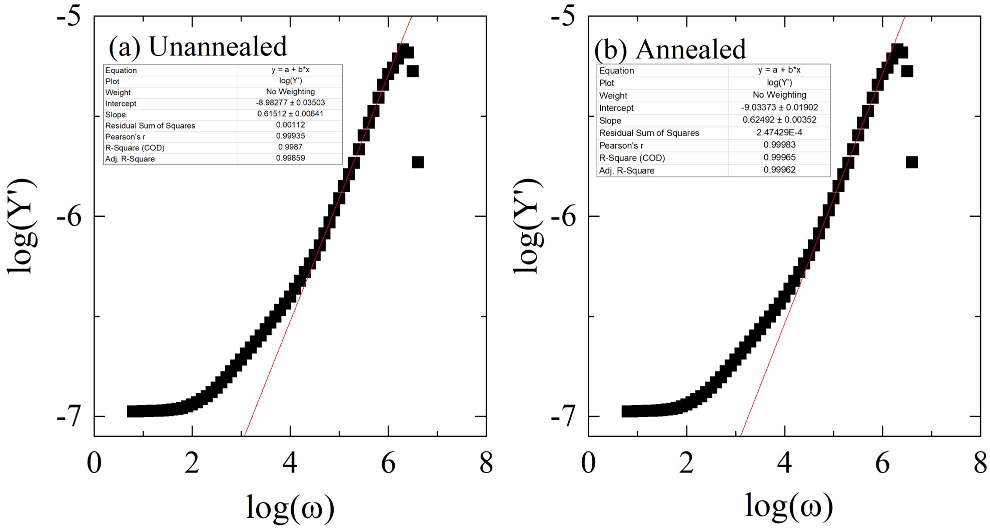

Figure 5.41: Real admittance vs angular frequency for x=0.05 Nb:BFPT65 polycrystalline ceramics (a) before annealing, and (b) after annealing. Real admittance vs angular frequency plots for all other compositions are found in Appendix B

In the high frequency region an almost linear trend is observed, the gradient of which represents the value for the exponent, m, and $\log[Bcos(m\pi/2)]$ represents the intercept of $log(Y')$ at ω=1Hz. Once the parameters had been assigned to B and m, initial hand fitting was carried out using ZView. All parameters were then free to change until a minimum value for chi^2 was achieved. When carrying out analysis for each temperature, values for the resistances (R_1 and R_2), capacitances (C_1 and C_2) and A were free parameters, however m was fixed throughout each temperature scan. The need to make m a fixed parameter is highlighted in Ref. [186] in which it is observed to result in less erratic resistance and capacitance values. Although in reality the distribution of relaxation times may vary at each temperature, allowing all parameters to be free parameters may result in false minima fitting results and therefore values for resistances and capacitances become less valid.

Figure 5.42 and 5.43 show the complex impedance and complex modulus plots for unannealed and annealed x=0.05 Nb:BFPT65. All other complex impedance and modulus plots can be found in Appendix B.

(a) x=0.05 Not annealed

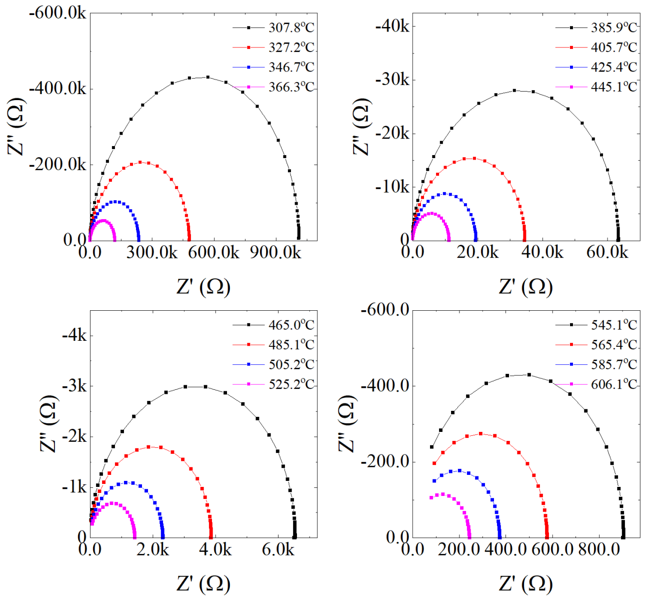

(b) x=0.05 Annealed

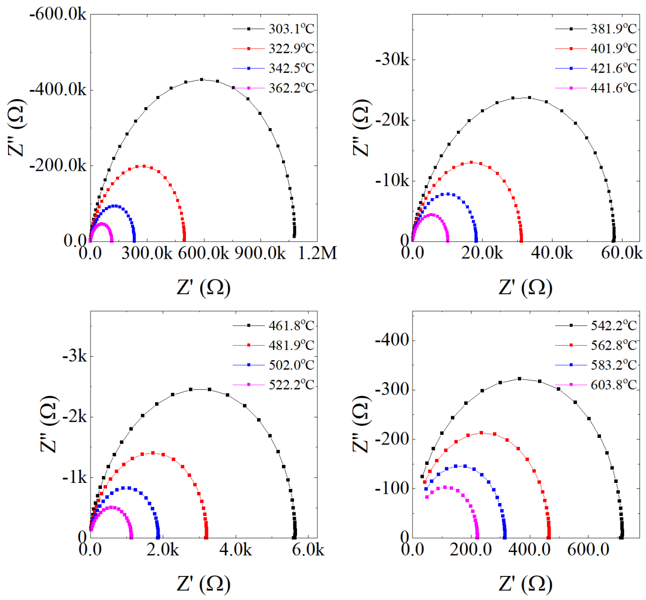

Figure 5.42: Complex impedance plots for (a) unannealed x=0.05 Nb:BFPT65 from 307.8°C to 606.1°C and (b) annealed x=0.05 Nb:BFPT65 from 303.1°C to 603.8°C

(a) x=0.05 Not Annealed

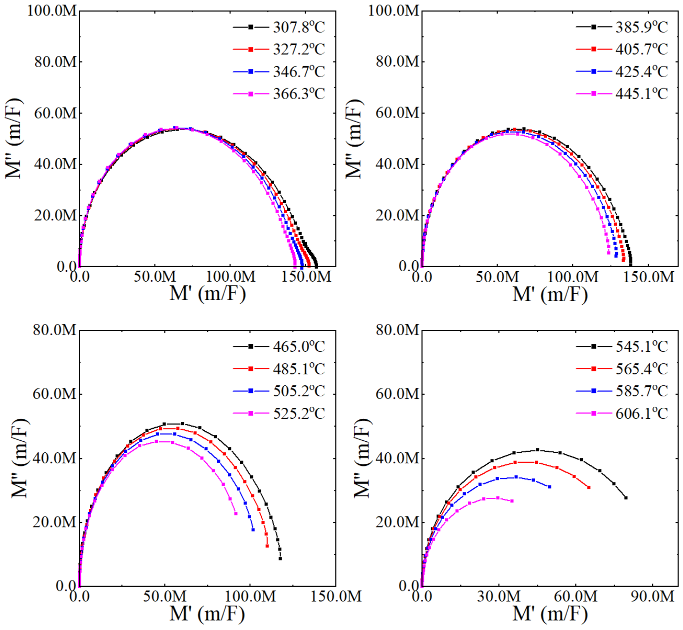

(b) x=0.05 Annealed

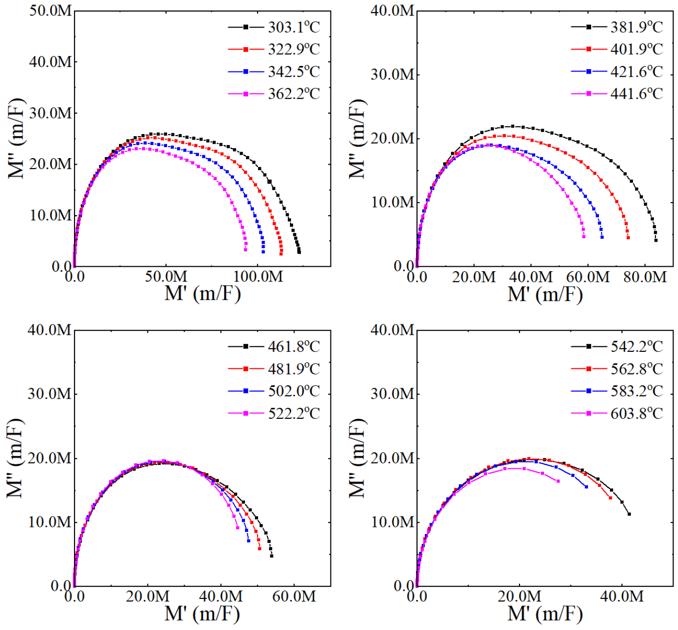

Figure 5.43: Complex modulus plots for (a) unannealed x=0.05 Nb:BFPT65 from 307.8°C to 606.1°C and (b) annealed x=0.05 Nb:BFPT65 from 303.1°C to 603.8°C

All complex impedance plots were analysed using equivalent circuit D from Table 5.4. Table 5.6 and 5.7 show the fitting results for x=0.05 Nb-doped samples before and after annealing. Fitting results for all other compositions can be found in Appendix B.

Table 5.6: Impedance spectroscopy fitting results for x=0.05 Nb-doped, unannealed BFPT65 from 307.8°C to 585.7°C

Temperature (°C)	C_1 (nF)	B	m	R_1 (Ω)	C_2 (nF)	R_2 (Ω)
307.8	0.458	6.40×10^{-9}	0.60461	409000	1.180	611000
327.2	0.479	8.15×10^{-9}	0.60461	194000	1.160	290000
346.7	0.511	1.04×10^{-8}	0.60461	90991	1.090	147000
366.3	0.548	1.31×10^{-8}	0.60461	43603	1.030	77101
385.9	0.590	1.60×10^{-8}	0.60461	21642	0.986	42026
405.7	0.627	1.91×10^{-8}	0.60461	11498	0.971	23180
425.4	0.681	2.26×10^{-8}	0.60461	6124	0.939	13423
445.1	0.760	2.58×10^{-8}	0.60461	3233	0.901	7999
465.0	0.861	3.02×10^{-8}	0.60461	1744	0.871	4800
485.1	1.020	3.66×10^{-8}	0.60461	899.0	0.829	2971
505.2	1.200	4.51×10^{-8}	0.60461	492.0	0.818	1833
525.2	1.430	5.39×10^{-8}	0.60461	269.4	0.819	1161
545.1	1.630	6.47×10^{-8}	0.60461	163.1	0.858	742.1
565.4	1.770	2.17×10^{-7}	0.60461	91.23	0.890	486.2
585.7	1.800	3.67×10^{-7}	0.60461	46.11	0.969	327.8

Table 5.7: Impedance spectroscopy fitting results for x=0.05 Nb-doped, annealed BFPT65 from 303.1°C to 603.8°C

Temperature (°C)	C_1 (nF)	B	m	R_1 (Ω)	C_2 (nF)	R_2 (Ω)
303.1	0.457	2.37×10^{-8}	0.59163	536000	2.97	575000
322.9	0.495	3.25×10^{-8}	0.59163	232000	2.87	276000
342.5	0.544	4.44×10^{-8}	0.59163	103000	2.80	135000
362.2	0.606	5.99×10^{-8}	0.59163	46815	2.74	68528
381.9	0.686	7.90×10^{-8}	0.59163	22093	2.72	36249
401.9	0.798	1.03×10^{-7}	0.59163	10920	2.69	20502
421.6	0.975	1.35×10^{-7}	0.59163	5382	2.53	12977
441.6	1.170	1.51×10^{-7}	0.59163	2838	2.46	7337
461.8	1.370	1.51×10^{-7}	0.59163	1554	2.44	4099
481.9	1.510	1.53×10^{-7}	0.59163	906.3	2.48	2305
502.0	1.670	1.39×10^{-7}	0.59163	536.2	2.50	1339
522.2	1.820	1.18×10^{-7}	0.59163	344.9	2.59	787.9
542.2	1.980	8.03×10^{-8}	0.59163	241.8	2.75	472.5
562.8	2.160	2.08×10^{-7}	0.59163	127.3	2.26	339.1
583.2	2.460	2.68×10^{-7}	0.59163	76.41	2.14	239.3
603.8	2.610	3.82×10^{-7}	0.59163	48.13	2.15	173.4

5.3.5.3 Activation Energy and Conductivity

The activation energy of each conduction mechanism was calculated by fitting Cole-Cole plots as in Figure 5.42 and values for the resistance of the grain (R_1) and grain boundary (R_2) were obtained by extrapolation. The activation energy of a conduction mechanism can be calculated using an Arrhenius type plot:

$$\frac{1}{R_i} = \Lambda \exp \frac{-E_A}{k_b T} \tag{5.27}$$

Where R_i is the resistance of either the grain or grain boundary, Λ is a pre-exponential factor, E_A is the activation energy, k_b is the Boltzmann constant and T is the temperature. Initial plots of $\ln(1/R_i)$ against $1/T$ were generated, the gradients were extrapolated, multiplied by the Boltzmann constant and converted from joules to electron volts to give the activation energy.

Figure 5.44 shows the Arrhenius plots for unannealed and annealed x=0.05 Nb-doped BFPT65. The Arrhenius plots for unannealed and annealed x=0.00, 0.01, 0.02, 0.10, 0.20 and 0.30 can be found in Appendix B. Although the main focus of this study will be on the activation energies in the lower temperature region, it is worth noting that at high temperatures, there is an increase in the gradient of $\ln(1/R_1)$ for compositions x=0.01, 0.02 and 0.05, the E_A for which increases from 1.737eV for x=0.01 Nb-doped BFPT65 to 1.876eV for x=0.02 and then decrease again for x=0.05 to 1.693eV. The large values of the activation energy implies that it is most likely that this conduction mechanism is the result of A-site vacancy hopping which due to the relatively large distance between the A-site ions requiring a large amount of energy to occur. For undoped, x=0.10, x=0.20 & x=0.30 doped samples the high temperature high gradient region is not present. For highly doped samples, this may be due to the presence of the pyrochlore structure which is more rigid and therefore ions and vacancies require more energy and higher temperatures than are measured here to displace.

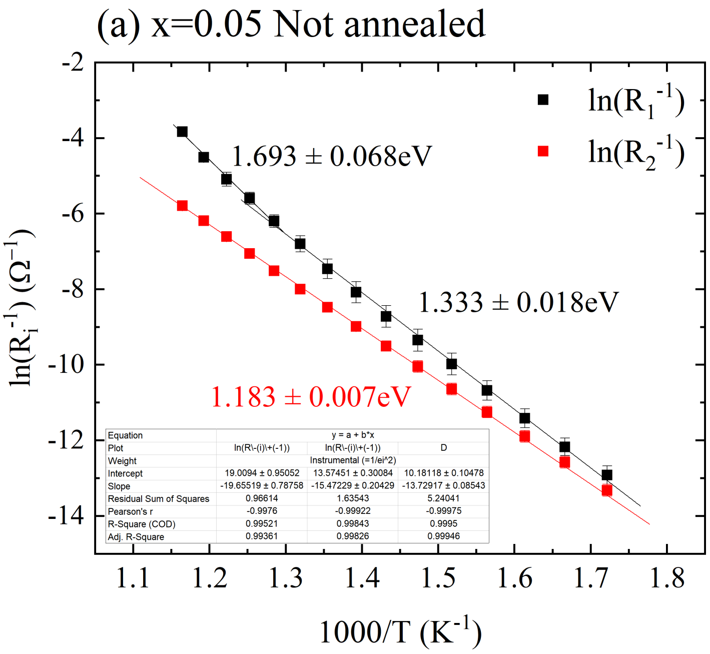
(a) x=0.05 Not annealed

Equation	y = a + b*x		
Plot	ln(R\-(i)\+(-1))	ln(R\-(i)\+(-1))	D
Weight	Instrumental (=1/ei^2)		
Intercept	19.0094 ± 0.95052	13.57451 ± 0.30084	10.18118 ± 0.10478
Slope	-19.65519 ± 0.78758	-15.47229 ± 0.20429	-13.72917 ± 0.08543
Residual Sum of Squares	0.96614	1.63543	5.24041
Pearson's r	-0.9976	-0.99922	-0.99975
R-Square (COD)	0.99521	0.99843	0.9995
Adj. R-Square	0.99361	0.99826	0.99946

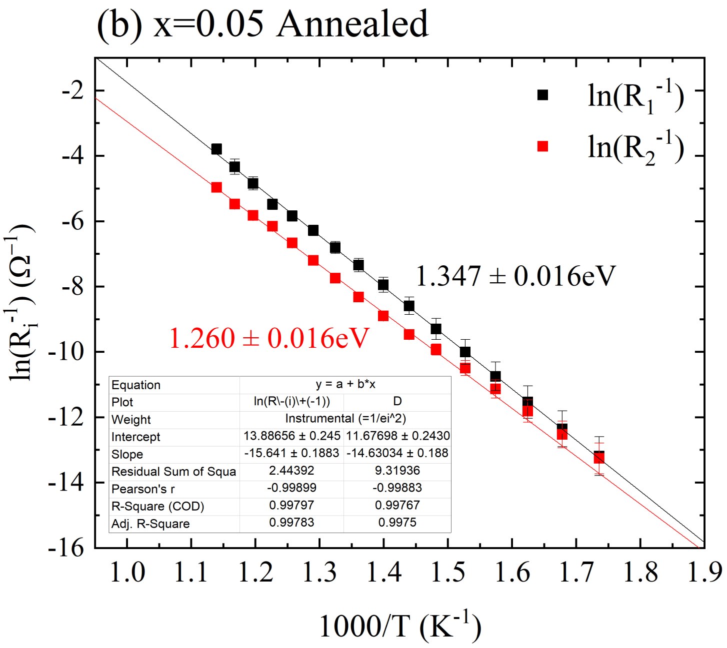

Equation	y = a + b*x	
Plot	ln(R\-(i)\+(-1))	D
Weight	Instrumental (=1/ei^2)	
Intercept	13.88656 ± 0.245	11.67698 ± 0.2430
Slope	-15.641 ± 0.1883	-14.63034 ± 0.188
Residual Sum of Squa	2.44392	9.31936
Pearson's r	-0.99899	-0.99883
R-Square (COD)	0.99797	0.99767
Adj. R-Square	0.99783	0.9975

Figure 5.44: Arrhenius plots for x=0.05 Nb:BFPT65 polycrystalline ceramics (a) before annealing, and (b) after annealing

Figure 5.45 shows the activation energy for the grain and grain boundary for unannealed and annealed samples as a function of Nb content. The lowest activation energy can be observed for undoped BFPT where an activation energy of 1.200eV and 1.001eV are calculated for the grain and grain boundary energies for unannealed BFPT and 1.204eV and 1.106eV for the annealed sample. The difference between the activation energies of the two conduction mechanisms implies a difference in concentration of oxygen vacancies between the grain and grain boundary.

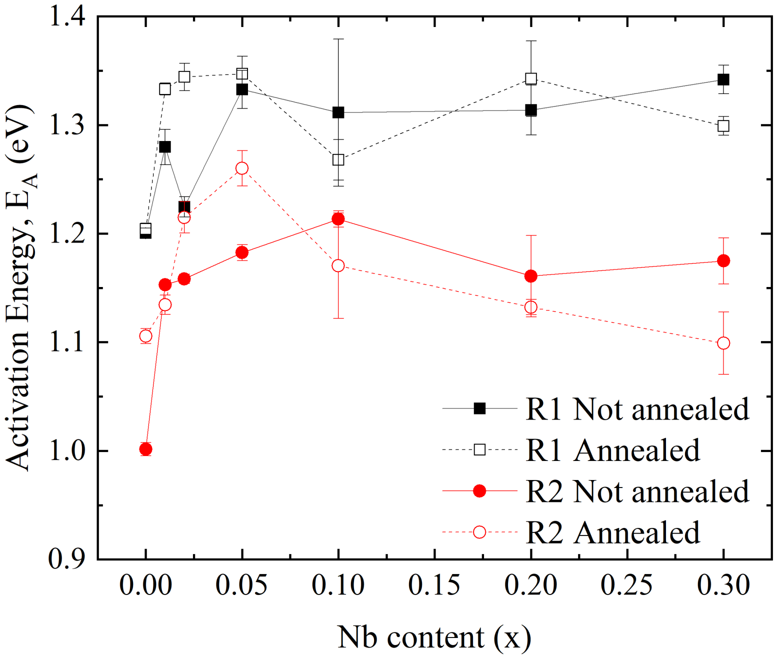

Figure 5.45: Activation energy for conduction mechanisms within the grain (■) and grain boundary (●) vs Nb content. Solid and dashed lines represent unannealed and annealed samples, respectively

Bell et al. [55] postulated that the two conduction mechanisms present in $BiFeO_3$-$PbTiO_3$ ceramics were Fe^{2+}/Fe^{3+} hopping and oxygen vacancy conduction as shown in Figure 5.46 and 5.47. Oxygen vacancy conductivity originates due to the high coordination number of oxygen ions and therefore the relative ease of hopping for ionic defects. Oxygen vacancies can also act as a bridge for Fe^{2+}/Fe^{3+} hopping. Due to coulombic interactions, oxygen vacancies can attract electrons from nearby Fe^{3+} ions. However they do not possess enough energy to trap the charge carrier which then 'hops' to the adjacent B-site ion.

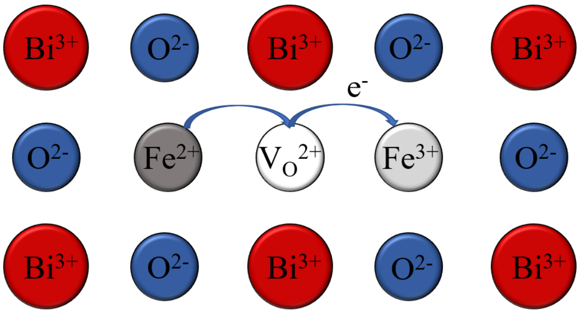

Figure 5.46: Illustration of Fe^{2+}/Fe^{3+} in a 3+:3+ perovskite. Although the name suggests movement of the B-site ion, the conduction is facilitated by hopping of electrons which oxidise and reduce neighbouring iron ions using weakly bonding oxygen vacancies as a bridge

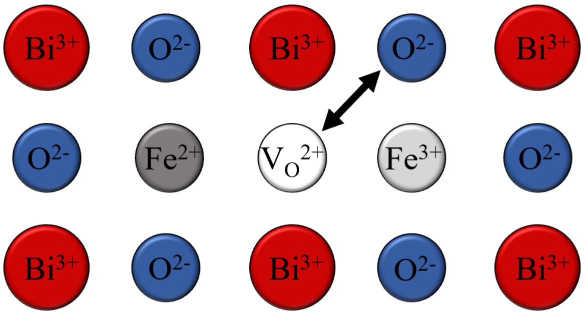

Figure 5.47: Illustration of oxygen vacancy conduction in a 3+:3+ perovskite. Due to the closely packed nature of the oxygen ions, oxygen vacancy hopping is relatively easily achieved

For undoped $BiFeO_3$-$PbTiO_3$, oxygen vacancies can form in three ways during synthesis:

- Volatility of A-site oxides:
  $Bi_2O_3 \rightarrow Bi_2O_3^v \uparrow + 2V_{Bi}''' + 3V_O^{\cdot\cdot}$
  $PbO \rightarrow PbO^v \uparrow + V_{Pb}'' + V_O^{\cdot\cdot}$
- Independent oxygen loss:
  $O_O^X \rightarrow \frac{1}{2}O_2 \uparrow + V_O^{\cdot\cdot} + 2e'$
- Oxide impurities:
  $0.65[Bi_{Bi}^x + (1-x)Fe_{Fe}^X + (x)Fe'_{Fe} + (3 - \frac{x}{2})V_O^{\cdot\cdot}] + 0.35[Pb_{Pb}^X + Ti_{Ti}^X + 3O_O^X]$

The addition of Nb aims to replenish oxygen vacancies by providing an excess of oxygen ions to the lattice. Not only will the replenishment of oxygen vacancies reduce oxygen vacancy concentration but may also bridge the gap which facilitates Fe^{2+}/Fe^{3+} hopping. Furthermore Nb has the ability to reduce the free charge carrier concentration generated through Equation 5.28 as shown in Equation 5.29:

$$4Fe_{Fe}^X \rightarrow 4Fe'_{Fe} + 4h^{\cdot} \tag{5.28}$$

$$Nb_2O_5 + 4h^{\cdot} \rightarrow 2Nb_{Fe}^{\cdot\cdot} + 3O_O^X + O_2 \tag{5.29}$$

The addition of Nb increases the activation energy for both grain and grain boundary mechanisms for both unannealed and annealed samples implying the reduction in oxygen vacancy concentration. Figure 5.48 and 5.49 show the low signal AC conductivity, σ_{AC}, calculated using Equation 5.30 and low signal DC conductivity, σ_{DC}, calculated using the extrapolated resistance values through Cole-Cole plot fitting.

$$\sigma_{AC} = \omega \epsilon_r \epsilon_0 tan\delta \tag{5.30}$$

Where ω is angular frequency, ϵ_r is the relative permittivity, ϵ_0 is the permittivity of free space, and $tan\delta$ is the dissipation factor.

Both the low signal AC and DC measurements show a decrease in the conductivity with the introduction of Nb except at x=0.20 where a small increase is observed. This is further evidence that the substitution of Nb into the lattice reduces the oxygen vacancy concentration and therefore the conductivity.

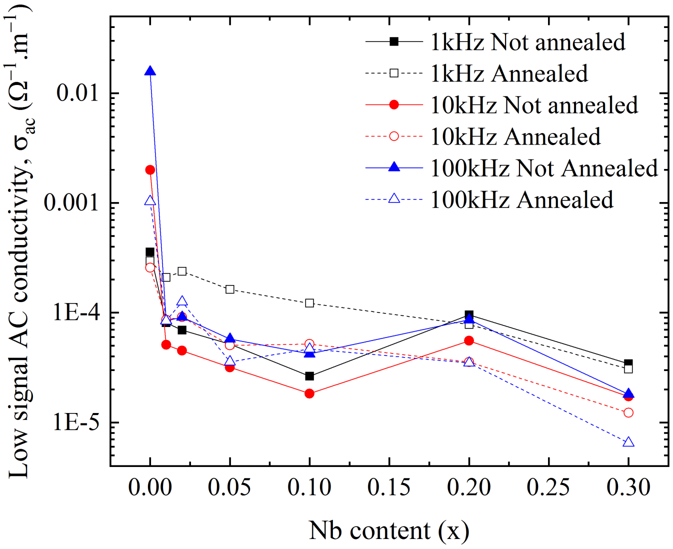

Figure 5.48: Low signal (1V) AC conductivity vs Nb content. Solid and dashed lines represent conductivity of unannealed and annealed samples, respectively

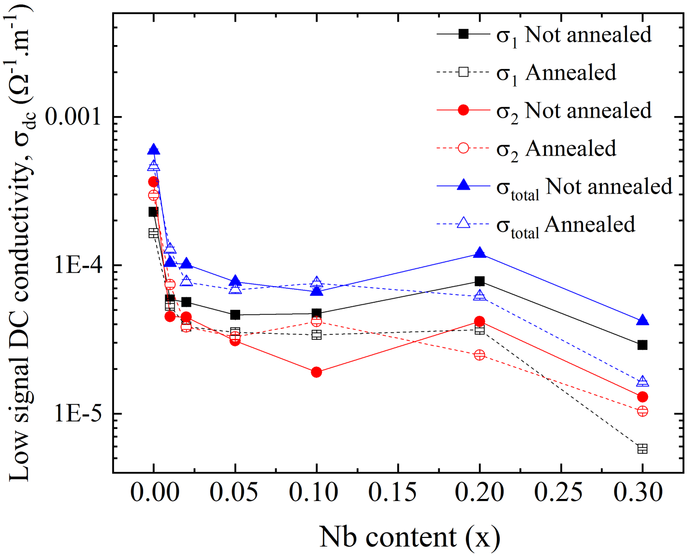

Figure 5.49: Low signal (1V) DC conductivity vs Nb content. Solid and dashed lines represent conductivity of unannealed and annealed samples, respectively

5.3.5.4 Comparison to Piezoelectric and Ferroelectric Properties

It is postulated that the difference in the activation energies from the grain and grain boundary conduction mechanisms (ΔE_A) shown in Equation 5.31 may be an indicator of electrochemical heterogeneity.

$$\Delta E_A = E_A^{gb} - E_A^{g} \tag{5.31}$$

Where E_A^{gb} and E_A^{g} are the activation energies of the grain boundary and grain conduction mechanisms, repsectively.

As shown in Figure 5.50 if the difference between the two is large it implies that there is a larger ionic or valence concentration within that region that contributes to different conduction mechanisms. When the difference between the two activation energy tends to zero, a more electrochemical homogeneous structure may result.

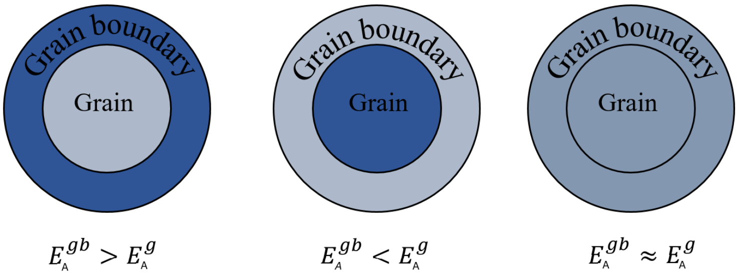

Figure 5.50: Schematic demonstrating the activation energy of conduction mechanisms within the grain and grain boundary and its relation to electrochemical heterogeneity

The values for ΔE_A for the unannealed and annealed samples have been compared to the piezoelectric d_{33} coefficient of the unannealed and annealed samples in Figure 5.51. For unannealed samples it is difficult to see a trend between the two. Arguably the trend between x=0.01, 0.02, and 0.05 Nb doped samples are similar to that of the ΔE_A. However ΔE_A is in very good agreement with the piezoelectric d_{33} coefficient for the annealed samples suggesting that the improved piezoelectric properties are due to the increasing homogeneity within the ceramic after annealing.

(a) Not Annealed

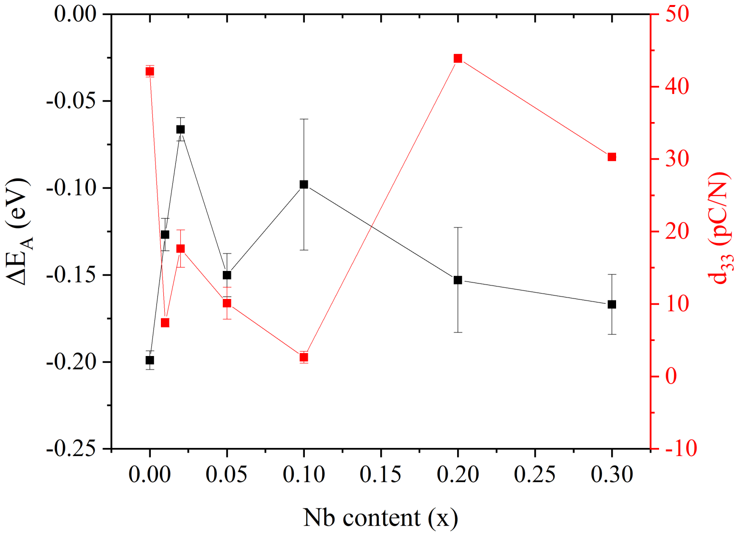

(b) Annealed

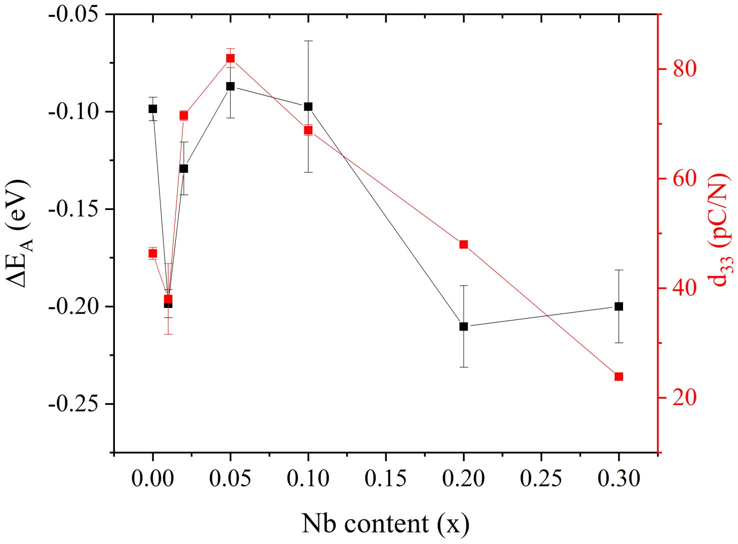

Figure 5.51: The difference in conduction mechanism activation energy ΔE_A described in Equation 5.31, against d_{33} for (a) unannealed and (b) annealed samples

The most likely explanation for this is the difference in cooling rate between the sintering regime and the annealing regime which are 20°C/hour and 50°C/hour, respectively. It has been shown by DFT calculations that defects will arrange themselves in clusters or planes if given enough time to do so [204]. A cooling rate of 20°C/hour during sintering provides an abundance of time for defects to arrange themselves in this way. These defect regions clamp domain walls, reducing their mobility and ultimately the piezoelectric performance. When a sample is annealed, the defects will redistribute due to the large amount of thermal energy above T_C. However a cooling rate of 50°C/hour provides insufficient time for defects to arrange themselves as before. Therefore when these samples are poled, domain wall clamping decreases and therefore domain wall mobility and piezoelectric activity increases.

Figure 5.52 show strain and polarisation vs electric field for all compositions before and after annealing. For highly defective perovskite samples (x=0.01, 0.02, 0.05 & 0.10) there is a significant difference between the annealed and non-annealed P/x v E loops. Non-annealed samples show significant pinching in the polarisation v electric field loops suppressing the remanent polarisation. Strain field loops also show low response to external field with x=0.01, 0.02, 0.05 and 0.10 samples showing the least response. Annealed samples show wider polarisation loops with reduced pinching effects and enhanced maximum polarisation and remanent polarisation. This widening of the PE loops is indicative of increasing domain wall mobility. Strain-field loops also show enhancement in comparison to non-annealed samples also evidencing a reduction in domain wall clamping.

Pure $0.65BiFeO_3$-$0.35PbTiO_3$ samples and highly doped BFPT65 samples (x=0.20 and x=0.30) show a decrease in the maximum polarisation. However the strain-field measurements remain relatively similar in comparison to compositions mentioned earlier. The ferroelectric properties between the annealed and unannealed samples mimic those of the piezoelectric properties in which samples containing x=0.01, 0.02, 0.05 and 0.10 show the most significant improvement after annealing whereas x=0.00, 0.20 and 0.30 samples show behaviour that is almost independent of annealing.

For all compositions, noisy strain-electric field loops were acquired even after averaging multiple loops. The significantly large noise coupled with the low values for the strain response highlight the extreme ferroelectric hardness of this solid solution.

An interesting feature of the strain-electric field loops for x=0.01, 0.02, 0.05 and 0.10 samples is the anisotropic nature. Using x=0.01 for example (Figure 5.52 (b)), when the electric field is positive a maximum strain of approximately 0.025% is measured however when the electric field is reversed a maximum strain of approximately 0.045% is measured. There is also remanent strain observed through off-centre strain from the origin.

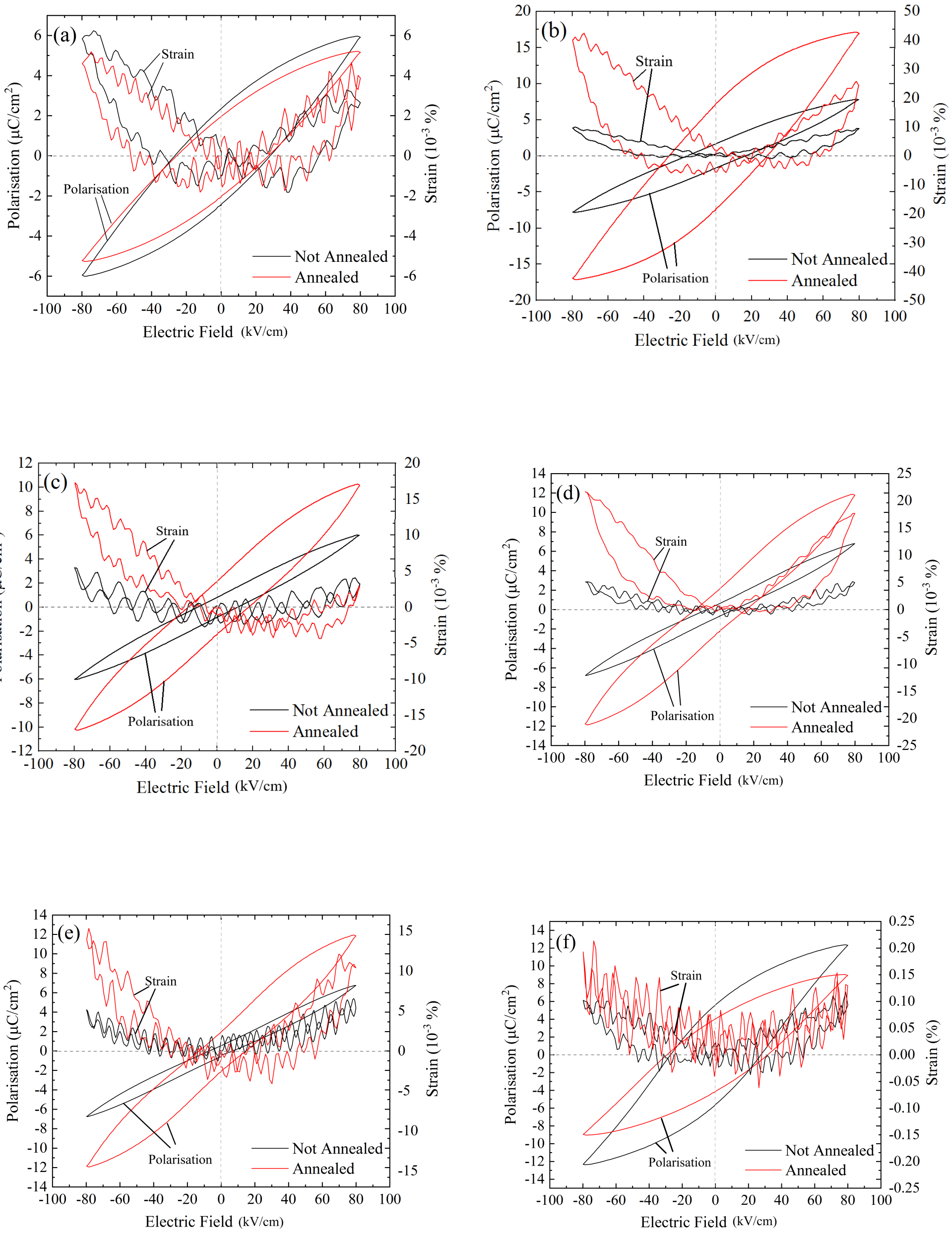

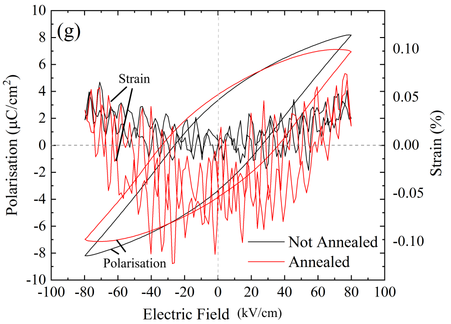

Figure 5.52: Polarisation and strain vs electric field loops for x= (a) 0.00, (b) 0.01, (c) 0.02, (d) 0.05, (e) 0.10, (f) 0.20, and (g) 0.30 Nb:BFPT65. Black lines represent P-E and x-E loops before annealing and red lines represent P-E and x-E loops after annealing

It is thought that the maximum polarisation and remanent polarisation for x=0.01 would mimic the piezoelectric behaviour by showing little response to the external field however the opposite is observed. An explanation for this could be the influence of temperature of the samples when undergoing high voltage testing or poling. All P-E and butterfly loops were carried out at room temperature whereas poling was carried out at 75°C. The shape and size of x=0.01 Nb-doped P-E loops suggests that although the sample is not fully saturated, it is close to reaching it and therefore the remanent polarisation and maximum polarisation at 75° may show little difference to that shown in Figure 5.52 (b). However for x=0.02, 0.05 and 0.10 samples, pinching is still observed even after annealing. The increase in temperature may result in significant swelling of the PE loop to a point where the remanent polarisation and maximum polarisation far exceed values for x=0.01 Nb-doped samples and therefore are able to exhibit greater piezoelectric activity. Polarisation vs electric field loops and butterfly loops as a function of temperature may confirm this.

An interesting observation is the asymmetry of butterfly loops for x=0.01, 0.02, 0.05 and 0.10 Nb samples. This phenomenon is a result of the migration of mobile defects under electrical loading which generates an internal bias field resulting in strain hysteresis asymmetry [205,206] and has been observed in other bismuth-based materials [207,208].

5.3.6 Effect of Annealing Cooling Rate on Piezoelectric and Ferroelectric Properties

In the previous section, it is hypothesised that the difference in the cooling rate between sintering and annealing results in the enhancement of piezoelectric activity in x=0.01, 0.02, 0.05 and 0.10 Nb:BFPT65 polycrystalline ceramics. In order to test this hypothesis, x=0.02 Nb:BFPT65 polycrystalline ceramics were annealed with different programmed cooling rates to observe whether a greater cooling rate would result in improved piezoelectric properties. Samples were fabricated and annealed using an identical heating rate, maximum temperature and dwell time to those mentioned in Section 5.2.2. Programmed cooling rates of 10°C/hour, 20°C/hour, 100°C/hour were used as well as air quenched and water quenched samples and compared to results obtained in this study for samples with an annealing cooling rate of 50°C/hour.

Figure 5.53 and 5.54 show the piezoelectric charge coefficients vs cooling rate and the piezoelectric voltage coefficients vs cooling rate for x=0.02 Nb-doped samples, respectively. Samples cooled at 10°C/hour and 20°C/hour show largely suppressed piezoelectric coefficients with values of 4.4pC/N and 5.1pC/N, respectively. When a greater cooling rate is used, the d_{33} increases to 71.5pC/N for 50°C/hour cooling and 94.2pC/N for 100°C/hour. As postulated in the previous section this increase in piezoelectric activity with increase in cooling rate is evidence for the limiting of defect cluster and defect plane formations which clamp domain walls and reduce the piezoelectric properties, and therefore samples with a more dispersed defect distribution have an increased extrinsic contribution to the piezoelectric effect.

For quenched samples the piezoelectric properties are reduced to 43.3 and 19.2pC/N for air quenched and water quenched samples, respectively. It can also be observed using Figure 5.53 and Figure 5.54 that the 31 and hydrostatic mode follows a similar trend to the 33 mode where the values peak at 100°C/hour cooling rate and decrease for quenched samples.

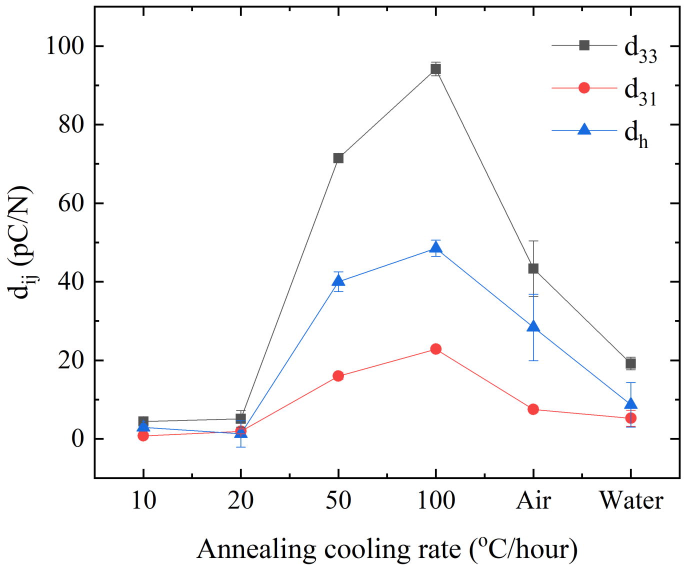

Figure 5.53: Piezoelectric d_{ij} coefficients for x=0.02 Nb-doped BFPT65 polycrystalline ceramics as a function of the annealing cooling rate

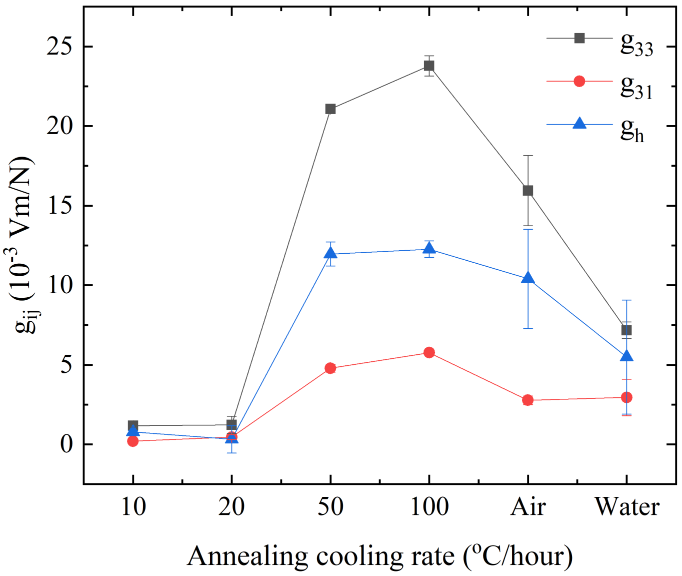

Figure 5.54: Piezoelectric g_{ij} coefficients for x=0.02 Nb-doped BFPT65 polycrystalline ceramics as a function of the annealing cooling rate

Figure 5.55 shows the polarisation vs electric field and strain vs electric field loops for samples of different cooling rates. Similar to trends in the piezoelectric properties, the maximum polarisation and remanent polarisation (Figure 5.56) shows that the most electrically enhanced samples occur when cooled at 100°C/hour before deteriorating for quenched samples. Samples with slow cooling rates show pinched polarisation loops which are indicative of domain wall clamping whereas samples cooled at 50°C/hour and 100°C/hour possess more ideal and wider P-E loops due to the increased domain wall mobility and enhancement of the extrinsic contribution to piezoelectricity. Although quenched samples are found to have inferior maximum polarisation, remanent polarisation and piezoelectric properties than samples cooled at 100°C/hour the shape of the P-E loops do not suggest any pinching effects implying that the suppression of the ferroelectric and piezoelectric properties may stem from other influences unrelated to the defect chemistry.

Similar trends can be observed in the strain-field loops shown in Figure 5.57 in which samples cooled at 10°C/hr and 20°C/hr show little response to the external electric field. Samples cooled at 50°C/hr and 100°C/hr show the most enhanced response to the electric field and response from quenched samples decrease again.

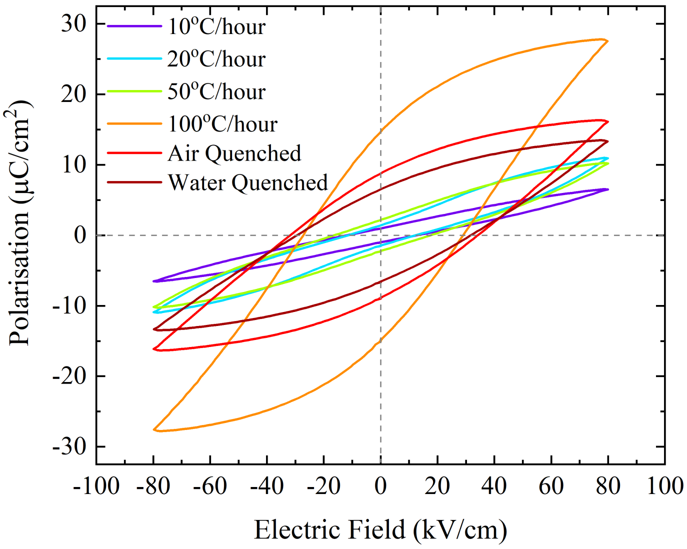

Figure 5.55: Polarisation vs electric field loops for x=0.02 Nb-doped BFPT65 polycrystalline ceramics as a function of the annealing cooling rate

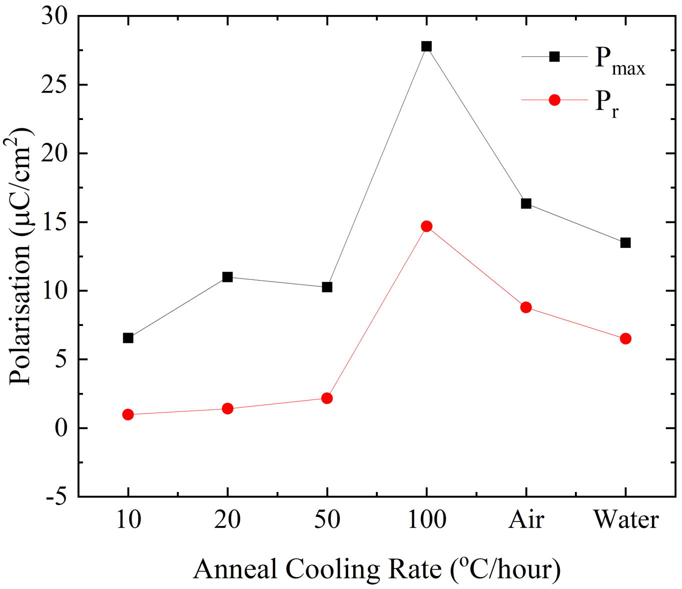

Figure 5.56: Maximum polarisation and remanent polarisation from Figure 5.55 as a function of the annealing cooling rate

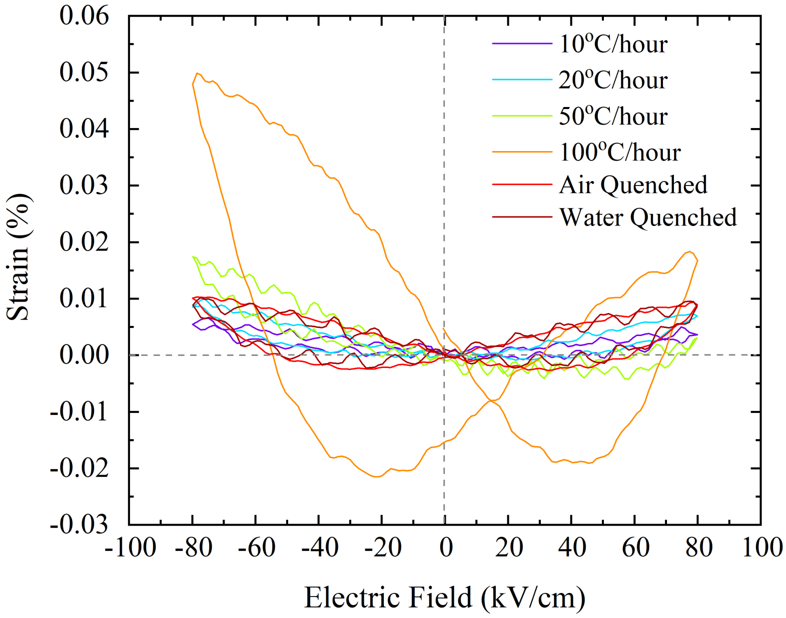

Figure 5.57: Strain vs electric field loops for x=0.02 Nb-doped BFPT65 polycrystalline ceramics as a function of the annealing cooling rate

Although the initial increase in piezoelectric and ferroelectric properties with annealing cooling rate has been attributed to the increase in defect distribution, the reason for the decrease in piezoelectric and ferroelectric properties for quenched samples is unclear. An explanation for this could be the increased amount of intergranular stress.

When a ceramic undergoes a phase transition from cubic to tetragonal upon cooling through T_C, individual grains will experience a volume expansion as a result. When samples are cooled at <100°C/hour, it allows time for grains to ease into configurations so as to minimise the stress between them. However when samples are quenched the grain configuration cannot arrange themselves into comfortable positions and therefore the intergranular stresses are significant enough to suppress contributions to the piezoelectric effect. As discussed in Chapter 3, this may also lead to a decrease in either domain wall density or the suppression of domain wall nucleation and hence reduce the piezoelectric activity.

This explanation may also be used to describe the discrepancy between experimental observations in this study for $BiFeO_3$-$PbTiO_3$ and experimental observations for bismuth ferrite - barium titanate, $BiFeO_3$-$BaTiO_3$ (BFBT). Zheng et al. [209] have shown that quenching BFBT improves the piezoelectric properties due to the increased distribution of defects which inhibit domain wall motion similar to observations in this study and $BiFeO_3$ polycrystalline ceramics [210]. However BFBT is unlikely to show a suppression of intrinsic contributions through intergranular stresses due to the significantly smaller increase in volume when cooling through the Curie temperature. X-ray diffraction studies have found this solid solution to be pseudo-cubic implying little volume expansion and therefore having no limit on the cooling rate [209].

5.3.7 X-Ray Photoelectron Spectroscopy

In order to shed light on the effect of Nb doping on conductivity, X-ray photoelectron spectroscopy has been carried out to understand the changes in ionic valence state as a function of Nb content and the relation to electrical properties. Attention will be paid mostly to the oxygen and B-site ions, however XPS spectra and fits have also been carried out for A-site ions for completeness. Details on experimental procedure can be found in section 5.2.10.

Figure 5.58 show the XPS spectra and fittings for Pb, Bi, O, Fe, Ti and Nb ions for x=0.05 Nb-doped samples. The XPS spectra and fits for all other compositions can be found in Appendix C. The Pb4f peaks at 136.4eV and 141.3eV can be attributed to the $4f_{7/2}$ and $4f_{5/2}$ orbitals for metallic Pb, whilst the peaks located at 137.9eV and 142.7eV can be attributed to the $4f_{7/2}$ and $4f_{5/2}$ orbitals for PbO ions and are found to be in good agreement with literature [188, 211, 212]. The presence of elemental Pb ions is most likely the result of Ar^+ sputter cleaning of the sample and has been observed in

$PbTiO_3$ films which show splitting of both the $4f_{7/2}$and $4f_{5/2}$ peak after sputtering [213]. The phenomenon of elemental formation of Pb has been studied by Wang et al. [214] where the authors explain that as an energetic incident ion such as Ar^+ collides with the surface of the sample, a series of collisions occur which may disrupt the crystallography and lead to an amorphization of the surface layer. Furthermore the incoming ion results in a rapid heating and cooling process which in turn leads to the precipitation of Pb which possesses the lowest melting point of the possible configurations (Pb, PbO, Ti, TiO_2, and $PbTiO_3$).

The Bi4f peaks at 157.0eV and 162.3eV can be attributed to the $4f_{7/2}$ and $4f_{5/2}$ peaks for elemental Bi, whilst peaks at 158.6eV and 164.0eV can be attributed to the $4f_{7/2}$ and $4f_{5/2}$ peaks for Bi_2O_3 and are again found to be in good agreement with literature [188, 215]. The presence of metallic Bi^0 has also been attributed to ionic bombardment as mentioned previously for Pb^0 [216, 217].

For the O1s region, a clear dominant peak which can be assigned to the in-lattice oxygen ions is located at 529.7eV and a clear shoulder at higher binding energies can be attributed to bonding with hydroxide groups on the surface which can also be interpolated as 'dangling bonds' left by oxygen vacancies at 532.1eV [218]. The slight deviation at lower binding energies between the raw data and envelope may be due to the small presence of C-O bonding due to impurities on the sample surface.

For Fe2p ions, the peaks at 711.2eV and 709.6eV can be assigned to Fe^{3+} and Fe^{2+}, respectively, and for Ti2p ions the peaks at 458.9eV and 457.8eV are assigned to Ti^{4+} and Ti^{3+}, respectively. Due to insufficient signal-to-noise for the Nb3p peaks, it is assumed that they remain 5+ throughout, an assumption that is supported by literature [219–222].

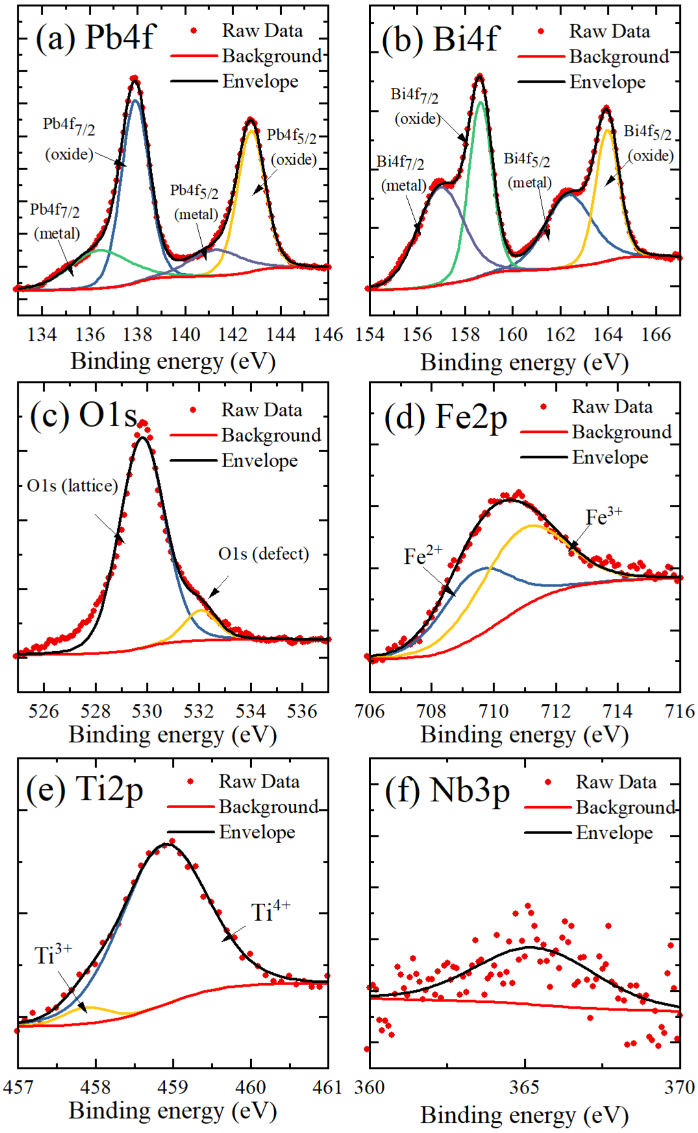

Figure 5.58: X-ray photoelectron spectroscopy spectra and fits for (a) Pb4f, (b) Bi4d, (c) O1s, (d) Fe2p, (e) Ti2p, and (f) Nb3p orbitals for unannealed, x=0.05 Nb:BFPT65 polycrystalline ceramics

Figure 5.59 shows the relative concentrations of ionic valence as a function of Nb content for unannealed samples. The relationship between the presence of metallic A-site ions with respect to oxidised A-site ions and loss of volatiles through processing is unclear. However it may be deduced that for Pb4f orbitals the concentration of Pb^{2+} is dominant with little (<5%) presence of Pb^0 for x=0.02, 0.10, 0.20 and 0.30 doped samples. For x=0.05 there is a significant increase in the presence of Pb0 (27.5%). A similar trend can be observed for the bismuth 4f orbitals with the highest presence of Bi^{3+} observed in x=0.02, 0.10, 0.20 and 0.30 with a significant increase in the metallic species for x=0.05.

For the O1s peaks, undoped samples start with a defect concentration of approximately 36.9% which may contribute to the high conductivity. Despite Figure 5.48 and 5.49 showing a reduction in conductivity with x=0.01 Nb, which is evidence for a reduction in oxygen vacancy concentration, it is found to be unchanged for x=0.01 doped samples. The concentration of oxygen lattice ions increases to 82.7% and 90.6% for x=0.02 and x=0.05 Nb-doped samples, respectively. The lattice oxygen concentration then decreases to 66.3% for x=0.10 and 51.1% for x=0.20 and finally increasing again to 86.4% for x=0.30.

For the Fe2p region, undoped BFPT65 samples are found to possess approximately 50/50 ratio between Fe^{3+}/Fe^{2+} ions. The Fe^{3+} concentration increases to 71.5% for x=0.01 and 78.6% for x=0.02. The Fe^{3+} decreases significantly to 55.6% for x=0.05. Although it is mentioned previously that the relationship between A-site metal ion presence and loss of volatiles through processing is unclear, the similar trend between A-site metal ion presence and Fe^{2+} concentration for x=0.05 may provide a relation. When lead loss and bismuth loss occurs, it can be electrochemically neutralised through the formation of oxygen vacancies using Equations 5.32 and 5.33:

$$PbO_s \rightarrow PbO_V \uparrow + V''_{Pb} + V_O^{\cdot\cdot} \tag{5.32}$$

$$Bi_2O_{3s} \rightarrow Bi_2O_{3V} \uparrow + 2V'''_{Bi} + 3V_O^{\cdot\cdot} \tag{5.33}$$

In the case of x=0.05 Nb-doped samples, the formation of oxygen vacancies is suppressed through the introduction of Nb and therefore the electrochemical neutrality is maintained through the reduction of Fe^{3+} and generation of free charge carriers.

$$\begin{gathered}3O_O^X + 3V_O^{\cdot\cdot} + (2-2x)Fe_{Fe}^X + (x)Nb_2O_5 \rightarrow \\ (2-4x)Fe_{Fe}^X + (2x)Fe'_{Fe} + (2x)Nb_{Fe}^{\cdot\cdot} + 6O_O^X + O_2 \uparrow + (6-2x)h^{\cdot}\end{gathered} \tag{5.34}$$

The commitment to consistent processing throughout this study means the reason for the exaggerated loss of volatiles for this composition is unclear. Fe^{3+} concentration increases again for x=0.10 Nb samples to 79.3% and decreases again to 57.8% and 48.3% for x=0.20 and x=0.30 Nb-doped samples, respectively. The decrease in Fe^{3+} concentration may be due to over-doping which may contribute to an increase in free charge carriers above a certain threshold or the reduction in Fe^{3+}.

For Ti ions, there is a significant proportion of Ti^{3+} ions for undoped BFPT which, similar to the reduction of Fe ions, can contribute to the free charge carrier concentration which results in significant conductivity.

$$Ti^{4+} \rightarrow Ti^{3+} + h^{+} \tag{5.35}$$

For x=0.01 Nb, the concentration of Ti^{3+} increases to 50.2%. Up until this point the decrease in the piezoelectric activity with the introduction of x=0.01 Nb is unclear, however XPS analysis may provide an answer. As shown in Figure 5.59 there is a significant concentration of Ti^{3+} most likely due to the loss of volatiles and a significant number of oxygen vacancies due to insufficient Nb. The significant number of these defects will likely result in the increase in Ti^{3+}-$V_O^{\cdot\cdot}$ bonding which forms a local field pinning domain walls. This increase in domain wall pinning results in a ferroelectrically harder material and is the reason for the initial decrease in the d_{33} with x=0.01 Nb even after annealing. At higher Nb contents the concentration of oxygen vacancies decreases and therefore reduces the Ti^{3+}-$V_O^{\cdot\cdot}$ concentration and subsequent domain wall pinning. For x=0.02 samples, the concentration of Ti^{3+} decreases to 14.3% and then increases to 23.1% for x=0.05 Nb-doped samples. The reason for the increase in Ti^{3+} concentration may be due to the loss of volatiles during fabrication, similar to what is observed for Fe^{2+} ions. The concentration of Ti^{3+} ions decreases again for highly Nb-doped samples and remains approximately 3.0%.

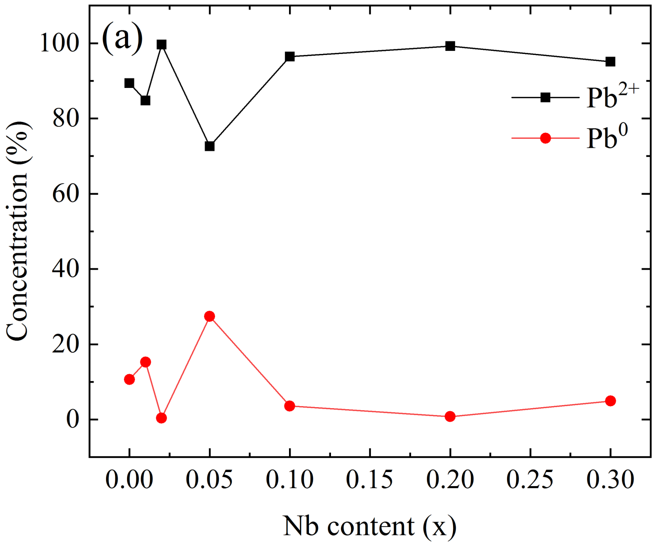

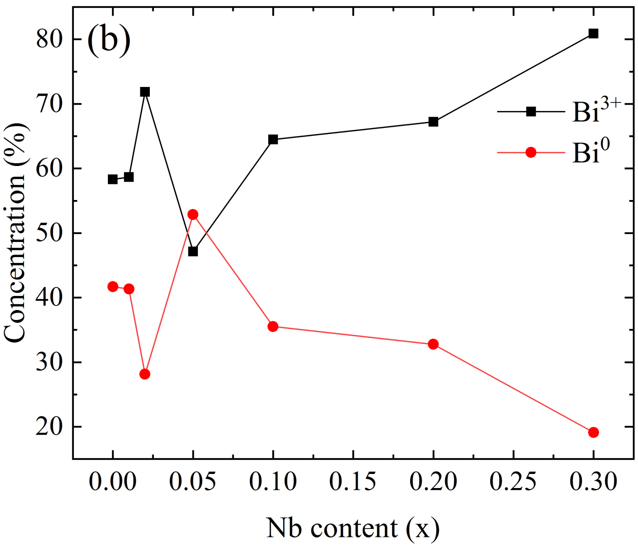
(b)
Concentration (%)
80
70
60
50
40
30
20
0.00
0.05
0.10
0.15
0.20
0.25
0.30
Nb content (x)
Bi^{3+}
Bi^{0}

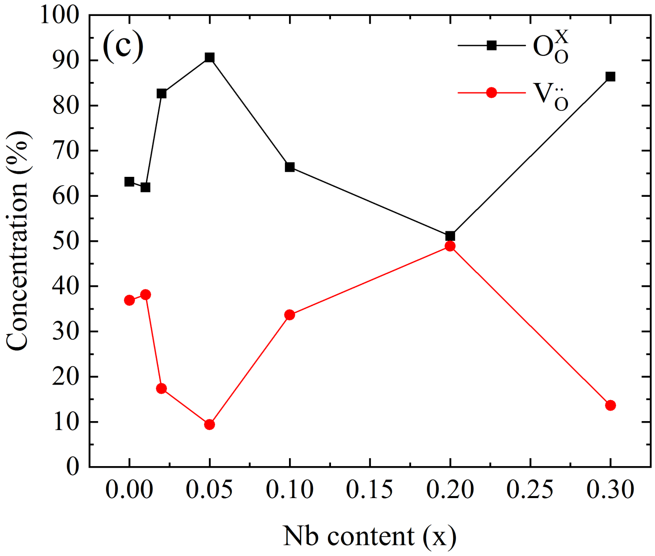
(c)
Concentration (%)
100
90
80
70
60
50
40
30
20
10
0
0.00
0.05
0.10
0.15
0.20
0.25
0.30
Nb content (x)
O_O^X
$V_{\ddot{O}}$

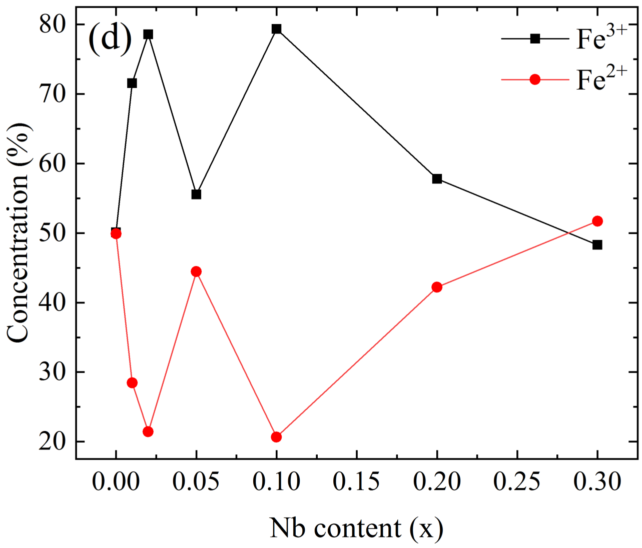

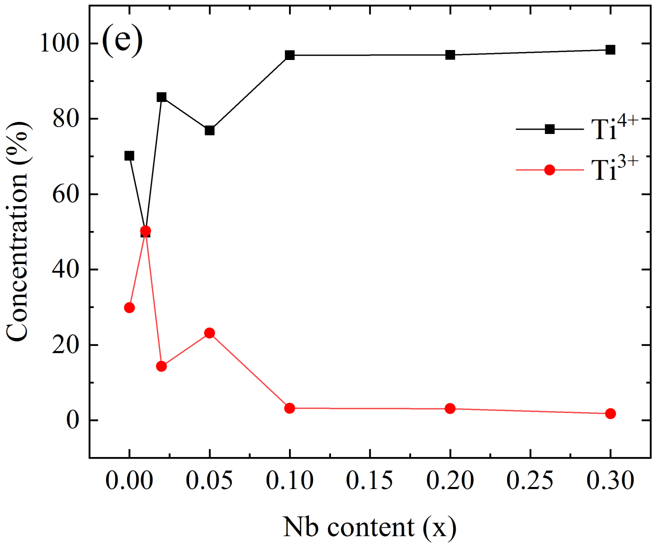

Figure 5.59: Relative concentration of (a) Pb^{2+} and metallic Pb^0 ions, (b) Bi^{3+} and metallic Bi^0 ions, (c) Lattice O_O^X and defect $V_O^{\cdot\cdot}$ ions, (d) Fe^{3+} and Fe^{2+} ions, and (e) Ti^{3+} and Ti^{4+} ions as a function of Nb content for unannealed BFPT65 samples

When comparing the chemical and electrical properties, three key observations can be made. Firstly there is a clear correlation between the concentration of oxygen ions within the lattice in Figure 5.59 (c) and the piezoelectric d_{33} for annealed samples shown in Figure 5.29. Although there is a discrepancy between the two trends at x=0.30 Nb-doped samples, this is because XPS analysis shows the concentration of valence states within both the piezoelectric perovskite region and the non-piezoelectric pyrochlore phase whereas the contribution to the d_{33} response is purely from the perovskite phase.

The second key observation is the relationship between the high signal leakage current which reflects the conductivity of a sample and the concentration of Fe^{2+} ions shown in Figure 5.60. This indicates that although the oxygen vacancy concentration will still be an important influence in the assisting of Fe^{3+}/Fe^{2+} hopping, the main contribution to the bulk conductivity is the concentration of Fe^{2+} ions which is an indication of free charge carrier concentration.

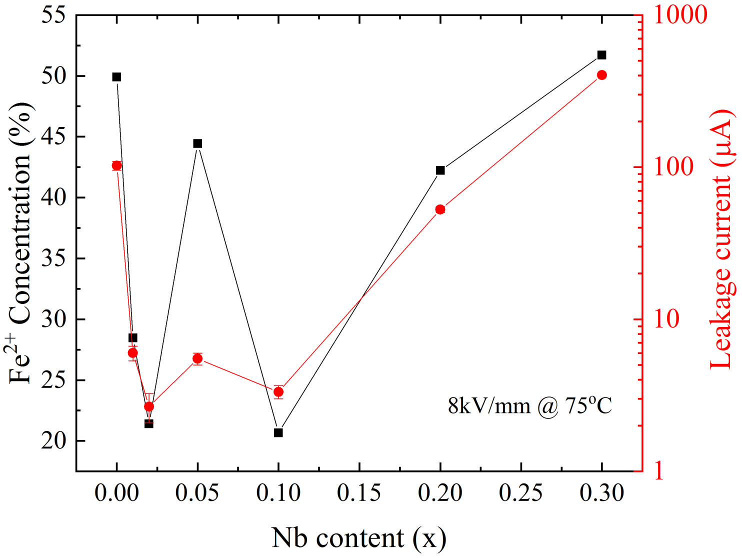

Figure 5.60: Fe^{2+} concentration and leakage current measured during poling at 8kV/mm at 75°C as a function of Nb content

The final observation is the coherence between the chemical properties of unannealed samples and the electrical analysis of annealed samples. This is of significance as it is evidence that the improvement of the piezoelectric properties is due to the redistribution of defects rather than replenishment. Conventional wisdom suggests that this should be the case as the annealing is not carried out in an O_2 atmosphere nor in the presence of additional Bi or Pb powder. However this assumption is useful to observe rather than speculate. Due to time restraints, XPS analysis was carried out only for unannealed samples and for a complete study XPS should also be carried out on annealed samples. If the above hypothesis is correct and the improvement in piezoelectric performance is primarily down to defect distribution, then the concentration of valence states particularly of oxygen ions should remain the same as those for unannealed samples.

5.4 Summary

The characterisation of $0.65Bi_{(1-2x/3)}Fe_{(1-x)}Nb_xO_3$-$0.35PbTiO_3$ (x=0.00, 0.01, 0.02, 0.05, 0.10, 0.20, 0.30) polycrystalline ceramics has been carried in this chapter. Structural characterisation using X-ray diffraction (Section 5.3.1) showed a mixed phase $P4mm$+$R3c$ pervoskite structure for all samples. Samples with Nb content x=0.05 give rise to a pyrochlore phase which becomes more prominent with increaseing Nb content. This phenomenon is also observed in scanning electron micrscopy studies shown in Section 5.3.2 with the increasing presence of non-textured areas which lack domain structure with Nb content. Permittivity vs temperature (Section 5.3.3) and impedance spectroscopy (Section 5.3.5) show the emergence of a significant conduction relaxation mechanism after annealing, and a significant increase in piezoelectric properties (Section 5.3.4) is also observed after annealing. It is thought that the discrepancy in cooling rate between sintering and annealing results in a higher and lower order of defect clustering which clamp domain walls, similar to what is observed in other $BiFeO_3$-based ferroelectrics. A short anneal cooling rate study (Section 5.3.6) showed that a faster cooling rate resulted in larger piezoelectric properties up to 100°C/hr, with air and water quenching samples showing smaller piezoelectric d_{ij} and g_{ij} coefficients due to an increased degree of intergranular stress. X-ray photoelectron spectroscopy (Section 5.3.7) showed a correlation between the concentration of oxygen ions before annealing and the piezoelectric properties after annealing, implying that the improvement of piezoelectric properties is a defect redistribution effect rather than a result of vacancy replenishment. With regards to conductivity, the substitution of Fe^{3+} for Nb^{5+} improves the insulative properties evidenced by a reduction in low signal (1V) AC and DC conductivity (Figure 5.48 & 5.49) for all doped samples compared to undoped BFPT. High signal (8kV/mm) leakage current at 75°C also decreases for Nb content x=0.01, 0.02, 0.05 and 0.10 compared to undoped material. Further work to this project is highlighted in Section 6.1.

Chapter 6

Conclusions

As stated in Chapter 1, the aims and objectives of this project were:

- To understand the mechanisms from a fundamental materials science perspective that drive a high piezoelectric voltage coefficient and study the scientific and practical limitations
- Use this knowledge to propose other materials that may outperform current military grade devices

This work has led to three main outcomes: the identification of the mechanism and the scientific and practical limitations of high g_{ij} piezoelectric materials, provided evidence for the solid solution between $BiFeO_3$ and $PbTiO_3$ possessing improved g_{ij} coefficients compared to current military grade devices and previously reported work, and highlight the viability of Nb-doping in combatting the conductivity and improving functionality of $BiFeO_3$-$PbTiO_3$.

Chapter 3 showed from a materials science perspective that tetragonality is the main mechanism behind the g_{ij} coefficient for single crystals and textured ceramics. For polycrystalline ceramics, the introduction of significant microstructural effects such as intergranular stresses and pinning of domain walls at grain boundaries suppress the g_{ij} coefficients above 2-3% tetragonality. Despite previous reports claiming a relationship between electronegativity and g_{33} coefficient, no such relationship was observed when considering a wider range of materials. This work also highlighted the exhaustion of possible material candidates in polycrystalline form for achieving larger g_{ij}. The main conclusion to this work shows that a significant increase in g_{ij} will most likely be found in $BiFeO_3$-$PbTiO_3$ and $Bi(Zn,Ti)O_3$-$PbTiO_3$ in single crystal or textured ceramic form. Ultimately it is up to industry's agenda, budget and consumer demand which dictates whether these piezoelectrics will take single crystal or textured form. However the scalability of large single crystal fabrication for highly tetragonal materials remains questionable, and a more suitable approach may be the use of textured ceramics in the future.

In order to provide supportive evidence for the enhanced g_{ij} coefficient in $BiFeO_3$-$PbTiO_3$, Landau-Devonshire theory was used in Chapter 4 to calculate the dielectric and piezoelectric properties. A coherence between theoretical and experimentally derived phase diagrams was observed when the compositional dependence is modelled as a linear relationship between the Landau coefficients of each end member. Most significantly, it provided a theoretical location of the morphotropic phase boundary being $0.696BiFeO_3$-$0.304PbTiO_3$ at 25°C. However this method failed to correctly describe the spontaneous strain behaviour and therefore the dielectric and piezoelectric properties were not considered. By treating the compositional dependence as an external tensile stress acting to elongate the unit cell within the tetragonal region in order to mimic experimental observations, the dielectric and piezoelectric properties could be extracted. The g_{33}, g_{31} and g_h of $0.70BiFeO_3$-$0.30PbTiO_3$ were calculated to be 207.9×10^{-3}, -60.7×10^{-3} and 78.8×10^{-3} Vm/N, respectively, exceeding previously reported values of any material both experimentally and theoretically.

Although $BiFeO_3$-$PbTiO_3$ may possess desirable voltage coefficients, the solid solution is plagued with ferroelectric hardness and large conductivity. Chapter 5 aimed to tackle both issues through Nb-doping of polycrystalline samples. Initially x=0.01, 0.02, 0.05, 0.10 Nb appears to suppress piezoelectric activity. However after annealing, all d_{ij} and g_{ij} for these compositions improve. With regards to ferroelectric hardness and functionality, the improvement of the d_{33} from 46.3pC/N for undoped BFPT to 82.0pC/N for x=0.05 Nb-doped BFPT65 is evidence for softening. At higher Nb quantities, an undesirable non-piezoelectric secondary phase becomes more prominent and thus reduces the d_{33}. All Nb quantities showed a reduction in low signal AC and DC conductivity with the initial introduction of x=0.01 niobium decreasing the conductivity by an order of magnitude. For high field signal (8kV/mm), the leakage current at 75°C decreases from 102.3μA for undoped BFPT to 6.0μA, 2.7μA, 5.5μA, 3.3μA and 52.7μA for x=0.01, 0.02, 0.05, 0.10 and 0.20 Nb samples. x=0.30 samples exhibited a leakage current of 403.0μA.

It was shown that the difference in activation energies of the grain and grain boundary conduction mechanisms, which may be used as a measure of electrochemical heterogeneity within the grain, can be directly compared to the piezoelectric coefficients of annealed samples. This also implies that the improved performance of the samples after annealing is a defect related phenomenon and it was hypothesised that the difference in cooling rate between the sintering and annealing regimes was responsible. When samples are initially fabricated, a slow cooling rate is employed to relieve the stresses associated with the cubic to tetragonal transition. This slow cooling rate gives time for defects to arrange themselves in clusters and planes which inhibit domain wall motion and reduce the extrinsic contribution to piezoelectricity. During annealing the defects are redistributed and the faster cooling rate results in a greater defect distribution which reduces domain wall clamping and therefore piezoelectric properties are improved. An annealing cooling rate study partially confirmed this hypothesis however showed that quenching reduces the piezoelectric activity contrary to what is observed for $BiFeO_3$-$BaTiO_3$ polycrystalline ceramics. This discrepancy is due to the far greater elastic stresses that are associated with $BiFeO_3$-$PbTiO_3$. Finally XPS on unannealed samples showed a correlation between the chemical valence states of ions and defects and the piezoelectric properties, showing further evidence for the hypothesis that defect distribution and reduced domain wall clamping is the mechanism behind enhanced piezoelectric activity.

6.1 Future Work

With regards to further understanding the science behind the voltage coefficient, more datapoints are always useful as they may support and cement hypotheses in this thesis. More specifically, datapoints from a wider range of materials may help shed light on the relationship, if any, between the voltage coefficient and electronegativity.

According to Figure 3.5 the limit of tetragonality in polycrystalline materials lies at approximately 2-3% at which point intergranular stresses suppress the g_{ij} coefficient. In single crystals this limit is eliminated due to the lack of grain boundaries and possession of long-range translational symmetry. It would be interesting to investigate whether the microstructural effects that are observed in polycrystalline samples and ultimately limit the g_{33} at high tetragonalities are also present in textured ceramic form. As of yet there are not enough datapoints to investigate this, however evidence suggests that if a tetragonality limit exists, that it is above the 2-3% observed in polycrystalline samples. As mentioned in Section 3.3.1, work on textured modified lead titanate ceramics achieved a g_{33} of $115\text{x}10^{-3}$Vm/N suggesting that textured ceramics follow a trend more familiar with single crystals. Although the tetragonality is not quoted in this work, the tetragonality is estimated to be between 4-5% based on other work of similar composition.

With regards to future work associated with the Landau-Devonshire description of $BiFeO_3$-$PbTiO_3$ two key points of interest arises. Firstly, it will be useful to experimentally determine the compositional dependence between the Landau coefficients of each end member. Although this ideally should be done by measuring the properties of single crystals, this problem may be bypassed by using polycrystalline samples and similar mathematical methodology to that of Ref. [161]. Secondly is the exploration of modelling the unusual spontaneous strain by other means. One potential alternative could be by modelling the elongation of the unit cell as a result of a bias field as opposed to an external tensile stress. This will be interesting as the additional free energy term due to the electric field incorporates the polarisation as P^1 which differs from the tensile stress model which incorporates the polarisation as P^2. Therefore, the electric field term will drop out of calculations one step earlier than the tensile stress term when differentiating the free energy twice in order to calculate material properties.

With regards to future work associated with Nb-doped BFPT65, there are two branches of future work; material performance and further study of defect chemistry. The piezoelectric performance of Nb-doped BFPT65 may be improved by the following ways:

- **Optimisation of poling conditions** – the poling regime for this study (8kV/mm, 75°C, 5 minutes) was determined through optimisation of pure BFPT65 samples, conditions which were ultimately limited by the significant conductivity and breakdown of samples. The reduction in conductivity with Nb substitution suggests that poling at higher fields, higher temperatures and for longer times may be achievable which in turn may improve piezoelectric performance.

- **Niobium content optimisation** – For many of the piezoelectric properties (d_{33}, d_{31}, g_{33}, and g_h), x=0.05 Nb possessed the highest values. Fabricating and testing a range of Nb contents between x=0.02-0.10 will indicate more precisely the highest piezoelectric performance x=0.02-0.10.

- **Annealing cooling rate study** – As shown in Section 5.3.6, the cooling rate of the annealing regime has a significant influence on the piezoelectric activity. An optimisation study will find the point at which the suppression of piezoelectric activity from intergranular stresses due to high cooling rates outweighs the piezoelectric enhancement contribution from reduced domain wall pinning.

- **(x)BiFeO$_3$-(1-x)PbTiO$_3$ composition** – in this study a base stoichiometry of 0.65BiFeO$_3$-0.35PbTiO$_3$ was chosen (a) to be close enough to the MPB in an attempt to exploit the large spontaneous strain, and (b) to be far enough away from the MPB so that the introduction of dopants would not result in samples becoming purely rhombohedral. Although large tetragonalities were achieved, the coexistence of $P4mm$ and $R3c$ phases results in the improvement of the dielectric properties which limits the g_{ij} coefficients. Therefore, it may be of value to investigate the solid solution of (x)BiFeO$_3$-(1-x)PbTiO$_3$ at BiFeO$_3$ content x<0.40 where the spontaneous strain is still larger than lead titanate but possesses a pure $P4mm$ phase.

With regards to further understanding the science behind the defect chemistry in Nb-doped BFPT systems, two main investigations would be useful. First is the carrying out of X-ray photoelectron spectroscopy on annealed samples and comparing the chemical properties with those shown in Section 5.3.7. The second would be a more thorough elemental imaging and mapping through energy dispersive X-ray (EDX). In this work the aggressive chemical etching resulted in intragranular pores making EDX chemical analysis of the core-shell structure difficult. By optimising time of submergence in etchant and/or investigating less aggressive etchants, it may be possible to preserve the sample throughout the grain which would allow for thorough EDX analysis. Elemental mapping before and after annealing would shed light on which elements and defects are present within the grain and grain boundaries and the degree of defect distribution at different annealing cooling rates.

Chapter 7

Bibliography

[1] A. J. Moulson and J. M. Herbert. *Electroceramics: Materials, Properties, Applications,* 2nd edition. Chichester: John Wiley & Sons, 2003.

[2] CTS. PZT Materials, Product: 3265HD, Datasheet [online], 2018. [Date accessed: 17/01/2020. Available from: https://www.ctscorp.com/wp-content/uploads/CTS_-PZT-Materials_Complete-Properties_20180829.pdf].

[3] TRS Technologies. High Performance PMN-PT Piezoelectric Single Crystals, Product: X2b, Datasheet [online]. [Date accessed: 17/01/2020. Avaible from: http://www.trstechnologies.com/Materials/High-Performance-PMN-PT-Piezoelectric-Single-Crystal].

[4] M. Kahn, D. P. Burks, I. Burn, W. A. Schulze, and L. M. Levinson. *Electronic Ceramics: Properties, Devices and Applications.* New York: Marcel Dekker, 1988.

[5] C. R. Bowen, V. Y. Topolov, and H. A. Kim. *Modern Piezoelectric Energy-Harvesting Materials*, volume 238. Switzerland: Springer International Publishing, 2016.

[6] L. Atzori, A. Iera, and G. Morabito. The Internet of Things: A Survey. *Computer Networks*, 54(15):2787–2805, 2010.

[7] J. R. Hook and H. E. Hall. *Solid State Physics,* 2nd edition. Chichester: John Wiley & Sons Ltd, 2013.

[8] C. Suryanarayana and M. G. Norton. *X-Ray Diffraction: A Practical Approach,* 2nd edition. New York: Springer Science & Business Media, 2013.

[9] C. Hammond. *The Basics of Crystallography and Diffraction,* 3rd edition. New York: Oxford University Press Inc., 2009.

[10] M. T. Sebastian. *Dielectric Materials for Wireless Communication.* Amsterdam: Elsevier, 2008.

[11] T. Ishihara. *Perovskite Oxide for Solid Oxide Fuel Cells.* New York: Springer Science & Business Media, 2009.

[12] H. D. Megaw. Ferroelectricity and Crystal Structure. II. *Acta Crystallographica*, 7(2):187–194, 1954.

[13] R. E. Smallman and R. J. Bishop. *Modern Physical Metallurgy and Materials Engineering.* Oxford: Elsevier Science Ltd., 1999.

[14] G. Murray, C. White, and W. Weise. *Introduction to Engineering Materials: Behavior: Properties, and Selection.* New York: Marcel Dekker, Inc., 1993.

[15] G. G. Raju. *Dielectrics in Electric Fields.* New York: Taylor & Francis, 2003.

[16] T. Mitsui. Ferroelectrics and Antiferroelectrics. In *Handbook of Condensed Matter and Materials Data*, pages 903–938. Heidelberg: Springer, 2005.

[17] Y. Xu. *Ferroelectric Materials and Their Applications.* Amsterdam: Elsevier Science Publishers B.V., 2013.

[18] D. Court, C. Cmolik, and H. Jaffe. Piezoelectric Properties of Polycrystalline Lead Titanate Zirconate Compositions. *Proceedings of the Institute of Radio Engineers*, 48(2):220–229, 1960.

[19] K. Uchino. *Ferroelectric Devices,* 2nd edition. Boca Raton: CRC Press, 2010.

[20] B. Jaffe, H. H. Jaffe, and W. R. Cook. *Piezoelectric Ceramics.* London: Academic Press Inc., 1971.

[21] J. Guyonnet. Domain Walls in Ferroelectric Materials. In *Ferroelectric Domain Walls: Statics, Dynamics, and Functionalities Revealed by Atomic Force Microscopy*, pages 7–24. Switzerland: Springer Interenational Publishing, 2014.

[22] D. Damjanovic. Hysteresis in Piezoelectric and Ferroelectric Materials. *The Science of Hysteresis*, 3:337–465, 2006.

[23] D. Damjanovic. Ferroelectric, Dielectric and Piezoelectric Properties of Ferroelectric Thin Films and Ceramics. *Reports on Progress in Physics*, 61(9):1267, 1998.

[24] A. B. Kounga, T. Granzow, E. Aulbach, M. Hinterstein, and J. Rödel. High-Temperature Poling of Ferroelectrics. *Journal of Applied Physics*, 104(2):024116, 2008.

[25] A. K. Batra and M. D. Aggarwal. *Pyroelectric Materials: Infrared Detectors, Particle Accelerators and Energy Harvesters*. Washington: SPIE Press, 2013.

[26] W. B. White. Basic Science of Advanced Ceramics. In *Handbook of Advanced Ceramics: Materials, Applications, Processing and Properties*, chapter 1, pages 3–80. London: Academic Press Inc., 2003.

[27] A. Halliyal, A. Safari, A. S. Bhalla, R. E. Newnham, and L. E. Cross. Grain-Oriented Glass-Ceramics for Piezoelectric Devices. *Journal of the American Ceramic Society*, 67(5):331–335, 1984.

[28] A. J. Bell. Factors Influencing the Piezoelectric Behaviour of PZT and Other "Morphotropic Phase Boundary" Ferroelectrics. *Journal of Materials Science*, 41(1):13–25, 2006.

[29] H. Janocha. *Adaptronics and Smart Structures: Basics, Materials, Design, and Applications*. Heidelberg: Springer, 1999.

[30] S. Trolier-McKinstry, S. Zhang, A. J. Bell, and X. Tan. High-Performance Piezoelectric Crystals, Ceramics, and Films. *Annual Review of Materials Research*, (0), 2017.

[31] W. Jo, E. Erdem, R. A. Eichel, J. Glaum, T. Granzow, D. Damjanovic, and J. Rödel. Effect of Nb-Donor and Fe-Acceptor Dopants in $(Bi_{1/2}Na_{1/2})TiO_3$-$BaTiO_3$-$(K_{0.5}Na_{0.5})NbO_3$ Lead-Free Piezoceramics. *Journal of Applied Physics*, 108(1):014110, 2010.

[32] G. Shirane, S. Hoshino, and K. Suzuki. X-ray Study of the Phase Transition in Lead Titanate. *Physical Review*, 80(6):1105, 1950.

[33] V. G. Bhide, M. S. Hegde, and K. G. Deshmukh. Ferroelectric Properties of Lead Titanate. *Journal of the American Ceramic Society*, 51(10):565–568, 1968.

[34] J. Tichỳ, J. Erhart, E. Kittinger, and J. Prívratská. *Fundamentals of Piezoelectric Sensorics: Mechanical, Dielectric, and Thermodynamical Properties of Piezoelectric Materials.* New York: Springer Science & Business Media, 2010.

[35] T. Stevenson, D. G. Martin, P. I. Cowin, A. Blumfield, A. J. Bell, T. P. Comyn, and P. M. Weaver. Piezoelectric Materials for High Temperature Transducers and Actuators. *Journal of Materials Science: Materials in Electronics*, 26(12):9256–9267, 2015.

[36] V. V. S. S. Sai Sunder, A. Halliyal, and A. M. Umarji. Investigation of Tetragonal Distortion in the $PbTiO_3$–$BiFeO_3$ System by High-Temperature X-ray Diffraction. *Journal of Materials Research*, 10(5):1301–1306, 1995.

[37] P. Royen and K. Swars. Das System Wismutoxyd-Eisenoxyd im Bereich von 0 bis 55mol% Eisenoxyd (The System of Bismuth Oxide Iron Oxide Range from 0 to 55mol% Iron Oxide). *Angewandte Chemie*, 69(24):779–779, 1957.

[38] J. Wu, Z. Fan, D. Xiao, J. Zhu, and J. Wang. Multiferroic Bismuth Ferrite-Based Materials for Multifunctional Applications: Ceramic Bulks, Thin Films and Nanostructures. *Progress in Materials Science*, 84:335–402, 2016.

[39] G. Catalan and J. F. Scott. Physics and Applications of Bismuth Ferrite. *Advanced Materials*, 21(24):2463–2485, 2009.

[40] X. Chen, J. Wang, G. Yuan, D. Wu, J. Liu, J. Yin, and Z. Liu. Structure, Ferroelectric and Piezoelectric Properties of Multiferroic $Bi_{0.875}Sm_{0.125}FeO_3$ Ceramics. *Journal of Alloys and Compounds*, 541:173–176, 2012.

[41] G. L. Yuan and S. W. Or. Enhanced Piezoelectric and Pyroelectric Effects in Single-Phase Multiferroic $Bi_{1-x}Nd_xFeO_3$ (x= 0-0.15) Ceramics. *Applied Physics Letters*, 88(6):062905, 2006.

[42] Q. Xu, H. Zai, D. Wu, Y. K. Tang, and M. X. Xu. The Magnetic Properties of $BiFeO_3$ and $Bi(Fe_{0.95}Zn_{0.05})O_3$. *Journal of Alloys and Compounds*, 485(1-2):13–16, 2009.

[43] M. Kumar and K. L. Yadav. Rapid Liquid Phase Sintered Mn Doped $BiFeO_3$ Ceramics with Enhanced Polarization and Weak Magnetization. *Applied Physics Letters*, 91(24):242901, 2007.

[44] Y. Wei, X. Wang, J. Jia, and X. Wang. Multiferroic and Piezoelectric Properties of 0.65$BiFeO_3$-0.35$BaTiO_3$ Ceramic with Pseudo-Cubic Symmetry. *Ceramics International*, 38(4):3499–3502, 2012.

[45] Z. Z. Ma, Z. M. Tian, J. Q. Li, C. H. Wang, S. X. Huo, H. N. Duan, and S. L. Yuan. Enhanced Polarization and Magnetization in Multiferroic (1-x)$BiFeO_3$-x$SrTiO_3$ Solid Solution. *Solid State Sciences*, 13(12):2196–2200, 2011.

[46] T. Stevenson and T. P. Comyn. Piezoelectric Properties of $BiFeO_3$–$PbTiO_3$ Ceramics. *Journal de Physique IV*, 128:13–17, 2005.

[47] S. A. Fedulov, P. B. Ladyzhinskii, I. L. Pyatigorskaya, and Y. N. Venevtsev. Complete Phase Diagram of the $PbTiO_3$-$BiFeO_3$ System. *Soviet Physics-Solid State*, 6(2):375–378, 1964.

[48] D. I. Woodward, I. M. Reaney, R. E. Eitel, and C. A. Randall. Crystal and Domain Structure of the $BiFeO_3$-$PbTiO_3$ Solid Solution. *Journal of Applied Physics*, 94(5):3313–3318, 2003.

[49] W. M. Zhu, H. Y. Guo, and Z. G. Ye. Structural and Magnetic Characterization of Multiferroic $(BiFeO_3)_{1-x}$–$(PbTiO_3)_x$ Solid Solutions. *Physical Review B*, 78(1):014401, 2008.

[50] S. Bhattacharjee and D. Pandey. Stability of the Various Crystallographic Phases of the Multiferroic (1- x)$BiFeO_3$-(x)$PbTiO_3$ System as a Function of Composition and Temperature. *Journal of Applied Physics*, 107(12):124112, 2010.

[51] T. Leist, T. Granzow, W. Jo, and J. Rödel. Effect of Tetragonal Distortion on Ferroelectric Domain Switching: A Case Study on La-doped $BiFeO_3$-$PbTiO_3$ Ceramics. *Journal of Applied Physics*, 108(1):014103, 2010.

[52] R. T. Smith, G. D. Achenbach, R. Gerson, and W. J. James. Dielectric Properties of Solid Solutions of $BiFeO_3$ with Pb(Ti, Zr)O_3 at High Temperature and High Frequency. *Journal of Applied Physics*, 39(1):70–74, 1968.

[53] T. Leist, W. Jo, T. Comyn, A. J. Bell, and J. Rödel. Shift in Morphotropic Phase Boundary in La-doped $BiFeO_3$–$PbTiO_3$ Piezoceramics. *Japanese Journal of Applied Physics*, 48(12R):120205, 2009.

[54] T. Stevenson, J. Bennett, A. P. Brown, T. Wines, A. J. Bell, R. I. Smith, and T. P. Comyn. Reversible Piezomagnetoelectric Switching in Bulk Polycrystalline Ceramics. *APL Materials*, 2(8):086105, 2014.

[55] A. J. Bell, T. Schlegel, M. Alduraibi, M. A. Khan, T. P. Comyn, and J. Rodel. Impedance Spectroscopy of Mn-doped $BiFeO_3$-$PbTiO_3$ Ceramics. In *2006 15th IEEE International Symposium on the Applications of Ferroelectrics*, pages 128–131. IEEE, 2006.

[56] J. Chen and J. Cheng. Enhanced High-Field Strain and Reduced High-Temperature Dielectric Loss in $0.6(Bi_{0.9}La_{0.1})(Fe_{1-x}Ti_x)O_3$–$0.4PbTiO_3$ Piezoelectric Ceramics. *Ceramics International*, 41(1):1617–1621, 2015.

[57] D. Pang, C. He, and X. Long. Multiferroic Ternary Solid Solution System of $BiFeO_3$-$NdFeO_3$-$PbTiO_3$. *Journal of Alloys and Compounds*, 709:16–23, 2017.

[58] N. Kumar, B. Narayan, M. Kumar, A. K. Singh, S. Dhiman, and S. Kumar. Effect of Nd $^{3+}$ Substitution on Structural, Ferroelectric, Magnetic and Electrical Properties of $BiFeO_3$-$PbTiO_3$ Binary System. *SN Applied Sciences*, 1(8):874, 2019.

[59] W. M. Zhu and Z. G. Ye. Effects of Chemical Modification on the Electrical Properties of $0.67BiFeO_3$–$0.33PbTiO_3$ Ferroelectric Ceramics. *Ceramics International*, 30(7):1435–1442, 2004.

[60] T. Sahu and B. Behera. Investigation on Structural, Dielectric and Ferroelectric Properties of Samarium-Substituted $BiFeO_3$-$PbTiO_3$ Composites. *Journal of Advanced Dielectrics*, 7(01):1750001, 2017.

[61] T. Sahu, A. K. Patra, and B. Behera. Effect of Gadolinium Doping on Structural, Ferroic and Electrical Properties of $0.8BiGd_xFe_{1-x}O_3$-$0.2PbTiO_3$ (x = 0.00, 0.05, 0.10, 0.15 and 0.20) Composites. *Journal of Alloys and Compounds*, 695:2273–2284, 2017.

[62] J. Cheng, Z. Meng, and L. E. Cross. High-Field and High-t_C Piezoelectric Ceramics Based on Bi(Ga, Fe)O_3-$PbTiO_3$ Crystalline Solutions. *Journal of Applied Physics*, 98(8):084102, 2005.

[63] R. Zuo, Y. Wu, J. Fu, S. Su, and L. Li. Influences of Dopants on $BiFeO_3$–$PbTiO_3$ Ferroelectric Ceramics. *Materials Chemistry and Physics*, 113(1):361–364, 2009.

[64] J. R. Cheng and L. E. Cross. Lanthanum and Gallium co-Modified $BiFeO_3$-$PbTiO_3$ Crystalline Solutions: Lead Reduced Morphotropic Phase Boundary (MPB) Piezoelectric Ceramics. In *IEEE Symposium on Ultrasonics, 2003*, volume 1, pages 354–357. IEEE, 2003.

[65] J. R. Cheng, R. Eitel, and L. E. Cross. Lanthanum-Modified (1-x)$(Bi_{0.8}La_{0.2})(Ga_{0.05}Fe_{0.95})O_3$- x$PbTiO_3$ Crystalline Solutions: Novel Morphotropic Phase-Boundary Lead-Reduced Piezoelectrics. *Journal of the American Ceramic Society*, 86(12):2111–2115, 2003.

[66] A. Safari and E. K. Akdogan. *Piezoelectric and Acoustic Materials for Transducer Applications*. New York: Springer Science & Business Media, 2008.

[67] K. Uchino. *Piezoelectric Actuators and Ultrasonic Motors*, volume 1. Norwell, Kluwer Academic Publishers, 1997.

[68] W. Heywang, K. Lubitz, and W. Wersing. *Piezoelectricity: Evolution and Future of a Technology*, volume 114. Heidelberg: Springer Science & Business Media, 2008.

[69] Alfa Aesar. 11365 Niobium (v) oxide, 99.5% (metals basis), [online], 2020. [Date accessed: 10/06/2020. Available from: https://www.alfa.com/en/catalog/011365/].

[70] Acmite Market Intelligence. Market Report: World Piezoelectric Device Market. 2010.

[71] James F Tressler. Piezoelectric Transducer Designs for Sonar Applications. In *Piezoelectric and acoustic materials for transducer applications*, pages 217–239. New York: Springer, 2008.

[72] C. H. Sherman and J. L. Butler. *Transducers and Arrays for Underwater Sound,* 2nd edition, volume 4. Switzerland: Springer, 2016.

[73] T. Seebeck. Magnetische Polarisation der Metalle und Erze Durch Temperatur-Differenz (Magnetic Polarisation of Metals and Ores by Temperature Difference). *Abhandlungen der Deutschen Akademie der Wissenschaften zu Berlin*, pages 265–373, 1823.

[74] D. D. Pollock. *The Theory and Properties of Thermocouple Elements*. Baltimore: American Society for Testing and Materials, 1971.

[75] H. Liu, Q. Wang, W. Sheng, X. Wang, K. Zhang, L. Du, and J. Zhou. Humidity Sensors with Shielding Electrode Under Interdigitated Electrode. *Sensors*, 19(3):659, 2019.

[76] A. J. Bell. A Classical Mechanics Model for the Interpretation of Piezoelectric Property Data. *Journal of Applied Physics*, 118(22):224103, 2015.

[77] S. Zhang and F. Li. High Performance Ferroelectric Relaxor-$PbTiO_3$ Single Crystals: Status and Perspective. *Journal of Applied Physics*, 111(3):031301, 2012.

[78] S. Dong, J. F. Li, and D. Viehland. Longitudinal and Transverse Magnetoelectric Voltage Coefficients of Magnetostrictive-Piezoelectric Laminate Composite: Theory. *IEEE Transactions on Ultrasonics, Ferroelectrics, and Frequency Control*, 50(10):1253–1261, 2003.

[79] W. Tian, Z. Ling, W. Yu, and J. Shi. A Review of MEMS Scale Piezoelectric Energy Harvester. *Applied Sciences*, 8(4):645, 2018.

[80] D. Hu, M. Yao, Y. Fan, C. Ma, M. Fan, and M. Liu. Strategies to Achieve High Performance Piezoelectric Nanogenerators. *Nano Energy*, 2018.

[81] F. Narita and M. Fox. A Review on Piezoelectric, Magnetostrictive, and Magnetoelectric Materials and Device Technologies for Energy Harvesting Applications. *Advanced Engineering Materials*, 20(5):1700743, 2018.

[82] A. F. Devonshire. CIX. Theory of Barium Titanate—Part II. *The London, Edinburgh, and Dublin Philosophical Magazine and Journal of Science*, 42(333):1065–1079, 1951.

[83] T. Qi, I. Grinberg, and A. M. Rappe. Correlations Between Tetragonality, Polarization, and Ionic Displacement in $PbTiO_3$-Derived Ferroelectric Perovskite Solid Solutions. *Physical Review B*, 82(13):134113, 2010.

[84] R. E. Cohen. Origin of Ferroelectricity in Perovskite Oxides. *Nature*, 358(6382):136–138, 1992.

[85] R. D. Shannon. Revised Effective Ionic Radii and Systematic Studies of Interatomic Distances in Halides and Chalcogenides. *Acta Crystallographica Section A: Crystal Physics, Diffraction, Theoretical and General Crystallography*, 32(5):751–767, 1976.

[86] R. Seshadri and N. A. Hill. Visualizing the Role of Bi 6s "Lone Pairs" in the Off-Center Distortion in Ferromagnetic $BiMnO_3$. *Chemistry of Materials*, 13(9):2892–2899, 2001.

[87] I. Inbar and R. E. Cohen. Comparison of the Electronic Structures and Energetics of Ferroelectric $LiNbO_3$ and $LiTaO_3$. *Physical Review B*, 53(3):1193, 1996.

[88] C. M. I. Okoye. Theoretical Study of the Electronic Structure, Chemical Bonding and Optical Properties of $KNbO_3$ in the Paraelectric Cubic Phase. *Journal of Physics: Condensed Matter*, 15(35):5945, 2003.

[89] M. Davis, M. Budimir, D. Damjanovic, and N. Setter. Rotator and Extender Ferroelectrics: Importance of the Shear Coefficient to the Piezoelectric Properties of Domain-Engineered Crystals and Ceramics. *Journal of Applied Physics*, 101(5):054112, 2007.

[90] Z. A. Li, H. X. Yang, H. F. Tian, J. Q. Li, J. Cheng, and J. Chen. Transmission Electron Microscopy Study of Multiferroic $(Bi_{1-x}La_x)FeO_3$–$PbTiO_3$ with x= 0.1, 0.2, and 0.3. *Applied Physics Letters*, 90(18):182904, 2007.

[91] S-H Yoon, M-Y Kim, and D. Kim. Influence of Tetragonality (c/a) on Dielectric Nonlinearity and Direct Current (DC) Bias Characteristics of (1-x)$BaTiO_3$-(x)$Bi_{0.5}Na_{0.5}TiO_3$ Ceramics. *Journal of Applied Physics*, 122(15):154103, 2017.

[92] G. Tutuncu, B. Li, K. Bowman, and J. L. Jones. Domain Wall Motion and Electromechanical Strain in Lead-Free Piezoelectrics: Insight From the Model System (1- x)$Ba(Zr_{0.2}Ti_{0.8})O_3$–(x)$(Ba_{0.7}Ca_{0.3})TiO_3$ Using In Situ High-Energy X-Ray Diffraction During Application of Electric Fields. *Journal of Applied Physics*, 115(14):144104, 2014.

[93] C. R. Bowen, A. Perry, A. C. F. Lewis, and H. Kara. Processing and Properties of Porous Piezoelectric Materials with High Hydrostatic Figures of Merit. *Journal of the European Ceramic Society*, 24(2):541–545, 2004.

[94] D. A. Hall, A. Steuwer, B. Cherdhirunkorn, T. Mori, and P. J. Withers. A High Energy Synchrotron X-Ray Study of Crystallographic Texture and Lattice Strain in Soft Lead Zirconate Titanate Ceramics. *Journal of Applied Physics*, 96(8):4245–4252, 2004.

[95] D. M. Marincel, H. Zhang, A. Kumar, S. Jesse, S. V. Kalinin, W. M. Rainforth, I. M. Reaney, C. A. Randall, and S. Trolier-McKinstry. Influence of a Single Grain Boundary on Domain Wall Motion in Ferroelectrics. *Advanced Functional Materials*, 24(10):1409–1417, 2014.

[96] D. M. Marincel, H. Zhang, S. Jesse, A. Belianinov, M. B. Okatan, S. V. Kalinin, W. M. Rainforth, I. M. Reaney, C. A. Randall, and S. Trolier-McKinstry. Domain Wall Motion Across Various Grain Boundaries in Ferroelectric Thin Films. *Journal of the American Ceramic Society*, 98(6):1848–1857, 2015.

[97] J-F Li, K. Wang, F-Y. Zhu, L-Q. Cheng, and F-Z. Yao. (K,Na)NbO_3-Based Lead-Free Piezoceramics: Fundamental Aspects, Processing Technologies, and Remaining Challenges. *Journal of the American Ceramic Society*, 96(12):3677–3696, 2013.

[98] C. W. Ahn, G. Han, J. Ryu, W. H. Yoon, J. J. Choi, B. D. Hahn, J. W. Kim, J. H. Choi, and D. S. Park. Composition Design Rule for High Piezoelectric Voltage Coefficient in $(K_{0.5}Na_{0.5})NbO_3$ Based Pb-free Ceramics. *Japanese Journal of Applied Physics*, 51(9S2):09MD10, 2012.

[99] C. W. Ahn, J. J. Choi, J. Ryu, W. H. Yoon, B. D. Hahn, J. W. Kim, J. H. Choi, and D. S. Park. Composition Design Rule for Energy Harvesting Devices in Piezoelectric Perovskite Ceramics. *Materials Letters*, 141:323–326, 2015.

[100] Y. Yamashita, K. Yokoyama, H. Honda, and T. Takahashi. (Pb, Ca)$((Co_{1/2}W_{1/2}), Ti)O_3$ Piezoelectric Ceramics and their Applications. *Japanese Journal of Applied Physics*, 20(S4):183, 1981.

[101] D. Stansfield and A. Elliott. *Underwater Electroacoustic Transducers,* 2nd edition. Los Altos: Peninsula Publishing, 2017.

[102] H. Dong, J. Wang, Y. Wang, W. Zhong, and P. Zhang. Piezoelectric and Dielectric Properties of $(x)Pb(Y_{1/2}Nb_{1/2})O_3$-$(1-x)Pb(Ti_{1/2}Zr_{1/2})O_3$ Ceramics. *Ferroelectrics*, 248(1):33–43, 2000.

[103] R. Tickoo, R. P. Tandon, V. K. Hans, K. K. Bamzai, and P. N. Kotru. Electromechanical and Piezoelectric Studies of Lanthanum Modified Lead Titanate Ceramics. *Materials Science and Engineering: B*, 100(1):47–52, 2003.

[104] S. Singh, C. Prakash, and K. K. Raina. Microstructure and Electron Properties of Sm Modified Lead Calcium Titanate Ceramics. *Journal of Alloys and Compounds*, 492(1-2):717–722, 2010.

[105] M. Sharma, H. Sharma, and K. K. Raina. Comparison of Piezoelectricity in Ta^{5+} and La^{3+} Substituted Lead Calcium Titanate Ceramics. *Journal of Physics and Chemistry of Solids*, 69(10):2584–2588, 2008.

[106] S. Singh, O. P. Thakur, C. Prakash, and K. K. Raina. Structural and Electrical Properties of Lanthanum-Substituted Lead Titanate Ceramics. *Phase Transitions*, 78(7-8):655–667, 2005.

[107] I. Ueda and S. Ikegami. Piezoelectric Properties of Modified $PbTiO_3$ Ceramics. *Japanese Journal of Applied Physics*, 7(3):236, 1968.

[108] D. Garcia and J. A. Eiras. Piezoelectric and Dielectric Properties of Some La, Mn Modified $PbTiO_3$ Ceramics. *Ferroelectrics*, 123(1):51–59, 1991.

[109] A. G. Kalinichev, J. D. Bass, B. N. Sun, and D. A. Payne. Elastic Properties of Tetragonal $PbTiO_3$ Single Crystals by Brillouin Scattering. *Journal of Materials Research*, 12(10):2623–2627, 1997.

[110] V. G. Gavrilyachenko and E. G. Fesenko. Piezoelectric Effect in Lead Titanate Single Crystals. *Soviet Physics Crystallography, USSR*, 16(3):549–+, 1971.

[111] Z. Li, M. Grimsditch, X. Xu, and S. K. Chan. The Elastic, Piezoelectric and Dielectric Constants of Tetragonal $PbTiO_3$ Single Crystals. *Ferroelectrics*, 141(1):313–325, 1993.

[112] M. J. Haun, E. Furman, S. J. Jang, H. A. McKinstry, and L. E. Cross. Thermodynamic Theory of $PbTiO_3$. *Journal of Applied Physics*, 62(8):3331–3338, 1987.

[113] K. Oka, H. Unoki, H. Yamaguchi, and H. Takahashi. Crystal Growth of $PbTiO_3$ by the Top-Seeded Solution-Growth Method. *Journal of Crystal Growth*, 166(1-4):380–383, 1996.

[114] C. T. A. Suchicital and D. A. Payne. Flux Growth of Single Crystal Lead Titanate. *Journal of Crystal Growth*, 104(2):211–217, 1990.

[115] N. Maffei and G. A. Rossetti Jr. Float-Zone Growth and Properties of Ferroelectric Lead Titanate. *Journal of Materials Research*, 19(3):827–833, 2004.

[116] B. N. Sun, Y. Huang, and D. A. Payne. Growth of Large $PbTiO_3$ Crystals by a Self-Flux Technique. *Journal of Crystal Growth*, 128(1-4):867–870, 1993.

[117] S. Balakumar, S. G. Moorthy, G. Bocelli, and C. Subramanian. Growth of Lead Calcium Titanate Single Crystals and their Characterisations. *Ferroelectrics*, 207(1):497–505, 1998.

[118] S. G. Moorthy, F. J. Kumar, S. Balakumar, and C. Subramanian. Growth of Lead Titanate Single Crystals and their Characterization. *Journal of the Korean Physical Society*, 32:S1214–S1216, 1998.

[119] X. H. Dai, Z. Li, X. Z. Xu, S. K. Chan, and D. J. Lam. Dielectric Frequency Dispersion Behavior in Flux Grown $PbTiO_3$ Single Crystals. *Ferroelectrics*, 135(1):39–48, 1992.

[120] J. Suchanicz and K. Wojcik. Effect of External Stress on Dielectric Properties of $PbTiO_3$ Single Crystal. *Materials Science and Engineering: B*, 104(1-2):31–35, 2003.

[121] S. Fujii, Y. Sugie, M. Kobune, and T. Yamamoto. Effects of Li_2O and Na_2O Addition on Growth and Electrical Properties of $PbTiO_3$ Single Crystals. *Journal of the Ceramic Society of Japan*, 100(1166):1179–1183, 1992.

[122] S. Fujii, Y. Sugie, M. Kobune, and T. Yamamoto. Electrical Properties of $PbTiO_3$ Single Crystals Grown from PbO-Cu_2O Flux Method. *Journal of the Ceramic Society of Japan*, 101(1177):1062–1064, 1993.

[123] S. G. Moorthy, S. Balakumar, F. J. Kumar, C. Subramanian, and P. Ramasamy. Growth and Characterization of $Pb_{1-x}Ca_xTiO_3$ Single Crystals by Self-Flux Technique. *Materials Chemistry and Physics*, 57(3):281–284, 1999.

[124] M. Kobune, Y. Hayashi, and S. Fujii. Growth and Pyroelectric Properties of Ru-Doped $PbTiO_3$ Crystals by Flux Cooling Method. *Journal of the Ceramic Society of Japan*, 103(1203):1129–1134, 1995.

[125] B. C. Grabmaier. $PbTiO_3$ Grown From The Melt. *Ferroelectrics*, 13(1):501–503, 1976.

[126] R. J. Nelmes and W. F. Kuhs. The Crystal Structure of Tetragonal $PbTiO_3$ at Room Temperature and at 700K. *Solid State Communications*, 54(8):721–723, 1985.

[127] J. P. Remeika and A. M. Glass. The Growth and Ferroelectric Properties of High Resistivity Single Crystals of Lead Titanate. *Materials Research Bulletin*, 5(1):37–45, 1970.

[128] C. C. Chou, C. S. Hou, and T. H. Yeh. Domain Pinning Behavior of Ferroelectric $Pb_{1-x}Sr_xTiO_3$ Ceramics. *Journal of the European Ceramic Society*, 25(12):2505–2508, 2005.

[129] Innovia Materials. PMN-PT and PIN-PMN-PT Crystal, Webpage [online]. [Date accessed: 17/01/2020. Available from: http://www.innoviamaterials.com/about/?120.html].

[130] C. B. Carter and M. G. Norton. *Ceramic Materials: Science and Engineering.* New York: Springer Science & Business Media, 2007.

[131] F. Li, S. Zhang, Z. Xu, X. Wei, J. Luo, and T. R. Shrout. Electromechanical Properties of Tetragonal $Pb(In_{1/2}Nb_{1/2})O_3$-$Pb(Mg_{1/3}Nb_{2/3})O_3$-$PbTiO_3$ Ferroelectric Crystals. *Journal of Applied Physics*, 107(5):054107, 2010.

[132] S. Singh, O. P. Thakur, and C. Prakash. Dielectric and Piezoelectric Properties of Microwave Processed Sm-Substituted PCT Ceramics. *Journal of Physics D: Applied Physics*, 38(10):1621, 2005.

[133] MTI Corporation. $BaTiO_3$ (100) 5x5x1mm, 2SP, Substrate Grade, product: Btoa050510s2us, Webpage [online]. [Date accessed: 17/01/2020. Available from: https://www.mtixtl.com/BTO-a-050510-S2.aspx].

[134] MaTecK. $BaTiO_3$ - Barium Titanate Crystal, Webpage [online]. Date accessed: 17/01/2020. Available from: https://mateck.com/info/batio3-barium-titanate-crystal.html.

[135] Biotain. Barium Titanate ($BaTiO_3$) Single Crystal, Webpage [online]. [Date accessed: 17/01/2020. Available from: http://www.crystal-material.com/Single-Crystal-Materials/Barium-titanate-BaTiO3-single-crystal.html.

[136] Y. S. Yoo, M. K. Kang, J. H. Han, H. Kim, and D. Y. Kim. Fabrication of $BaTiO_3$ Single Crystals by Using the Exaggerated Grain Growth Method. *Journal of the European Ceramic Society*, 17(14):1725–1727, 1997.

[137] G. L. Messing, S. Trolier-McKinstry, E. M. Sabolsky, C. Duran, S. Kwon, B. Brahmaroutu, P. Park, H. Yilmaz, P. W. Rehrig, and K. B. Eitel. Templated Grain

Growth of Textured Piezoelectric Ceramics. *Critical Reviews in Solid State and Materials Sciences*, 29(2):45–96, 2004.

[138] G. L. Messing, S. Poterala, Y. Chang, T. Frueh, E. R. Kupp, B. H. Watson, R. L. Walton, M. J. Brova, A-K Hofer, and R. Bermejo. Texture-Engineered Ceramics—Property Enhancements Through Crystallographic Tailoring. *Journal of Materials Research*, 32(17):3219–3241, 2017.

[139] B. Liu, P. Li, B. Shen, J. Zhai, Y. Zhang, F. Li, and X. Liu. Simultaneously Enhanced Piezoelectric Response and Piezoelectric Voltage Coefficient in Textured KNN-Based Ceramics. *Journal of the American Ceramic Society*, 101(1):265–273, 2018.

[140] Y. Liu, Y. Chang, E. Sun, F. Li, S. Zhang, B. Yang, Y. Sun, J. Wu, and W. Cao. Significantly Enhanced Energy-Harvesting Performance and Superior Fatigue-Resistant Behavior in [001] c-Textured $BaTiO_3$-Based Lead-Free Piezoceramics. *ACS Applied Materials & Interfaces*, 10(37):31488–31497, 2018.

[141] Y. Yan, J. E. Zhou, D. Maurya, Y. U. Wang, and S. Priya. Giant Piezoelectric Voltage Coefficient in Grain-Oriented Modified $PbTiO_3$ Material. *Nature Communications*, 7:13089, 2016.

[142] S. Zhang, L. Lebrun, S. Rhee, R. E. Eitel, C. A. Randall, and T. R. Shrout. Crystal Growth and Characterization of New High Curie Temperature (1- x)$BiScO_3$–(x)$PbTiO_3$ Single Crystals. *Journal of Crystal Growth*, 236(1-3):210–216, 2002.

[143] S. Zhang, C. A. Randall, and T. R. Shrout. Dielectric, Piezoelectric and Elastic Properties of Tetragonal $BiScO_3$-$PbTiO_3$ Single Crystal with Single Domain. *Solid State Communications*, 131(1):41–45, 2004.

[144] Z. Liu, H. Wu, A. Paterson, Z. Luo, W. Ren, and Z. G. Ye. High Curie-Temperature (T_C) Piezo-/Ferroelectric Single Crystals with Bismuth-Based Complex Perovskites: Growth, Structures and Properties. *Acta Materialia*, 136:32–38, 2017.

[145] A. J. Bell, A. X. Levander, S. L. Turner, and T. P. Comyn. Internal Stress and Phase Coexistence in Bismuth Ferrite-Lead Titanate Ceramics. In *2007 Sixteenth IEEE International Symposium on the Applications of Ferroelectrics*, pages 406–409. IEEE, 2007.

[146] S. Bhattacharjee, S. Tripathi, and D. Pandey. Morphotropic Phase Boundary in (1- x)$BiFeO_3$–(x)$PbTiO_3$: Phase Coexistence Region and Unusually Large Tetragonality. *Applied Physics Letters*, 91(4):042903, 2007.

[147] T. L. Burnett, T. P. Comyn, and A. J. Bell. Flux Growth of $BiFeO_3$–$PbTiO_3$ Single Crystals. *Journal of Crystal Growth*, 285(1-2):156–161, 2005.

[148] W. M. Zhu, H. Y. Guo, and Z. G. Ye. Structure and Properties of Multiferroic (1-x)$BiFeO_3$–(x)$PbTiO_3$ Single Crystals. *Journal of Materials Research*, 22(8):2136–2143, 2007.

[149] J. S. Park, T. K. Song, M. H. Kim, W. J. Kim, D. Do, S. S. Kim, and K. S. Choi. A Phenomenological Approach to Phase Transition Temperatures of Pb(Zr, Ti)O_3-$BiFeO_3$ System. *Ferroelectrics*, 450(1):16–20, 2013.

[150] P. Chandra and P. B. Littlewood. *A Landau Primer for Ferroelectrics*, pages 69–116. Heidelberg: Springer, 2007.

[151] A. F. Devonshire. XCVI. Theory of Barium Titanate: Part I. *The London, Edinburgh, and Dublin Philosophical Magazine and Journal of Science*, 40(309):1040–1063, 1949.

[152] X. Lu, H. Li, and W. Cao. Landau Expansion Parameters for $BaTiO_3$. *Journal of Applied Physics*, 114(22):224106, 2013.

[153] W. J. Merz. Double Hysteresis Loop of $BaTiO_3$ at the Curie Point. *Physical Review*, 91(3):513, 1953.

[154] W. R. Buessem, L. E. Cross, and A. K. Goswami. Phenomenological Theory of High Permittivity in Fine-Grained Barium Titanate. *Journal of the American Ceramic Society*, 49(1):33–36, 1966.

[155] A. J. Bell and L. E. Cross. A Phenomenological Gibbs Function for $BaTiO_3$ Giving Correct E-field Dependence of all Ferroelectric Phase Changes. *Ferroelectrics*, 59(1):197–203, 1984.

[156] N. A. Pertsev, A. G. Zembilgotov, and A. K. Tagantsev. Effect of Mechanical Boundary Conditions on Phase Diagrams of Epitaxial Ferroelectric Thin Films. *Physical Review Letters*, 80(9):1988, 1998.

[157] Y. L. Li, L. E. Cross, and L. Q. Chen. A Phenomenological Thermodynamic Potential for $BaTiO_3$ Single Crystals. *Journal of Applied Physics*, 98(6):064101, 2005.

[158] Y. L. Wang, A. K. Tagantsev, D. Damjanovic, N. Setter, V. K. Yarmarkin, A. I. Sokolov, and I. A. Lukyanchuk. Landau Thermodynamic Potential for $BaTiO_3$. *Journal of Applied Physics*, 101(10):104115, 2007.

[159] M. J. Haun, E. Furman, S. J. Jang, and L. E. Cross. Thermodynamic Theory of the Lead Zirconate-Titanate Solid Solution System, Part I: Phenomenology. *Ferroelectrics*, 99(1):13–25, 1989.

[160] M. J. Haun, E. Furman, H. A. McKinstry, and L. E. Cross. Thermodynamic Theory of the Lead Zirconate-Titanate Solid Solution System, Part II: Tricritical Behavior. *Ferroelectrics*, 99(1):27–44, 1989.

[161] M. J. Haun, Z. Q. Zhuang, E. Furman, S. J. Jang, and L. E. Cross. Thermodynamic Theory of the Lead Zirconate-Titanate Solid Solution System, Part III: Curie Constant and Sixth-Order Polarization Interaction Dielectric Stiffness Coefficients. *Ferroelectrics*, 99(1):45–54, 1989.

[162] M. J. Haun, E. Furman, T. R. Halemane, and L. E. Cross. Thermodynamic Theory of the Lead Zirconate-Titanate Solid Solution System, Part IV: Tilting of the Oxygen Octahedra. *Ferroelectrics*, 99(1):55–62, 1989.

[163] M. J. Haun, E. Furman, S. J. Jang, and L. E. Cross. Thermodynamic Theory of the Lead Zirconate-Titanate Solid Solution System Part V: Theoretical Calculations. *Ferroelectrics*, 99(1):63–86, 1989.

[164] A. A. Heitmann and G. A. Rossetti Jr. Thermodynamics of Ferroelectric Solid Solutions with Morphotropic Phase Boundaries. *Journal of the American Ceramic Society*, 97(6):1661–1685, 2014.

[165] J. Peng, D. Shan, Y. Liu, K. Pan, C. Lei, N. He, Z. Zhang, and Q. Yang. A Thermodynamic Potential for Barium Zirconate Titanate Solid Solutions. *npj Computational Materials*, 4(1):66, 2018.

[166] G. P. Cao, H. B. Huang, D. S. Liang, and X. Q. Ma. A Phenomenological Potential and Ferroelectric Properties of $BaTiO_3$–$CaTiO_3$ Solid Solution. *Ceramics International*, 43(9):6671–6676, 2017.

[167] Y. H. Hsieh, F. Xue, T. Yang, H. J. Liu, Y. Zhu, Y. C. Chen, Q. Zhan, C. G. Duan, L. Q. Chen, and Q. He. Permanent Ferroelectric Retention of $BiFeO_3$ Mesocrystal. *Nature Communications*, 7:13199, 2016.

[168] G. Rupprecht and R. O. Bell. Dielectric Constant in Paraelectric Perovskites. *Phys. Rev.*, 135:A748–A752, Aug 1964.

[169] V. Kothai, B. Narayan, K. Brajesh, S. D. Kaushik, V. Siruguri, and R. Ranjan. Ferroelectric Phase Coexistence by Crystallite Size Reduction in $BiFeO_3$-$PbTiO_3$. *Physical Review B*, 90:155115, 2014.

[170] C. G. Cambridge, T. P. Comyn, T. Stevenson, and A. J. Bell. Growth and Characterization of High Quality $BiFeO_3$-$PbTiO_3$ Single Crystals. *Integrated Ferroelectrics*, 132(1):1–8, 2012.

[171] E. H. Bogardus and R. Roy. Effects of Strain Induced by Pressing and Grinding $BaTiO_3$ and SiO_2. *Journal of the American Ceramic Society*, 48(4):205–207, 1965.

[172] M. Khan. *Preparation and Properties of Bismuth Ferrite Lead Titanate Thin Films Prepared by Pulsed Laser Deposition.* PhD thesis, University of Leeds, 2008.

[173] S. F. Yuk, K. C. Pitike, S. M. Nakhmanson, M. Eisenbach, Y. W. Li, and V. R. Cooper. Towards an Accurate Description of Perovskite Ferroelectrics: Exchange and Correlation Effects. *Scientific reports*, 7:43482, 2017.

[174] G. A. Rossett Jr, K. R. Udayakumar, M. J. Haun, and L. E. Cross. Thermodynamic Theory of Single-Crystal Lead Titanate with Consideration of Elastic Boundary Conditions. *Journal of the American Ceramic Society*, 73(11):3334–3338, 1990.

[175] CeramTec. Piezoceramic Hard Materials Material Data, product: Pzt400 and pzt800 series. Datasheet [online]. Date accessed: 17/01/2020. Available from: https://www.ceramtec.com/files/ms_piezoceramic-hard-materials_en_de.pdf.

[176] CeramTec. Piezoceramic Soft Materials Material Data, product: Pzt500 series, Datasheet [online]. [Date accessed: 17/01/2020. Available from: https://www.ceramtec.com/files/ms_piezoceramic-soft-materials_en_de.pdf].

[177] B. D. Cullity and S. R. Stock. *Elements of X-ray Diffraction,* 3rd edition. New York: Prentice-Hall, 2001.

[178] J. T. Bennett. *Development of Bismuth Ferrite Derived Piezoelectric Ceramics for High Temperature Applications.* PhD thesis, University of Leeds, 2014.

[179] P. W. Hawkes and J. C. H. Spence. *Science of Microscopy.* New York: Springer Science & Business Media, 2008.

[180] R. W. Kelsall, I. W. Hamley, and M. Geoghegan. *Nanoscale Science and Technology.* Chichester: John Wiley & Sons Ltd., 2005.

[181] M. G. Cain. *Characterisation of Ferroelectric Bulk Materials and Thin Films.* Dordrecht: Springer, 2014.

[182] B. Ando and S. Graziani. Basic Measurements for the Characterization of Ferroelectric Devices. *IEEE transactions on instrumentation and measurement*, 54(3):1054–1060, 2005.

[183] S. J. Parry. *KN-based Lead-free Ferroelectric Materials for SONAR Applications.* PhD thesis, University of Leeds, 2019.

[184] J. Bhattarai, V. Mikhaylov, D. Neupane, B. Nepal Bishal, A. Demchenko, and K. Stine. *Carbohydrate–Protein Interactions Studied Using Electrochemical Impedance Spectroscopy.* 2017.

[185] A. R. West, D. C. Sinclair, and N. Hirose. Characterization of Electrical Materials, Especially Ferroelectrics, by Impedance Spectroscopy. *Journal of Electroceramics*, 1(1):65–71, 1997.

[186] E. J. Abram, D. C. Sinclair, and A. R. West. A Strategy for Analysis and Modelling of Impedance Spectroscopy Data of Electroceramics: Doped Lanthanum Gallate. *Journal of Electroceramics*, 10(3):165–177, 2003.

[187] J. T. S. Irvine, D. C. Sinclair, and A. R. West. Electroceramics: Characterization by Impedance Spectroscopy. *Advanced Materials*, 2(3):132–138, 1990.

[188] D. Briggs. *Handbook of X-Ray and Ultraviolet Photoelectron Spectroscopy.* London: Heyden, 1977.

[189] J. F. Watts and J. Wolstenholme. An Introduction to Surface Analysis by XPS and AES. *An Introduction to Surface Analysis by XPS and AES*, page 224, 2003.

[190] T. Stevenson. *Magnetic and Electric Properties of Bismuth Ferrite Lead Titanate Ceramics.* PhD thesis, University of Leeds, 2010.

[191] B. H. Toby. R Factors in Rietveld Analysis: How Good is Good Enough? *Powder Diffraction*, 21(1):67–70, 2006.

[192] T. Burnett. *Growth and Characterization of Bismuth Ferrite Lead Titanate Single Crystals*. PhD thesis, University of Leeds, 2009.

[193] M. I. Mendelson. Average Grain Size in Polycrystalline Ceramics. *Journal of the American Ceramic society*, 52(8):443–446, 1969.

[194] J. F. Moulder and J. Chastain. Handbook of X-ray Photoelectron Spectroscopy: A Reference book of standard spectra for identification and interpretation of xps data, 6th edition. *Eden Prairie, Minn: Perkin-Elmer Corporation*, 1992.

[195] B. Fang, Y. Shan, K. Tezuka, and H. Imoto. Phase Formation, Microstructure and Physical Properties of Lead Iron Scandium Niobate. *Journal of the European Ceramic Society*, 26(6):867–873, 2006.

[196] W. Li, H. Zeng, K. Zhao, J. Hao, and J. Zhai. Structural, Dielectric and Piezoelectric Properties of $(Bi_{0.5}Na_{0.5})TiO_3$-$(Bi_{0.5}k_{0.5})TiO_3$-$Bi(Zn_{0.5}Ti_{0.5})O_3$ Thin Films Prepared by Sol-Gel Method. *Ceramics International*, 40(6):7947–7951, 2014.

[197] H. Dong, X-J. Zheng, W. Li, Y-Q. Gong, J-F. Peng, and Z. Zhu. The Dielectric Relaxation Behavior of $(Na_{0.82}K_{0.18})_{0.5}Bi_{0.5}TiO_3$ Ferroelectric Thin Film. *Journal of Applied Physics*, 110(12):124109, 2011.

[198] G. Zhang, S. Liu, Y. Yu, Y. Zeng, Y. Zhang, X. Hu, and S. Jiang. Microstructure and Electrical Properties of $(Pb_{0.87}Ba_{0.1}La_{0.02})(Zr_{0.68}Sn_{0.24}Ti_{0.08})O_3$ Anti-Ferroelectric Ceramics Fabricated by the Hot-Press Sintering Method. *Journal of the European Ceramic Society*, 33(1):113–121, 2013.

[199] P. Gerthsen, K. H. Härdtl, and N. A. Schmidt. Correlation of Mechanical and Electrical Losses in Ferroelectric Ceramics. *Journal of Applied Physics*, 51(2):1131–1134, 1980.

[200] R. Gerson. Variation in Ferroelectric Characteristics of Lead Zirconate Titanate Ceramics Due to Minor Chemical Modifications. *Journal of Applied Physics*, 31(1):188–194, 1960.

[201] B. M. Fraygola, A. Chandrasekanar, D. Bahati, U. Salazar, A. Biancoli, N. Marzari, D. Damjanovic, and N. Setter. Piezoelectric Softening by Nb Sub-

stitution in (Ba, Pb)ZrO_3 Ceramics. *Journal of the American Ceramic Society*, 100(5):1885–1895, 2017.

[202] H-S. Han, I-K. Hong, Y-M. Kong, J-S. Lee, and W. Jo. Effect of Nb Doping on the Dielectric and Strain Properties of Lead-Free 0.94($Bi_{1/2}Na_{1/2}$)TiO_3-0.06$BaTiO_3$ Ceramics. *Journal of the Korean Ceramic Society*, 53(2):145–149, 2016.

[203] J-C. M'Peko, A. G. Peixoto, E. Jiménez, and L. M. Gaggero-Sager. Electrical Properties of Nb-Doped PZT 65/35 Ceramics: Influence of Nb and Excess PbO. *Journal of Electroceramics*, 15(2):167–176, 2005.

[204] Y. A. Genenko, J. Glaum, M. J. Hoffmann, and K. Albe. Mechanisms of Aging and Fatigue in Ferroelectrics. *Materials Science and Engineering: B*, 192:52–82, 2015.

[205] N. Balke, D. C. Lupascu, T. Granzow, and J. Rödel. Fatigue of Lead Zirconate Titanate Ceramics. I: Unipolar and DC Loading. *Journal of the American Ceramic Society*, 90(4):1081–1087, 2007.

[206] D. Lupascu and J. Rödel. Fatigue in Bulk Lead Zirconate Titanate Actuator Materials. *Advanced Engineering Materials*, 7(10):882–898, 2005.

[207] Z. Liu, B. Wu, and J. Wu. Reduced Dielectric Loss and High Piezoelectric Constant in Ce and Mn co-doped $BiScO_3$-$PbCe_xTi_{1-x}O_3$-Bi($Zn_{0.5}Ti_{0.5}$)O_3 Ceramics. *Ceramics International*, 44(14):16483–16488, 2018.

[208] J. Chen, G. Jin, C-M. Wang, and J. Cheng. Reduced Dielectric Loss and Strain Hysteresis in Fe and Mn comodified High-Temperature $BiScO_3$-$PbTiO_3$ Ceramics. *Journal of the American Ceramic Society*, 97(12):3890–3896, 2014.

[209] T. Zheng and J. Wu. Quenched Bismuth Ferrite-Barium Titanate Lead-Free Piezoelectric Ceramics. *Journal of Alloys and Compounds*, 676:505–512, 2016.

[210] T. Rojac, M. Kosec, B. Budic, N. Setter, and D. Damjanovic. Strong Ferroelectric Domain-Wall Pinning in $BiFeO_3$ Ceramics. *Journal of Applied Physics*, 108(7):074107, 2010.

[211] V. V. Burungale, R. S. Devan, S. A. Pawar, N. S. Harale, V. L. Patil, V. K. Rao, Y-R. Ma, J. Eun, J. H. Kim, and P. S. Patil. Chemically Synthesized PbS Nano Particulate Thin Films for a Rapid NO_2 Gas Sensor. *Materials Science-Poland*, 34(1):204–211, 2016.

[212] R. W. Hewitt and N. Winograd. Investigation of the Oxidation of Polycrystalline Lead by XPS and SIMS. *Surface Science*, 78(1):1–14, 1978.

[213] C. J. Lu, A. X. Kuang, and G. Y. Huang. X-ray Photoelectron Spectroscopy Study on Composition and Structure of Sol-Gel Derived $PbTiO_3$ Thin Films. *Journal of Applied Physics*, 80(1):202–206, 1996.

[214] Y. Wang, B. Qu, W. Zhong, P. Zhang, and K. Wang. Ion Implantation in $PbTiO_3$ Films. *Journal of Applied Physics*, 72(8):3726–3729, 1992.

[215] X. Liu, H. Cao, and J. Yin. Generation and Photocatalytic Activities of Bi @ Bi_2O_3 Microspheres. *Nano Research*, 4(5):470–482, 2011.

[216] D. A. Zatsepin, A. F. Zatsepin, D. W. Boukhvalov, and N. V. Gavrilov. Bi-Doped Silica Glass: A Combined XPS–DFT Study of Electronic Structure and Pleomorphic Imperfections. *Journal of Alloys and Compounds*, 829:154459, 2020.

[217] P. W. Wang, M. Guttag, and C-S. Tu. Surface Modification of Multiferroic $BiFeO_3$ Ceramic by Argon Sputtering. *Journal of Surface Engineered Materials and Advanced Technology*, 2014, 2014.

[218] A. Sarkar and G. G. Khan. The Formation and Detection Techniques of Oxygen Vacancies in Titanium Oxide-Based Nanostructures. *Nanoscale*, 11(8):3414–3444, 2019.

[219] D. Wojcieszak, M. Mazur, D. Kaczmarek, P. Mazur, B. Szponar, J. Domaradzki, and L. Kepinski. Influence of the Surface Properties on Bactericidal and Fungicidal Activity of Magnetron Sputtered Ti–Ag and Nb–Ag Thin Films. *Materials Science and Engineering: C*, 62:86–95, 2016.

[220] H. Brunckova, L. Medvecky, A. Kovalcikova, M. Fides, E. Mudra, J. Durisin, M. Sebek, M. Kanuchova, and J. Skvarla. Structural and Mechanical Properties of $La_{1/3}NbO_3$ and $La_{1/3}TaO_3$ Thin Films Prepared by Chemical Solution Deposition. *Journal of Rare Earths*, 35(11):1115–1125, 2017.

[221] T. K. Ghorai. Synthesis of Spherical Mesoporous Titania Modified Iron-Niobate Nanoclusters for Photocatalytic Reduction of 4-Nitrophenol. *Journal of Materials Research and Technology*, 4(2):133–143, 2015.

[222] K. Shi, Y. Zhang, J. Zhang, and Z. Xie. Electrochemical Properties of Niobium Coating for Biomedical Application. *Coatings*, 9(9):546, 2019.

[223] Q. Jian-Hua, W. Xiu-Qin, Y. Ning-Yi, and D. Jian-Ning. Piezoelectric and Electro-Optic Properties of Tetragonal (1- x)Pb($Mg_{1/3}Nb_{2/3}$)O_3-(x)$PbTiO_3$ Single Crystals by Phenomenological Theory. *Chinese Physics B*, 24(7):077701, 2015.

[224] D. Huo, Q. Wang, W. Lü, L. Zheng, X. Lu, J. Liu, Y. Jing, L. Yang, and R. Zhang. Characterization of Full Tensor Properties of Single-Domain Tetragonal 0.63Pb($Mg_{1/3}Nb_{2/3}$)O_3-0.37$PbTiO_3$ Single Crystal Using Only One Sample. *Ceramics International*, 44(7):8358–8362, 2018.

[225] K. Qian, B. Fang, Q. Du, J. Ding, X. Zhao, and H. Luo. Phase Development and Electrical Properties of Pb($Mg_{1/3}Nb_{2/3}O_3$-$PbTiO_3$ Ceramics Prepared by Partial Oxalate Route. *Physica Status Solidi (A)*, 210(6):1149–1156, 2013.

[226] Y. Jing, L. Zheng, W. Lü, Z. Xi, P. Zheng, J. Du, and R. Zhang. Full Tensor Properties of Single-Domain Tetragonal 0.63Pb($Mg_{1/3}Nb_{2/3}$)O_3-0.37$PbTiO_3$ Single Crystal and Their Orientation Dependence. *Physica Status Solidi (B)*, 253(10):1994–2000, 2016.

[227] D. Berlincourt and H. Jaffe. Elastic and Piezoelectric Coefficients of Single-Crystal Barium Titanate. *Physical Review*, 111(1):143, 1958.

[228] H. D. Megaw. G. Solids. Crystal Structure of Barium Titanium Oxide and Other Double Oxides of the Perovskite Type. *Transactions of the Faraday Society*, 42:A224–A231, 1946.

[229] K. Song, Z. Li, S. Fan, M. Ma, H. Guo, and Z. Xu. Growth and Electrical Properties Characterization of Pb($In_{1/2}Nb_{1/2}$)O_3-$PbTiO_3$ Tetragonal Single Crystal by the Modified Flux-Bridgman Method. *Journal of Crystal Growth*, 468:382–386, 2017.

[230] J. Du, Z. Xu, R. Chu, J. Hao, W. Li, and P. Zheng. Enhanced Electrical Properties of Lead-Free (1- x)($K_{0.44}Na_{0.52}Li_{0.04}$)($Nb_{0.91}$ $Ta_{0.05}Sb_{0.04}$)O_3–(x)$SrZrO_3$ Ceramics. *Journal of Materials Science: Materials in Electronics*, 27(6):6535–6541, 2016.

[231] L. M. Troilo, D. Damjanovic, and R. E. Newnham. Modified Lead Calcium Titanate Ceramics with a Relatively Large Dielectric Constant for Hydrophone Applications. *Journal of the American Ceramic Society*, 77(3):857–859, 1994.

[232] N. Ichinose and T. Takahashi. Piezoelectric Properties in the $PbTiO_3$-$Pb(Cd_{1/2}W_{1/2})O_3$ System Modified with MnO_2 and NiO. *Materials Research Bulletin*, 9(11):1517–1523, 1974.

[233] M. Kobune, W. Adachi, K. Kitada, A. Mineshige, T. Yazawa, H. Yamaguchi, and K. Honda. Fabrication of High-Density $(Bi,La)(Zn,Mg,Ti)O_3$–$PbTiO_3$ Solid Solutions with Ferroelectric and Piezoelectric Functionalities by Microstructural Control. *Japanese Journal of Applied Physics*, 47(9S):7664, 2008.

[234] L. Zhang, X. Hou, and J. Yu. Ferroelectric and Piezoelectric Properties of High Temperature $(Bi, La)FeO_3$-$Bi(Zn_{1/2}Ti_{1/2})O_3$-$PbTiO_3$ Ceramics at Rhombohedral/Tetragonal Coexistent Phase. *Japanese Journal of Applied Physics*, 54(8):081501, 2015.

[235] A. Dwivedi and C. A. Randall. Morphotropic Phase Boundary in High Temperature Ferroelectric $(x)Bi(Zn_{1/2}Ti_{1/2})O_3$-$(y)PbZrO_3$-$(z)PbTiO_3$ Perovskite Ternary Solid Solution. *Materials Letters*, 65(9):1308–1311, 2011.

[236] X. Hou and J. Yu. Novel $0.50(Bi_{1-x}La_x)FeO_3$–$0.35PbTiO_3$–$0.15Bi(Zn_{1/2}Ti_{1/2})O_3$ Piezoelectric Ceramics for High Temperature High Frequency Filters. *Japanese Journal of Applied Physics*, 52(6R):061501, 2013.

[237] R. Zuo, Y. Liu, S. Su, X. Chu, and X. Wang. Phase Transformation Behavior and Electrical Properties of $Pb(Zr_{0.56}Ti_{0.44})O_3$–$Bi(Zn_{0.5}Ti_{0.5})O_3$ Solid Solution Ceramics. *Journal of the American Ceramic Society*, 94(12):4340–4344, 2011.

[238] F. An, W. He, T. Wang, and J. Yu. Preparation and Electrical Properties of Modified Lead Titanate Ceramics. *Ferroelectrics*, 409(1):62–65, 2010.

[239] T. Sareein, W. Hu, X. Tan, and R. Yimnirun. The Morphotropic Phase Boundary in the $(1\text{-}x)PbZrO_3$–$(x)[0.3Bi(Zn_{1/2}Ti_{1/2})O_3$–$0.7PbTiO_3]$ Perovskite Solid Solution. *Journal of Materials Science*, 47(4):1774–1779, 2012.

Appendix A

Table of Material Properties from Literature

Table A.1: Dielectric and piezoelectric properties of tetragonal single crystals from literature used in Figure 3.2. *Calculated values. †Theoretical work. ‡Tetragonality (c/a) taken from other literature for identical materials and compositions

Material	c/a	$\epsilon_{11}^T/\epsilon_0$	$\epsilon_{33}^T/\epsilon_0$	d_{33} (pC/N)	d_{31} (pC/N)	d_{15} (pC/N)	d_h (pC/N)	g_{33} (10^{-3}Vm/N)	g_{31} (10^{-3}Vm/N)	g_{15} (10^{-3}Vm/N)	g_h (10^{-3}Vm/N)	Ref.
$PbTiO_3$ (I)	1.067	134	100	136.6	-22.8	63.8	91.0*	154.3*	-25.8*	53.8*	102.8*	[109]
$PbTiO_3$ (II)	1.067	139	114	156.4	-49.9	69.6	56.6*	155.0*	-49.4*	56.6*	56.1*	[109]
$PbTiO_3$ (III)	1.066‡		126	117.0	-25.0		67.0	104.9*	-22.4*		60.1*	[110], [112]‡
$PbTiO_3$ (IV)	1.066‡	130	80	83.7	-27.5	60.2	28.7*	118.2*	-38.8*	52.3*	40.5*	[111], [112]‡
$PbTiO_3$ (V)†	1.066	124	67	79.1	-23.1	56.1	32.9*	134.1*	-39.2*	50.9*	55.8*	[112]
PMN-0.38PT (I)†	1.002		834	145.0	-62.0		21.0*	19.6*	-8.4*		2.8*	[223]
PMN-0.40PT (I)†	1.003		713	143.0	-62.0		19.0*	22.7*	-9.8*		3.0*	[223]
PMN-0.37PT (I)	1.013‡	13190	710	291.0	-123.0	1450	45.0*	46,3	-19.6	12.4	7.2*	[224], [225]‡
PMN-0.37PT (II)	1.013‡	12550	775	307.0	-130.0	1410	47.0*	44.8	-19.0	12.7	6.8*	[226], [225]‡
0.14Bi(Zn,Ti)O_3-0.86$PbTiO_3$	1.070		120	138.0				129.9*				[144]
0.38Bi(Zn,Nb)O_3-0.62$PbTiO_3$			250	157.0				71.0*				[144]
0.4$PbZrO_3$-0.6$PbTiO_3$†	1.036	498	197	162.0	-58.9	169.0	44.2*	92.9	-33.8	38.4	25.3*	[163]
0.3$PbZrO_3$-0.7$PbTiO_3$†	1.043	218	116	104.0	-32.6	78.6	38.8*	101.0	-31.8	40.8	37.4*	[163]
0.2$PbZrO_3$-0.8$PbTiO_3$†	1.053	143	86	87.2	-26.2	57.0	34.8*	114.0	-34.2	44.9	45.6*	[163]
0.1$PbZrO_3$-0.9$PbTiO_3$†	1.061	121	73	81.2	-23.9	52.1	33.4*	124.0	-37.1	48.6	49.8*	[163]
$BaTiO_3$ (I)	1.011	2920	168	85.6	-34.5	392.0	16.6*	57.5	-23.0	15.2	11.5*	[227]
$BaTiO_3$ (II)†	1.010‡	4000	225	165.0	-63.0		39.0*	82.8*	-31.6*		19.6*	[82], [228]‡
Tetragonal $BiScO_3$-$PbTiO_3$	1.023		820	440.0	-162.0		116.0*	60.6	-22.3		11.5*	[143]
PZN-12PT & 1.020‡	1.020‡		870	576.0	-217.0		142.0*	74.9	-28.2		18.4*	[143], [142]‡
34$BiScO_3$-0.66$PbTiO_3$	1.030		300	200.0	-44.0		112.0*	75.3*	-16.6*		42.2*	[142]
PIN-0.44PTO_3	1.019		1219	610.0				56.5*				[229]
Tetragonal PIN-PMN-PT	1.009	15000	1090	530.0	-200.0	2350.0	130.0*	55.0	-20.6*	16.4	13.8*	[131]
PIN-PMN-0.38PT	1.009		1800	1000.0				62.8*				[131]
PIN-PMN-(0.39-0.41)PT	1.011		1100	500.0				51.4*				[131]
PIN-PMN-0.42PT	1.016		800	600.0				84.7*				[131]

Table A.2: Dielectric and piezoelectric properties of tetragonal polycrystalline ceramics from literature used in Figure 3.5 and 3.9. *Calculated values

Material	c/a	$\epsilon_{33}^T/\epsilon_0$	d_{33} (pC/N)	d_{31} (pC/N)	d_h (pC/N)	g_{33} (10^{-3}Vm/N)	g_{31} (10^{-3}Vm/N)	g_h (10^{-3}Vm/N)	Ref.
KNNLTS	1.015	923	235.0			28.8*			[230]
KNNLTS-0.01SZ	1.014	875	243.0			31.4*			[230]
KNNLTS-0.04SZ	1.013	826	257.0			35.2*			[230]
KNNLTS-0.08SZ	1.013	921	221.0			27.1*			[230]
KNNLTS-0.10SZ	1.013	969	189.0			22.0*			[230]
KNNL	1.021	534	235.0			49.7*			[97]
KNNL (II)	1.021	760	280.0			41.6*			[97]
KNNS	1.006	850	204.0			27.1*			[97]
KNNLT	1.014	540	206.0			43.1*			[97]
KNNLT (II)	1.014	1146	208.0			20.5*			[97]
KNNLT(III)	1.014	666	268.0			45.5*			[97]
KNNLT (IV)	1.021	650	276.0			48.0*			[97]
KNNLT (V)	1.016	1290	263.0			23.0*			[97]
KNNLS	1.014	1335	212.0			17.9*			[97]
KNNLS (II)	1.014	1464	280.0			21.6*			[97]
KNNLS (III)	1.014	1000	240.0			27.1*			[97]
KNNLTS (II)	1.013	1570	416.0			29.9*			[97]
KNNLTS (III)	1.008	2064	335.0			18.3*			[97]
KNNLTS (IV)	1.012	1352	250.0			20.9*			[97]
KNNLTS (V)	1.010	1503	252.0			18.9*			[97]
KNNLTS (VI)	1.014	689	264.0			43.3*			[97]
0.98KNN-0.02BiFeO_3	1.009	1150	253.0			24.9*			[97]
0.95KNLN-0.05CaZrO_3	1.016	1088	216.0			22.4*			[97]
0.975KNNLTS-0.025BaZr$\mathrm{O_3}$	1.006	3400	365.0			12.1*			[97]
0.94KNN-0.06Ba($\mathrm{Zr_{0.05}Ti_{0.95}}$)$\mathrm{O_3}$	1.014	1191	234.0			22.2*			[97]
0.95KNN-0.05$\mathrm{SrTiO_3}$	1.010	1147	220.0			21.7*			[97]
0.987KNN-0.013$\mathrm{BiFeO_3}$	1.008	905	173.0			21.6*			[97]
0.99KNNLT-0.01$\mathrm{BiFeO_3}$	1.013	1140	200.0			19.8*			[97]
0.98KNN-0.02($\mathrm{Bi_{0.5}K_{0.5}}$)$\mathrm{TiO_3}$	1.014	1260	251.0			22.5*			[97]

$Pb_{0.76}Ca_{0.24}Ti_{0.98}Mn_{0.02}O_3$	1.057	150*	45.0	-2.0	41.0	34.0	-1.5	31.0	[104]
$Pb_{0.73}Sm_{0.02}Ca_{0.24}Ti_{0.98}Mn_{0.02}O_3$	1.048	197*	55.0	-2.1	50.7	31.5	-1.2	29.1	[104]
$Pb_{0.70}Sm_{0.04}Ca_{0.24}Ti_{0.98}Mn_{0.02}O_3$	1.046	233*	62.0	-2.4	57.3	30.1	-1.2	27.8	[104]
$Pb_{0.67}Sm_{0.06}Ca_{0.24}Ti_{0.98}Mn_{0.02}O_3$	1.034	267*	70.0	-2.6	64.8	29.6	-1.1	27.4	[104]
$Pb_{0.64}Sm_{0.08}Ca_{0.24}Ti_{0.98}Mn_{0.02}O_3$	1.023	389*	76.0	-2.7	70.6	22.1	-0.8	20.5	[104]
$Pb_{0.76}Ca_{0.24}Ti_{0.98}Mn_{0.02}O_3$	1.057	150*	45.0	-2.0	41.0	34.0	-1.5	31.0	[106]
$Pb_{0.74}La_{0.02}Ca_{0.24}Ti_{0.98}Mn_{0.02}O_3$	1.047	177*	54.0	-2.2	49.6	34.4	-1.4	31.6	[106]
$Pb_{0.72}La_{0.04}Ca_{0.24}Ti_{0.98}Mn_{0.02}O_3$	1.037	239*	60.0	-2.4	55.2	28.4	-1.1	26.1	[106]
$Pb_{0.70}La_{0.06}Ca_{0.24}Ti_{0.98}Mn_{0.02}O_3$	1.032	338*	75.0	-2.6	69.8	25.1	-0.9	23.4	[106]
$Pb_{0.68}La_{0.08}Ca_{0.24}Ti_{0.98}Mn_{0.02}O_3$	1.028	296*	85.0	-3.0	79.0	32.5	-0.3	24.1	[106]
$(Pb_{0.76}Ca_{0.24})((Co_{0.5}W_{0.5})_{0.04}Ti_{0.96})O_3$	1.031	209	68.2	-3.2	61.9*	36.8	-1.7	33.4*	[100]
$PbTiO_3 + 0.05Bi_{2/3}TiO_3$	1.057	176	9.1	-3.1	2.9*	6.6	-2.1	2.4*	[107]
$PbTiO_3 + 0.05PbZn_{1/3}Nb_{2/3}O_3$	1.059	226	47.0	-7.0	33.0*	23.0	-3.5	16.0*	[107]
$PbTiO_3 + 0.05PbNb_{4/5}O_3$	1.049	226	37.0	-10.0	17.0*	16.0	-5.2	5.6*	[107]
$PbTiO_3 + 0.025$ $BiZn_{1/2}Ti_{1/2}O_3$	1.061	183	43.0	-2.5	38.0*	23.0	-1.5	20.0*	[107]
$PbTiO_3 + 0.05BiZn_{1/2}Ti_{1/2}O_3$	1.062	147	37.0	-3.9	29.2*	28.0	-3.0	22.0*	[107]
$PbTiO_3 + 0.025$ $Bi_{2/3}Zn_{1/3}Nb_{2/3}O_3$	1.061	200	15.0	-4.4	6.2*	7.9	-2.5	2.9*	[107]
$PbTiO_3 + 0.05$ $Bi_{2/3}Zn_{1/3}Nb_{2/3}O_3$	1.057	203	47.0	-7.4	32.2*	28.0	-4.1	19.8*	[107]
$Sr{:}Pb_{0.65}Ca_{0.31}Ti_{0.94}(Co_{1/2}W_{1/2})_{0.06}O_3$	1.008	509	86.0	-2.5	81.0	19.1*	-0.6*	18.0	[231]
$Pb(Ti_{0.96}(Cd_{0.5}W_{0.5})_{0.04})O_3 +$ 0.3wt% MnO2 + 0.4wt% NiO	1.055	190	56.0	-5.9	44.2*	33.0	-5.9	26.3*	[232]
$(Pb_{0.975}La_{0.025})(Ti_{0.99}Mn_{0.01})O_3$	1.051	220	52.8	-5.8	41.3	27.1	-3.0	21.2	[108]
$(Pb_{0.985}La_{0.015})(Ti_{0.99}Mn_{0.01})O_3$	1.021	379	62.0	-8.0	45.9	18.5	-2.4	13.7	[108]
$(Pb_{0.985}La_{0.015})Ti_{0.99}O_3$	1.021	503	83.8	-16.5	50.8	20.0	-3.9	12.1	[108]
$0.33(Bi_{0.7}La_{0.3})(Zn_{0.5}Ti_{0.5})O_3$ - $0.67PbTiO_3$	1.044	314	30.6	-11.0	8.7	11.0*	-3.9	3.1	[233]
$0.33(Bi_{0.6}La_{0.4})(Zn_{0.5}Ti_{0.5})O_3$ - $0.67PbTiO_3$	1.031	410	56.3	-13.2	29.9	15.5*	-3.7	8.2	[233]
0.33(Bi0.5La0.5)(Zn0.5Ti0.5)O3 - 0.67PbTiO3	1.023	528	70.1	-18.4	33.3	15.0*	-3.9	7.1	[233]

BF60-BZT14-PT26	1.124	264	16.0	6.8*	[234]
BF60-BZT15-PT25	1.098	258	27.0	11.8*	[234]
BF59-BZT15-PT26	1.109	258	41.0	18.0*	[234]
BF53-BZT15-PT32	1.176	302	30.0	11.2*	[234]
LF1-BF58-BZT15-PT26	1.104	265	39.0	16.6*	[234]
LF1-BF57-BZT15-PT26	1.106	260	47.0	20.4*	[234]
LF2.5-BF47.5-BZT15-PT35	1.128	367	43.0	13.2*	[234]
0.95PT-0.05BZT	1.062	147	37.0	28.4*	[234]
MLT	1.063	170	51.0	33.9*	[235]
0.54BF - 0.26PT-0.15BZT-0.05PZ	1.100	330	78.0	26.7*	[236]
0.52BF - 0.28PT-0.15BZT-0.05PZ	1.090	349	80.0	25.9*	[236]
0.50BF - 0.30PT-0.15BZT-0.05PZ	1.080	365	85.0	26.3*	[236]
0.1BZT-0.5PZ-0.4PT	1.013	978	300.0	34.7*	[236]
$0.50BiFeO_3$-$0.35PbTiO_3$-$0.15Bi(Zn_{0.5}Ti_{0.5})O_3$	1.150	191	0.5	0.3*	[236]
$0.50[(Bi_{0.95}La_{0.05})FeO_3]$-$0.35PbTiO_3$-$0.15Bi(Zn_{0.5}Ti_{0.5})O_3$	1.129	364	43.2	13.4*	[236]
$0.50[(Bi_{0.92}La_{0.08})FeO_3]$-$0.35PbTiO_3$-$0.15Bi(Zn_{0.5}Ti_{0.5})O_3$	1.116	448	58.8	14.8*	[236]
$0.50[(Bi_{0.9}La_{0.1})FeO_3]$-$0.35PbTiO_3$-$0.15Bi(Zn_{1/2}Ti_{1/2})O_3$	1.078	369	67.0	20.5*	[236]
$0.50[(Bi_{0.8}La_{0.2})FeO_3]$-$0.35PbTiO_3$-$0.15Bi(Zn_{0.5}Ti_{0.5})O_3$	1.047	901	129.4	16.2*	[236]
$0.88Pb(Zr_{0.56}Ti_{0.44})O_3$-$0.12Bi(Zn_{0.5}Ti_{0.5})O_3$	1.012	1430	365.0	28.8*	[237]
0.6PT-0.3BZT-0.1BF	1.105	170	1.5	1.0*	[238]
$0.48PbZrO_3$-$0.52[0.3Bi(Zn_{0.5}Ti_{0.5})O_3$-$0.7PbTiO_3]$	1.010	729	106.0	16.4*	[239]
$0.50PbZrO_3$-$0.50[0.3Bi(Zn_{0.5}Ti_{0.5})O_3$-$0.7PbTiO_3]$	1.018	946	159.0	19.0*	[239]
$0.52PbZrO_3$-$0.48[0.3Bi(Zn_{0.5}Ti_{0.5})O_3$-$0.7PbTiO_3]$	1.019	1080	311.0	32.5*	[239]
$0.54PbZrO_3$-$0.46(0.3Bi(Zn_{0/5}Ti_{0.5})O_3$-$0.7PbTiO_3]$	1.020	1160	213.0	20.7*	[239]
$0.56PbZrO_3$-$0.44[0.3Bi(Zn_{0.5}Ti_{0.5})O_3$-$0.7PbTiO_3]$	1.020	1020	134.0	14.8*	[239]

Appendix B

Supplementary Impedance Spectroscopy Data

B.1 Bode Impedance Plots

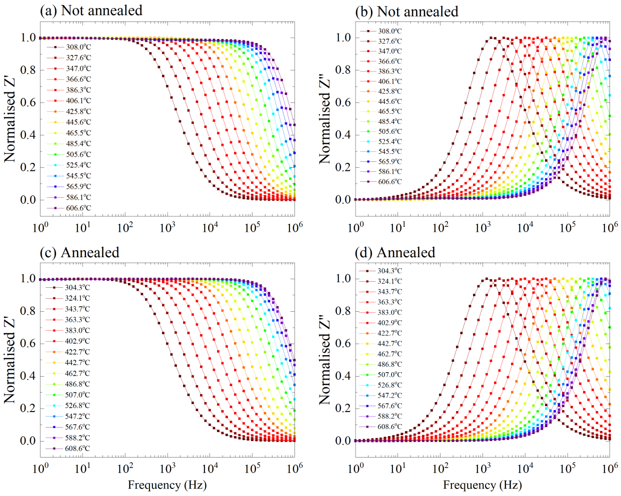

Figure B.1: (a) Real and (b) imaginary impedance for undoped BFPT65 before annealing, and (c) real and (d) imaginary impedance for undoped BFPT65 after annealing

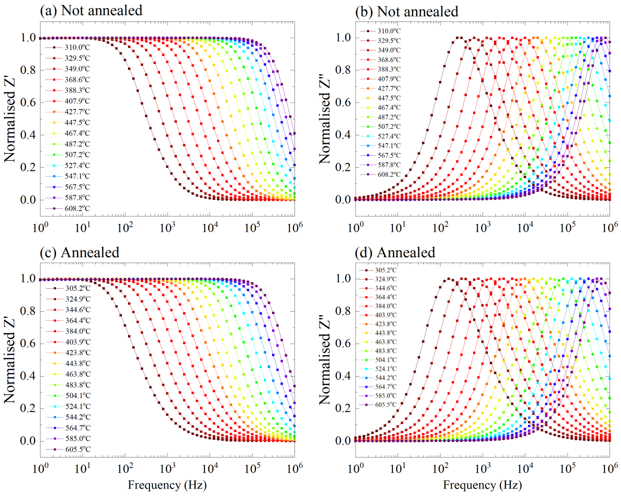

Figure B.2: (a) Real and (b) imaginary impedance for x=0.01 Nb:BFPT65 before annealing, and (c) real and (d) imaginary impedance for x=0.01 Nb:BFPT65 after annealing

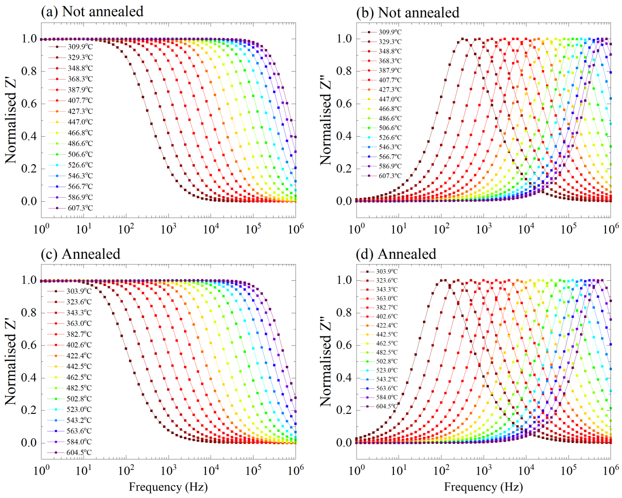

Figure B.3: (a) Real and (b) imaginary impedance for x=0.02 Nb:BFPT65 before annealing, and (c) real and (d) imaginary impedance for x=0.02 Nb:BFPT65 after annealing

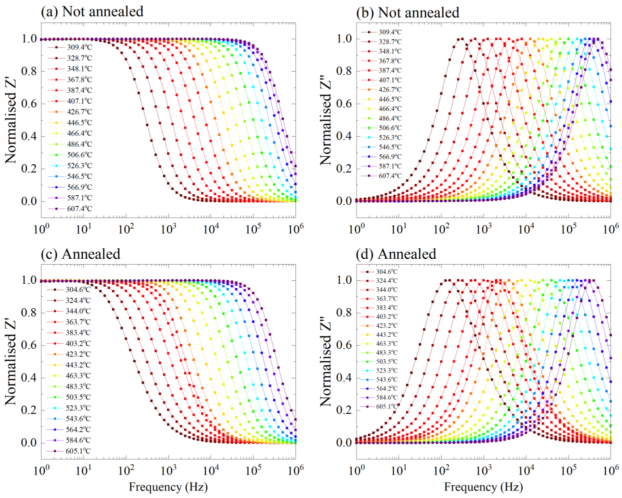

Figure B.4: (a) Real and (b) imaginary impedance for x=0.10 Nb:BFPT65 before annealing, and (c) real and (d) imaginary impedance for x=0.10 Nb:BFPT65 after annealing

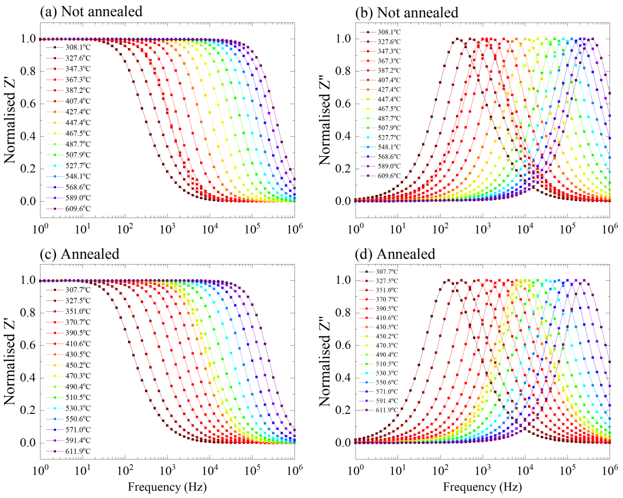

Figure B.5: (a) Real and (b) imaginary impedance for x=0.20 Nb:BFPT65 before annealing, and (c) real and (d) imaginary impedance for x=0.20 Nb:BFPT65 after annealing

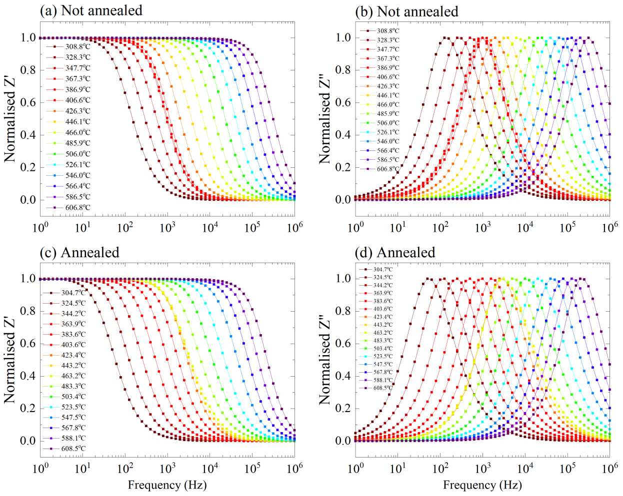

Figure B.6: (a) Real and (b) imaginary impedance for x=0.30 Nb:BFPT65 before annealing, and (c) real and (d) imaginary impedance for x=0.30 Nb:BFPT65 after annealing

B.2 Bode Modulus Plots

(a) Not annealed (b) Not annealed

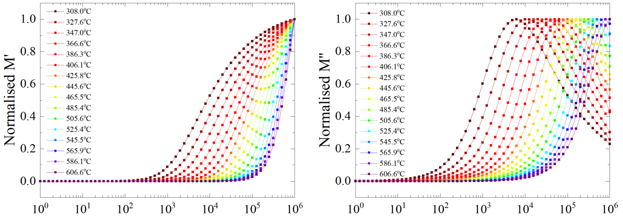

(c) Annealed (d) Annealed

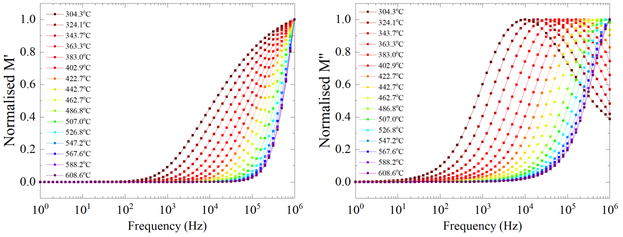

Figure B.7: (a) Real and (b) imaginary modulus for undoped BFPT65 before annealing, and (c) real and (d) imaginary modulus for undoped BFPT65 after annealing

(a) Not annealed (b) Not annealed

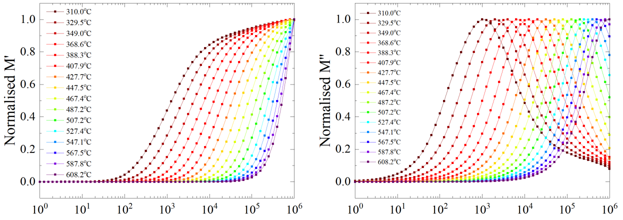

(c) Annealed (d) Annealed

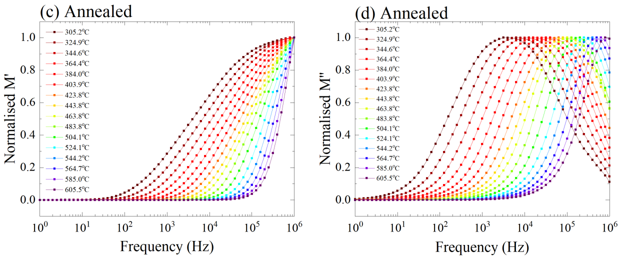

Figure B.8: (a) Real and (b) imaginary modulus for x=0.01 Nb:BFPT65 before annealing, and (c) real and (d) imaginary modulus for x=0.01 Nb:BFPT65 after annealing

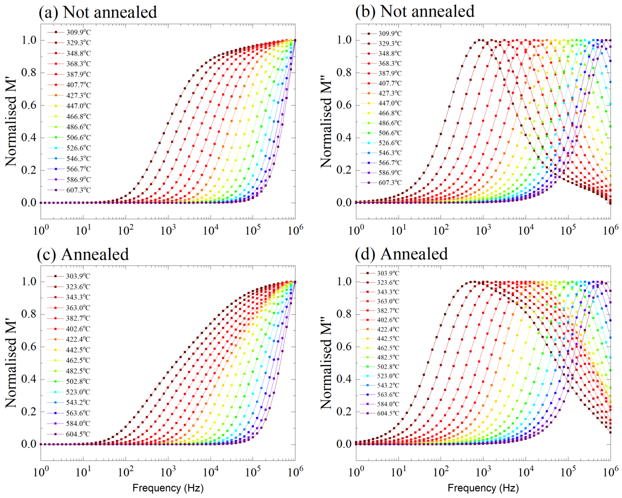

Figure B.9: (a) Real and (b) imaginary modulus for x=0.02 Nb:BFPT65 before annealing, and (c) real and (d) imaginary modulus for x=0.02 Nb:BFPT65 after annealing

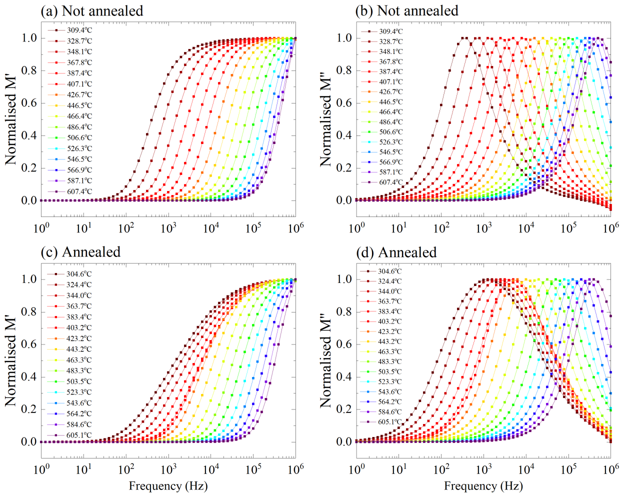

Figure B.10: (a) Real and (b) imaginary modulus for x=0.10 Nb:BFPT65 before annealing, and (c) real and (d) imaginary modulus for x=0.10 Nb:BFPT65 after annealing

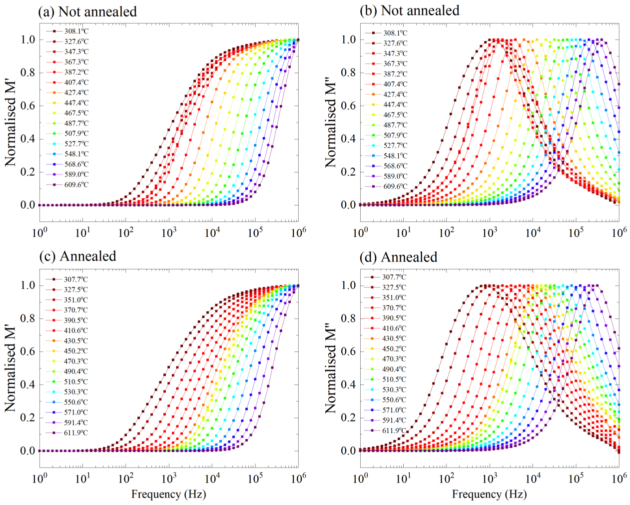

Figure B.11: (a) Real and (b) imaginary modulus for x=0.20 Nb:BFPT65 before annealing, and (c) real and (d) imaginary modulus for x=0.20 Nb:BFPT65 after annealing

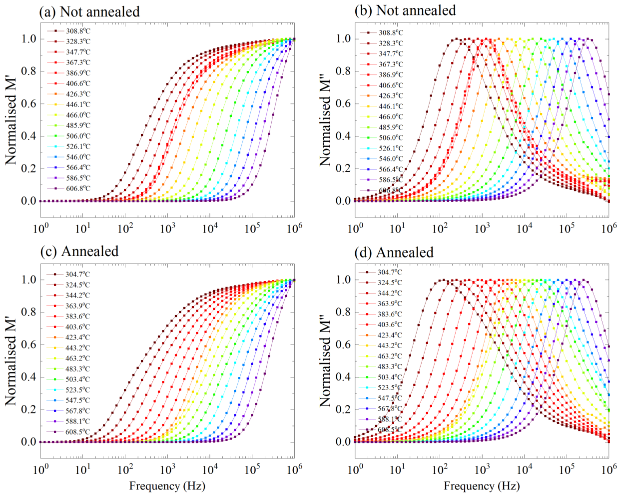

Figure B.12: (a) Real and (b) imaginary modulus for x=0.30 Nb:BFPT65 before annealing, and (c) real and (d) imaginary modulus for x=0.30 Nb:BFPT65 after annealing

B.3 Real Admittance v Angular Frequency

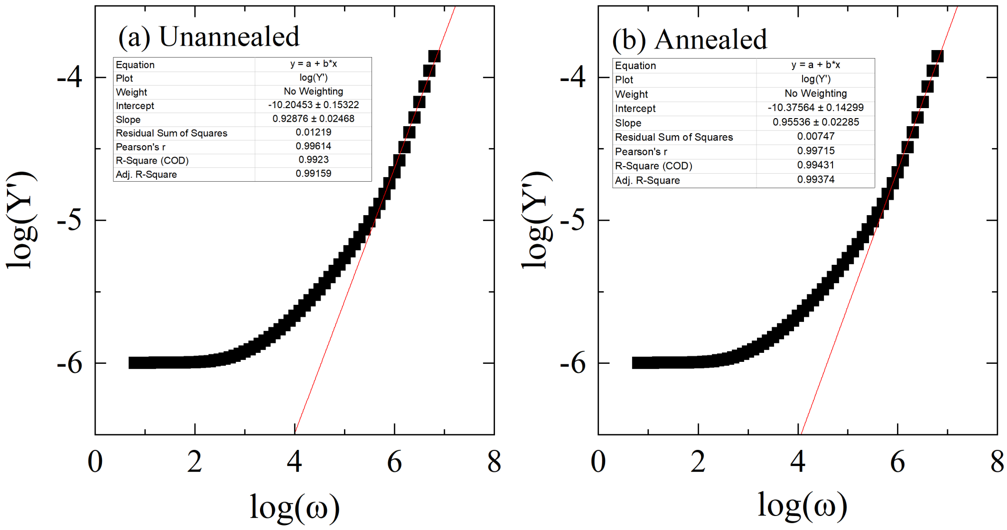

Equation	y = a + b*x
Plot	log(Y')
Weight	No Weighting
Intercept	-10.20453 ± 0.15322
Slope	0.92876 ± 0.02468
Residual Sum of Squares	0.01219
Pearson's r	0.99614
R-Square (COD)	0.9923
Adj. R-Square	0.99159

Equation	y = a + b*x
Plot	log(Y')
Weight	No Weighting
Intercept	-10.37564 ± 0.14299
Slope	0.95536 ± 0.02285
Residual Sum of Squares	0.00747
Pearson's r	0.99715
R-Square (COD)	0.99431
Adj. R-Square	0.99374

Figure B.13: Real admittance vs angular frequency for undoped BFPT65 polycrystalline ceramics (a) before annealing, and (b) after annealing

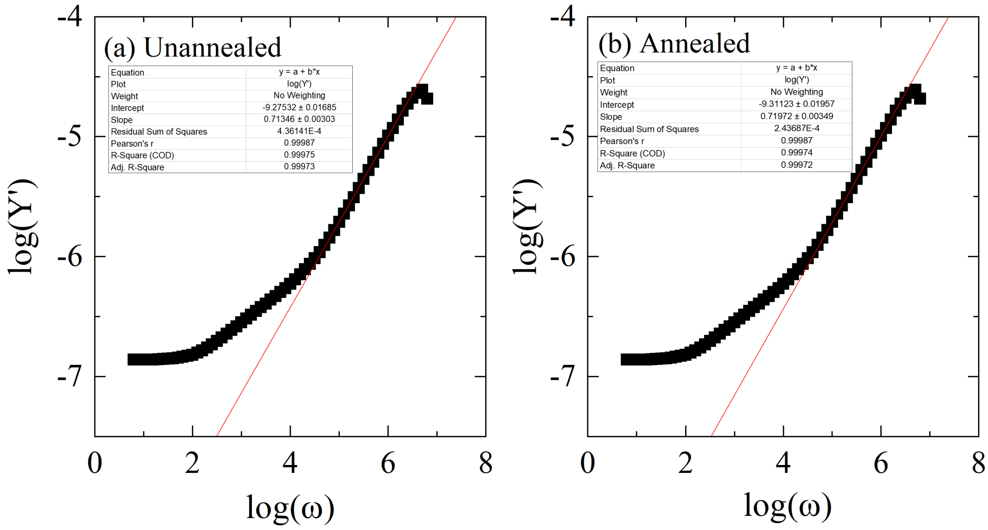

Equation	y = a + b*x
Plot	log(Y')
Weight	No Weighting
Intercept	-9.27532 ± 0.01685
Slope	0.71346 ± 0.00303
Residual Sum of Squares	4.36141E-4
Pearson's r	0.99987
R-Square (COD)	0.99975
Adj. R-Square	0.99973

Equation	y = a + b*x
Plot	log(Y')
Weight	No Weighting
Intercept	-9.31123 ± 0.01957
Slope	0.71972 ± 0.00349
Residual Sum of Squares	2.43687E-4
Pearson's r	0.99987
R-Square (COD)	0.99974
Adj. R-Square	0.99972

Figure B.14: Real admittance vs angular frequency for x=0.01 Nb:BFPT65 polycrystalline ceramics (a) before annealing, and (b) after annealing

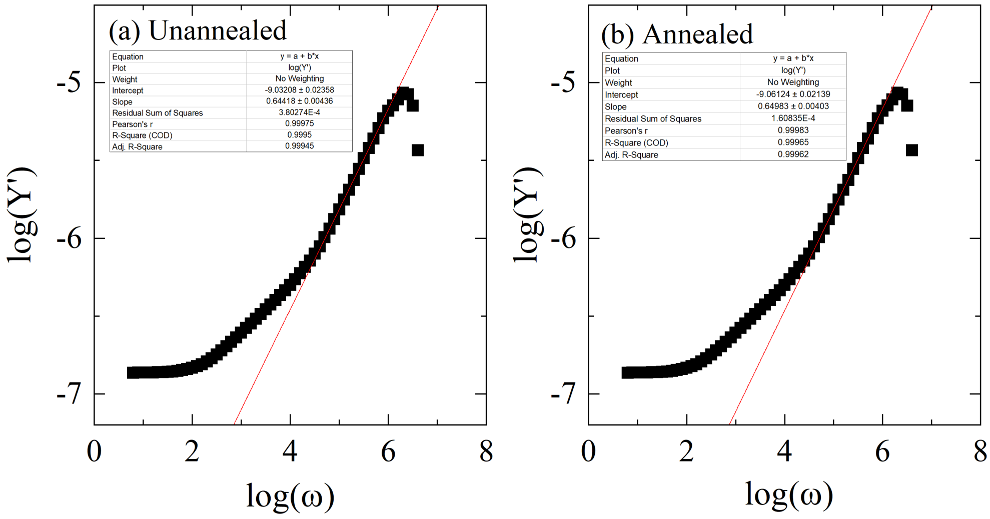

Equation	y = a + b*x
Plot	log(Y')
Weight	No Weighting
Intercept	-9.03208 ± 0.02358
Slope	0.64418 ± 0.00436
Residual Sum of Squares	3.80274E-4
Pearson's r	0.99975
R-Square (COD)	0.9995
Adj. R-Square	0.99945

Equation	y = a + b*x
Plot	log(Y')
Weight	No Weighting
Intercept	-9.06124 ± 0.02139
Slope	0.64983 ± 0.00403
Residual Sum of Squares	1.60835E-4
Pearson's r	0.99983
R-Square (COD)	0.99965
Adj. R-Square	0.99962

Figure B.15: Real admittance vs angular frequency for x=0.02 Nb:BFPT65 polycrystalline ceramics (a) before annealing, and (b) after annealing

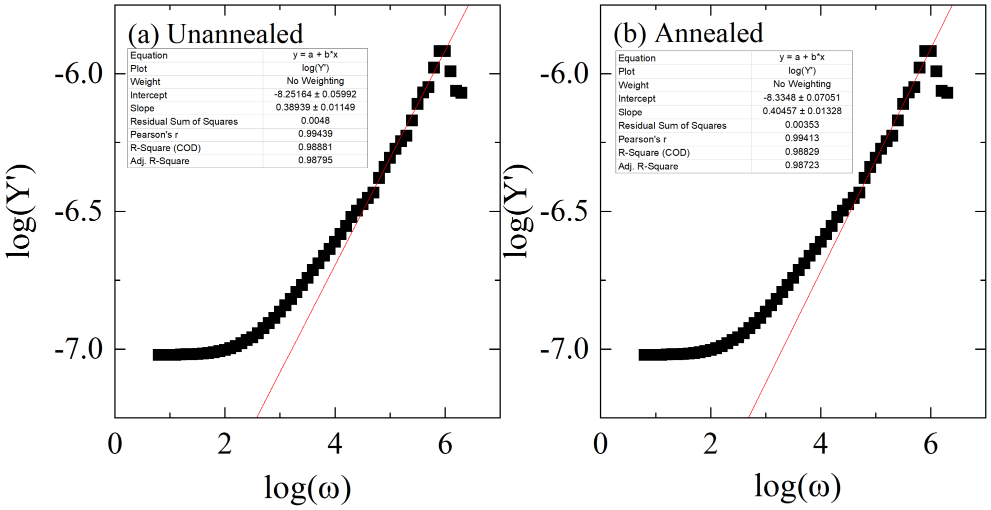

Equation	y = a + b*x
Plot	log(Y')
Weight	No Weighting
Intercept	-8.25164 ± 0.05992
Slope	0.38939 ± 0.01149
Residual Sum of Squares	0.0048
Pearson's r	0.99439
R-Square (COD)	0.98881
Adj. R-Square	0.98795

Equation	y = a + b*x
Plot	log(Y')
Weight	No Weighting
Intercept	-8.3348 ± 0.07051
Slope	0.40457 ± 0.01328
Residual Sum of Squares	0.00353
Pearson's r	0.99413
R-Square (COD)	0.98829
Adj. R-Square	0.98723

Figure B.16: Real admittance vs angular frequency for x=0.10 Nb:BFPT65 polycrystalline ceramics (a) before annealing, and (b) after annealing

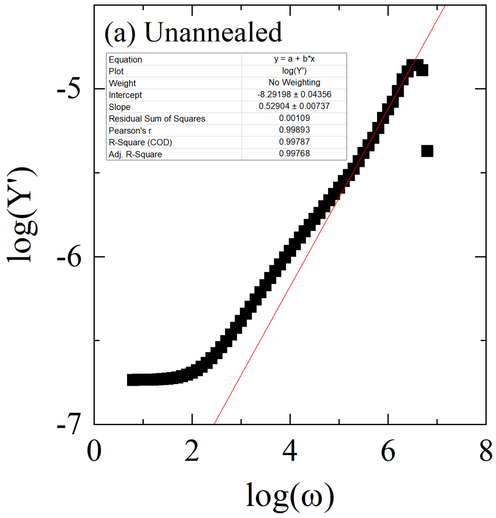

Equation	y = a + b*x
Plot	log(Y')
Weight	No Weighting
Intercept	-8.29198 ± 0.04356
Slope	0.52904 ± 0.00737
Residual Sum of Squares	0.00109
Pearson's r	0.99893
R-Square (COD)	0.99787
Adj. R-Square	0.99768

Equation	y = a + b*x
Plot	log(Y')
Weight	No Weighting
Intercept	-8.1315 ± 0.05294
Slope	0.50258 ± 0.00918
Residual Sum of Squares	0.00401
Pearson's r	0.99767
R-Square (COD)	0.99535
Adj. R-Square	0.99502

Figure B.17: Real admittance vs angular frequency for x=0.20 Nb:BFPT65 polycrystalline ceramics (a) before annealing, and (b) after annealing

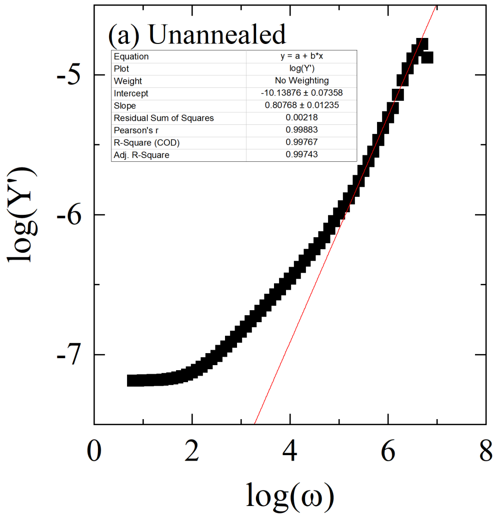

Equation	y = a + b*x
Plot	log(Y')
Weight	No Weighting
Intercept	-10.13876 ± 0.07358
Slope	0.80768 ± 0.01235
Residual Sum of Squares	0.00218
Pearson's r	0.99883
R-Square (COD)	0.99767
Adj. R-Square	0.99743

Equation	y = a + b*x
Plot	log(Y')
Weight	No Weighting
Intercept	-10.10948 ± 0.06516
Slope	0.8026 ± 0.01084
Residual Sum of Squares	0.00235
Pearson's r	0.999
R-Square (COD)	0.998
Adj. R-Square	0.99781

Figure B.18: Real admittance vs angular frequency for x=0.30 Nb:BFPT65 polycrystalline ceramics (a) before annealing, and (b) after annealing

B.4 Complex Impedance Plots

(a) x=0.00 Not annealed

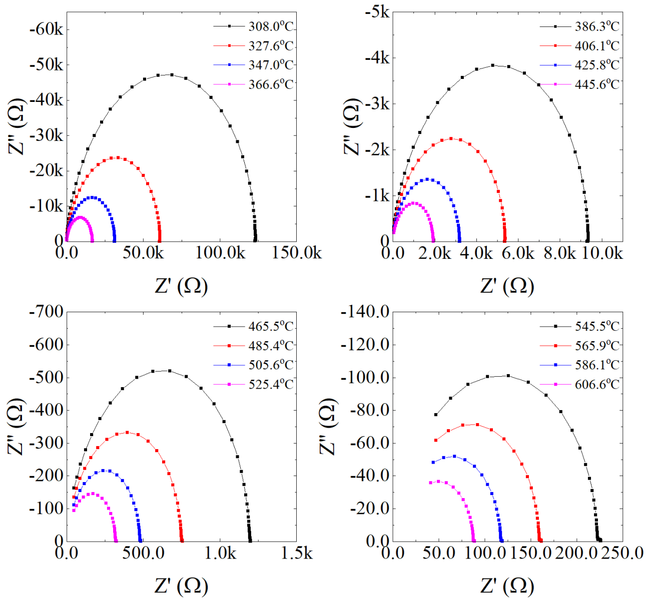

(b) x=0.00 Annealed

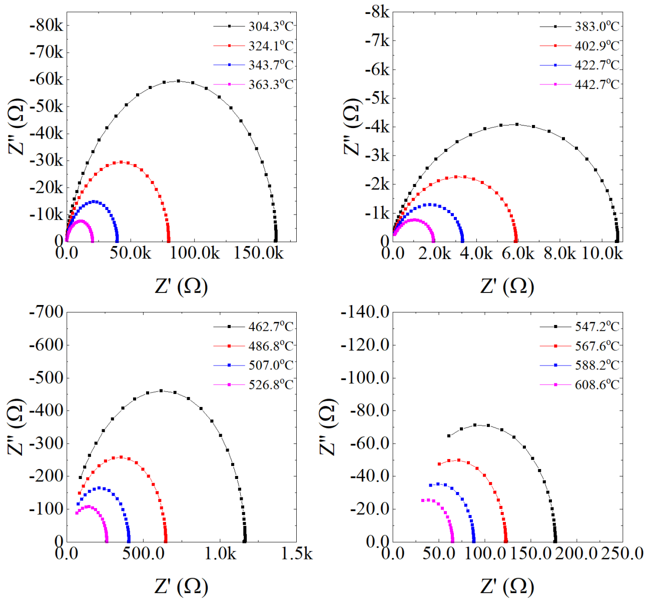

Figure B.19: Complex impedance plots for (a) undoped, unannealed BFPT65 from 308.0°C to 606.6°C and (b) undoped, annealed BFPT65 from 304.3°C to 608.6°C

(a) x=0.01 Not annealed

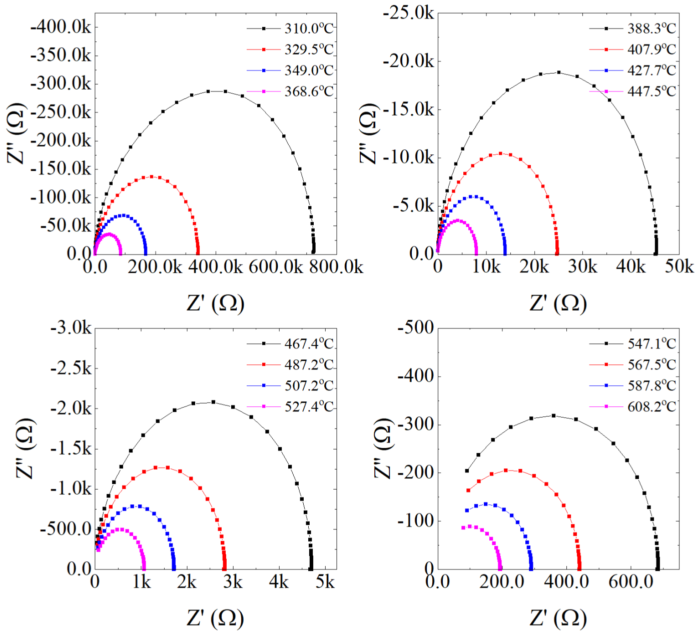

(b) x=0.01 Annealed

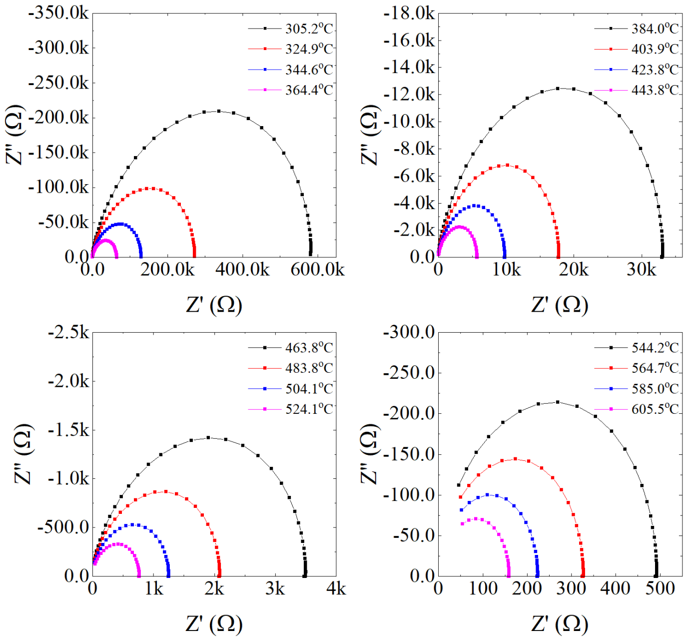

Figure B.20: Complex impedance plots for (a) unannealed x=0.01 Nb:BFPT65 from 310.0°C to 608.2°C and (b) annealed x=0.01 Nb:BFPT65 from 305.2°C to 605.5°C

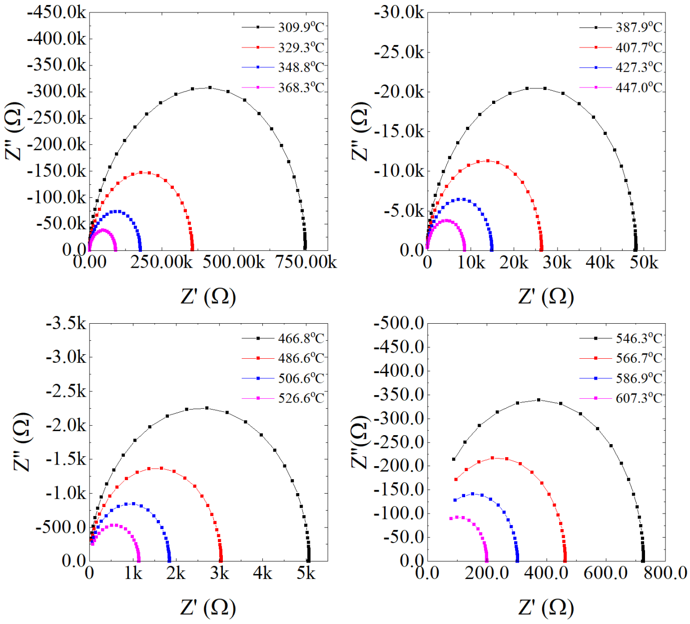

(a) x=0.02 Not annealed

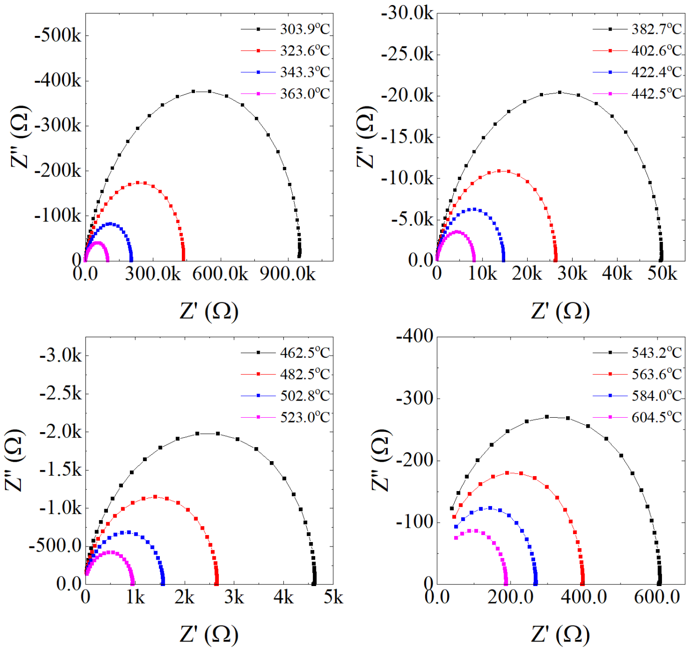

(b) x=0.02 Annealed

Figure B.21: Complex impedance plots for (a) unannealed x=0.02 Nb:BFPT65 from 309.9°C to 607.3°C and (b) annealed x=0.02 Nb:BFPT65 from 303.9°C to 604.5°C

(a) x=0.10 Not annealed

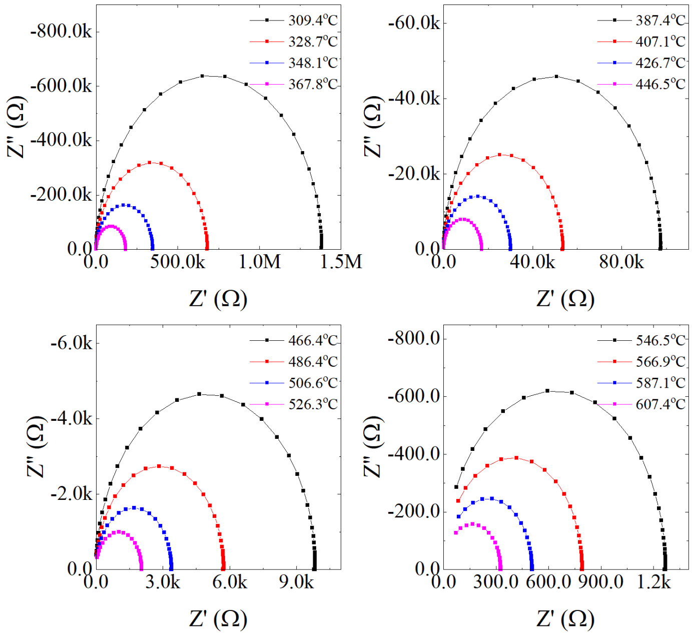

(b) x=0.10 Annealed

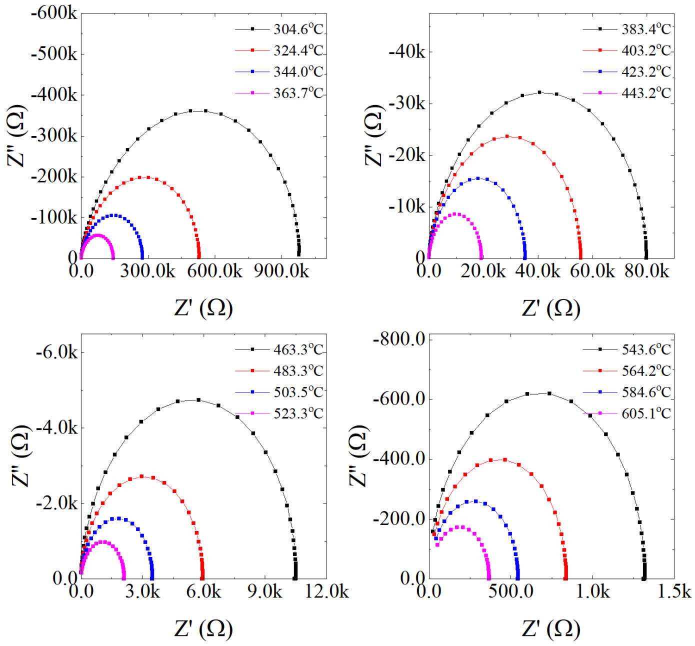

Figure B.22: Complex impedance plots for (a) unannealed x=0.10 Nb:BFPT65 from 309.4°C to 607.4°C and (b) annealed x=0.10 Nb:BFPT65 from 304.6°C to 605.1°C

(a) x=0.20 Not annealed

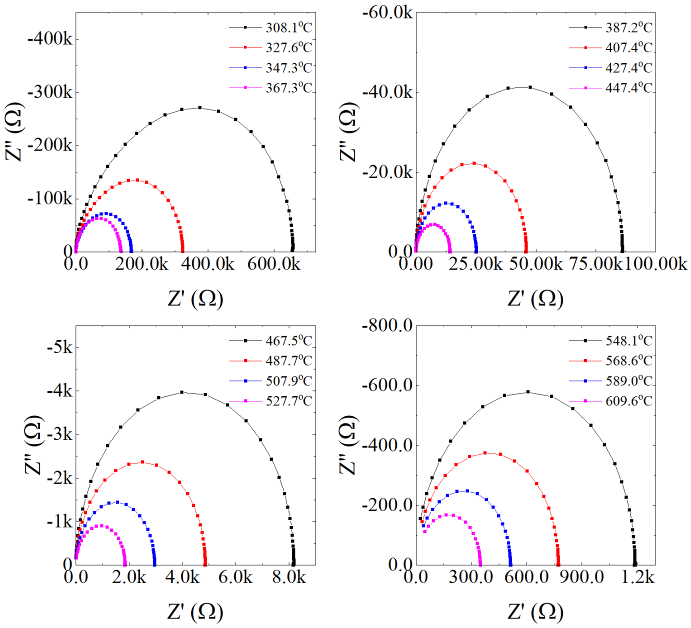

(b) x=0.20 Annealed

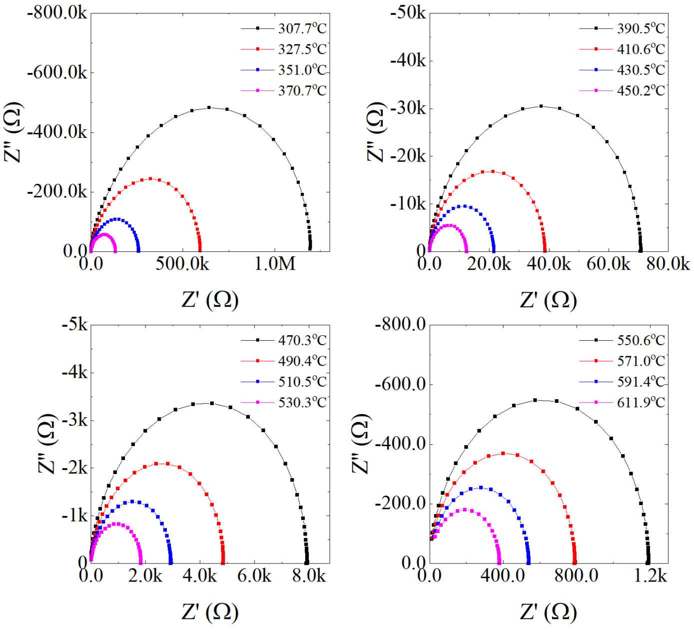

Figure B.23: Complex impedance plots for (a) unannealed x=0.20 Nb:BFPT65 from 308.1°C to 609.6°C and (b) annealed x=0.20 Nb:BFPT65 from 308.1°C to 609.6°C

(a) x=0.30 Not annealed

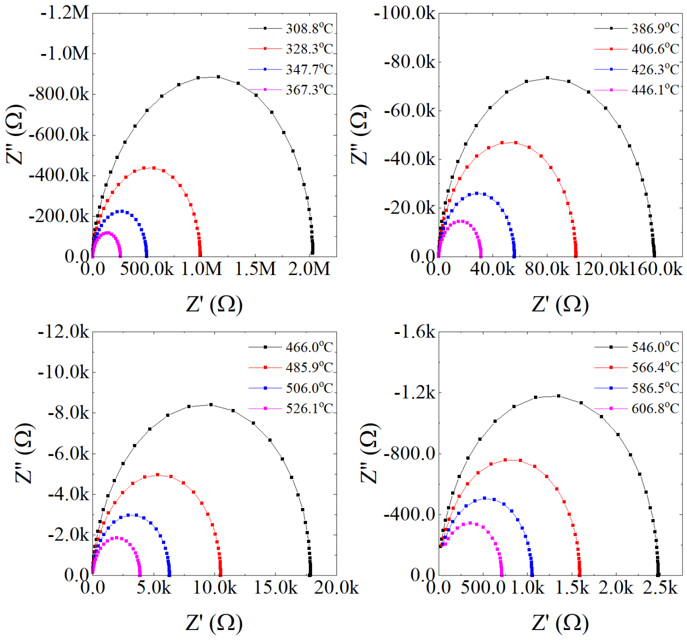

(b) x=0.30 Annealed

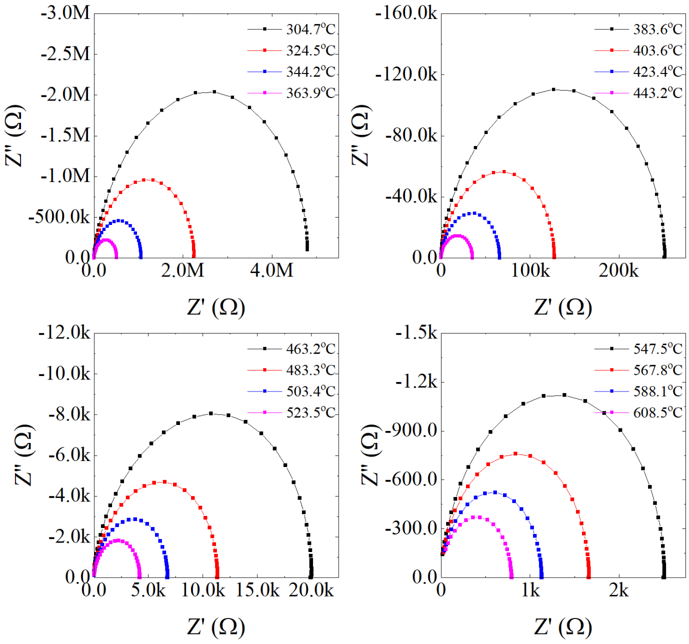

Figure B.24: Complex impedance plots for (a) unannealed x=0.30 Nb:BFPT65 from 308.8°C to 606.8°C and (b) annealed x=0.30 Nb:BFPT65 from 304.7°C to 608.5°C

B.5 Complex Modulus Plots

(a) x=0.00 Not annealed

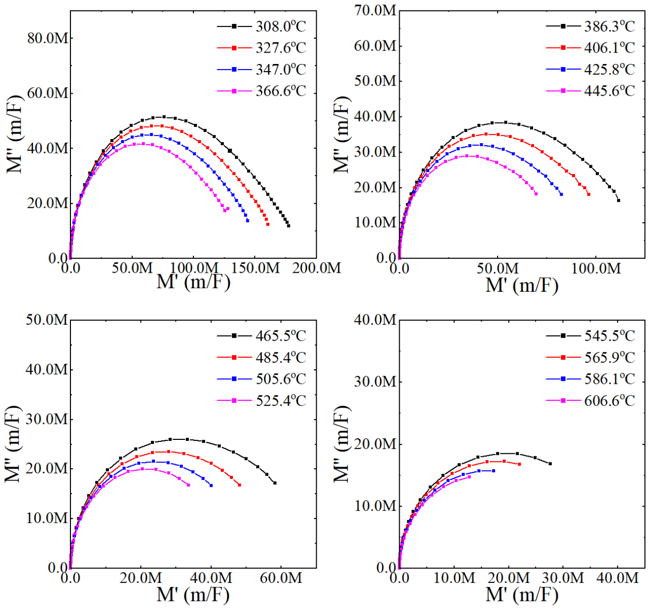

(b) x=0.00 Annealed

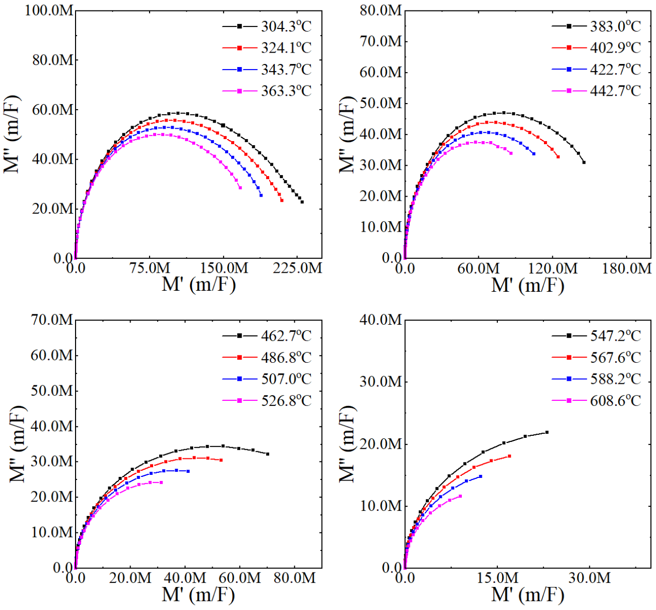

Figure B.25: Complex modulus plots for (a) unannealed x=0.00 Nb:BFPT65 from 308.0°C to 606.6°C and (b) annealed x=0.00 Nb:BFPT65 from 304.3°C to 608.6°C

(a) x=0.01 Not Annealed

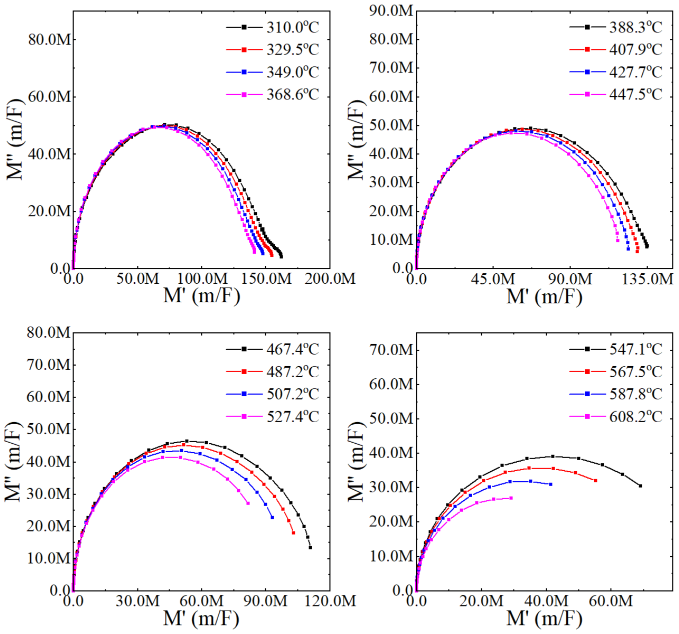

(b) x=0.01 Annealed

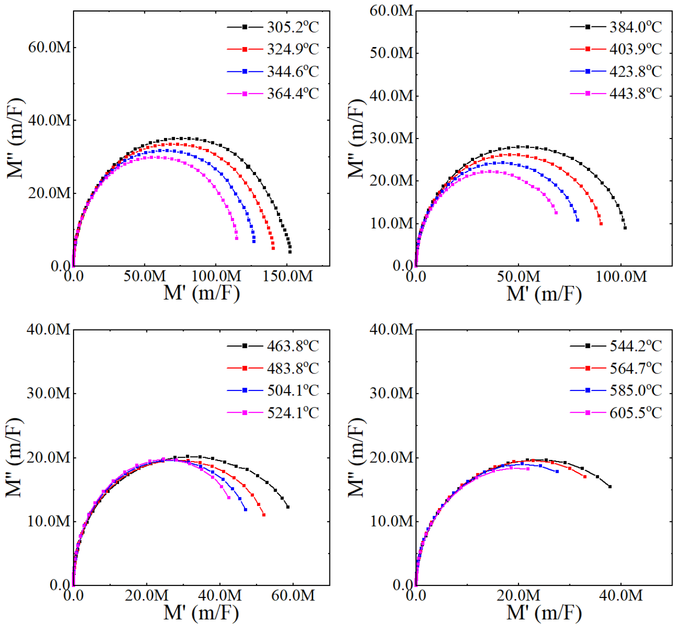

Figure B.26: Complex modulus plots for (a) unannealed x=0.01 Nb:BFPT65 from 310.0°C to 608.2°C and (b) annealed x=0.01 Nb:BFPT65 from 305.2°C to 605.5°C

(a) x=0.02 Not Annealed

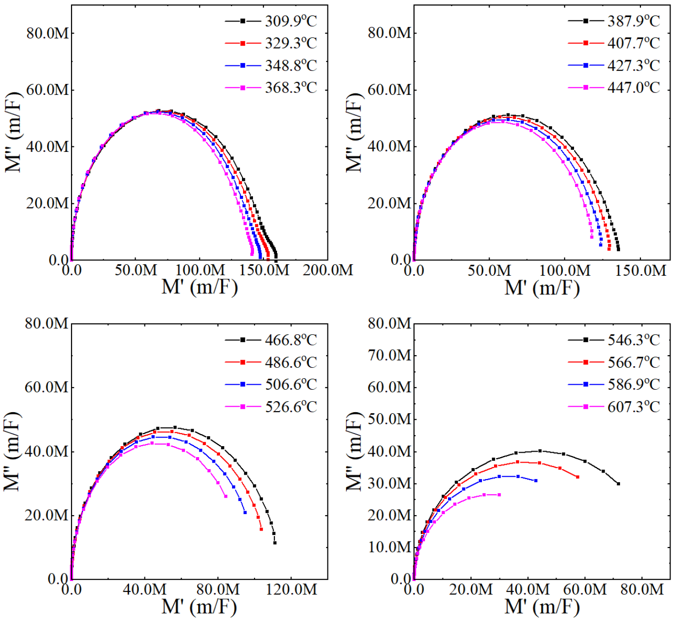

(b) x=0.02 Annealed

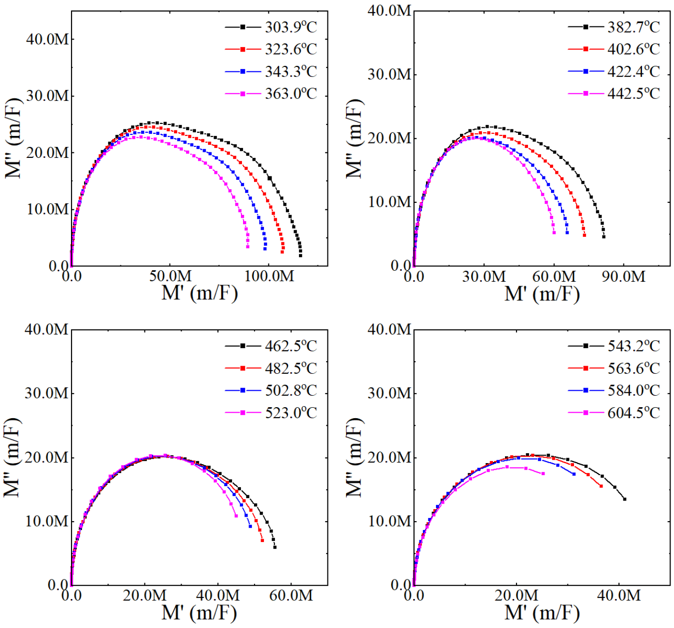

Figure B.27: Complex modulus plots for (a) unannealed x=0.02 Nb:BFPT65 from 309.9°C to 607.3°C and (b) annealed x=0.02 Nb:BFPT65 from 303.9°C to 604.5°C

(a) x=0.10 Not Annealed

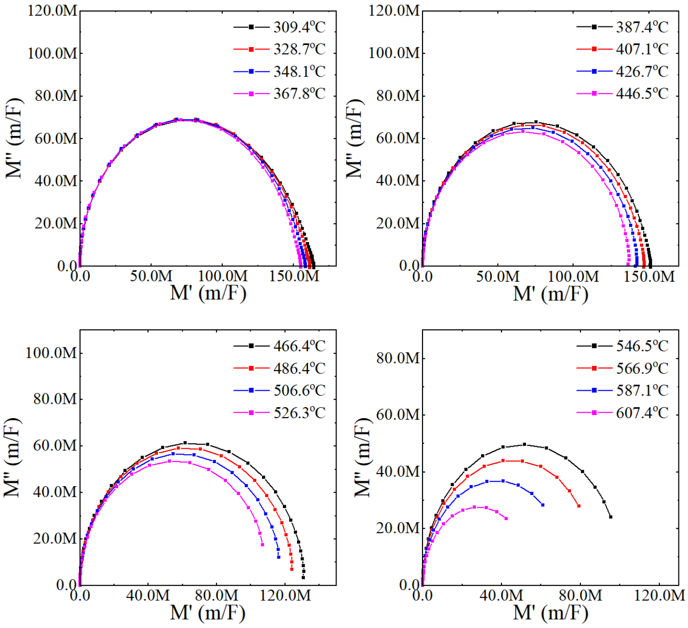

(b) x=0.10 Annealed

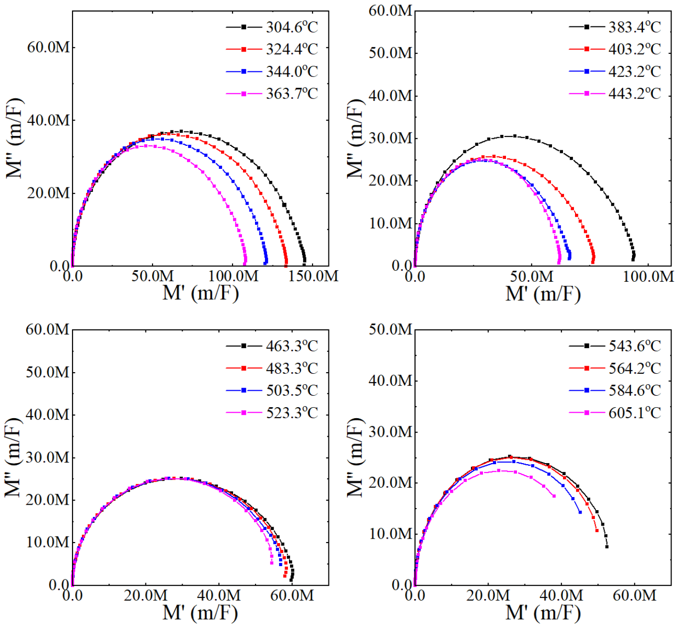

Figure B.28: Complex modulus plots for (a) unannealed x=0.10 Nb:BFPT65 from 309.4°C to 607.4°C and (b) annealed x=0.10 Nb:BFPT65 from 304.6°C to 605.1°C

(a) x=0.20 Not Annealed

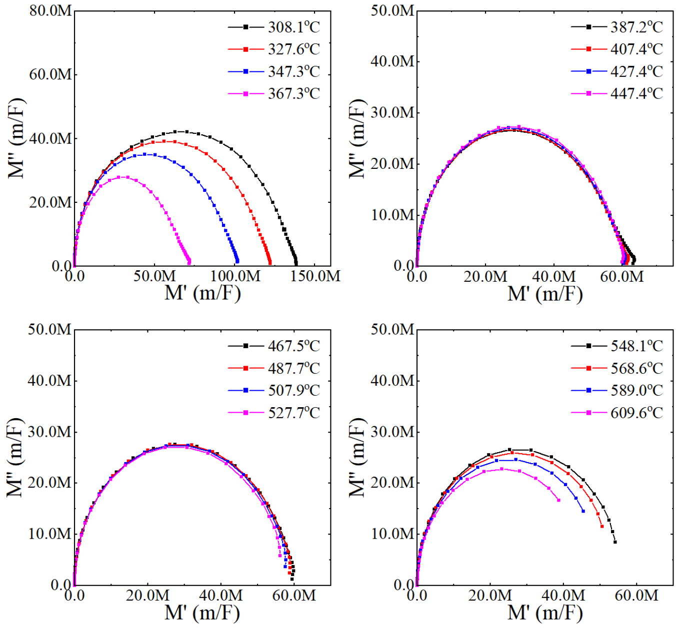

(b) x=0.20 Annealed

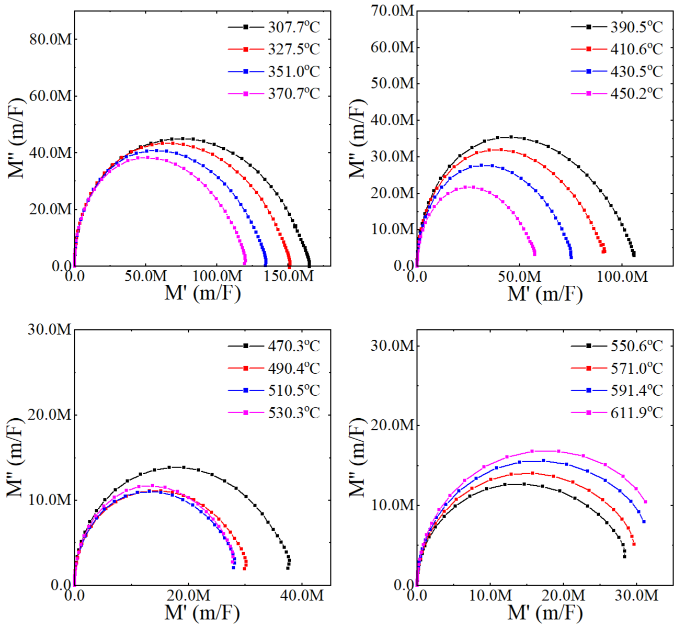

Figure B.29: Complex modulus plots for (a) unannealed x=0.20 Nb:BFPT65 from 308.1°C to 609.6°C and (b) annealed x=0.20 Nb:BFPT65 from 308.1°C to 609.6°C

(a) x=0.30 Not Annealed

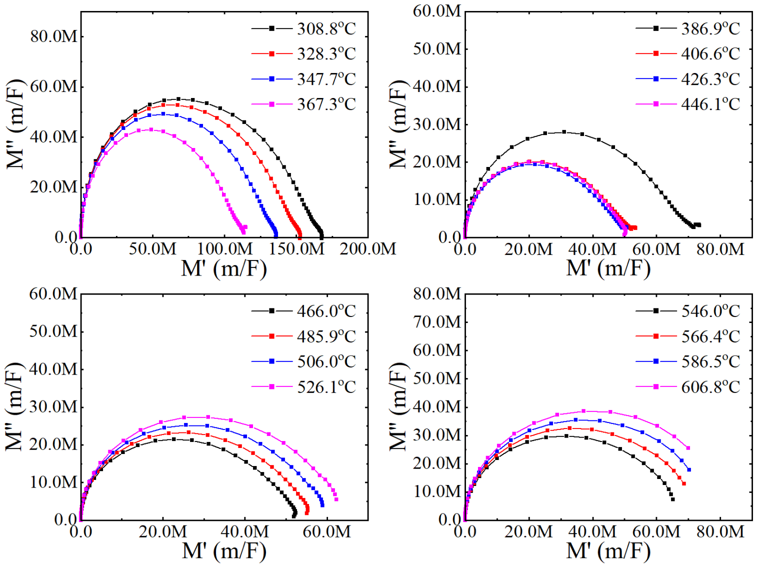

(b) x=0.30 Annealed

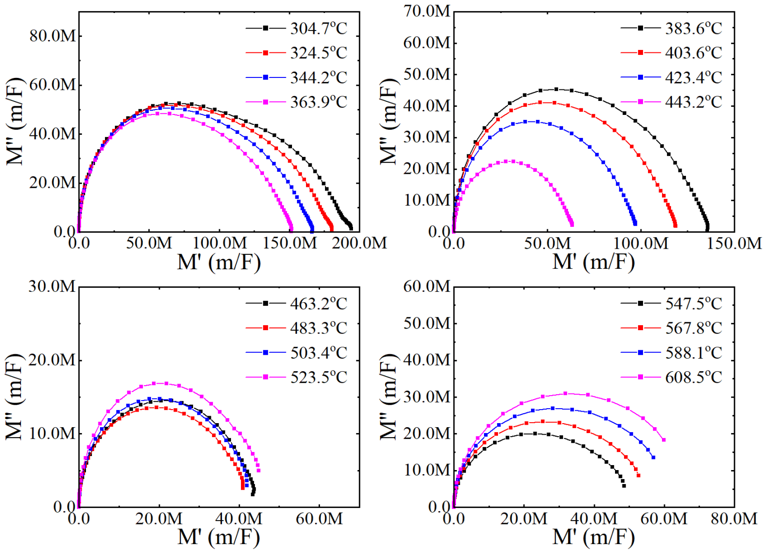

Figure B.30: Complex modulus plots for (a) unannealed x=0.30 Nb:BFPT65 from 308.8°C to 606.8°C and (b) annealed x=0.30 Nb:BFPT65 from 304.7°C to 608.5°C

B.6 Table of Cole-Cole Fittings

Table B.1: Impedance spectroscopy fitting results for unannealed x=0.00 BFPT65:Nb from 308.0°C to 485.4°C

Temperature (°C)	C_1 (nF)	B	m	R_1 (Ω)	C_2 (nF)	R_2 (Ω)
308.0	0.311	1.24×10^{-8}	0.65432	73092	2.68	51097
327.6	0.342	1.68×10^{-8}	0.65432	34258	2.47	27044
347.0	0.382	2.24×10^{-8}	0.65432	16573	2.29	14980
366.6	0.435	2.96×10^{-8}	0.65432	8306	2.17	8559
386.3	0.502	3.83×10^{-8}	0.65432	4359	2.13	5025
406.1	0.585	4.97×10^{-8}	0.65432	2380	2.12	3014
425.8	0.693	6.28×10^{-8}	0.65432	1358	2.17	1849
445.6	0.803	8.72×10^{-8}	0.65432	763.9	2.15	1177
465.5	0.989	1.05×10^{-7}	0.65432	454.0	2.28	746.1
485.4	1.170	1.59×10^{-7}	0.65432	265.4	2.28	488.6

Table B.2: Impedance spectroscopy fitting results for annealed x=0.00 Nb:BFPT65 from 304.3°C to 567.6°C

Temperature (°C)	C_1 (nF)	B	m	R_1 (Ω)	C_2 (nF)	R_2 (Ω)
304.3	0.219	1.65×10^{-8}	0.63101	107000	3.14	59322
324.1	0.234	2.23×10^{-8}	0.63101	49717	2.89	31152
343.7	0.252	2.98×10^{-8}	0.63101	23624	2.72	16506
363.3	0.275	3.91×10^{-8}	0.63101	11623	2.63	8885
383.0	0.305	5.02×10^{-8}	0.63101	5938	2.61	4901
402.9	0.343	6.32×10^{-8}	0.63101	3166	2.63	2774
422.7	0.393	7.82×10^{-8}	0.63101	1736	2.69	1619
442.7	0.450	9.71×10^{-8}	0.63101	976.4	2.73	979.1
462.7	0.537	1.14×10^{-7}	0.63101	561.7	2.83	606.3
486.8	0.637	1.34×10^{-7}	0.63101	302.9	3.02	346.1
507.0	0.776	1.49×10^{-7}	0.63101	189.4	3.29	218.3
526.8	0.994	1.54×10^{-7}	0.63101	124.5	3.77	138.8
547.2	1.010	1.62×10^{-7}	0.63101	84.11	4.26	92.96
567.6	1.210	1.91×10^{-7}	0.63101	56.14	4.65	66.98

Table B.3: Impedance spectroscopy fitting results for unannealed x=0.01 Nb:BFPT65 from 310.0°C to 608.2°C

Temperature (°C)	C_1 (nF)	B	m	R_1 (Ω)	C_2 (nF)	R_2 (Ω)
310.0	0.389	5.50×10^{-9}	0.64628	317000	1.80	412000
329.5	0.408	6.81×10^{-9}	0.64628	153000	1.78	191000
349.0	0.431	8.37×10^{-9}	0.64628	74884	1.71	94144
368.6	0.457	1.02×10^{-8}	0.64628	37450	1.62	48495
388.3	0.483	1.23×10^{-8}	0.64628	19642	1.56	25791
407.9	0.522	1.41×10^{-8}	0.64628	10254	1.47	14575
427.7	0.565	1.64×10^{-8}	0.64628	5567	1.39	8448
447.5	0.620	1.92×10^{-8}	0.64628	3047	1.31	5003
467.4	0.699	2.33×10^{-8}	0.64628	1648	1.22	3063
487.2	0.798	2.87×10^{-8}	0.64628	907	1.15	1917
507.2	0.930	3.29×10^{-8}	0.64628	517.7	1.12	1203
527.4	1.150	4.53×10^{-8}	0.64628	250.1	1.02	820.5
547.1	1.310	6.09×10^{-8}	0.64628	144.4	1.03	540.2
567.5	1.460	9.50×10^{-8}	0.64628	81.4	1.06	359.3
587.8	1.450	1.42×10^{-7}	0.64628	48.74	1.16	242.1
608.2	0.909	2.08×10^{-7}	0.64628	24.83	1.29	169.1

Table B.4: Impedance spectroscopy fitting results for annealed x=0.01 Nb:BFPT65 from 305.2°C to 605.5°C

Temperature (°C)	C_1 (nF)	B	m	R_1 (Ω)	C_2 (nF)	R_2 (Ω)
305.2	0.344	2.79×10^{-8}	0.57405	349000	4.49	251000
324.9	0.371	3.83×10^{-8}	0.57405	157000	4.24	122000
344.6	0.405	5.25×10^{-8}	0.57405	71533	4.01	60718
364.4	0.448	7.04×10^{-8}	0.57405	33749	3.82	31737
384.0	0.502	9.25×10^{-8}	0.57405	16554	3.74	16981
403.9	0.570	1.19×10^{-7}	0.57405	8488	3.70	9475
423.8	0.657	1.50×10^{-7}	0.57405	4484	3.73	5411
443.8	0.756	1.93×10^{-7}	0.57405	2501	3.74	3242
463.8	0.924	2.42×10^{-7}	0.57405	1343	3.42	2174
483.8	1.160	2.41×10^{-7}	0.57405	732.6	3.18	1363
504.1	1.360	2.28×10^{-7}	0.57405	433.0	3.11	820.5
524.1	1.510	2.29×10^{-7}	0.57405	256.8	2.97	512.7
544.2	1.670	2.38×10^{-7}	0.57405	161.4	2.85	331.2
564.7	1.820	2.48×10^{-7}	0.57405	100.3	2.69	226.6
585.0	1.990	2.49×10^{-7}	0.57405	65.6	2.63	158.4
605.5	1.940	2.57×10^{-7}	0.57405	43.4	2.61	115.9

Table B.5: Impedance spectroscopy fitting results for unannealed x=0.02 Nb:BFPT65 from 309.9°C to 607.3°C

Temperature (°C)	C_1 (nF)	B	m	R_1 (Ω)	C_2 (nF)	R_2 (Ω)
309.9	0.418	6.68×10^{-9}	0.60776	333000	1.48	420000
329.3	0.436	8.67×10^{-9}	0.60776	161000	1.47	198000
348.8	0.462	1.09×10^{-8}	0.60776	77833	1.42	99198
368.3	0.489	1.34×10^{-8}	0.60776	38966	1.38	51675
387.9	0.515	1.62×10^{-8}	0.60776	20682	1.37	27698
407.7	0.542	1.92×10^{-8}	0.60776	11362	1.38	15124
427.3	0.576	2.24×10^{-8}	0.60776	6372	1.37	8581
447.0	0.619	2.57×10^{-8}	0.60776	3638	1.36	5002
466.8	0.678	3.06×10^{-8}	0.60776	2083	1.31	2996
486.8	0.747	3.69×10^{-8}	0.60776	1221	1.28	1824
506.6	0.848	4.60×10^{-8}	0.60776	700.0	1.23	1150
526.6	1.000	5.87×10^{-8}	0.60776	377.8	1.15	766.2
546.3	1.170	6.58×10^{-8}	0.60776	216.8	1.15	509.7
566.7	1.380	1.12×10^{-7}	0.60776	119.0	1.15	344.9
586.9	1.590	1.79×10^{-7}	0.60776	62.22	1.20	241.0
607.3	1.180	4.46×10^{-7}	0.60776	26.27	1.29	173.7

Table B.6: Impedance spectroscopy fitting results for annealed x=0.02 Nb:BFPT65 from 303.9°C to 604.5°C

Temperature (°C)	C_1 (nF)	B	m	R_1 (Ω)	C_2 (nF)	R_2 (Ω)
303.9	0.483	2.18×10^{-8}	0.60416	487000	3.20	490000
323.6	0.521	2.97×10^{-8}	0.60416	211000	3.11	234000
343.3	0.568	4.02×10^{-8}	0.60416	93338	3.02	114000
363.0	0.627	5.36×10^{-8}	0.60416	42561	2.95	57516
382.7	0.701	6.98×10^{-8}	0.60416	20118	2.90	30180
402.6	0.799	8.80×10^{-8}	0.60416	9990	2.86	16566
422.4	0.934	1.10×10^{-7}	0.60416	5089	2.71	9790
442.5	1.080	1.20×10^{-7}	0.60416	2737	2.68	5524
462.5	1.220	1.26×10^{-7}	0.60416	1521	2.67	3117
482.5	1.340	1.30×10^{-7}	0.60416	888.5	2.70	1774
502.8	1.440	1.38×10^{-7}	0.60416	533.5	2.71	1039
523.0	1.600	1.19×10^{-7}	0.60416	346.2	2.84	610.2
543.2	1.720	1.52×10^{-7}	0.60416	208.7	2.62	398.4
563.6	1.980	1.78×10^{-7}	0.60416	121.1	2.39	276.1
584.0	2.140	2.23×10^{-7}	0.60416	71.39	2.24	197.7
604.5	2.390	2.42×10^{-7}	0.60416	44.63	2.27	143.5

Table B.7: Impedance spectroscopy fitting results for unannealed x=0.10 Nb:BFPT65 from 309.4°C to 607.4°C

Temperature (°C)	C_1 (nF)	B	m	R_1 (Ω)	C_2 (nF)	R_2 (Ω)
309.4	0.652	9.21×10^{-9}	0.53563	400000	0.627	993000
328.7	0.724	1.31×10^{-8}	0.53563	180000	0.591	506000
348.1	0.743	1.58×10^{-8}	0.53563	94809	0.599	254000
367.8	0.766	1.84×10^{-8}	0.53563	49729	0.607	133000
387.4	0.743	1.83×10^{-8}	0.53563	29112	0.652	68962
407.1	0.682	1.67×10^{-8}	0.53563	18986	0.748	34823
426.7	0.654	1.54×10^{-8}	0.53563	11812	0.843	18385
446.5	0.661	1.53×10^{-8}	0.53563	7028	0.907	10116
466.4	0.675	1.63×10^{-8}	0.53563	4276	0.972	5608
486.4	0.856	2.01×10^{-8}	0.53563	1940	0.838	3788
506.6	0.952	4.05×10^{-8}	0.53563	1127	0.843	2259
526.3	1.150	3.88×10^{-8}	0.53563	615.8	0.818	1428
546.5	1.440	3.67×10^{-8}	0.53563	330.2	0.812	937.9
566.9	1.580	7.97×10^{-9}	0.53563	215.5	0.829	576.4
587.1	3.350	7.84×10^{-9}	0.53563	54.17	0.847	451.7
607.4	3.350	1.79×10^{-9}	0.53563	31.38	1.12	294.9

Table B.8: Impedance spectroscopy fitting results for annealed x=0.10 Nb:BFPT65 from 304.6°C to 605.1°C

Temperature (°C)	C_1 (nF)	B	m	R_1 (Ω)	C_2 (nF)	R_2 (Ω)
304.6	0.457	2.69×10^{-8}	0.53032	557000	3.00	453000
324.4	0.495	3.24×10^{-8}	0.53032	289000	2.77	253000
344.0	0.544	4.09×10^{-8}	0.53032	144000	2.60	137000
363.7	0.606	5.26×10^{-8}	0.53032	71854	2.49	74946
383.4	0.686	6.71×10^{-8}	0.53032	37234	2.40	43534
403.2	0.798	9.57×10^{-8}	0.53032	19886	2.09	36262
423.2	0.975	1.10×10^{-7}	0.53032	10952	1.91	24496
443.2	1.170	9.75×10^{-8}	0.53032	5606	1.87	13660
463.3	1.370	9.48×10^{-8}	0.53032	2856	1.82	7670
483.3	1.510	9.15×10^{-8}	0.53032	1581	1.80	4373
503.5	1.670	1.19×10^{-7}	0.53032	1015	1.85	2484
523.3	1.820	5.95×10^{-8}	0.53032	578.3	1.81	1525
543.6	1.980	4.17×10^{-8}	0.53032	411.9	1.91	908.7
564.2	2.160	2.23×10^{-8}	0.53032	315.4	2.16	552.8
584.6	2.460	3.99×10^{-7}	0.53032	106.9	1.53	437.3
605.1	2.610	1.28×10^{-6}	0.53032	46.95	1.49	320.3

Table B.9: Impedance spectroscopy fitting results for unannealed x=0.20 Nb:BFPT65 from 308.1°C to 589.0°C

Temperature (°C)	C_1 (nF)	B	m	R_1 (Ω)	C_2 (nF)	R_2 (Ω)
308.1	0.521	2.53×10^{-8}	0.51625	232000	1.58	432000
327.6	0.614	3.45×10^{-8}	0.51625	117000	1.60	211000
347.3	0.802	5.10×10^{-8}	0.51625	58874	1.60	111000
367.3	1.840	1.73×10^{-7}	0.51625	27864	1.30	110000
387.2	3.180	4.48×10^{-7}	0.51625	8696	1.18	77930
407.4	3.640	5.43×10^{-7}	0.51625	4068	1.16	42107
427.4	4.000	5.88×10^{-7}	0.51625	2116	1.15	23151
447.4	4.290	6.04×10^{-7}	0.51625	1171	1.14	13080
467.5	4.470	5.75×10^{-7}	0.51625	697.8	1.15	7498
487.7	4.540	6.42×10^{-7}	0.51625	442.3	1.15	4428
507.9	4.390	5.18×10^{-7}	0.51625	307.1	1.19	2657
527.7	4.530	6.59×10^{-7}	0.51625	189.2	1.20	1663
548.1	4.480	5.33×10^{-7}	0.51625	126.1	1.24	1064
568.6	3.930	3.65×10^{-7}	0.51625	110.1	1.35	663.4
589.0	4.730	3.26×10^{-6}	0.51625	46.09	1.29	468.1

Table B.10: Impedance spectroscopy fitting results for annealed x=0.20 Nb:BFPT65 from 307.7°C to 611.9°C

Temperature (°C)	C_1 (nF)	B	m	R_1 (Ω)	C_2 (nF)	R_2 (Ω)
307.7	0.411	2.30×10^{-8}	0.52083	492000	1.58	728000
327.5	0.464	3.13×10^{-8}	0.52083	234000	1.50	370000
351.0	0.547	4.63×10^{-8}	0.52083	96153	1.46	167000
370.7	0.643	6.43×10^{-8}	0.52083	46273	1.44	88926
390.5	0.769	8.88×10^{-8}	0.52083	22978	1.47	48444
410.6	0.936	1.23×10^{-7}	0.52083	12038	1.56	26938
430.5	1.210	1.65×10^{-7}	0.52083	6250	1.72	15453
450.2	1.600	2.45×10^{-7}	0.52083	3682	2.18	8816
470.3	2.040	2.82×10^{-7}	0.52083	2904	4.37	5072
490.4	2.710	4.12×10^{-7}	0.52083	1516	4.82	3368
510.5	3.190	5.17×10^{-7}	0.52083	824.9	4.43	2115
530.3	3.570	5.37×10^{-7}	0.52083	494.6	3.99	1346
550.6	3.840	4.65×10^{-7}	0.52083	316.3	3.61	878.6
571.0	4.350	9.46×10^{-7}	0.52083	145.8	2.74	646.2
591.4	4.250	2.51×10^{-6}	0.52083	76.11	2.23	464.9
611.9	4.000	3.95×10^{-6}	0.52083	47.20	1.99	334.1

Table B.11: Impedance spectroscopy fitting results for unannealed x=0.30 Nb:BFPT65 from 308.8°C to 606.8°C

Temperature (°C)	C_1 (nF)	B	m	R_1 (Ω)	C_2 (nF)	R_2 (Ω)
308.8	0.481	5.16×10^{-9}	0.62706	631000	0.947	1410000
328.3	0.540	6.85×10^{-9}	0.62706	327000	0.989	673000
347.7	0.627	9.64×10^{-9}	0.62706	168000	1.040	334000
367.3	0.831	1.67×10^{-8}	0.62706	79951	1.060	179000
386.9	1.470	4.41×10^{-8}	0.62706	43894	1.420	116000
406.6	2.020	6.49×10^{-8}	0.62706	23868	1.910	78182
426.3	2.200	8.23×10^{-8}	0.62706	11679	1.940	44615
446.1	2.450	9.39×10^{-8}	0.62706	5157	1.790	26192
466.0	2.530	1.03×10^{-7}	0.62706	2677	1.640	15221
485.9	2.460	1.15×10^{-7}	0.62706	1577	1.520	8938
506.0	2.250	1.46×10^{-7}	0.62706	1022	1.410	5295
526.1	2.240	1.58×10^{-7}	0.62706	598.4	1.280	3297
546.0	2.310	1.34×10^{-7}	0.62706	373.9	1.180	2105
566.4	2.230	2.13×10^{-7}	0.62706	198.2	1.030	1395
586.5	2.180	1.21×10^{-7}	0.62706	164.3	1.000	890.5
606.8	2.070	1.78×10^{-7}	0.62706	115.1	0.911	598.7

Table B.12: Impedance spectroscopy fitting results for annealed x=0.30 Nb:BFPT65 from 304.7°C to 608.5°C

Temperature (°C)	C_1 (nF)	B	m	R_1 (Ω)	C_2 (nF)	R_2 (Ω)
304.7	0.386	1.29×10^{-8}	0.52766	3160000	0.996	176000
324.5	0.430	4.10×10^{-9}	0.52766	2310000	1.120	54344
344.2	0.465	4.98×10^{-9}	0.52766	1070000	1.200	30345
363.9	0.511	6.03×10^{-9}	0.52766	506000	1.310	17181
383.6	0.574	7.20×10^{-9}	0.52766	246000	1.430	10169
403.6	0.662	8.60×10^{-9}	0.52766	123000	1.600	6241
423.4	0.810	1.11×10^{-8}	0.52766	62684	1.930	3800
443.2	1.340	3.46×10^{-8}	0.52766	33035	2.520	2918
463.2	2.230	6.58×10^{-8}	0.52766	18456	2.920	1896
483.3	2.270	7.34×10^{-8}	0.52766	10592	3.280	932.6
503.4	2.130	6.70×10^{-8}	0.52766	6249	3.350	586.2
523.5	1.860	5.87×10^{-8}	0.52766	3874	3.450	361.7
547.5	1.640	4.30×10^{-8}	0.52766	2267	3.320	252.2
567.8	1.450	3.77×10^{-8}	0.52766	1480	3.240	188.1
588.1	1.210	3.07×10^{-8}	0.52766	1024	3.010	109.3
608.5	1.010	3.90×10^{-8}	0.52766	731.9	3.570	63.72

B.7 Arrhenius Plots

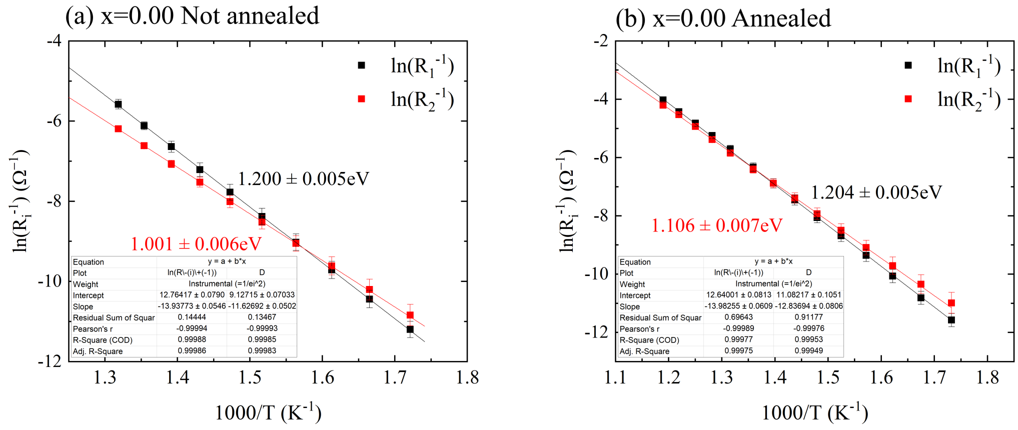
(a) x=0.00 Not annealed

(b) x=0.00 Annealed

Equation	y = a + b*x	
Plot	ln(R\-(i)\+(-1))	D
Weight	Instrumental (=1/ei^2)	
Intercept	12.76417 ± 0.0790	9.12715 ± 0.07033
Slope	-13.93773 ± 0.0546	-11.62692 ± 0.0502
Residual Sum of Squar	0.14444	0.13467
Pearson's r	-0.99994	-0.99993
R-Square (COD)	0.99988	0.99985
Adj. R-Square	0.99986	0.99983

Equation	y = a + b*x	
Plot	ln(R\-(i)\+(-1))	D
Weight	Instrumental (=1/ei^2)	
Intercept	12.64001 ± 0.0813	11.08217 ± 0.1051
Slope	-13.98255 ± 0.0609	-12.83694 ± 0.0806
Residual Sum of Squar	0.69643	0.91177
Pearson's r	-0.99989	-0.99976
R-Square (COD)	0.99977	0.99953
Adj. R-Square	0.99975	0.99949

Figure B.31: Arrhenius plots for x=0.00 Nb:BFPT65 polycrystalline ceramics (a) before annealing, and (b) after annealing

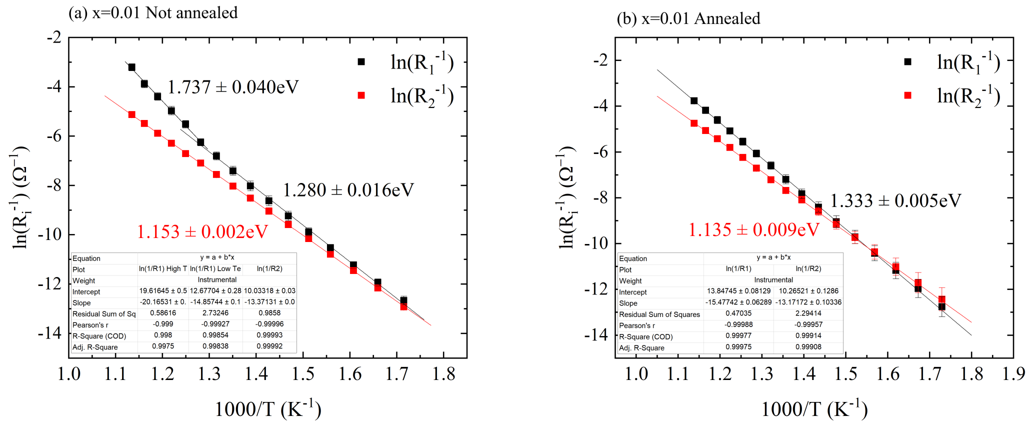
(a) x=0.01 Not annealed

(b) x=0.01 Annealed

Equation	y = a + b*x		
Plot	ln(1/R1) High T	ln(1/R1) Low Te	ln(1/R2)
Weight	Instrumental		
Intercept	19.61645 ± 0.5	12.67704 ± 0.28	10.03318 ± 0.03
Slope	-20.16531 ± 0.	-14.85744 ± 0.1	-13.37131 ± 0.0
Residual Sum of Sq	0.58616	2.73246	0.9858
Pearson's r	-0.999	-0.99927	-0.99996
R-Square (COD)	0.998	0.99854	0.99993
Adj. R-Square	0.9975	0.99838	0.99992

Equation	y = a + b*x	
Plot	ln(1/R1)	ln(1/R2)
Weight	Instrumental	
Intercept	13.84745 ± 0.08129	10.26521 ± 0.1286
Slope	-15.47742 ± 0.06289	-13.17172 ± 0.10336
Residual Sum of Squares	0.47035	2.29414
Pearson's r	-0.99988	-0.99957
R-Square (COD)	0.99977	0.99914
Adj. R-Square	0.99975	0.99908

Figure B.32: Arrhenius plots for x=0.01 Nb:BFPT65 polycrystalline ceramics (a) before annealing, and (b) after annealing

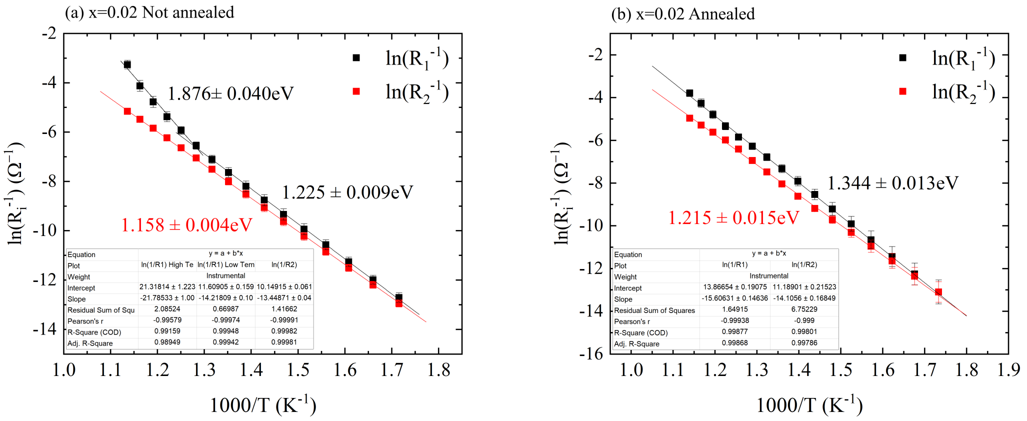

Equation	y = a + b*x		
Plot	ln(1/R1) High Te	ln(1/R1) Low Tem	ln(1/R2)
Weight	Instrumental		
Intercept	21.31814 ± 1.223	11.60905 ± 0.159	10.14915 ± 0.061
Slope	-21.78533 ± 1.00	-14.21809 ± 0.10	-13.44871 ± 0.04
Residual Sum of Squ	2.08524	0.66987	1.41662
Pearson's r	-0.99579	-0.99974	-0.99991
R-Square (COD)	0.99159	0.99948	0.99982
Adj. R-Square	0.98949	0.99942	0.99981

Equation	y = a + b*x	
Plot	ln(1/R1)	ln(1/R2)
Weight	Instrumental	
Intercept	13.86654 ± 0.19075	11.18901 ± 0.21523
Slope	-15.60631 ± 0.14636	-14.1056 ± 0.16849
Residual Sum of Squares	1.64915	6.75229
Pearson's r	-0.99938	-0.999
R-Square (COD)	0.99877	0.99801
Adj. R-Square	0.99868	0.99786

Figure B.33: Arrhenius plots for x=0.02 Nb:BFPT65 polycrystalline ceramics (a) before annealing, and (b) after annealing

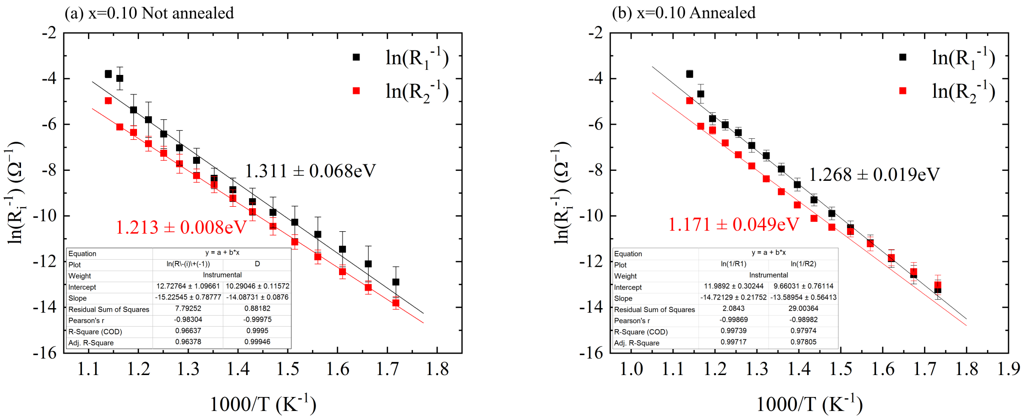

Equation	y = a + b*x	
Plot	ln(R\-(i)\+(-1))	D
Weight	Instrumental	
Intercept	12.72764 ± 1.09661	10.29046 ± 0.11572
Slope	-15.22545 ± 0.78777	-14.08731 ± 0.0876
Residual Sum of Squares	7.79252	0.88182
Pearson's r	-0.98304	-0.99975
R-Square (COD)	0.96637	0.9995
Adj. R-Square	0.96378	0.99946

Equation	y = a + b*x	
Plot	ln(1/R1)	ln(1/R2)
Weight	Instrumental	
Intercept	11.9892 ± 0.30244	9.66031 ± 0.76114
Slope	-14.72129 ± 0.21752	-13.58954 ± 0.56413
Residual Sum of Squares	2.0843	29.00364
Pearson's r	-0.99869	-0.98982
R-Square (COD)	0.99739	0.97974
Adj. R-Square	0.99717	0.97805

Figure B.34: Arrhenius plots for x=0.10 Nb:BFPT65 polycrystalline ceramics (a) before annealing, and (b) after annealing

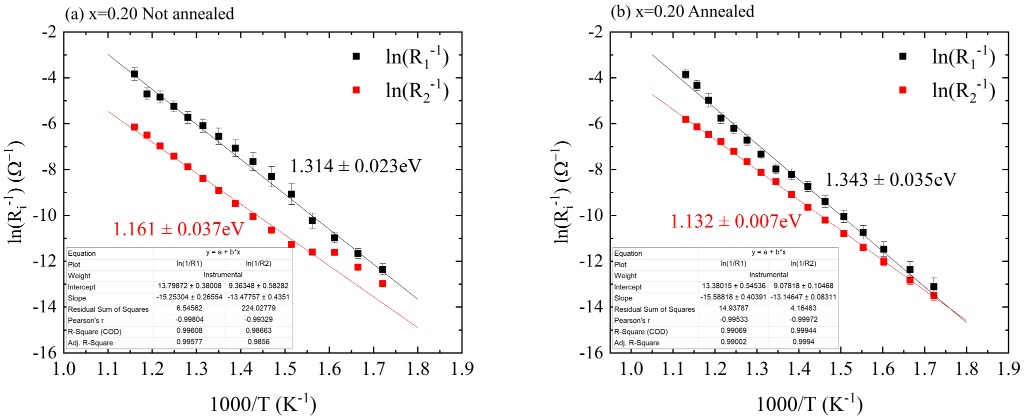

Equation	y = a + b*x	
Plot	ln(1/R1)	ln(1/R2)
Weight	Instrumental	
Intercept	13.79872 ± 0.38008	9.36348 ± 0.58282
Slope	-15.25304 ± 0.26554	-13.47757 ± 0.4351
Residual Sum of Squares	6.54562	224.02779
Pearson's r	-0.99804	-0.99329
R-Square (COD)	0.99608	0.98663
Adj. R-Square	0.99577	0.9856

Equation	y = a + b*x	
Plot	ln(1/R1)	ln(1/R2)
Weight	Instrumental	
Intercept	13.38015 ± 0.54536	9.07818 ± 0.10468
Slope	-15.58818 ± 0.40391	-13.14647 ± 0.08311
Residual Sum of Squares	14.93787	4.16483
Pearson's r	-0.99533	-0.99972
R-Square (COD)	0.99069	0.99944
Adj. R-Square	0.99002	0.9994

Figure B.35: Arrhenius plots for x=0.20 Nb:BFPT65 polycrystalline ceramics (a) before annealing, and (b) after annealing

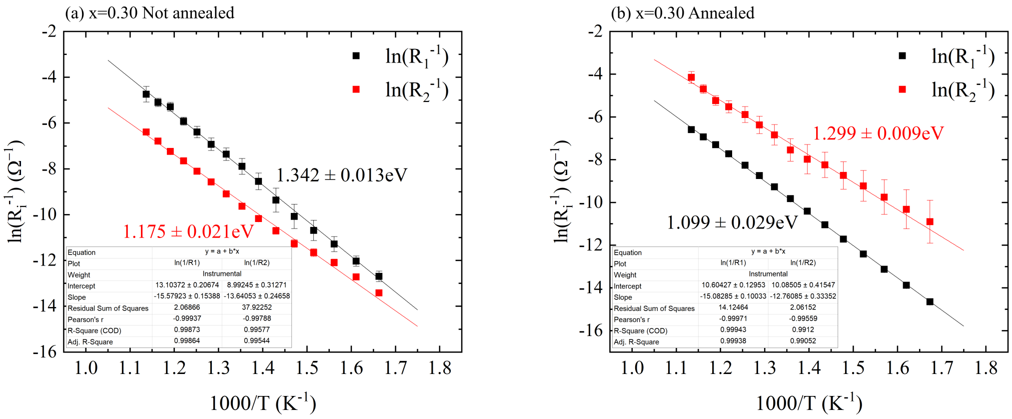

Equation	y = a + b*x	
Plot	ln(1/R1)	ln(1/R2)
Weight	Instrumental	
Intercept	13.10372 ± 0.20674	8.99245 ± 0.31271
Slope	-15.57923 ± 0.15388	-13.64053 ± 0.24658
Residual Sum of Squares	2.06866	37.92252
Pearson's r	-0.99937	-0.99788
R-Square (COD)	0.99873	0.99577
Adj. R-Square	0.99864	0.99544

Equation	y = a + b*x	
Plot	ln(1/R1)	ln(1/R2)
Weight	Instrumental	
Intercept	10.60427 ± 0.12953	10.08505 ± 0.41547
Slope	-15.08285 ± 0.10033	-12.76085 ± 0.33352
Residual Sum of Squares	14.12464	2.06152
Pearson's r	-0.99971	-0.99559
R-Square (COD)	0.99943	0.9912
Adj. R-Square	0.99938	0.99052

Figure B.36: Arrhenius plots for x=0.30 Nb:BFPT65 polycrystalline ceramics (a) before annealing, and (b) after annealing

Appendix C

Supplementary XPS Data

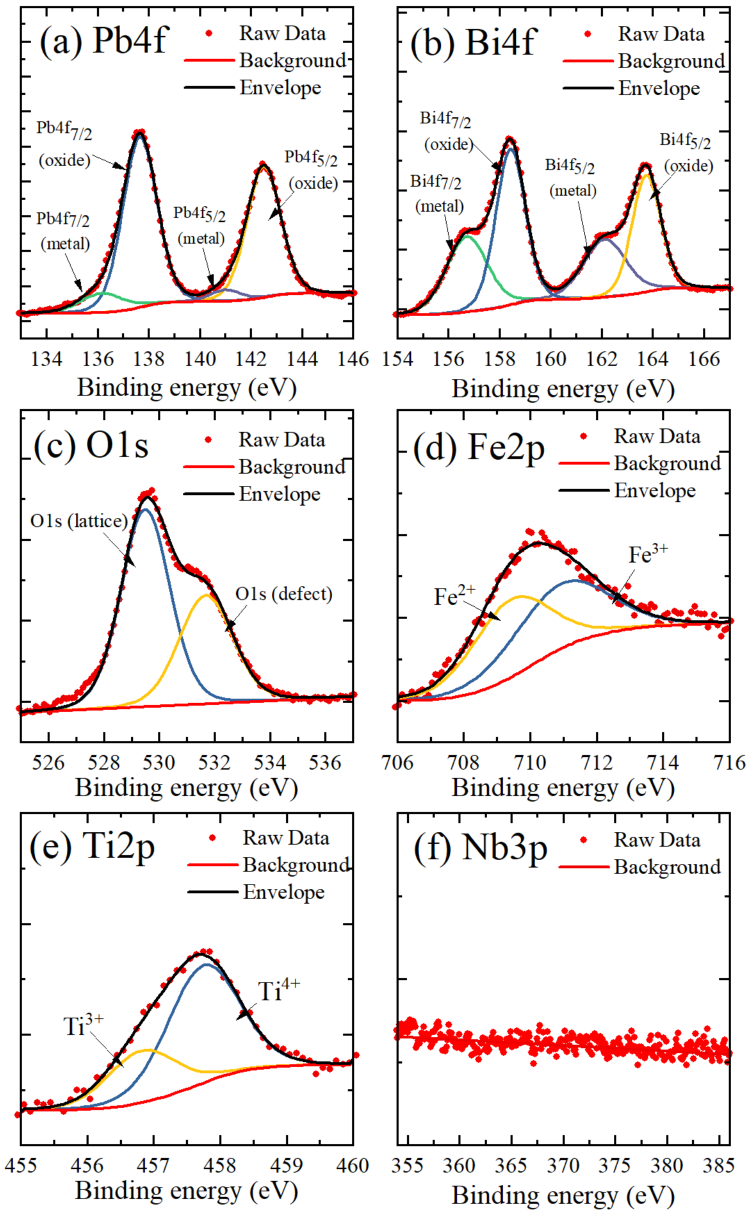

Figure C.1: X-ray photoelectron spectroscopy spectra and fits for (a) Pb4f, (b) Bi4d, (c) O1s, (d) Fe2p, (e) Ti2p, and (f) Nb3p orbitals for unannealed, undoped BFPT65 polycrystalline ceramics

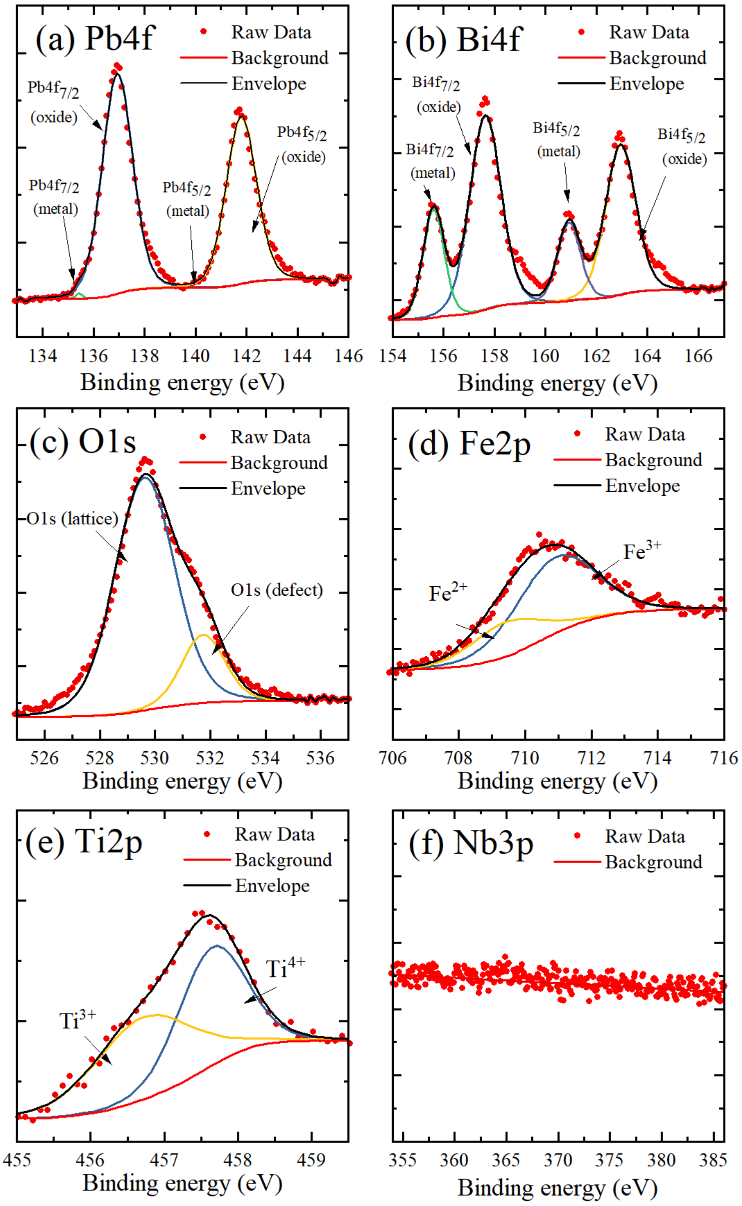

Figure C.2: X-ray photoelectron spectroscopy spectra and fits for (a) Pb4f, (b) Bi4d, (c) O1s, (d) Fe2p, (e) Ti2p, and (f) Nb3p orbitals for unannealed, x=0.01 Nb:BFPT65 polycrystalline ceramics

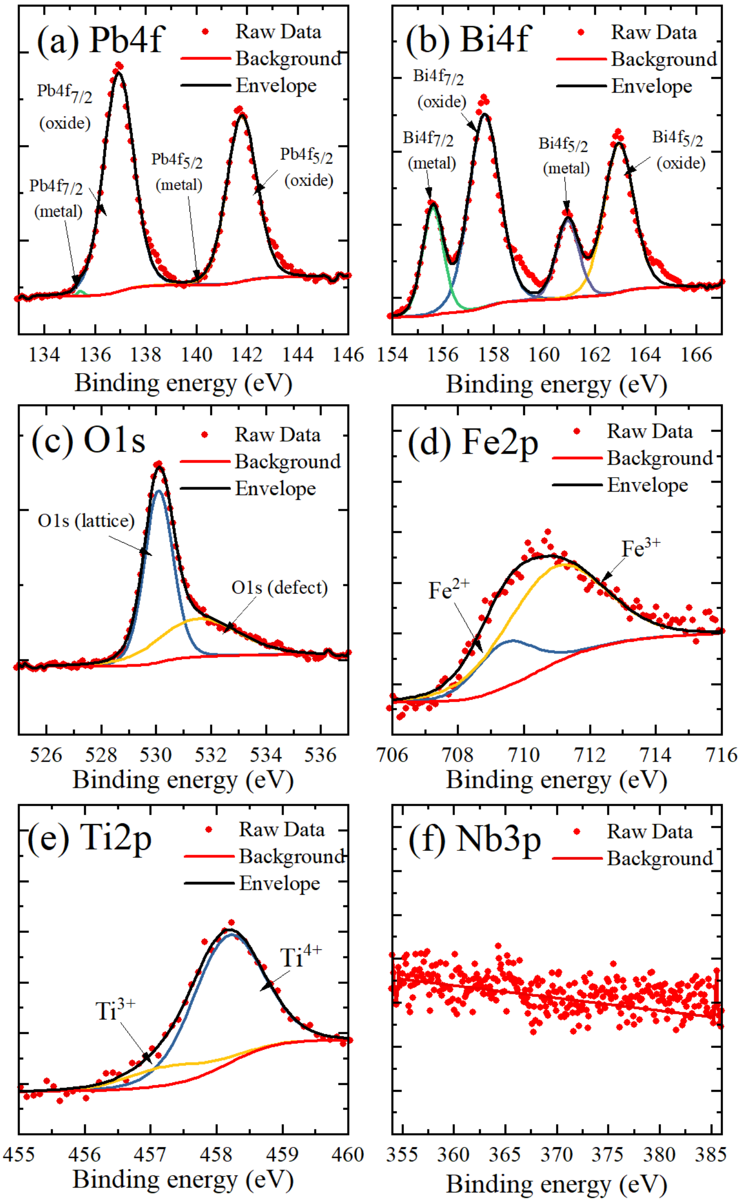

Figure C.3: X-ray photoelectron spectroscopy spectra and fits for (a) Pb4f, (b) Bi4d, (c) O1s, (d) Fe2p, (e) Ti2p, and (f) Nb3p orbitals for unannealed, x=0.02 Nb:BFPT65 polycrystalline ceramics

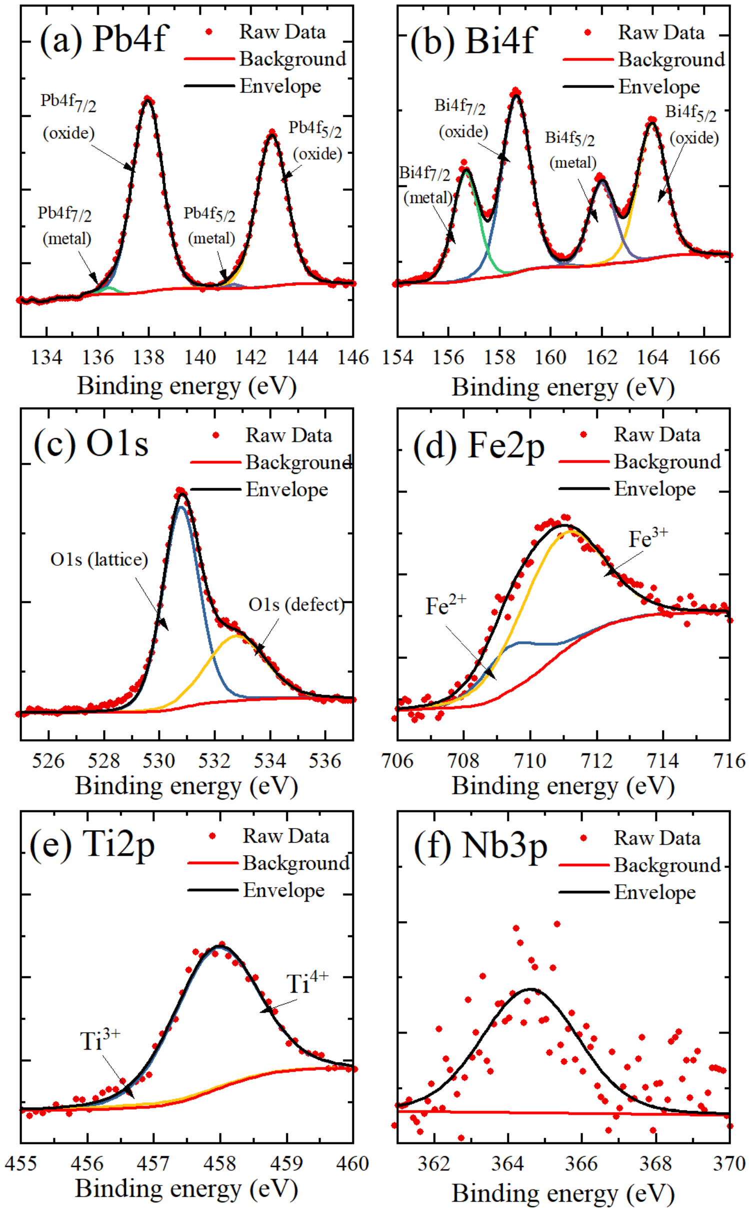

Figure C.4: X-ray photoelectron spectroscopy spectra and fits for (a) Pb4f, (b) Bi4d, (c) O1s, (d) Fe2p, (e) Ti2p, and (f) Nb3p orbitals for unannealed, x=0.10 Nb:BFPT65 polycrystalline ceramics

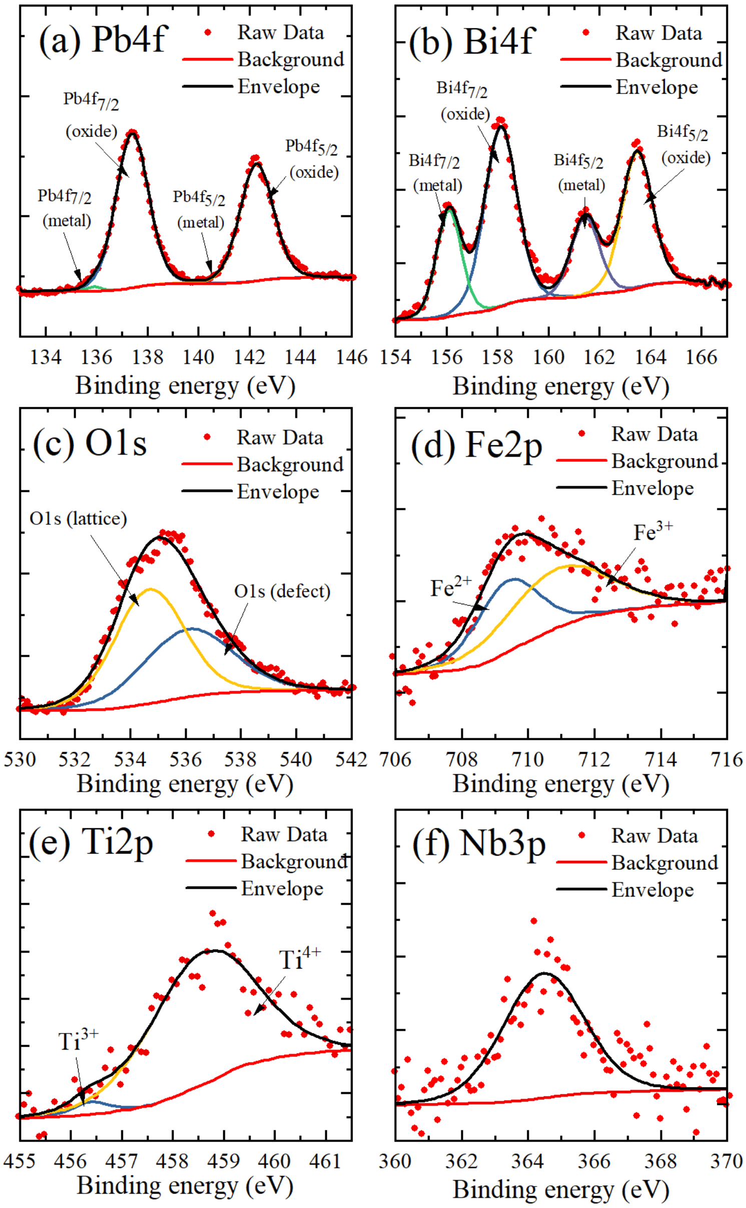

Figure C.5: X-ray photoelectron spectroscopy spectra and fits for (a) Pb4f, (b) Bi4d, (c) O1s, (d) Fe2p, (e) Ti2p, and (f) Nb3p orbitals for unannealed, x=0.20 Nb:BFPT65 polycrystalline ceramics

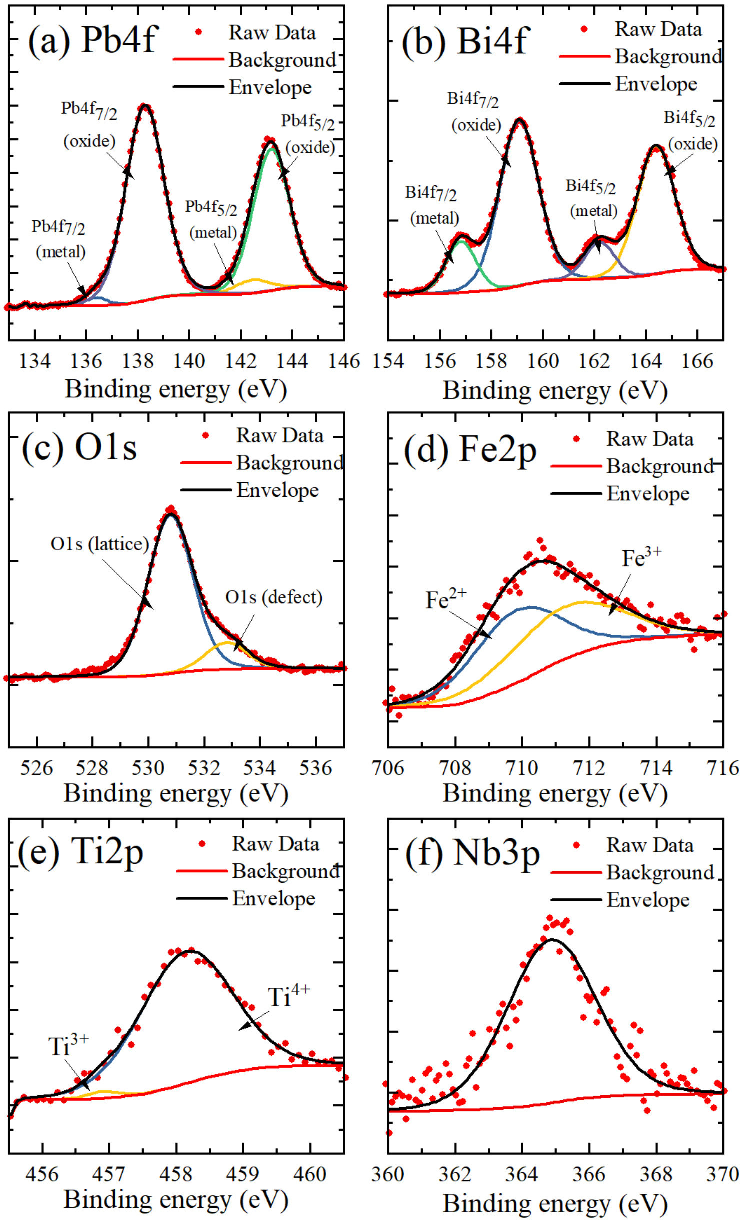

Figure C.6: X-ray photoelectron spectroscopy spectra and fits for (a) Pb4f, (b) Bi4d, (c) O1s, (d) Fe2p, (e) Ti2p, and (f) Nb3p orbitals for unannealed, x=0.30 Nb:BFPT65 polycrystalline ceramics

Appendix D

List of Meetings and Conferences

Date	Conference	Location	Presented work
April 2016	Sustainable functional materials	Scarborough, UK	
July 2016	Thales UK Ltd PhD Symposium	Cheadle, UK	Talk
August 2016	International Symposium on Applications of Ferroelectrics	Darmstadt, DEU	Poster
October 2016	Thales UK Ltd Conference	Templecombe, UK	Talk
February 2017	Thales UK Ltd Conference	Sparkford, UK	Talk
May 2017	International Symposium on Applications of Ferroelectrics	Atlanta, USA	Poster
November 2017	Thales UK Ltd Conference	Leeds, UK	Talk
May 2018	International Symposium on Applications of Ferroelectrics	Hiroshima, JPN	Talk
November 2018	Thales UK Ltd Conference	Reading, UK	Talk
May 2019	International Symposium on Applications of Ferroelectrics	Lausanne, CHE	Poster
December 2019	IOM3 Future Materials Conference	Leeds, UK	Talk

Made in Yorkshire